INAUGURAL - DISSERTATION

zur

Erlangung der Doktorwürde

der

Naturwissenschaftlich - Mathematischen

Gesamtfakultät

der Ruprecht - Karls - Universität

Heidelberg

vorgelegt von

Dipl.-Phys. Michael Clemens Herbst

aus Hildesheim (Niedersachsen)

Tag der mündlichen Prüfung: 23. November 2011

A Search for R-parity Violating Squark Production with the H1 Experiment at HERA

Gutachter: Prof. Dr. Hans-Christian Schultz-Coulon
Prof. Dr. Ulrich Uwer

Kurzfassung

In dieser Arbeit wird eine Suche nach R-paritätsverletzender Supersymmetrie vorgestellt, welche die kompletten HERA Daten analysiert, die bei einer Schwerpunktsenergie von $\sqrt{s} = 319$ GeV mit dem H1 Detektor aufgezeichnet wurden. Die Daten entsprechen einer integrierten Luminosität von 255 pb^{-1} in Positron-Proton- und 183 pb^{-1} in Elektron-Proton-Kollisionen. Einzelne Squarks können im untersuchten Modell resonant durch eine Lepton-Quark-Squark Kopplung λ' erzeugt werden. Mehrere exklusive Kanäle werden untersucht, die auf den Topologien der erwarteten Endzustände der Squarkzerfälle basieren. Die untersuchten Zerfallsmoden der Squarks umfassen direkte Zerfälle, aber auch Zerfälle, die supersymmetrische Partnerteilchen der Eich-Bosonen enthalten und zu Kaskadenzerfällen führen. Die Selektionskanäle basieren entweder auf einem Elektron oder einem Neutrino im Endzustand, und können weitere Jets und Leptonen enthalten. Die selektierten Ereignisse werden mit Vorhersagen des Standard-Modells verglichen. Keine signifikanten Abweichungen von der Untergrunderwartung in den Selektionskanälen konnte festgestellt werden. Die Ergebnisse werden im Rahmen des Minimal-Supersymmetrischen-Standardmodells und des minimalen Supergravitations-Modells interpretiert. Ausschlussgrenzen für die R-paritätsverletzenden Kopplungen λ'_{1j1} und λ'_{11k}, sowie für supersymmetrische Modellparameter, werden bestimmt, unter der Annahme, dass nur eine der Kopplungen die Produktion und den Zerfall von Squarks dominiert. Für eine Stärke der R-paritätsverletzenden Kopplungen, die vergleichbar mit der elektromagnetischen Kopplungsstärke λ'_{1j1} bzw. $\lambda'_{11k} = \sqrt{4\pi\alpha_{em}} = 0.3$ ist, können Squarkmassen von $\tilde{u}^j_L$ Squarks bis zu 275 GeV und von $\tilde{d}^k_R$ Squarks sogar bis zu 290 GeV für alle Squarkgenerationen $j, k = 1, 2, 3$ auf 95% Konfidenzniveau ausgeschlossen werden.

Abstract

A search for R-parity violating supersymmetry is performed in the complete HERA data set taken at a centre-of-mass energy of $\sqrt{s} = 319$ GeV with the H1 detector. The integrated luminosity of the data sets corresponds to 255 pb^{-1} of positron-proton, and 183 pb^{-1} of electron-proton collision data. By introducing a lepton-quark-squark coupling λ' the resonant production of single squarks is expected. Several exclusive selection channels, based on the topologies of final states expected from direct squark decays, and squark decays via gauginos are defined. The selection channels are based on an electron or a neutrino in the final state, and may contain further jets and leptons. All of the selection channels show a good agreement with the background expectation from standard model processes. The results are interpreted in terms of exclusion limits, obtained for the minimal supersymmetric standard model, and for the minimal supergravity model, constraining the strength of the R-parity violating couplings λ'_{1j1} and λ'_{11k}, and the supersymmetric model parameters, under the single coupling dominance hypothesis. For an $R\!\!\!/_p$ coupling strength comparable to the electromagnetic coupling strength, λ'_{1j1} or $\lambda'_{11k} = \sqrt{4\pi\alpha_{em}} = 0.3$, squark masses up to 275 GeV are excluded for $\tilde{u}^j_L$ squarks, with $\tilde{d}^k_R$ squarks further excluded up to 290 GeV, for all three squark generations $j, k = 1, 2, 3$ at the 95% confidence level.

Contents

1 Introduction

"Are you the only institution doing this job?"
inquired Mr Tompkins. "Oh no! Similar machines exist in
Brookhaven National Laboratory on Long Island, New York;
in CERN (Corporation Europeenne de Recherche Nucleaire)
Laboratory near Geneva in Switzerland, and in
Shchelkunchik (Nutcracker) Laboratory near Moscow in Russia.
They are all looking for a needle in a haystack, and, by God,
they find one once in a while!"

from "Mr Tompkins explores the atom"
by George Gamow, The University Press (1951).

The discovery of the atomic nucleus, the electron, the neutrinos, and particles, which are only found naturally in cosmic showers initiated by high-energetic particles from across the universe, made scientists curious about exploring further the inner mechanisms by which matter in the universe is created and interacts. From fundamental science emerged many revolutionary new theories in the last century: from Maxwell's description of electromagnetism; over Einstein's theory of general relativity; the discovery and classification of a complete zoo of elementary particles and fundamental interactions; to an increasingly accurate description of the creation and history of the universe. Much progress has been made in the field of elementary particles in the last decades, which led to a simple framework incorporating the elementary particles and the fundamental interactions: the standard model of particle physics.

Today, a great effort is spent on understanding the mechanism by which elementary particles acquire their masses. The Higgs boson is expected to be the key to the generation of mass of the fundamental particles, and the last missing observation in the standard model particle zoo. Particle physics does not end with the discovery of the Higgs boson, if at all. More fundamental theories have been proposed, extending the standard model by adding new particles and interactions.

This work contributes to the scientific progress in a search for new particles, which extend the known theory of the standard model. The complete data set collected during 15 years of operation of the electron-proton storage ring HERA at DESY (Hamburg, Germany) is analysed in a search for new particles, which are called squarks. These squarks emerge in the so called theory of supersymmetry, which extends the particle content of the standard model. Supersymmetry proposes a new symmetry interrelating bosons with fermions. This remarkable symmetry would resolve some of the existing issues of the standard model theory. Squarks are expected to be created in direct interactions of electrons and quarks of the proton, making HERA an ideally suited testing ground. Previous searches for supersymmetry have shown no sign for new physics processes at HERA. The data sets analysed in the course of this work represent an increase of a factor of ≈ 13 for electron-proton, and a factor of ≈ 4 for positron-proton collision data, compared to previously performed searches at HERA. Also in

this work, no deviation of the data from the predictions of the standard model could be discovered. However, the existing constraints on new physics scenarios could be further extended into previously unexplored regions [1].

With the end of HERA operation, this analysis may represent the final word on supersymmetry searches in the collected data set. Other high energy collider experiments, like the Large Hadron Collider at CERN, and the TeVatron collider, at Fermilab, are able to probe new physics scenarios in much higher energy domains. These experiments are also expected to find signs of the Higgs boson in the near future. Searches for new physics have already been performed at these experiments, but did also find no signs up to now.

The hunt for the *needle in a haystack* continues.

Chapter 2 summarises some aspects of the standard model theory relevant to the presented analysis, and introduces the basic concepts of supersymmetry. The HERA storage ring and the H1 experiment are introduced in chapter 3. Monte Carlo generators used for standard model predictions are discussed in chapter 4. The object reconstruction methods are explained in chapter 5, and the methods for the reconstruction of global event and object quantities are discussed in chapter 6. Criteria ensuring a good quality of the analysed data sets are presented in chapter 7. The data analysis is discussed in chapter 8, and the results are interpreted in chapter 9. Chapter 10 concludes with a summary of the presented analysis. Appendix A contains some supplementary material.

Appendix B contains details on a supersymmetry search performed with the ATLAS experiment at the LHC, and presents a cross check of the constraints derived for the masses of supersymmetric particles.

2 Theory

In this chapter, an introduction to the basic concepts of the standard model theory is given. The physics processes at HERA are discussed, and a motivation for theories beyond the standard model is given. Supersymmetry, as a candidate for a new physics scenario, is introduced, and previous searches for new physics are discussed.

2.1 The Standard Model of Particle Physics

The standard model (SM) of particle physics is a renormalisable quantum field theory, which describes the fundamental processes of interaction between the fundamental building blocks of matter [2; 3]. It describes the electroweak and strong interactions between particles based on the gauge group $SU(3)_C \times SU(2)_L \times U(1)_Y$, where the indices indicate the type of charge the symmetry gauge groups act on: the color C; the weak isospin L; and the weak hypercharge Y, respectively.

Standard Model Particle Content

Two fundamentally different kinds of elementary particles are distinguished within the SM: Half-integer spin fermions describe matter particles, whereas integer spin bosons represent gauge quanta, which mediate electroweak and strong interactions between the matter particles. Fermions are further distinguished into leptons ℓ and quarks q. Leptons exist in six different flavours, three electrically charged lepton flavours with $Q/e = -1$, in units of the elementary charge e, and three electrically neutral lepton flavours, so called neutrinos. Quarks exist also in six flavours, three *up-type* flavour quarks with positive electric charge $Q/e = +\frac{2}{3}$, and three *down-type* flavour quarks with negative electric charge $Q/e = -\frac{1}{3}$. Quarks and leptons can be arranged in three generations $i = 1, 2, 3$, which each contain a charged lepton ℓ_i^-, a corresponding neutrino $\nu_{\ell,i}$, an up-type flavour quark u_i, and a down-type flavour quark d_i.

The first generation consists of the lightest leptons and quarks, and contains the electron e^-, the electron-neutrino ν_e, the up-quark u, and the down-quark d. The second generation contains heavier versions of the first generation fermions, and consists of the muon μ^-, the muon-neutrino ν_μ, the charm quark c, and the strange quark s. The third generation contains the heaviest versions of leptons and quarks, and contains the tau lepton τ^-, the tau-neutrino ν_τ, the top quark t, and the bottom quark b. For each fermion f also the antifermion $\bar{f}$ state exists with inverted charge, *e.g.* the antielectron is also called positron e^+.

Leptons participate only in electroweak interactions, while quarks, which carry color charge, are also subject to the strong interaction. Each quark flavour can carry three different color charges (red, green, blue). Quarks are the constituents of all hadronic matter, *i.e.* baryons (qqq) and mesons ($q\bar{q}$). Contrary to leptons, quarks are not observed as free particles, and must always be confined inside colorless objects. The

particles of the first generation build up the ordinary matter in the universe. Second and third generation particles are mainly produced in high-energy interactions.

Table 2.1 shows a summary of the SM fermions, arranged in weak isospin doublets L and Q, and singlets E, U and D, respectively. The third component of the weak isospin T_3, and the electric charge Q of a particle are connected via the weak hypercharge Y by the relation $Q = T_3 + Y/2$. The baryon number B and the lepton number L are quantum numbers, which are conserved in the SM interactions.

The well established theory of gravity is not included in the SM framework. Compared to the electroweak and strong interactions, gravitational interactions between elementary particles are completely negligible. Furthermore, the theory of gravity is not renormalisable.

Strong Interaction

Quarks were first postulated in 1964 by M. Gell-Mann in form of the quark model [4]. From this picture emerged Quantum Chromo Dynamics (QCD), which is based on the symmetry gauge group $SU(3)_C$. The $SU(3)_C$ gauge group describes the strong interactions between particles with color charge. The generators of the $SU(3)_C$ gauge group are the Gell-Mann matrices G_i. Quarks transform as triplets under $SU(3)_C$ gauge transformations. Leptons on the other hand, as non-colored objects, transform as singlets under $SU(3)_C$, and do participate in strong interaction. The gauge bosons of the strong interaction are the eight massless gluons g_i, $i = 1, .., 8$. They carry color charge themselves, and are thus subject to self-interactions. The strength of the strong interaction, given by the strong coupling α_s, increases with increasing distance between two color charges. This leads to the so called confinement which explains why quarks cannot be observed as free particles, but can only be confined inside colorless hadrons. Experimentally, quarks are only observed as jets, which are collimated showers of hadrons. The opposite effect, a decreasing strong coupling for decreasing distances between color charges, is known as asymptotic freedom. Quarks are considered to behave as quasi-free particles, when confined inside a hadron, e.g. the neutron or the proton. Asymptotic freedom corresponds to a small strong coupling α_s, and is a pre-requisite for perturbative calculations in QCD.

Electroweak Interaction

The electroweak theory, or GSW theory [5], designed by S.L. Glashow, A. Salam and S. Weinberg during 1961-67, gives a unified description for the electromagnetic and weak interactions. The electroweak formalism is based on the symmetry group $SU(2)_L \times U(1)_Y$. The weak hypercharge Y is the generator of the gauge group $U(1)_Y$. For the weak isospin, the Pauli matrices σ_i are the generators of the gauge group $SU(2)_L$. The intermediate weak bosons W^+, W^-, W^0, and the B^0 boson mediate the electroweak force between fermions with coupling constants g and g'. After electroweak symmetry breaking is introduced by the Higgs mechanism (see following section), the neutral intermediate weak bosons W^0 and B^0 mix via the Weinberg angle θ_W to form the neutral mass eigenstates of the electroweak interaction, the Z^0-boson and the massless photon γ:

$$\begin{pmatrix} \gamma \\ Z^0 \end{pmatrix} = \begin{pmatrix} \cos\theta_W & \sin\theta_W \\ -\sin\theta_W & \cos\theta_W \end{pmatrix} \begin{pmatrix} B^0 \\ W^0 \end{pmatrix}$$

The electroweak couplings g' and g are related via the Weinberg angle $\frac{g'}{g} = \tan(\theta_W)$, which can be expressed by the masses of the W and Z bosons:

$$\sin^2\theta_W = 1 - \frac{M_W^2}{M_Z^2} \ .$$

The experimental value of θ_W depends on the momentum transfer Q at which it is measured in particle interactions, and on the used renormalisation scheme. A precise measurement in e^+e^- collisions at the Z boson mass yields in the modified minimal subtraction scheme $\overline{MS}$ a value of $\sin^2(\theta_W) = 0.23108 \pm 0.00005$ [6], which corresponds to a weak mixing angle $\theta_W \approx 28.7°$.

The electromagnetic interaction is mediated via the massless photon with coupling constant α_{qed} between all fermions with an electric charge. The weak interaction is mediated via the exchange of the weak vector gauge bosons $W^\pm$ and Z^0. The neutral weak gauge boson Z^0 can be exchanged by all fermions. By contrast, the charged weak gauge bosons $W^\pm$ only couple to left-handed fermions. To account for this parity violation in weak interactions, which was observed first in 1957 [7], fermions are treated differently depending on their chirality state. A fermion field $\psi = \psi_L + \psi_R$ is defined, as the linear combination of a left-handed ψ_L and a right-handed ψ_R component.

$$\psi_L^{\ell_i} = \begin{pmatrix} \nu_i \\ \ell_i^- \end{pmatrix}_L , \qquad \psi_L^{q_i} = \begin{pmatrix} u_i \\ d_i' \end{pmatrix}_L \qquad \begin{array}{l} \psi_R^{\ell_i} = \ell_{i,R},\ \psi_R^{u_i} = u_{i,R},\ \psi_R^{d_i'} = d_{i,R}' \\ i = 1,2,3 \text{ family generation index} \end{array}$$

The left-handed fermions belong to isospin doublets of the symmetry gauge group $SU(2)_L$, whereas the right-handed fermions transform as singlets. For down-type quarks, the weak physical eigenstates d', s', b' arise from the mass eigenstates d, s, b through mixing via the Cabibbo-Kobayashi-Maskawa [8] (CKM) matrix V_{CKM} : $d_i' = \sum_j V_{ij} d_j$. Four parameters are introduced to parametrise the unitary CKM-matrix: three angles and one CP-violating phase. The neutrino is treated with zero mass in the SM, and thus only left-handed neutrinos exist. Although neutrinos are considered massless in the SM theory, measurements of atmospheric and solar neutrino fluxes have established masses for neutrinos. A formalism exists which mixes the neutrino mass eigenstates to form flavour eigenstates via the Pontecorvo-Maki-Nakagawa-Sakata [9] (PMNS) mixing matrix V_{PMNS}. Some properties of the SM interactions are summarised in Table 2.2.

The Higgs Mechanism

The SM Lagrangian consists of a part for the electroweak and strong gauge interactions, and a part that contains the Higgs potential and the Higgs Yukawa interactions [10]. Because explicit mass terms in the SM Lagrangian are not invariant under $SU(2)_L$ gauge transformations, and would destroy the renormalisability of the SM theory, the

Higgs mechanism is needed to generate masses of fermions and weak gauge bosons, invented in 1964 by P. Higgs [11].

The Higgs mechanism introduces a complex scalar field H, which transforms as an isospin doublet under $SU(2)_L$ in the SM. The potential for this Higgs field is given by

$$V(H) = m^2(H^\dagger H) + \frac{\lambda}{2}(H^\dagger H)^2 \quad \text{with} \quad \lambda > 0, \quad m^2 < 0,$$

with the Higgs mass parameter m^2 and the Higgs coupling constant λ. The electroweak symmetry is spontaneously broken by the Higgs field acquiring a non-vanishing vacuum expectation value $\nu = \sqrt{\lambda/m^2}$. One physical neutral scalar Higgs boson h^0 is expected to emerge from symmetry breaking, which is expected to have a mass in the order of the electroweak breaking scale $M_{EW} \sim 100$ GeV. The photon remains massless after symmetry breaking, fermions acquire mass coupling to the Higgs field, and the intermediate weak bosons mix to form the massive weak gauge bosons.

The scalar Higgs boson h^0 is the only particle of the SM theory that has not yet been discovered experimentally. The world's largest colliders are built to discover the mechanism that gives mass to the elementary particles. Searches at modern collider experiments constrain the Higgs mass parameter m_H at the 95% confidence level. The direct search for the SM Higgs boson at LEP has set a lower bound on the Higgs mass at $m_H > 114.4$ GeV [12]. The LEP Electroweak Working Group [13] has published indirect constraints on the Higgs mass, determined in a fit of the SM to precision electroweak measurements. The most probable value for the SM Higgs boson is determined to $m_H = 92^{+34}_{-26}$ GeV [13], which is already excluded by the direct search limit. An upper limit from this fit constrains the Higgs mass to be lower than $m_H < 161$ GeV. The χ^2 distribution of the fit is shown in Figure 2.1.

The TeVatron Electroweak Working Group [14] excluded in direct searches for the Higgs boson the mass range 100 GeV $< m_H <$ 108 GeV and 156 GeV $< m_H <$ 177 GeV using an integrated luminosity of 8.6 fb^{-1} [15]. Leaving only a small window open for the Higgs mass. Most recently, the LHC experiments ATLAS and CMS were able to join the hunt for the Higgs boson, and excluded already a wide range of Higgs scenarios using $1.0 - 2.3$ fb^{-1} for mass hypotheses: 146 GeV $< m_H <$ 232 GeV, 256 GeV $< m_H <$ 282 GeV, and 296 GeV $< m_H <$ 466 GeV by the ATLAS experiment [16]; and 145 GeV $< m_H <$ 216 GeV, 226 GeV $< m_H <$ 288 GeV, and 310 GeV $< m_H <$ 400 GeV by the CMS experiment [17]. Just a small range remains for the SM Higgs.

2.2 Electron-Proton Interactions in the Standard Model

The collisions of electrons[1] and protons at high energies can be studied at the HERA collider (see section 3.1) using the H1 apparatus (see section 3.2). A brief introduction to the SM physics processes at HERA is given in the following.

The HERA accelerator is often compared to a huge electron microscope: The high energetic electron probe is able to resolve the substructure of the proton in the scattering process. The process by which the structure of the proton can be explored is

[1] The term electron is used in a generic way henceforth, *i.e.* referring to the charge of the electron means distinguishing electrons and positrons.

	chiral fermion fields $\psi^{q,\ell}$			Q/e	T_3	Y	$SU(3)_C$, $SU(2)_L$	B	L
L	$\begin{pmatrix}\nu_e\\ e^-\end{pmatrix}_L$	$\begin{pmatrix}\nu_\mu\\ \mu^-\end{pmatrix}_L$	$\begin{pmatrix}\nu_\tau\\ \tau^-\end{pmatrix}_L$	0 -1	$+\frac{1}{2}$ $-\frac{1}{2}$	-1	$\mathbf{1},\mathbf{2}$	0 0	1 1
E	e^-_R	μ^-_R	τ^-_R	-1	0	-2	$\mathbf{1},\mathbf{1}$	0	1
Q	$\begin{pmatrix}u\\ d'\end{pmatrix}_L$	$\begin{pmatrix}c\\ s'\end{pmatrix}_L$	$\begin{pmatrix}t\\ b'\end{pmatrix}_L$	$+\frac{2}{3}$ $-\frac{1}{3}$	$+\frac{1}{2}$ $-\frac{1}{2}$	$+\frac{1}{3}$	$\mathbf{3},\mathbf{2}$	$+\frac{1}{3}$ $+\frac{1}{3}$	0 0
U	u_R	c_R	t_R	$+\frac{2}{3}$	0	$+\frac{4}{3}$	$\mathbf{3},\mathbf{1}$	$+\frac{1}{3}$	0
D	d'_R	s'_R	b'_R	$-\frac{1}{3}$	0	$-\frac{2}{3}$	$\mathbf{3},\mathbf{1}$	$+\frac{1}{3}$	0

Table 2.1: Summary of the particle field content of the SM. The electric charge Q, the third component of the weak isospin T_3, the weak hypercharge Y, the irreducible representation within the symmetry gauge groups $SU(3)_C$ and $SU(2)_L$, baryon number B, and lepton number L are given.

force	gauge symmetry group	generator	gauge bosons	Q/e	T_3	$SU(3)_C$, $SU(2)_L$
electromagnetic	$U(1)_{em}$	Q	γ	0	0	$\mathbf{1},\ \mathbf{1}$
weak	$SU(2)_L$	σ_i $(i=1,2,3)$	W^+ W^- Z^0	$+1$ -1 0	$+1$ -1 0	$\mathbf{1},\ \mathbf{3}$
electroweak	$SU(2)_L \times U(1)_Y$	Y σ_i $(i=1,2,3)$	B^0 W^1 W^2 W^3	0 $+1$ -1 0	0 $+1$ -1 0	$\mathbf{1},\ \mathbf{1}$ $\mathbf{1},\ \mathbf{3}$
strong	$SU(3)_C$	$G_i=\frac{\Lambda_i}{2}$ $(i=1,..,8)$	g_i	0	0	$\mathbf{8},\ \mathbf{1}$

Table 2.2: Summary of the gauge interactions in the SM. For each force, the underlying gauge symmetry groups, generators of the gauge symmetry groups, the gauge bosons mediating the force, the electric charge Q, the third component of the weak isospin T_3, and the irreducible representation within the symmetry gauge groups $SU(3)_C$ and $SU(2)_L$ are given. The weak hypercharge Y is 0 for all gauge bosons.

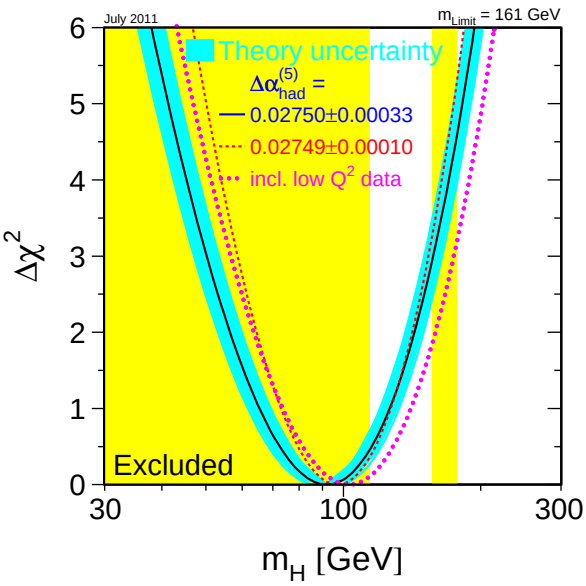

Figure 2.1: χ^2 distribution for the electroweak fit of the SM Higgs mass m_H obtained from precision electroweak measurements at high virtualities Q^2 in a fit of the SM [18]. The yellow band indicates exclusion limits from direct LEP [12] and TeVatron searches. More recent results from the TeVatron [15] and the LHC [16; 17] are available.

called deep-inelastic scattering (DIS) [19]. In a naive picture of the proton, the quark parton model (QPM) [20], the quantum numbers of the proton are explained by three quark constituents, which carry on average each 1/3 of the proton momentum, two u quarks, and one d quark. In the QPM, the partons are considered as non-interacting, quasi-free particles inside the proton. In the QCD description of a proton, it consists of interacting constituent partons, which are the so called valence quarks, and the so called sea of gluons and sea-quark pairs. The valence quark contribution of the partons to the proton structure is expressed in the u_v quark, and d_v valence quark probability densities in the proton, also called valence parton density functions (pdfs). Assumptions about the intrinsic flavour content of the proton influence the predictions for the pdfs.

In electron-proton scattering, the electron interacts via the exchange of a gauge boson with a constituent from the proton. The quantity that defines the resolving power of the electron probe inside the proton is the virtuality of the exchanged gauge boson Q^2, which corresponds to a spatial resolution $\Delta r \sim 1/Q$.

Depending on the type of the exchanged gauge bosons, different processes are distinguished in ep scattering at HERA. In lowest order neutral current (NC) DIS events an electrically neutral γ or Z^0 is exchanged between the electron and a quark from the proton, and an electron in addition to the hadronic final system X are expected in the final state ($ep \to e + X$). By the exchange of a charged $W^{\pm}$ with a quark the electron transforms into an electron-neutrino. The process is called charged current (CC) DIS, and a neutrino in addition to the hadronic final system is expected in the final state

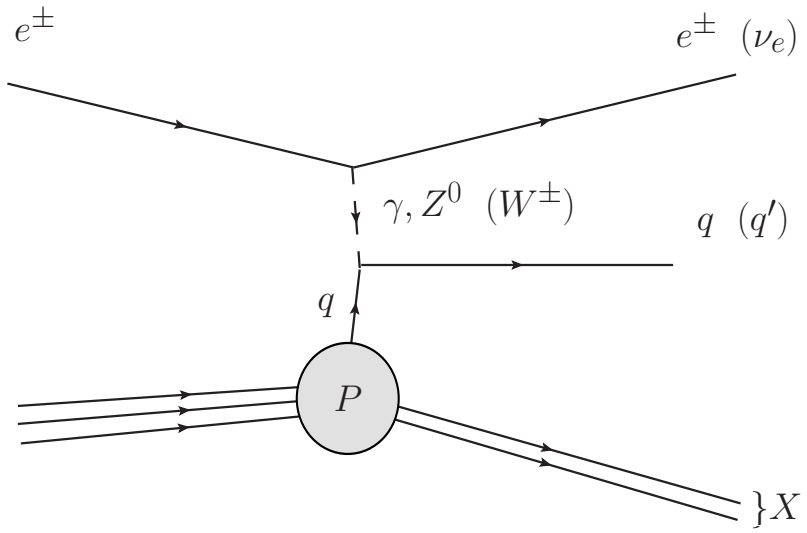

Figure 2.2: Schematic view of the deep-inelastic scattering processes at HERA. Shown is a generic diagram for lowest order neutral current and charged current processes with γ/Z and $W^{\pm}$ exchange between a parton (q) from the proton (P) and an electron ($e^{\pm}$), respectively. The outgoing scattered electron or electron-neutrino (ν_e), as well as the outgoing parton (q, q') and the hadronic final state (X) are also indicated.

($ep \to \nu + X$). A schematic drawing of the DIS processes is shown in Figure 2.2. For very low virtualities $Q^2 \approx 0$ GeV^2 of the exchanged photon, the scattering process is called photoproduction (γp). If the ep scattering process involves a gluon instead of a quark on the proton side, the process is called boson-gluon fusion, which is the dominant process to produce heavy quark flavours at HERA. The QCD equivalent to the QED Compton process, the QCD Compton process, by which quarks absorb virtual photons and emit gluon radiation, has a sizeable cross section in ep scattering.

Kinematics of DIS

The kinematics of the DIS scattering process are described in the naive QPM using four lorentz-invariant scalar quantities: the virtuality Q^2 of the exchanged boson in DIS; the momentum fraction x of the proton carried by the interacting quark; and the inelasticity y of the scattering process. Neglecting masses, the quantites are related by the squared centre-of-mass energy s by [19]

$$Q^2 = x \cdot y \cdot s \ .$$

Consequently, only two of the quantities are independent at a fixed centre-of-mass energy. For an electron-proton collider the squared centre-of-mass energy is given by the mandelstam variable $s = (p + k)^2 \approx 4E_e E_p$. With k denoting the incident electron four-vector, k' the outgoing electron four-vector, and p the incident proton four-vector, the virtuality of the exchanged boson is defined as

$$Q^2 = -q^2 = -(k - k')^2 \ ,$$

corresponding to the negative squared four-momentum transfer from the electron to the parton. The momentum fraction x carried by the struck parton can be identified with the Bjorken x scaling variable and is defined as [19]:

$$x = \frac{Q^2}{2 \cdot p \cdot q}$$

The fractional energy-loss of the incident electron describes the inelasticity y of an event and is calculated as [19]

$$y = \frac{p \cdot q}{p \cdot k}.$$

The experimental reconstruction of these quantities is discussed in section 6.1.

Neutral Current and Charged Current Cross Section in DIS

The NC DIS cross section formula in ep collisions can be expressed in terms of the generalised structure functions F_2, xF_3 and F_L. The neutral current Born-level cross section in the ultra-relativistic approximation is given by [21]:

$$\frac{d^2\sigma^B_{NC}}{dxdy} = \frac{2\pi\alpha^2_{qed}s}{Q^4}\left[Y_+F_2(x,Q^2) + Y_-xF_3(x,Q^2) - y^2F_L(x,Q^2)\right]$$

where the fine structure constant α_{qed} and the abbreviation $Y_\pm = 1 \pm (1-y)^2$ are used. A similar description holds for the CC DIS cross section, using the generalised structure functions W_2, W_3 and W_L for charged currents [21]:

$$\frac{d^2\sigma^B_{CC}}{dxdy} = \frac{G_\mu s}{4\pi}\left(\frac{M^2_W}{Q^2+M^2_W}\right)^2\left[Y_+W_2(x,Q^2) + Y_-W_3(x,Q^2) - y^2W_L(x,Q^2)\right]$$

where the fermi constant G_μ is used. The exchange of $W^\pm$ and Z^0 bosons in weak interactions is suppressed by their high masses in the propagators. At low values of Q^2, the exchange of photons dominates the scattering process. Only for high values of $Q^2 \gg M^2_W, M^2_Z$, the exchange of the electroweak bosons contributes significantly to the cross sections, which decrease as $1/Q^4$. Measurements of the NC DIS and CC DIS cross sections are shown in Figure 2.3a. For cross sections in ep scattering with a polarized lepton beam, a dependence on the lepton beam polarization is expected. A measurement of the CC DIS cross section is shown in Figure 2.3b. The structure functions in the cross sections depend on the pdfs. A HERA measurement of pdfs is shown in Figure 2.4.

2.3 Beyond the Standard Model

Despite the great success of the SM describing the phenomena observed at modern collider experiments, some fundamental issues arise questioning the naturalness of the theory. For example, why are there exactly 3 families of leptons and quarks? Is the unification of strong and electroweak interactions possible? Where does the mass hierarchy between elementary particles arise from? Why do we observe a matter-antimatter

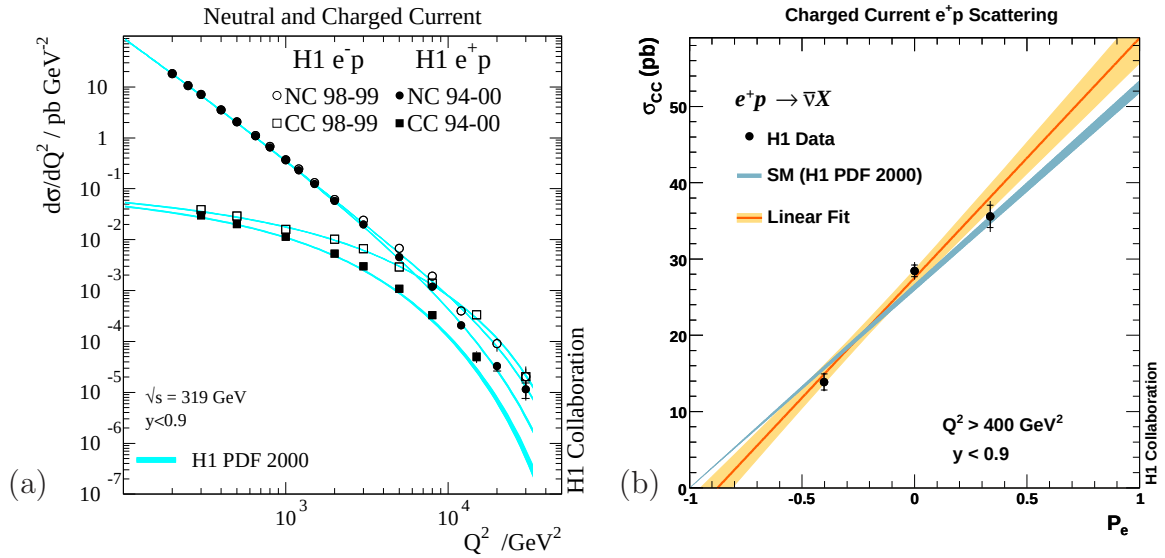

Figure 2.3: Shown is (a) a comparison of the measured differential cross sections $d\sigma_{NC}/dQ^2$ and $d\sigma_{CC}/dQ^2$ from e^+p and e^-p scattering at HERA from the H1 data (points, squares) with SM predictions (lines) [22]. (b) The positron beam polarisation P_e dependence of the total inclusive charged current cross section σ_{CC} measured at H1 (points) compared to Monte Carlo predictions (lines) is shown [23].

asymmetry in the universe? The most popular candidate for a theory beyond the SM is probably supersymmetry. Supersymmetry has been proposed to create an additional symmetry between fermions and bosons. Its mathematical structure allows to resolve some of the existing issues of the SM. It is considered a candidate for a grand unified theory (GUT) [10]. A GUT theory is expected to unify the fundamental interactions, and may also incorporate gravity.

The SM is expected to be the proper effective theory only up to a certain energy scale, where effects from new physics are expected to manifest itself. Physics up to the electroweak scale $M_{EW} \sim 100$ GeV, where the electroweak unification, or rather breaking, takes place, are well in agreement with the predictions of the SM. However, in GUT theories, a unification of the strong and electroweak interaction is expected at the scale $M_{GUT} \sim 10^{16}$ GeV [25]. The symmetry group $SU(3)_C \times SU(2)_L \times U(1)_Y$ of the SM could be embedded in a higher dimensional gauge symmetry group within GUT theories. The presence of these two distinctive scales M_{GUT} and M_{EW} is known as the hierarchy problem. A breaking mechanism for the GUT group and the electroweak theory, needs to be fine tuned at the level of $M_{GUT}/M_{EW} \sim 10^{-14}$ to produce the desired symmetry breaking pattern [10]. A further problem due to the huge difference in these scales arises from quadratic divergent corrections to the Higgs mass. Through loop diagrams, divergent contributions of fermions and bosons to the bare Higgs mass appear which can be regulated by imposing another scale, the cut-off scale Λ. The light Higgs mass depends then quadratically on the cut-off scale Λ and would result in a very heavy Higgs, not in agreement with a light Higgs expected from the electroweak

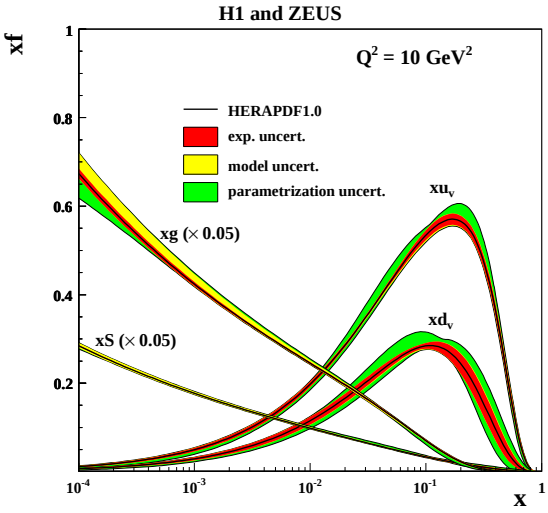

Figure 2.4: Results for fits of the parton distribution functions for valence quarks u_v, d_v, sea quarks S, and the gluon content g (S and g scaled down by a factor of 20) for momentum fractions x of the proton at $Q^2 = 10$ GeV^2 are shown, measured in a QCD analysis of the inclusive ep scattering cross section at HERA by the H1 and ZEUS experiments [24].

Higgs mechanism. The effect can be compensated by a redefinition of the bare Higgs mass which also has to be fine tuned to the level of $\sim 10^{-14}$. This level of fine tuning is considered to violate the naturalness of the theory. A solution for the hierarchy problem is provided in supersymmetric theories, where additional degrees of freedom, in form of additional particles, automatically cancel the divergent contributions, such that the naturalness problem does not occur [10].

A further drawback of the SM theory is found in the expected gauge coupling unification in connection with grand unification. The precise measurement of the gauge couplings allows to check their evolution to higher energy scales, and thus check unification numerically. It is found, that the unification of the gauge couplings at the GUT scale is impossible in the SM. Introducing additional degrees of freedom, again in the form of new particles, influences the evolution of the gauge couplings, and it has been shown that introducing a supersymmetric extension allows for a unification at M_{GUT} [25]. The unification is possible when the mass scale of new particles is in the order of $M_{SUSY} \sim 1$ TeV [10], and if there exists for every boson a new partner fermion, and vice versa.

Another hint for new physics comes from astronomy and cosmology. Measurements of the cosmic microwave background indicate that the visible baryonic matter only makes up for $\sim 5\%$ of the energy density of the universe. The energy density of the universe today is dominated by $\sim 23\%$ dark matter and $\sim 72\%$ dark energy. Photons and neutrinos contribute with $< 1\%$ to the energy density. Dark matter has been observed in astronomical measurements. Considering only the visible matter cannot explain deviations in mass calculations of galaxies, clusters of galaxies and the universe, as well as measurements of deviations from Newton's Law in trajectories

of galaxies, implying the existence of a substance which interacts gravitationally, but has not been observed directly yet. Therefore it is expected that dark matter has a gravitational mass, but does not interact via the electromagnetic interaction. None of the SM particles is a good candidate for dark matter. Even neutrinos, which interact only weakly, are not considered to be responsible for dark matter, since they are too light. It is expected that dark matter can be identified with a particle, which has not been observed so far. Some supersymmetric theories with an extended particle content with respect to the SM contain particles, which are good candidates for dark matter. The lightest supersymmetric particle, if not electrically charged and stable, represents a good candidate for dark matter. The nature of dark energy is still unknown. Dark energy is considered in cosmological models to be responsible for the expansion of the universe.

2.4 Supersymmetry

A brief introduction to the concepts of supersymmetry (SUSY) is given in the following. The foundations for SUSY were first proposed by J. Wess and B. Zumino 1974 [26]. The idea of SUSY is to introduce new particles which are superpartners of the SM particles. The generator $\mathcal{Q}$ of the SUSY algebra transforms fermions into bosons and vice versa, transforming SM particles into their superpartners [10].

$$\mathcal{Q}\,|\text{fermion}\rangle = |\text{boson}\rangle \qquad \text{and} \qquad \mathcal{Q}\,|\text{boson}\rangle = |\text{fermion}\rangle$$

The dimension N of the generator $\mathcal{Q}$ determines how many superpartners per SM particle exist. For $N = 1$ supersymmetry, the minimal extension with respect to the particle content, one additional particle per SM particle, called superparner, is predicted. A detailed description of the minimal supersymmetric standard model (MSSM) can be found elsewhere [27]. The following sections introduce briefly the new particles and their properties. Since none of these particles has been observed yet, supersymmetry must be broken, and the masses of the new particles, the mixing and phases in the MSSM introduce additional 105 free parameters for the supersymmetric extension, in addition to the 19 parameters of the SM.

Particle Content of the MSSM

The left-handed and right-handed fermions of the SM behave differently under gauge transformations, and therefore each chirality state must have its own scalar superpartner. The SM particles are grouped together with their superpartners in chiral supermultiplets [28]. The superpartners of the left- and right-handed electron are, for instance, the left- and right-handed selectrons $\tilde{e}_L$ and $\tilde{e}_R$, where the chirality refers to the SM partner. Similarly, the superpartners of muons and taus are referred to as smuons $\tilde{\mu}_{L,R}$ and staus $\tilde{\tau}_{L,R}$. This differentiation is obsolete for neutrinos, since SM neutrinos are always left-handed, and their superpartners, the sneutrinos, are denoted by $\tilde{\nu}_{e,\mu,\tau}$. The superpartners of quarks are so called squarks, and referred to as $\tilde{q}_L$ and $\tilde{q}_R$ with $q = u, c, t, d, s, b$. The properties of these scalar superpartners are identical to their SM partners, *i.e.* the superpartners of left-handed fermions (right-handed antifermions) couple in weak interactions to the superpartners of $W^{\pm}$ bosons, whereas the

superpartners of right-handed fermions (left-handed anti-fermions) do not.

Also the scalar Higgs boson must be grouped in a chiral supermultiplet in supersymmetric theories [28]. In order to avoid a gauge anomaly, it is required that there must be at least two chiral supermultiplets for the Higgs. From the point of mass generation, also two chiral Higgs supermultiplets are needed. One with hypercharge $Y = +1$, in order to have the necessary Yukawa couplings to give mass to up-type quarks with $Q/e = +2/3$, and a second Higgs supermultiplet with hypercharge $Y = -1$ is needed with Yukawa couplings to down-type quarks with $Q/e = -1/3$ and charged leptons with $Q/e = -1$. The new $SU(2)_L$ doublets H_u and H_d are

$$H_u = \begin{pmatrix} H_u^+ \\ H_u^0 \end{pmatrix} \qquad H_d = \begin{pmatrix} H_d^0 \\ H_d^- \end{pmatrix}.$$

The neutral scalar SM Higgs boson h^0 is considered to be a linear combination of the H_u^0 and H_d^0 components. In total, five physical Higgs particles emerge in the minimal supersymmetric extenstion: the rather light neutral h^0; the heavier neutral H^0; the charged H^+, H^-; and the pseudo-scalar A_0. The superpartners of the Higgs bosons are called higgsinos and denoted $\tilde{H}_u^+, \tilde{H}_u^0$ and $\tilde{H}_d^0, \tilde{H}_d^-$. The $SU(2)_L$ Higgs doublets acquire non-zero vacuum expectation values v_u and v_d, respectively. The ratio of Higgs vacuum expectation values $\tan\beta = v_u/v_d$ is a free parameter in the theory.

The vector gauge bosons of the SM are grouped together with their superpartners in gauge supermultiplets [28]. The gauge bosons mediating the electroweak interaction W^+, W^0, W^- and B^0 have fermionic superpartners, the winos $\tilde{W}^+, \tilde{W}^0, \tilde{W}^-$ and the bino $\tilde{B}^0$. The parameters M_1 and M_2 are the masses for the $\tilde{B}^0$ and $\tilde{W}^0$, respectively. The mixtures of $\tilde{W}^0$ and $\tilde{B}^0$ after electroweak symmetry breaking are called zino $\tilde{Z}$ and photino $\tilde{\gamma}$, corresponding to the superpartners of the SM Z^0 and γ. The superpartners of the $SU(3)_C$ color-octet gluons, mediating the strong interaction, are the color-octet gluinos $\tilde{g}$. The masses of gluinos are described by the parameter M_3. The superpartners of gauge bosons are called gauginos. The couplings of gauginos are considered to be the same as for their SM partner gauge bosons: electromagnetic, weak and strong coupling, respectively.

Mixing in the Gaugino Sector of the MSSM

Due to electroweak symmetry breaking effects, the superpartners of the gauge bosons and the higgsinos are not the mass eigenstates of the theory [28]. Mixing occurs between superpartners with the same quantum numbers. The neutral states photino $\tilde{\gamma}$, zino $\tilde{Z}$ and the two neutral higgsinos $\tilde{H}_1^0$ and $\tilde{H}_2^0$ mix to form four physical states, called neutralinos χ_i^0 with $i = 1, 2, 3, 4$. Similar mixing occurs in the charged gaugino and higgsino sector. The charged wino $\tilde{W}^\pm$ and the charged higgsino states $\tilde{H}_1^+$ and $\tilde{H}_2^-$ mix to form two physical states, called charginos $\chi_j^\pm$ with $j = 1, 2$. The indices i and j arrange the states by their masses, thus χ_1^0 gives for example the lightest neutralino state, which typically is in most SUSY models the lightest supersymmetric particle (LSP). The masses and the composition of neutralinos and charginos are determined by the bino and wino mass scales M_1 and M_2, respectively, and by the values of $\tan\beta$ and a mixing parameter μ, which describes the mixing of the Higgs doublets. The mass scales M_1 and M_2 can be related assuming gauge coupling unification at the GUT scale

by

$$M_1 = \frac{5}{3} \tan^2 \theta_W M_2.$$

The set of parameters $\mu, \tan\beta, M_2$ is sufficient to calculate the masses and composition of neutralinos and charginos, assuming a radiative electroweak symmetry breaking (REWSB) mechanism [29]. The neutralino mixing matrix N_{ij} in the $(\tilde{B}^0, \tilde{W}^0, \tilde{H}_u^0, \tilde{H}_d^0)$ basis and the transition to matrix entries N'_{ij} in the $(\tilde{\gamma}, \tilde{Z}, \tilde{H}_u^0, \tilde{H}_d^0)$ basis is given by [30]:

$$\begin{pmatrix} \chi_1^0 \\ \chi_2^0 \\ \chi_3^0 \\ \chi_4^0 \end{pmatrix} = N'_{ij} \begin{pmatrix} \tilde{\gamma} \\ \tilde{Z} \\ \tilde{H}_u^0 \\ \tilde{H}_d^0 \end{pmatrix} \qquad \begin{aligned} N'_{j1} &= N_{j1} \cos\theta_W + N_{j2} \sin\theta_W \\ N'_{j2} &= -N_{j1} \sin\theta_W + N_{j2} \cos\theta_W \\ N'_{j3} &= N_{j3} \\ N'_{j4} &= N_{j4} \end{aligned}$$

$$N_{ij} = \begin{pmatrix} M_1 & 0 & -m_Z \sin\theta_W \cos\beta & -m_Z \sin\theta_W \sin\beta \\ 0 & M_2 & -m_Z \cos\theta_W \cos\beta & -m_Z \cos\theta_W \sin\beta \\ -m_Z \sin\theta_W \cos\beta & -m_Z \cos\theta_W \cos\beta & 0 & -\mu \\ -m_Z \sin\theta_W \sin\beta & -m_Z \cos\theta_W \sin\beta & -\mu & 0 \end{pmatrix}$$

The mass spectra of neutralinos and charginos are illustrated in Figure 2.5 for $\tan\beta =$ 2, 6, 10 and 50 at $M_2 = 150$ GeV, as function of the Higgs mixing parameter μ. The values for μ, M_2 and $\tan\beta$ considered in this analysis are motivated by previous SUSY searches at LEP [31]. The masses of the gauginos χ_2^0 and $\chi_1^\pm$ are almost degenerate at $\mu = -200$ GeV, and close to the value of M_2. The mass of the χ_1^0 at $\mu = -200$ GeV is $M_2/2$. At $\mu = 200$ GeV, a stronger mass hierarchy between neutralinos and charginos is predicted. Visible is also the small region, where the lightest chargino state is even lighter than the lightest neutralino. For high $\tan\beta$, the mass spectra of neutralinos and charginos become nearly symmetric in μ. For the lightest neutralino χ_1^0, the dependence of the mass on the parameters μ and M_2 is shown for several values of $\tan\beta$ in Figure 2.6. The composition of neutralinos and charginos in terms of the superpartners of the gauge bosons is shown exemplary for the case of the lightest neutralino χ_1^0 in Figure 2.7 in the $\mu - M_2$ plane at several values of $\tan\beta$. This illustration evaluates the neutralino mixing matrix calculated with the SUSYGEN3 [32] software for the given set of parameters. A component is labelled dominant if the corresponding entries in the neutralino mixing matrix [30] squared N'^2_{ij} in the photino-zino-higgsino basis (N'^2_{1j} for χ_1^0) are bigger than the others. The clearest separation between a photino and zino dominated LSP is found for low $\tan\beta$, thus $\tan\beta = 2$ will be used to study consequences of the LSP composition. At high negative values of the parameter μ a dominant photino component, and for high positive values of μ a dominant zino component for the LSP is found. For increasing $\tan\beta$, the regions of photino and zino dominated χ_1^0 shift in the parameter space. This leads for example to photino dominated χ_1^0 scenarios at positive values of the parameter μ, and a small region of zino dominated χ_1^0 scenarios at negative values of μ for high $\tan\beta = 50$. The higgsino component increases as well for higher $\tan\beta$. The composition of neutralinos

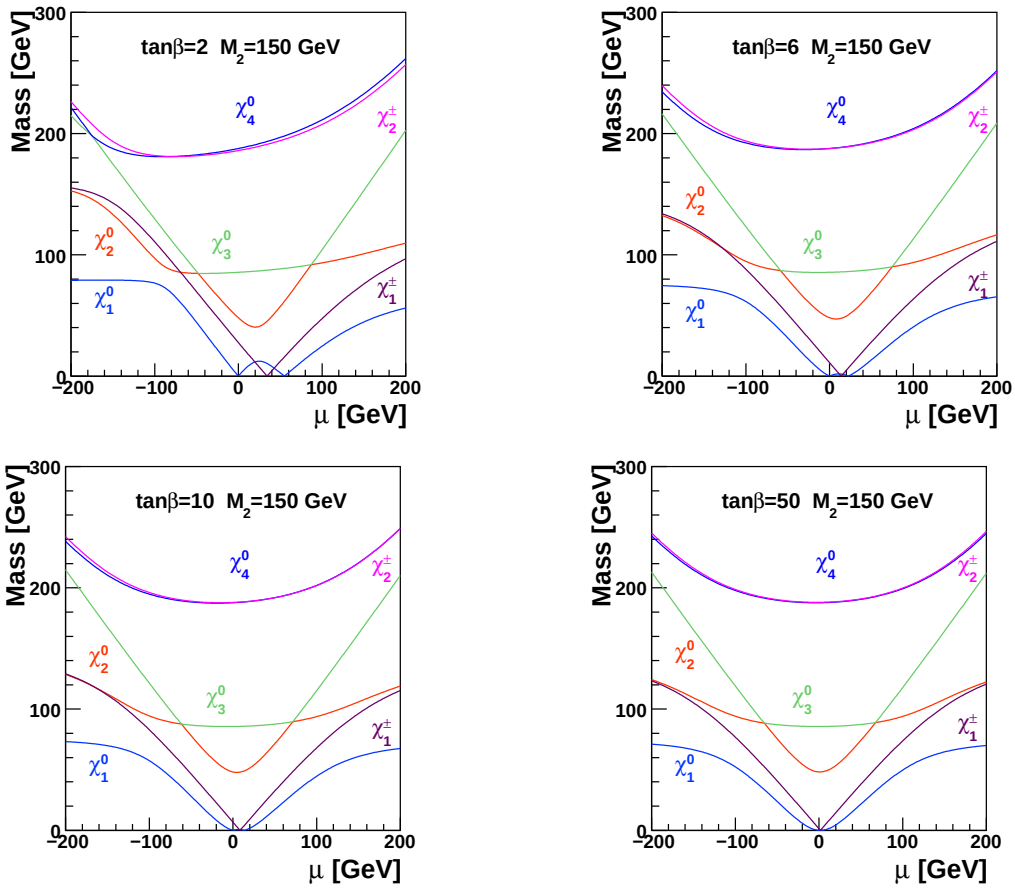

Figure 2.5: Dependence of neutralino χ_i^0 $(i = 1, 2, 3, 4)$ and chargino $\chi_j^\pm$ $(j = 1, 2)$ masses on the parameter μ for $\tan\beta = 2,\ 6,\ 10$ and 50 and $M_2 = 150$ GeV calculated with the SUSYGEN3 [32] software.

and charginos affects strongly the phenomenology of SUSY models, as the final state topologies expected from their decays vary depending on their composition.

Mixing in the Sfermion Sector of the MSSM

Mixing occurs also between the electroweak eigenstates and the mass eigenstates in the sfermion sector [10]. Although squarks and sleptons are spin-0 particles, they can have different chirality states, corresponding to the chirality of their SM partner. The left-handed squarks $\tilde{q}_L$ and sleptons $\tilde{\ell}_L$ mix with the right-handed squarks $\tilde{q}_R$ and sleptons $\tilde{\ell}_R$ to form the physical mass eigenstates $\tilde{q}_{1,2}$ and $\tilde{\ell}_{1,2}$ which can differ in their masses. The mixing matrix for the squared stop squark mass is for example given by [10]:

$$\begin{pmatrix} m_{\tilde{t}_L} & m_t(A_t - \mu\cot\beta) \\ m_t(A_t - \mu\cot\beta) & m_{\tilde{t}_R} \end{pmatrix}$$

The eigenvalues of this matrix are the mass eigenstates. The diagonal entries contain the trilinear top coupling A_t, the mixing parameter μ and $\tan\beta$, and the mass of the

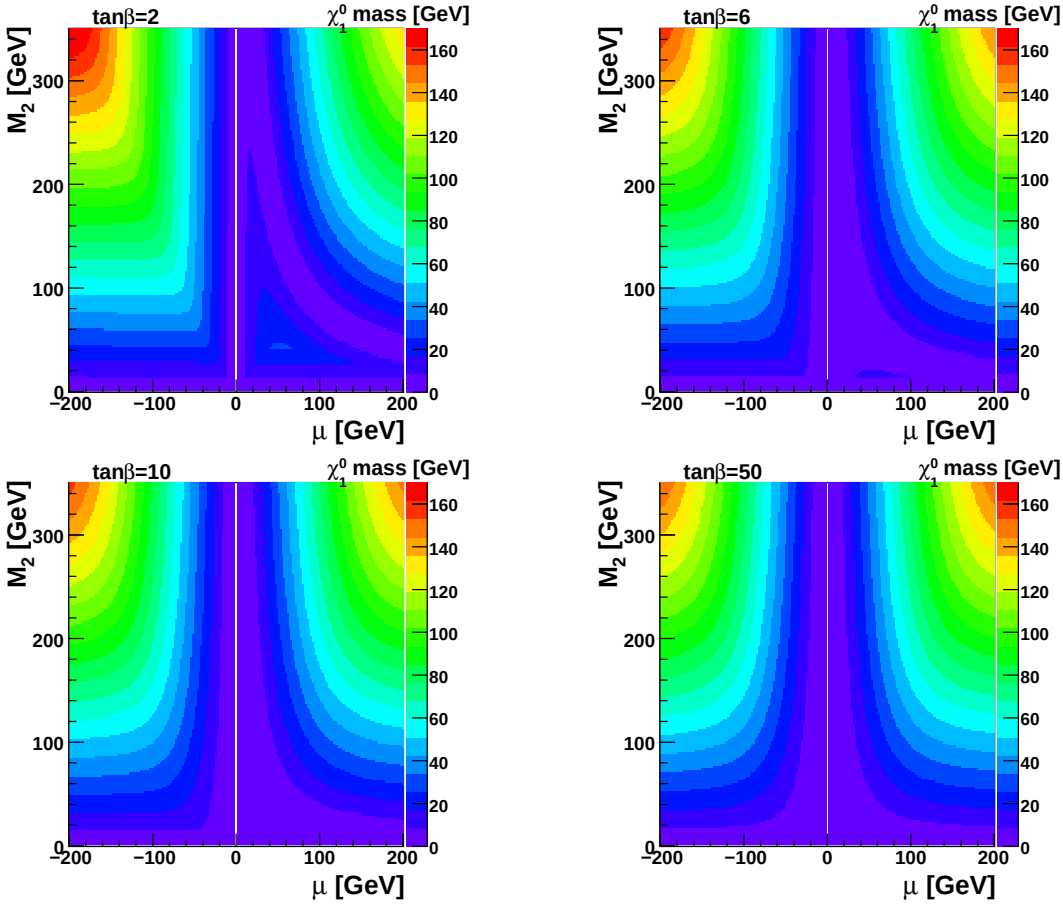

Figure 2.6: Mass of the lightest neutralino χ_1^0 in the $\mu - M_2$ plane for several values of $\tan\beta = 2,\ 6,\ 10$ and 50 calculated with the SUSYGEN3 [32] software. Models with $\mu = 0$ GeV have no REWSB solution. Upper limits from the LEP experiments constrain the mass for the lightest neutralino up to $M_{\chi_1^0} \gtrsim 40-50$ GeV at 95% confidence level [33].

top quark. For the other squarks and sleptons similar matrices are obtained. Thus, due to the high top quark mass in the diagonal, the strongest mixing effects are expected for the stop squark. The largest mixing effects are generally expected for third generation squarks and sleptons. A very light $\tilde{t}_1$ state, compared to the masses of the other squarks, is expected, making it the lightest squark in large parts of the supersymmetric parameter space. Large mixing effects are also expected for the sbottom and the stau. The mixing is expected to be small for small values of $\tan\beta$ and becomes significant for higher values of $\tan\beta$. The mixing and existence of light squark states affects the expected production cross sections, leading to larger cross sections for the light states. For very small masses of the SM partners the mixing effects are expected to be very weak. Thus first and second generation squarks and sleptons are expected to be almost unmixed and degenerate in mass.

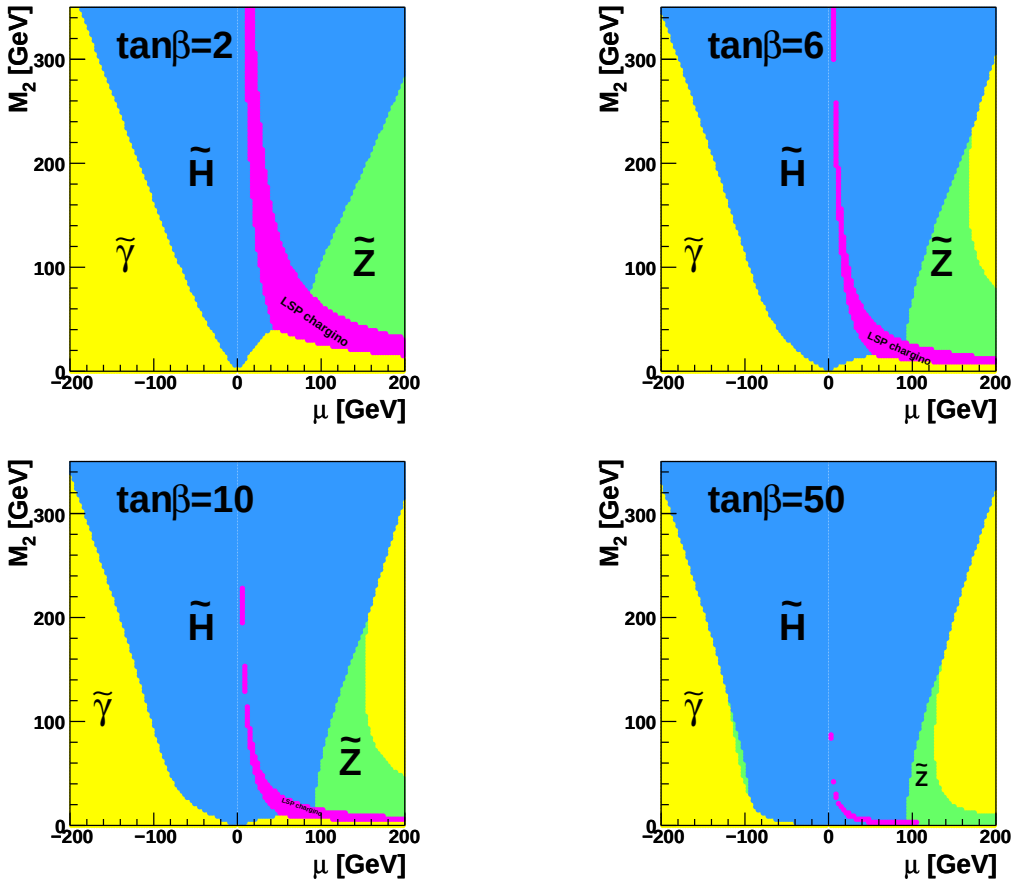

Figure 2.7: Composition of the lightest neutralino χ_1^0 expressed in the photino $\tilde{\gamma}$ (yellow region), zino $\tilde{Z}$ (green region), higgsino $\tilde{H}$ (blue region) basis in the $\mu - M_2$ plane for several values of $\tan\beta = 2,\ 6,\ 10$ and 50 calculated with the SUSYGEN3 [32] software. The component with the highest value $N_{ij}'^2$ with respect to the other components in the neutralino mixing matrix [30] is considered to be dominant. The region where the chargino is the LSP is also indicated (magenta region). A coarse grid ~ 3 GeV was used for the visualisation.

R-parity and the Proton Decay

The mathematical structure of supersymmetry uses the superspace notation with superfields which contain the objects within the supermultiplets. The interactions and masses of all particles are determined by a superpotential in the MSSM Lagrangian. Additional Yukawa interactions with respect to the SM theory appear in the construction of the MSSM Lagrangian [10]. An additional term describing the mixing between the Higgs fields is introduced, and a bilinear and three trilinear Yukawa terms, violating the baryon and lepton number conservation, appear in the superpotential of the most general, gauge invariant and renormalisable supersymmetric theory. Extending the $SU(2)_L$ doublets L and Q, and the singlets E, U and D (see table 2.1) to contain the supermultiplets, the trilinear Yukawa part of the superpotential can be written as [10]

$$\mathcal{W} = \lambda_{ijk} L_i L_j \bar{E}_k + \lambda'_{ijk} L_i Q_j \bar{D}_k + \lambda''_{ijk} \bar{U}_i \bar{U}_j \bar{D}_k \ ,$$

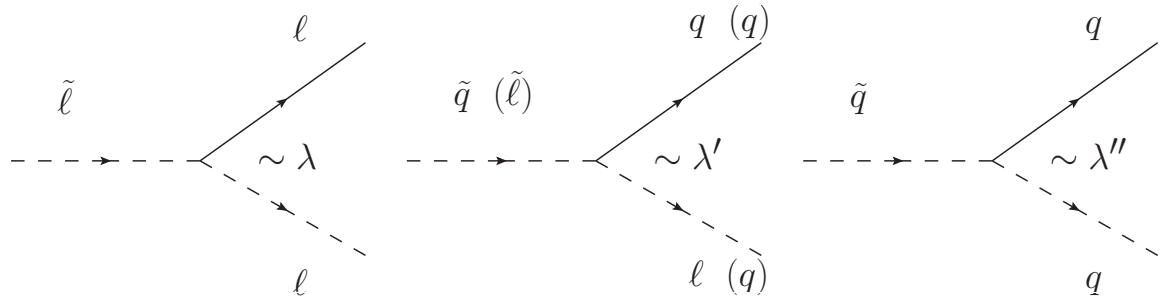

Figure 2.8: Generic diagrams for R_p violating terms in the superpotential (left) $\lambda LL\bar{E}$, (middle) $\lambda' LQ\bar{D}$ and (right) $\lambda'' \bar{U}\bar{U}\bar{D}$. The processes also violate lepton number conservation (left and middle) and baryon number conservation (right). The process in the middle couples leptons ℓ and quarks q to squarks $\tilde{q}$ or quarks to sleptons $\tilde{\ell}$ [34].

where $\lambda_{ijk}, \lambda'_{ijk}$ and λ''_{ijk} are 45 dimensionless Yukawa couplings and i, j, k denote the lepton or quark generation $1, 2, 3$. Including the first two terms in the SUSY Lagrangian leads to lepton number violating processes, coupling two SM fermions to a SUSY scalar. Including the third process leads to baryon number violating processes. Baryon and lepton number violating processes are absent in the SM, and therefore these terms have to be suppressed or excluded from the theory in order to agree with present observations, although there is no theoretical requirement that forbids these terms a priori in the superpotential. The existence of these additional Yukawa couplings would result in new types of interactions, as depicted in Figure 2.8. The phenomenology of SUSY models depends strongly upon the inclusion or exclusion of these terms, or rather the strength of the 45 couplings, since the new interactions allow the creation and decay of single squarks and sleptons via SM fermions. Also the LSP becomes unstable and decays via off-shell SUSY particles into SM particles.

A new multiplicative quantum number R-parity [35] is defined

$$R_p = (-1)^{3B-L+2S} \ ,$$

where B denotes the baryon number, L the lepton number and s the spin of a particle. It follows from this definition that $R_p = +1$ for all SM particles and $R_p = -1$ for all SUSY particles.

Conservation of R-parity ensures that the interactions in SUSY models are basically the same as in the SM. Two of three particles at an interaction vertex must be replaced by their superpartners. Hence, it follows that SUSY particles can only be produced pair-wise and that the lightest supersymmetric particle cannot decay into two SM particles. The latter consequence makes the LSP stable, and a good candidate for the dark matter observed in astrophyics.

The violation of R-parity ($\not{R}_p$) in elementary particle interactions has severe influence on the phenomenology of SUSY models [36], allowing additional Yukawa interactions. Introducing R-parity violating interactions, baryon and lepton number violating processes may lead to the instability of the proton and the subsequent decay into pion and electron $p \to \pi^0 e^+$ via a combination of the couplings λ' and λ''. Strong bounds on the product of these couplings are derived from proton lifetime measure-

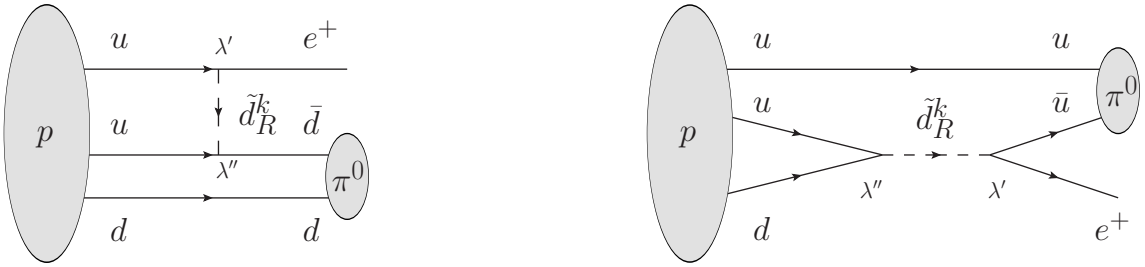

Figure 2.9: Proton decay into positron and neutral pion $p \to \pi^0 e^+$ in R-parity violating supersymmetry via a combination of the couplings λ' and λ'' [10].

ments $\tau(p \to \pi^0 e^+) > 8.2 \cdot 10^{33}$ years [6] in this decay mode. A diagram of the process is shown in Figure 2.9. The amplitude for this process is $\sim \lambda'\lambda''/m^2_{\tilde{d}_R}$ which constrains the product $\lambda' \cdot \lambda''$ to be smaller than 10^{25} for squark masses $m_{\tilde{d}_R}$ smaller than a few TeV [37]. A common assumption is therefore, that most of the $\not{R}_p$ couplings are zero and only an explicit single coupling dominates the phenomenology [35]. This single coupling dominance hypothesis will be used when supersymmetric scenarios are studied. The stability of the proton can also be guaranteed in R-parity violating models through the introduction of additional symmetries like baryon triality and proton hexality, discussed elsewhere [38]. Models for the spontaneous breaking of R-parity and explicit R-parity violation through bilinear terms have also been discussed in the literature [39].

Breaking of Supersymmetry

SUSY particles are expected to have the same properties as their SM partners. In particular, identical masses to their SM partners are expected for the superpartners. None of the additional particles, that appear in supersymmetric models, has been observed so far, therefore supersymmetry must be broken and the masses of SUSY particles are expected to be of the order of the SUSY breaking scale $M_{SUSY} \sim 1$ TeV [10].

Theorists have found various mechanisms for the breaking of supersymmetry. A hidden sector is assumed in most of these models from which the breaking is mediated via some messenger particle to the visible sector [10]. The type of messenger particle influences strongly the phenomenology of the specific supersymmetric model and allows usually a reduction of the 124 free parameters of the MSSM. The minimal supergravity (mSUGRA) model [29] includes gravity and assumes that supersymmetry breaking is mediated via gravitational interactions. A superpartner for the graviton that mediates gravity is introduced, called gravitino, which becomes massive. Gauge mediated symmetry breaking (GMSB) assumes mediation of the breaking by gauge particles and allows the construction of a renormalisable theory. The gravitino has typically a mass in the order of eV$-$keV in GMSB models and represents usually the LSP [10]. In these models, the type of the next-to-lightest supersymmetric particle determines the model phenomenology. Anomaly mediated symmetry breaking (AMSB) does not assume a direct mediation of the breaking from a hidden sector, but breaking due to a conformal anomaly [10]. The gaugino masses are generated in AMSB models at one loop, scalar masses at two loops, but the model yields tachyonic sleptons at tree level. The

expected mass spectra for SUSY particles at low energies vary strongly between these models, predicting almost degenerate neutralino and chargino states in the AMSB, and a usually larger ratio of squark to slepton masses in GMSB models than for mSUGRA models [10].

The mSUGRA Model

The mSUGRA model [29] in the $N = 1$ supersymmetry case is the most widely studied SUSY model and has been studied at HERA previously [34; 40]. The gravitino in mSUGRA does usually not affect the phenomenology in collider experiments due to its weak gravitational couplings and a mass in the order of the electroweak scale. For squarks and sleptons a common mass m_0 at the GUT scale is assumed in mSUGRA models. A relation between the gaugino mass scales M_1, M_2 and M_3

$$M_3 = \frac{\alpha_s}{\alpha} \sin^2 \theta_W M_2 = \frac{3}{5} \frac{\alpha_s}{\alpha} \cos^2 \theta_W M_1$$

is assumed, which unify at the GUT scale to a common gaugino mass $m_{1/2}$. The trilinear couplings are expected to unify to a common trilinear coupling A_0. Mixing in the sfermion and gaugino sector is determined by the Higgs mixing parameter μ and the ratio of Higgs vacuum expectation values $\tan\beta$. Requiring REWSB allows the construction of a complete mSUGRA model by the choice of the 5 parameters

$$m_0, \quad m_{1/2}, \quad A_0, \quad \tan\beta, \quad \text{sign}(\mu) \ ,$$

which yield a complete set of supersymmetric particle masses and couplings, calculated using renormalisation group equations [10]. The ratio of gaugino mass scales is at any energy scale

$$M_3 \ : \ M_2 \ : \ M_1 \ \approx 7 : 2 : 1 \ ,$$

predicting much higher masses for gluinos than for neutralinos and charginos in mSUGRA models.

R-parity Conserving Creation and Decay of SUSY particles

The interactions in the MSSM and mSUGRA models, which conserve R_p, are identical to the SM interactions with two of the particles exchanged for their superpartners [34]. The processes

$$\tilde{q} \rightarrow q\chi_i^0 \quad \text{and} \quad \tilde{q}_L \rightarrow q\chi_j^{\pm}$$

are considered to be the dominant R_p conserving decay modes for squarks studied in this analysis, since the masses of gluinos M_{gluino} are expected to be higher than the squark masses $M_{gluino} > M_{squark}$, with $M_{gluino} \sim 1$ TeV in the considered model scenarios. The decay of squarks to gluinos, if kinematically allowed, would proceed with the strong coupling g_s. In weak interactions, the chirality state of superpartners has to be accounted for. Only left-handed squarks $\tilde{q}_L$ and sleptons $\tilde{\ell}_L$ are allowed to couple to the wino component of charginos. Right-handed squarks $\tilde{q}_L$ decay almost completely to neutralinos, and couple only to the higgsino component of charginos with coupling strength proportional to the mass of the quark m_q. Left-handed squarks $\tilde{q}_L$,

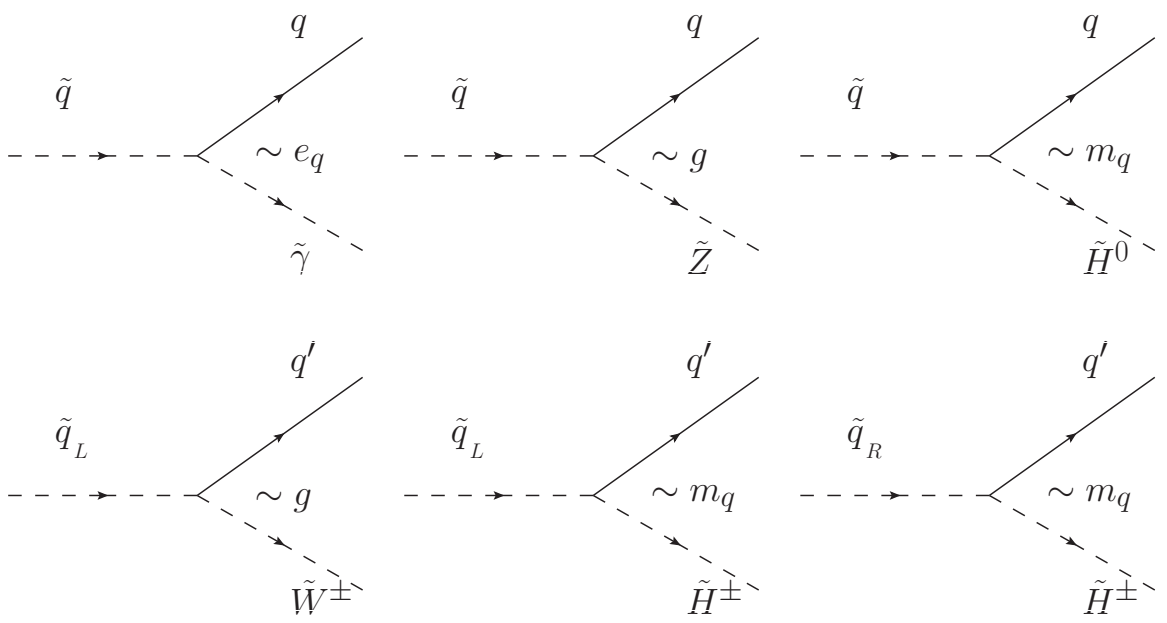

Figure 2.10: Feynman diagrams for R_p conserving squark decay into photino, zino, wino or higgsinos and a quark. Only left-handed squarks couple to winos. The coupling strength at the vertices correspond to the electromagnetic e_q and the weak coupling g strength, and the Higgs coupling to the mass of the quark m_q [34].

by contrast, will decay almost completely into charginos in electroweak interactions. Figure 2.10 shows diagrams for these processes and the couplings involved. Neutralino and chargino decay modes into a fermion and the scalar superpartner open up if kinematically allowed:

$$\chi_i^0 \to q\tilde{q}, \ell^\pm\tilde{\ell}^\mp, \nu\tilde{\nu} \quad \text{and} \quad \chi_i^\pm q\tilde{q}', \to \ell^\pm\tilde{\nu}, \nu\tilde{\ell}^\pm$$

Additional gaugino-higgsino-Higgs and gaugino-gaugino-vector boson couplings for neutralinos and charginos allow the decay of χ_1^0 and $\chi_1^\pm$ into a scalar Higgs h^0, and the heavier $H^0, H^\pm, A^0$ and $W^\pm, Z^0$ bosons, respectively, if kinematically allowed. Usually the h^0 is the lightest Higgs in SUSY models [34].

Additional R_p conserving neutralino and chargino three-body decays via off-shell particles open up, if the above mentioned two-body decays are kinematically inaccessible [41]. Neutralinos and charginos decay in cascades down to the LSP and fermion-(anti-)fermion $ff', (f\bar{f})$ pairs:

$$\chi_i^0 \to \chi_j^0 f\bar{f}, \quad \chi_i^0 \to \chi_j^\pm ff', \quad \chi_i^\pm \to \chi_j^\pm f\bar{f}, \quad \chi_2^\pm \to \chi_1^\pm f\bar{f}$$

Figure 2.11 shows diagrams for R_p conserving three-body decays of neutralinos and charginos. The Sleptons decay electroweak into neutralinos and charginos, and charged or neutral leptons:

$$\tilde{\ell^\pm} \to \ell^\pm\chi_i^0, \quad \tilde{\ell^\pm} \to \nu\chi_i^\pm, \quad \tilde{\nu} \to \ell^\mp\chi_i^\pm, \quad \tilde{\nu} \to \ell^\mp\chi_i^\pm$$

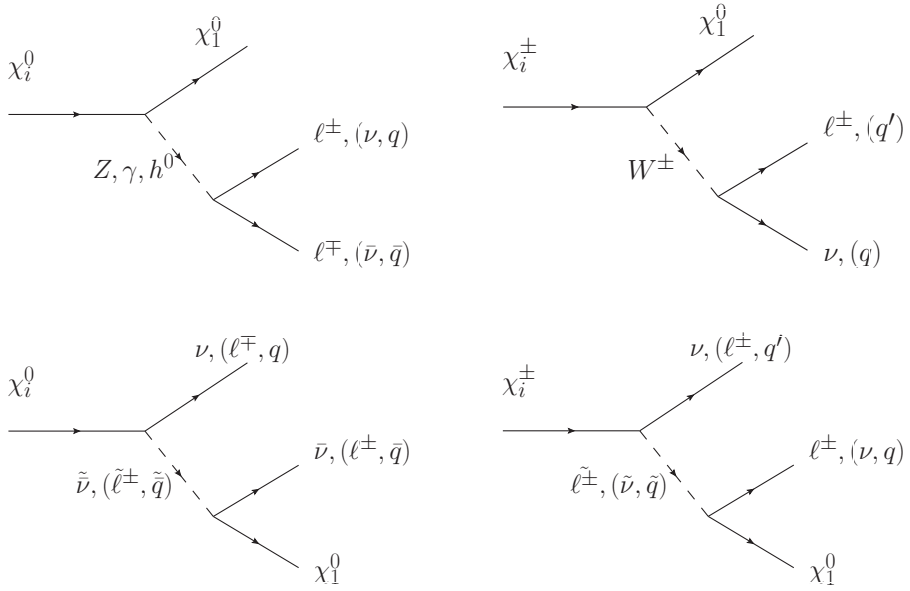

Figure 2.11: Feynman diagrams for R_p conserving three-body decay of neutralinos and charginos into fermion pairs and the LSP χ_1^0 [34; 41].

R-parity Violating Creation and Decay of SUSY particles

The Yukawa couplings λ, λ' and λ'' in R-parity violating models lead to couplings of single squarks and sleptons to SM particles. The lightest neutralino becomes unstable in $\not{R}_p$ models and may also decay into SM particles. Of special interest for this analysis are scenarios with a non-zero $\not{R}_p$ coupling λ', which allow the resonant production of single squarks in electron-proton collisions via a squark-quark-lepton vertex. For non-zero couplings λ' the direct decay of squarks into leptons and quarks opens up. The following interactions become possible in the MSSM Lagrangian considering the expansion of the $\lambda' LQD$ term in the $\not{R}_p$ superpotential [10]:

$$\mathcal{L}_{L_i Q_j \bar{D}_k} = \lambda'_{ijk}[-\tilde{e}^i_L u^j_L \bar{d}^k_R - e^i_L \tilde{u}^j_L \bar{d}^k_R - (\bar{e}^i_L)^c u^j_L \tilde{d}^{k*}_R$$

$$+\tilde{\nu^i_L} d^j_L \bar{d}^k_R + \nu^i_L \tilde{d}^j_L \bar{d}^k_R + (\bar{\nu}^i_L)^c d^j_L \tilde{d}^{k*}_R] + c.c.$$

Figure 2.12 shows diagrams for each of these processes.

Since squarks couple to leptons and quarks, they can be considered similar to leptoquarks (LQs) [42]. In fact, the cross section for the $\not{R}_p$ squark production is the same as for some LQs. There is a correspondence between the $\not{R}_p$ creation and decay of squarks and some scalar LQs [43]. The $\tilde{u}^j_L$ squarks and the scalar $\tilde{S}_{1/2}$ LQ, and the $\tilde{d}^k_R$ squarks and the scalar $\tilde{S}_0$ LQ have the same quantum numbers, and the direct decays to SM particles are identical. The difference is that also R_p conserving decays are possible for squarks. Because the resonant single production of squarks is possible in $\not{R}_p$ SUSY, in principle squarks with masses up to the centre-of-mass energy could be produced. Squarks at HERA can be produced by the fusion of the incoming lepton and a parton from the quark, thus the mass of a resonantly produced squark is given by the energy in the centre-of-mass system of the colliding electron and the quark. For a

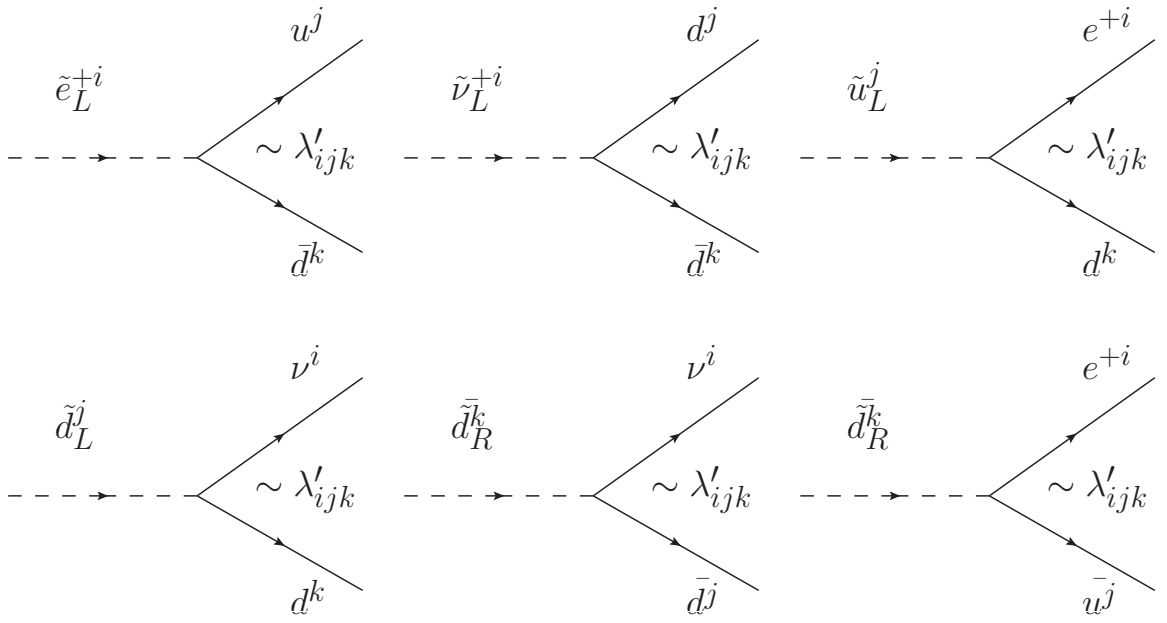

Figure 2.12: Feynman diagrams for $\not{R}_p$ interactions for non-zero couplings λ'_{ijk}. Each diagram represent a vertex from the $\lambda' LQD$ operator of the $\not{R}_p$ superpotential [34].

quark with the momentum fraction x, the mass is given by $M_{squark} = \sqrt{xs}$. Therefore, a resonance peak is expected for resonant squark production in the x distribution at $x = M^2_{squark}/s$ [34].

Considering the structure of the proton, it is much more probable that the electron interacts with one of the valence quarks, rather than with quarks and antiquarks from the sea. As a consequence, different dominant squark production processes are expected in e^+p and e^-p collisions, though in principle, the same processes are possible in both types of collisions. For an initial positron beam, it is expected that the dominant process is the production of a $\tilde{u}_L^j$ quark of generation $j = 1, 2, 3$ via the $\not{R}_p$ couplings λ'_{1j1}, whereas with an initial electron beam, the dominant process is expected to be the production of $\tilde{d}_R^k$ squarks of generation $k = 1, 2, 3$. The squark production cross sections for $\tilde{u}_L^j$ and $\tilde{d}_R^k$ are identical to the production of the $\tilde{S}_{1/2}$ and $\tilde{S}_0$ leptoquarks. The inclusive production cross sections for the dominant processes are derived from leptoquark production and can be expressed as [42]:

$$\sigma(e^+p \to \tilde{u}_L^j + X) \propto \lambda'^2_{1j1} \cdot d\left(x = \frac{m^2_{\tilde{u}_L^j}}{s}\right)$$

$$\sigma(e^-p \to \tilde{d}_R^k + X) \propto \lambda'^2_{11k} \cdot u\left(x = \frac{m^2_{\tilde{d}_R^k}}{s}\right)$$

The production cross sections depend quadratically on the value of the λ' couplings, and on the involved pdfs $u(x)$ and $d(x)$. The squared squark mass $m^2_{\tilde{q}}$ is chosen as the hard scale at which the pdfs are evaluated. Production cross sections are shown in Figure 2.13 for the processes $e^+p \longrightarrow \tilde{u}_L^j + X$ via a non-zero λ'_{1j1} coupling, and

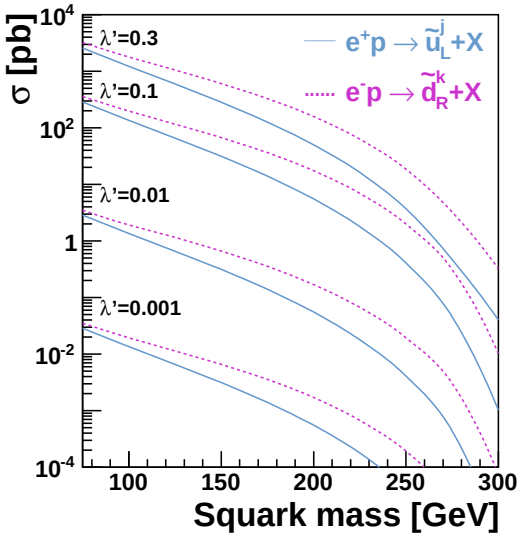

Figure 2.13: Inclusive cross sections σ for the processes $e^+p \longrightarrow \tilde{u}^j_L + X$ (straight line) via the $\not{R}_p$ coupling λ'_{1j1}, and $e^-p \longrightarrow \tilde{d}^k_R + X$ (dashed line) via λ'_{11k} at several values of the couplings $\lambda' = 0.3,\ 0.1,\ 0.01$ and 0.001.

$e^-p \longrightarrow \tilde{d}^k_R + X$ via a non-zero λ'_{11k} coupling for several values of the couplings λ'. At high mass, the production cross section for $\tilde{d}^k_R$ squarks in e^-p collisions is almost twice as high as the cross section for $\tilde{u}^j_L$ squark production in e^+p collisions, as expected from the higher $u(x)$ quark density in the proton with respect to the $d(x)$ quark density at medium to high x. For high squark masses, the squark production cross sections decrease rapidly, following the steep decrease of the parton densities at high $x \to 1$. The cross sections are obtained in this analysis using the leading order amplitudes for leptoquark production [42], corrected using multiplicative k-factors [44] to account for next-to-leading order effects.

The partial $\not{R}_p$ decay width for squarks decaying directly via the $\not{R}_p$ couplings λ' into electron-quark or neutrino-quark pairs is the same as for the decay of leptoquarks [34; 42], given by:

$$\Gamma_{\not{R}_p} = \frac{1}{16\pi}\lambda'^2_{1jk}\ M_{squark}$$

The variation of $\Gamma_{\not{R}_p}$ with the squark mass M_{squark} is only linear, while the coupling enters quadratically. *E.g.* for a coupling $\lambda'^2_{1jk} = 0.1$, a squark mass in the range $M_{squark} = 100 - 290$ GeV yields $\Gamma_{\not{R}_p}(M_{squark} = 100 - 290\ \text{GeV}) = 20 - 60$ MeV. Whereas for a coupling $\lambda'^2_{1jk} = 0.01$, the partial $\not{R}_p$ decay width is substantially smaller: $\Gamma_{\not{R}_p} = 200 - 600$ keV. The processes

$$\tilde{u}^j_L \xrightarrow{\lambda'_{1j1}} e^+d \quad \text{and} \quad \tilde{d}^k_R \xrightarrow{\lambda'_{11k}} e^+u, \quad \tilde{d}^k_R \xrightarrow{\lambda'_{11k}} \nu d$$

are considered for the direct decay of squarks. The $\lambda' LQD$ term contains the two $SU(2)_L$ supermultiplets L and Q, and the singlet supermultiplet D. Therefore, either

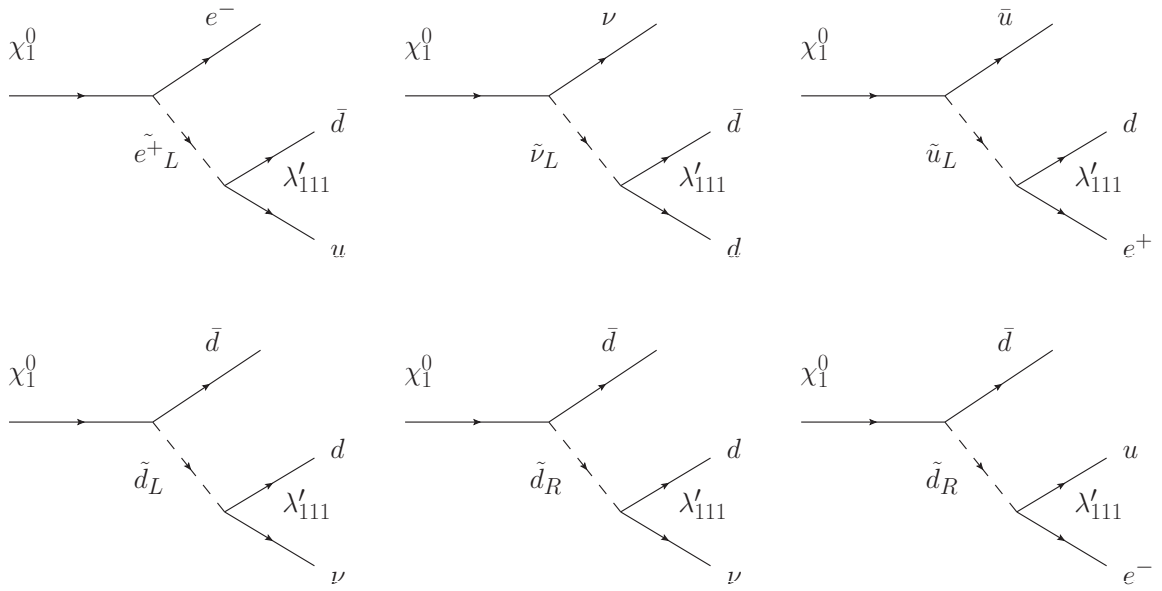

Figure 2.14: Feynman diagrams for $\not{R}_p$ three-body decay of the lightest neutralino χ_1^0 via λ'_{111} [34; 45].

interactions of the type eud or νdd are allowed. As a consequence, the right–handed $\tilde{d}_R^k$ squarks can decay either into $e^- + u$ or $\nu_e + d$, while the left-handed $\tilde{u}_L^j$ squarks decay into $e^+ + d$ only.

Via gauge interactions, the decay of squarks into gluinos, neutralinos and charginos is possible. The decay to gluinos is expected to be dominant if kinematically allowed. In the considered parameter space of the MSSM, the decay to gluinos can be neglected. For small values of λ', the decay to neutralinos and charginos is expected to dominate the branching ratio of squark decays. Higher neutralino and chargino states, produced in squark decays, decay in cascades down to the lightest neutralino or chargino which, in turn, have $\not{R}_p$ decay modes into SM fermions:

$$\chi_1^0 \xrightarrow{\lambda'} e^{\pm} q q', \quad \chi_1^0 \xrightarrow{\lambda'} \nu q \bar{q} \quad \text{and} \quad \chi_1^{\pm} \xrightarrow{\lambda'} e^{\pm} q \bar{q}, \quad \chi_1^{\pm} \xrightarrow{\lambda'} \nu q q'$$

Diagrams for the decay modes of the lightest neutralino via the $\not{R}_p$ coupling λ'_{111} are shown in Figure 2.14 [45]. The decay modes of the lightest chargino via the $\not{R}_p$ coupling λ'_{111} are shown in Figure 2.15 [46].

Indirect Constraints on $\not{R}_p$ Couplings

Additional constraints are derived from precision observables constraining the $\not{R}_p$ couplings $\lambda_{ijk}, \lambda'_{ijk}$ and λ''_{ijk}. The indirect limits derived from neutrinoless double beta decay experiments [47] ($\beta\beta0\nu$) and precision observables like tests of charged current universality [48] (CCU), as well as atomic parity violation [49] (APV), which constrain the couplings λ'_{1j1} and λ'_{11k}, will be introduced in the following. Updated values for the limits are shown here [35].

High precision measurements of the neutral current parity violation in muonic atoms and cesium atoms constrain the production of leptoquarks in ep interactions at high

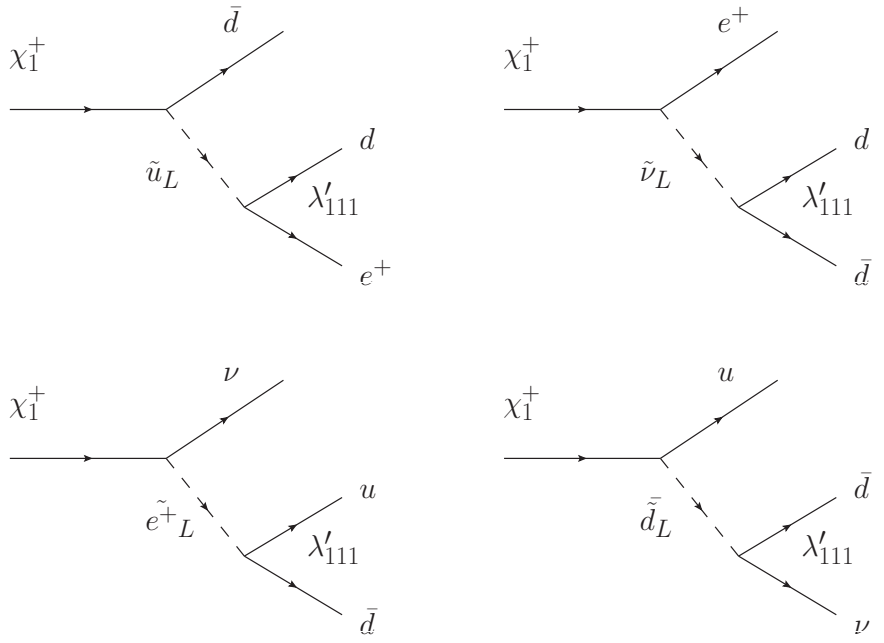

Figure 2.15: Feynman diagrams for $\not{R}_p$ three-body decay of the lightest chargino via via λ'_{111} [34; 46].

momentum transfer at HERA. The APV limits set constraints on the strength of λ'_{1j1} and λ'_{11k} couplings [35]:

$$\lambda'_{1j1}, \lambda'_{11k} < 0.03 \left(\frac{m_{\tilde{u}_L^j, \tilde{d}_R^k}}{100 \text{ GeV}} \right) \quad (j,k = 1,2,3)$$

A $\lambda' LQD$ operator would give extra contributions to semileptonic quark decays. Using experimental measurements of the V_{ud} CKM matrix element, a more severe CCU limit on the coupling λ'_{11k} is obtained [35]:

$$\lambda'_{11k} < 0.02 \left(\frac{m_{\tilde{d}_R^k}}{100 \text{ GeV}} \right) \quad (k = 1,2,3)$$

In the $\not{R}_p$ MSSM, the neutrinoless double beta decay becomes possible via a non-zero coupling λ'_{111} [35]. The limit from the non-observation of this process puts severe constraints on the coupling

$$\lambda'_{111} < 0.00033 \left(\frac{M_{squark} \cdot M_{squark}}{100 \cdot 100 \text{ GeV}^2} \right) \qquad M_{squark} = m_{\tilde{u}_L}, m_{\tilde{d}_R} \ .$$

The indirect limits assume the single coupling dominance hypothesis.

2.5 R-parity Violating Supersymmetry at HERA

The ep collider HERA (see section 3.1) is ideally suited to search for new particle production in lepton-hadron collisions. Allowing the R-parity violating interactions in SUSY models, opens the possibility for single resonant squark production via the LQD

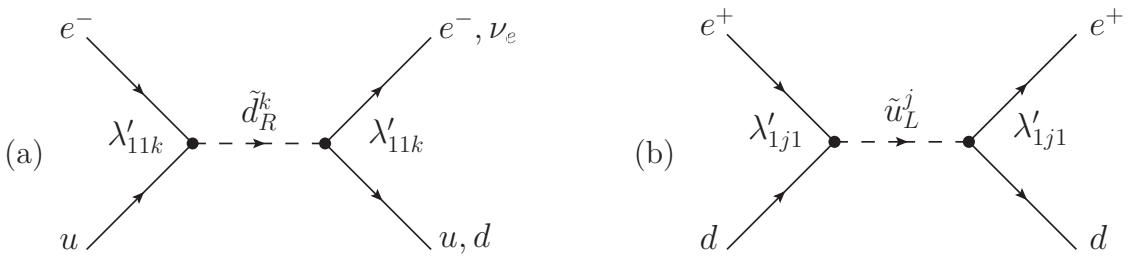

Figure 2.16: Feynman diagrams for the single resonant s-channel production of right–handed $\tilde{d}^k_R$ squarks in e^-p collisions (a) and left–handed $\tilde{u}^j_L$ squarks in e^+p collisions (b) with subsequent decays into SM particles via Yukawa couplings λ'_{11k} or λ'_{1j1}, respectively [1]. The right–handed $\tilde{d}^k_R$ squarks can decay either into $e^- + u$ or $\nu_e + d$, while the left-handed $\tilde{u}^j_L$ squarks decay into $e^+ + d$ only.

operator. A non-zero coupling λ'_{1jk} leads to the production of squarks with subsequent decay to SM particles, eventually over cascades of neutralinos, charginos, gluinos and possibly lighter squarks and sleptons. Previous searches for $\not{R}_p$ SUSY at HERA with the H1 experiment [50; 51; 52; 53] have shown no signs of an excess in data over the SM prediction, and set direct limits on the strength of the $\not{R}_p$ couplings.

Final State Topologies

Several exclusive selection channels are defined to select candidate events from $\not{R}_p$ squark production. Squark decays are expected to be visible as an excess of data events measured in the topologies over the SM background expectation. Depending on the decay mode of squarks, different particles in the final state of a squark decay are expected, and the following signal channels are distinguished [1]:

A single high transverse momentum (P_T) electron, balanced by a high P_T jet, is expected from direct $\not{R}_p$ decay of squarks, therefore a selection channel based on these objects, denoted eq channel is defined. For $\tilde{d}^k_R$ squarks, the decay to a neutrino balanced by a high P_T jet is expected, and a decay channel denoted νq channel is defined for candidate events. The $\tilde{u}^j_L$ squarks cannot decay into a neutrino and a single jet. These final states mimic the signatures of NC and CC DIS events at high Q^2 and a high amount of irreducible SM background is expected to contribute to the selections. Additional contributions by events with mis-identified particles are expected from photoproduction processes. Diagrams for the resonant production, followed by the subsequent direct decay, are shown in Figure 2.16. Squark decays involving gauginos produce more complex final states, with multiple leptons and jets. Decay modes which result in a single electron and multiple jets in the final state contribute to the eMJ channel. The charge of the final state electron can be measured, and is used to distinguish between candidate events for a right (same sign) charge and a wrong (opposite sign) charge channel $eMJ(RC)$ and $eMJ(WC)$, which are defined with respect to the incident electron charge. The $eMJ(RC)$ final state corresponds to the expected final state of higher order NC DIS events. The final state selected in the $eMJ(WC)$ channel, with an opposite sign electron, has no corresponding SM process, thus it is

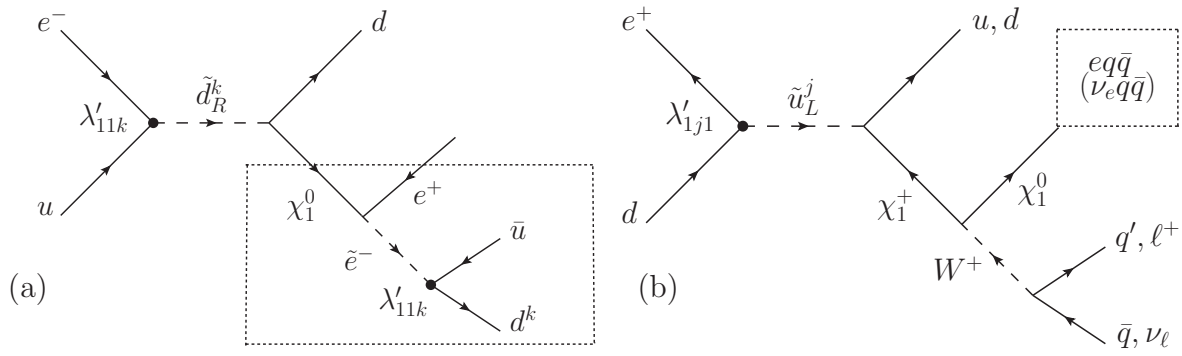

Figure 2.17: Feynman diagrams for squark decays proceeding via gauginos in the case of right–handed down–type squarks (a) and left–handed up–type squarks (b) with subsequent $R\!\!\!/_p$ decay into SM fermions via Yukawa couplings λ'_{11k} or λ'_{1j1}, respectively [1]. The resulting final states may contain multileptons and multijets. The right–handed $\tilde{d}^k_R$ squarks decay to neutralinos χ^0_i $(i = 1, 2, 3, 4)$ or gluinos $\tilde{g}$, and decays into charginos are suppressed. By contrast, $\tilde{u}^j_L$ squarks decay mainly to charginos χ^+_i $(i = 1, 2)$.

expected to be almost background free. Squark decay modes producing neutrinos and multiple jets in the final state are selected in the νMJ channel. The signature corresponds to higher order CC DIS events at high Q^2. Further final states including additional leptons from the cascade decay of gauginos are distinguished. Figure 2.17 exemplarily shows diagrams for squark decay modes leading to multijet and multilepton final states. Multijet events with two electrons are selected in the $eeMJ$ channel, multijet events with a muon and an electron in the $e\mu MJ$ channel. Final states with a neutrino, an electron and multijets contribute to the $e\nu MJ$ channel, and final states that contain a neutrino, a muon and multiple jets are selected in the $\nu\mu MJ$ channel. Only small contributions from higher order and rare SM processes are expected in these selection channels. Table 2.3 summarises the selection channels based on the final state topologies, and shows the typical processes leading to the selected final states.

2.6 SM Physics and Physics Beyond the SM at HERA

HERA physics has a wide spectrum, ranging from precision measurements of SM properties to searches for exotic particles in beyond the SM theories. A complete overview may be found elsewhere [54], a short summary of a few measurements is given in the following. The H1 experiment (as well as the ZEUS experiment) has measured precisely neutral and charged current cross sections [22], also with polarized electron and positron beams [23]. A combined measurement of the NC and CC DIS cross sections in ep collisions by the ZEUS and H1 experiments is shown in Figure 2.3a. The reduced cross section for CC DIS with respect to the NC DIS cross section at low Q^2 is due to the high mass of the electroweak bosons, and the propagator term of the massless photon, which gives the dominant contribution to the NC DIS cross section at low Q^2. For $Q^2 \gtrsim M_W^2 \approx 6500$ GeV^2 the NC and CC DIS cross sections become similar in magnitude. The influence of differences in the pdfs of the partons involved in the

scattering process leads to lower CC DIS cross sections for e^+p than for e^-p scattering. The helicity dependence of CC weak interactions is measured in the CC DIS cross section with a longitudinally polarised lepton beam, shown in Figure 2.3b. The total CC DIS cross section vanishes for full left-handed polarisation of the positron beam, due to left-handed positrons not coupling to the $W^\pm$ bosons.

The proton structure functions F_2 [24] and F_L [55], are extracted from DIS measurements, showing the scaling violations in the structure functions. The measurements are also necessary for a determination of pdfs [24] in the proton. A combined measurement of the pdfs for valence quarks, sea quarks and gluons in the proton by the ZEUS and H1 Collaborations is shown in Figure 2.4.

The measurements of dijet and multijet events [56] allow a determination of the running of the strong coupling α_s. Measurements of heavy quark production via charmed and beauty mesons [57] allow the determination of the charm and beauty contributions to the structure function $F_2^{c\bar{c},b\bar{b}}$ [58; 59].

The HERA measurements contribute strongly to the understanding of physics at other collider experiments and have delivered invaluable knowledge of the electroweak and strong interactions, and the structure of the proton.

Several searches for exotic particles and new interactions outside the SM have been performed by the H1 and ZEUS experiments at HERA. A general search for new phenomena [60], which covers many of the possible final states in the H1 detector, has seen overall good agreement with the SM predictions. No sign of first generation [61] and lepton flavour violating leptoquarks [62], and excited quark states [63] is found in the H1 data. An upper bound on the light quark radius ($R_q < 0.65 \cdot 10^{-18}$ m), and limits on the scale of compositeness, as well as on the gravitational scale in models with large extradimensions are derived from measurements of the NC DIS cross section at high Q^2 [64]. Exclusion limits on the strength of an anomalous coupling for single top quark production have also been derived [65]. A few spectacular events with high P_T leptons (e or μ) and large missing transverse momentum have been reported by the H1 and ZEUS experiments [66], but the effect is still in agreement with real W boson production. Previous searches for SUSY at H1 are introduced in the following section.

2.7 Searches for Supersymmetry

"Hadron-Elektron-Ring-Anlage" at DESY

This work follows in the line of many searches for SUSY at the H1 and ZEUS experiments at HERA, which was operated from 1992 – 2007. Searches for R-parity violating supersymmetry at HERA are inspired by an anomaly reported in 1997 [67]. An excess of high-Q^2 events, as expected from the production of leptoquarks or $\not{R}_p$ SUSY squarks [68; 69], was reported by the H1 and ZEUS experiments. Later, the excess decreased and vanished with more integrated luminosity, having been most likely due to statistical fluctuations. A relic of these events is still found today in the measurement of the single isolated lepton events by the H1 and ZEUS Collaborations [66]. A small excess was observed for final states with isolated leptons (electrons and muons), large missing transverse momentum and a large transverse momentum hadronic final state system, which also decreased again, and vanished in the combination of higher

luminosity data sets of the two experiments. The isolated lepton events also have an R-parity violating SUSY interpretation [70]. Searches for leptoquarks and squarks were regularly performed with increased integrated luminosity at the H1 [50; 51; 52; 53] and ZEUS [71; 72] experiments, but no sign of new physics has been discovered yet.

Large Electron-Positron Collider at CERN

The production of squarks in supersymmetric models has been studied at collider experiments at LEP at CERN (Swiss, Geneva), which was operated from 1989 to the year 2000. At LEP, electrons and positrons have been collided at a centre-of-mass energy of up to $\sqrt{s_{e^+e^-}} = 208$ GeV, allowing the pair-production of SUSY particles up to $\sim \sqrt{s_{e^+e^-}}/2 \approx 100$ GeV. In the R_p conserving MSSM, sleptons could be excluded at the 95% confidence level up to masses of $M_{\tilde{\ell}} \gtrsim 80 - 100$ GeV [73], depending on the considered slepton generation, and squarks excluded up to masses $M_{squark} \gtrsim 100$ GeV [74]. The lightest neutralino mass χ_1^0 is excluded up to masses of $M_{\chi_0^1} \gtrsim 40 - 50$ GeV from slepton, neutralino and chargino pair-production processes [33]. A specific search for $\not{R}_p$ SUSY sets limits on the couplings λ, λ' and λ'', assuming the single coupling dominance hypothesis. The analysis studies the pair-production of sleptons, neutralinos and charginos. Final states which contain multiple jets $N_{\text{jets}} \geq 4$, charged leptons and neutrinos are expected from decays via a non-zero λ' coupling. The production process is independent of the coupling λ', but it influences the decay branching ratios into the selected topologies. The limits obtained from λ' are used to exclude mSUGRA model parameters in the m_0 and $m_{1/2}$ parameter plane [75] (see section 9.3).

TeVatron at Fermilab National Accelerator Laboratory

Supersymmetry is also searched for extensively at the TeVatron collider at Fermilab (USA, Chicago), since its operation started 1983, by the CDF and D0 Collaborations. At the TeVatron, protons and antiprotons are collided at a centre-of-mass energy up to $\sqrt{s_{p\bar{p}}} = 1.96$ TeV. No evidence of SUSY has shown up so far in searches for Rp conserving SUSY. Strong limits on squark and gluino masses are set with the TeVatron data, in particluar for R_p conserving SUSY scenarios with a stable LSP [76]. For $\not{R}_p$ SUSY, there has been little activity recently at the TeVatron. Searches for $\not{R}_p$ SUSY in final states which contain multiple leptons have set constraints on the couplings λ, λ' and λ'' [77]. The published limit, most interesting for this analysis, is a search for final states with at least two electrons and four or more jets in the final state by the D0 experiment, which could be produced via a non-zero λ'_{1jk} ($j = 1, 2$ and $k = 1, 2, 3$) coupling from pair produced SUSY particles. The result has been interpreted in the mSUGRA model, and limits on the parameters $m_0, m_{1/2}$ have been derived [78] (see section 9.3). Other non-zero $\not{R}_p$ couplings have been searched for at the TeVatron. A search for non-zero λ'_{2jk} for $j, k = 1, 2$ couplings in resonant slepton production via an LQD operator and neutralino pair-production, with subsequent R-parity violating decay, resulting in final states with two muons and jets, has been performed at the TeVatron [79]. Also R-parity violation via the $LL\bar{E}$ operator, and a non-zero λ_{112} coupling, has been searched for at the TeVatron in trilepton ($\mu\mu\ell$ with $\ell = e, \mu$) final states [80].

Large Hadron Collider at CERN

The LHC at CERN (Swiss, Geneva) is expected to have the biggest discovery reach for new physics, and supersymmetry is already severely constrained by the first fb^{-1} of collected data. The LHC experiments, ATLAS and CMS, have laid their focus on supersymmetry with R-parity conservation. Searches for high-energetic jet final states and high missing energy [81], and final states with an additional lepton [82], as well as searches for hadronising massive stable particles [83], and several searches in final states with dileptons [84; 85] already constrain squark and gluino masses in the considered models to $M_{squark}, M_{gluino} \gtrsim 0.5 - 1$ TeV. More details of the ATLAS SUSY search in high-energetic jet final states and high missing energy are given in the appendix B.

A search for explicit $\not{R}_p$ couplings is perfomed by the ATLAS experiment in an analysis of final states, which contain high-mass electron muon pairs [86]. A tau-sneutrino $\tilde{\nu_\tau}$ could be produced via a non-zero λ'_{311} coupling in $d\bar{d}$ fusion, and the sneutrino decays subsequently via a non-zero λ_{312} coupling into $e\mu$ pairs. Limits on the sneutrino mass for fixed λ'_{311} and λ_{312} couplings, and limits on the couplings depending on the sneutrino mass have been derived.

Squarks in R-parity violating SUSY with a non-zero λ'_{ijk} coupling could be quickly discovered at the LHC, since in pair-wise production only the mass of squarks is relevant [87] and the coupling to leptons enters, when considering the decay channels easily visible at a hadron collider [88]. A search for leptoquarks by the ATLAS experiment already excludes masses for first generation LQs already up to $M_{LQ} > 376$ GeV and second generation LQs up to $M_{LQ} > 422$ GeV, assuming a branching fraction equal to 1 into the eq channel [89].

Decay Channel	Decay Processes	Expected Final State
eq	$\tilde{u}_L^j \xrightarrow{\lambda'} e^+ d$ $\tilde{d}_R^k \xrightarrow{\lambda'} e^- u$	high P_T $e^\pm$ + high P_T jet
νq	$\tilde{d}_R^k \xrightarrow{\lambda'} \nu d$	missing P_T + high P_T jet
$eMJ(RC)$ $eMJ(WC)$	$\tilde{q} \longrightarrow q\ X$ $\quad \xhookrightarrow{\lambda'} e^\pm \bar{q} q$ $\tilde{q} \longrightarrow q\ X$ $\quad \hookrightarrow \bar{q} q\ Y$ $\quad \xhookrightarrow{\lambda'} e^\pm q' q$	$e^\pm$ (both charge states) + multiple high P_T jets
νMJ	$\tilde{q} \longrightarrow q\ X$ $\quad \xhookrightarrow{\lambda'} \nu \bar{q} q$ $\tilde{q} \longrightarrow q\ X$ $\quad \hookrightarrow \bar{q} q\ Y$ $\quad \xhookrightarrow{\lambda'} \nu q' q$ $\tilde{q} \longrightarrow q\ X$ $\quad \hookrightarrow \bar{\nu} \nu\ Y$ $\quad \xhookrightarrow{\lambda'} \nu q' q$	missing P_T + multiple high P_T jets
$e\ell MJ$	$\tilde{q} \longrightarrow q\ X$ $\quad \hookrightarrow \ell^+ \nu\ Y$ $\quad \xhookrightarrow{\lambda'} e^\pm q' q$ $\tilde{q} \longrightarrow q\ X$ $\quad \hookrightarrow \ell^+ \ell^-\ Y$ $\quad \xhookrightarrow{\lambda'} e^\pm q' q$ $\tilde{q} \longrightarrow q\ X$ $\quad \hookrightarrow e^+ e^-\ Y$ $\quad \xhookrightarrow{\lambda'} \nu \bar{q} q$	$e^\pm$ + (multiple) $\ell^\pm$ ($e^\pm$ or $\mu^\pm$) (+ missing P_T) + multiple high P_T jets
$\nu\ell MJ$	$\tilde{q} \longrightarrow q\ X$ $\quad \hookrightarrow \ell^+ \nu\ Y$ $\quad \xhookrightarrow{\lambda'} \nu q' q$ $\tilde{q} \longrightarrow q\ X$ $\quad \hookrightarrow \nu \bar{\nu}\ Y$ $\quad \xhookrightarrow{\lambda'} e^\pm q' q$ $\tilde{q} \longrightarrow q\ X$ $\quad \hookrightarrow \mu^+ \mu^-\ Y$ $\quad \xhookrightarrow{\lambda'} \nu \bar{q} q$	missing P_T + (multiple) $\ell^\pm$ ($e^\pm$ or $\mu^\pm$) + multiple high P_T jets

Table 2.3: Decay channels arranged by expected final states [34; 40]. The decays of squarks $\tilde{q} = \tilde{d}_R^k, \tilde{u}_L^j$ proceed either directly via an $\not{R}_p$ coupling λ' or via cascades of neutralinos and charginos X, Y resulting in final states which contain charged leptons ℓ (electrons $e^\pm$ and muons $\mu^\pm$), neutrinos (ν, leading to missing P_T) and jets in different multiplicities. The X, Y initiating the $\not{R}_p$ decay is usually the lightest neutralino or chargino.

3 Experimental Setup

High energy physics experiments need a huge infrastructure in order to be able to probe physics at the smallest length scales accessible today. The DESY accelerator centre in Hamburg, Germany, provides such an infrastructure and maintained the world's only storage ring in which high energy collisions of leptons and hadrons could be studied. HERA was in operation during $1992-2007$, and the HERA experiments finished data-taking after 15 years of successful operation and many important results in the field of fundamental research. HERA delivered nearly 0.5 fb^{-1} for each of the two head-on collision experiments H1 and ZEUS. In the following, the HERA ring accelerator and the adjacent experiments will be presented, with the main focus on the H1 experiment.

3.1 HERA Storage Ring

The HERA storage ring was built in a circular tunnel of 6.4 km circumference placed $10-20$ m under ground. Two separate storage rings were installed in the HERA tunnel. One beam line with superconducting magnets that allowed for the acceleration of a proton beam to energies of $E_p = 920$ GeV and a beam line with normal conducting magnets allowing for the acceleration of an electron or positron beam to energies of $E_e = 27.5$ GeV. The centre-of-mass energy achieved in the collisions with these energies was $\sqrt{s} = 319$ GeV. The pre-acceleration of the electron and proton beams, before the injection into the HERA ring at injection energies of $E_e^{\text{inj}} = 14$ GeV and $E_p^{\text{inj}} = 40$ GeV, respectively, was achieved by a combination of linear accelerators, synchrotrons and the storage ring PETRA, as shown in Figure 3.1. The beams were stored in a bunch structure with $n_B^e = 189$ electron bunches and $n_B^p = 180$ proton bunches. Each bunch contained $N_e \approx 5 \cdot 10^{10}$ electrons or $N_p \approx 10^{11}$ protons, respectively, resulting in beam currents of $I_e \approx 50$ mA and $I_p \approx 100$ mA. The beams were crossed with a bunch crossing rate of 10.4 MHz corresponding to a bunch time interval of 96 ns between collisions. Two beam interaction regions were installed at the HERA ring for the multi-purpose experiments ZEUS and H1, studying head-on collisions of the beams. Also two fixed target experiments were installed at the HERA ring. The HERA-B experiment used the proton beam on a wire target to study heavy flavour quark production and especially properties of B meson physics. The fourth experiment at the HERA ring was the HERMES experiment, a fixed target experiment, which allowed studies of the spin structure of the proton using the electron beam on a polarised gas target.

A measure of the event rates of physics processes in ep collisions with known cross sections σ_{process} is the instantaneous luminosity $\mathcal{L}_{inst}$, which gives an instantaneous rate of events $N_{inst} = \mathcal{L}_{inst} \cdot \sigma_{\text{process}}$. The instantaneous luminosity for a ring collider depends on the size of the intersecting beam cross section σ_x, σ_y, the number of colliding bunches n_B, the revolution frequency of the intersecting beams ν, and on the number

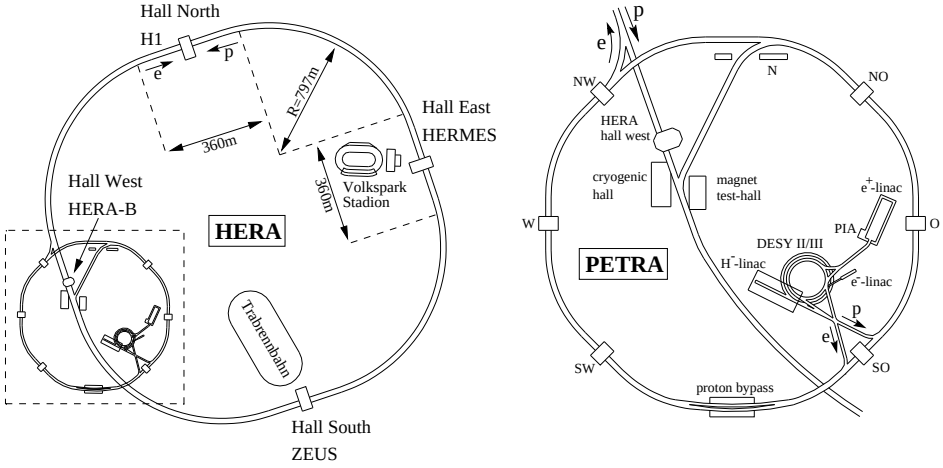

Figure 3.1: The HERA storage ring and the pre-accelerater infrastructure at DESY.

of particles per bunch N_e and N_p:

$$\mathcal{L}_{inst} \sim \nu \cdot n_B \cdot \frac{N_e \cdot N_p}{\sigma_x \cdot \sigma_y}$$

In 2001, the HERA beam optics were upgraded in order to reach an instantaneous luminosity of $\mathcal{L}_{inst} \approx 5 \cdot 10^{31}$ cm^{-2}s^{-1} [90], an increase of a factor ~ 5. The beam profile $\sigma_x \times \sigma_y$ in the transverse plane was improved from a size of 190 μm $\times$ 50 μm to 112 μm $\times$ 30 μm during the HERA upgrade. The running period before the upgrade is referred to as HERA-I operating phase, the high luminosity phase is called HERA-II period. Additionally, spin rotator magnets were installed during the upgrade in the vicinity of the ZEUS and H1 experiments. These allowed the rotation of the vertical polarization naturally built up over time in the lepton beam by the Sokolov-Ternov effect [91] into a longitudinal polarization providing longitudinally polarized leptons in the collisions with the proton beam [92]. The polarization was regularly altered to allow the experiments to collect equal amounts of collision data at positive and negative polarizations. Approximately 1 pb^{-1} of collision data could be delivered in a day of smooth operation in the final phase of high-energy running [93]. The integrated luminosity $\mathcal{L}_{int} = \int \mathcal{L}_{inst}\, dt$ over time collected by the H1 experiment during operation in the HERA-I and HERA-II periods is shown in Figure 3.2. This analysis uses the full data set taken with the H1 detector at a centre-of-mass energy $\sqrt{s} = 319$ GeV, in the years 1998 – 2007.

3.2 H1 Detector

The H1 detector at HERA is designed in conformance with the asymmetric beam energies of the accelerator and the pursued physics program. It was operated during 1992-2007 by the H1 Collaboration, with changes to the initial design [95] in upgrades performed in the winter shutdown 1994-1995, where the backward calorimetry [96] was changed, and in 2001 for improved beam optics, where parts of the tracking system

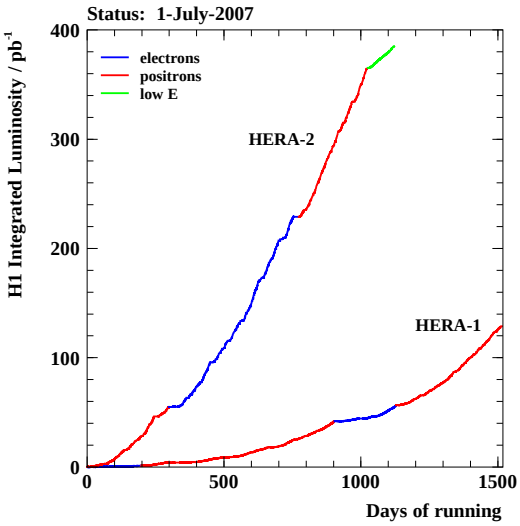

Figure 3.2: Integrated luminosity collected by the H1 detector during its operation between 1992 – 2007 [94]. The low and high luminosity running periods HERA-I (1992-2000) and HERA-II (2001-2007) are shown separately. The different colors indicate the use of electrons or positrons for the lepton beam. Also indicated is an additional running period with lower proton beam energies $E_p = 450$ GeV and $E_p = 575$ GeV (low E) at the end of HERA operation.

were changed. A detailed description of the initial design of the H1 detector with all its sub-components is given elsewhere [95]. The detector components essential to this analysis are briefly presented in the following. The description of the components depicts the initial HERA-I design, and changes during the HERA upgrade in 2001 are mentioned after that.

The H1 experiment uses a right-handed cartesian coordinate system with its origin at the interaction point to describe objects and parts of the detector. The z-axis points along the proton beam direction, which defines the forward direction. The polar angle θ and the transverse momenta of particles P_T are defined with respect to this axis. The pseudorapity is defined as $\eta = -\tan(\theta/2)$. The x and y-axis span the plane transverse to the beam axis with the x-axis pointing to the centre of the HERA ring and the y-axis pointing vertically upwards. The azimuthal angle ϕ defines the particle direction in the transverse plane.

A three dimensional view of the GEANT implementation of the H1 detector, and a technical drawing of the detector layout may be found in the appendix, in Figures A.1 and A.2, respectively. The subcomponents of the detector enclose the interaction region with nearly full solid angle coverage. Adjacent to the beam pipe, in the nominal interaction region, is a silicon detector. It is surrounded by a system of cylindrical jet chambers, roughly one meter in diameter. In the forward region additional tracking chambers are installed. In the backward region a backward drift chamber is installed, followed by a warm calorimeter. A cryostat, containing the liquid argon calorimeters, encloses the central and forward tracking chambers. The cryostat has an outer radius of ~ 2.5 meter and an inner radius of ~ 1 meter. The cryostat is completely surrounded by a solenoid providing the magnetic field for the momentum measurement of tracks,

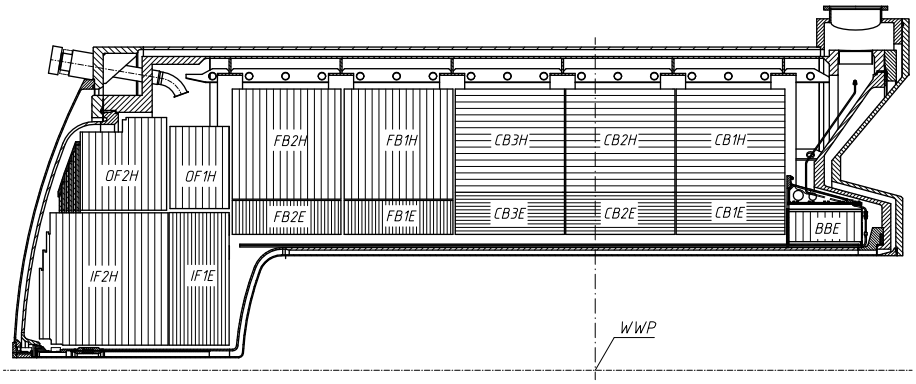

Figure 3.3: Schematic cross section view in the $y-z$ plane of the liquid argon calorimeter of the H1 detector. WWP denotes the nominal interaction point. The eight LAr wheels are labelled according to their position: inner and outer forward wheel ($IF1-2$ and $OF1-2$), forward barrel ($FB1-2$) and central barrel ($CB1-3$) and backward barrel endcap (BBE) with further division into an electromagnetic (E) and a hadronic (H) section [97].

and an iron yoke for the flux return of the solenoid magnet, which is interleaved with muon chambers. In the forward region, an additional muon system enclosing a toroid magnet is attached. The detector is completely embedded inside shielding material.

The Liquid Argon Calorimeter

The liquid argon (LAr) calorimeter [97] of the H1 detector was tailored to the needs of the physics program of the H1 experiment. The clear identification and the precise position and energy measurement of electrons was the main focus of the calorimeter design. The calorimeter also allowed the measurement of energy depositions by minimum ionizing particles, and jets with high particle densities [95]. The choice of a LAr calorimeter was made due to good stability and performance in calibration, the fine granularity that is needed for electron pion separation, and the homogeneous response [95]. The calorimeter is segmented into eight wheels along the z-axis. A schematic view of the calorimeter is shown in Figure 3.3, where the alignment of the active layers is visible. The calorimeter wheels in the barrel part ($CB1-3$, $FB1-2$, BBE) are segmented into eight identical stacks or octants in ϕ. The transition regions between the wheels and the octants have reduced acceptance, referred to as z and ϕ-cracks, respectively. The inner part forms the electromagnetic section, the outer part the hadronic section of the calorimeter. The hadronic stacks are built of welded stainless steel absorber plates interlaced with high-voltage pad readout cells between the plates, defining the liquid argon gaps. The electromagnetic stacks are built from piles of Pb plates covered on each side by epoxy-fibreglass (G10) boards. They are arranged in a sandwich structure separated by spacers for the liquid argon gaps. The electromagnetic section has a total thickness of 20 to 30 radiation lengths X_0, and covers a shower depth of ~ 1 hadronic interaction length λ_{int}. The central electromagnetic + hadronic section of the barrel covers a shower depth of about $\sim 5\lambda_{\text{int}}$, increasing to $\sim 8\lambda_{\text{int}}$ for showers in the forward direction. The read-out electronic consists of 45000 physical channels.

The whole calorimeter is embedded into a cryostat for the liquid argon.

The calorimeter covers the polar angle range $4° < \theta < 154°$ with full azimuthal acceptance. A precision of $\sigma(E)/E \approx 11\%/\sqrt{E/GeV} \oplus 1\%$ is reached for electromagnetic showers, and $\sigma(E)/E \approx 50\%/\sqrt{E/GeV} \oplus 2\%$ for hadronic energy depositions, determined in test-beam measurements [98].

The Spaghetti Calorimeter

The measurement of the LAr calorimeter is complemented in the backward section of the H1 detector by a lead/ fibre calorimeter (SpaCal) [99]. Its nickname, spaghetti calorimeter, originates from the design with long thin plastic scintillating fibres embedded in lead, and read out by photomultiplier tubes at one end. The fibres have diameters of 0.5 mm in the electromagnetic section, and 1 mm in the hadronic section, providing a spatial resolution of a few millimeters corresponding to an angular resolution of $1 - 2$ mrad. The total thickness of the SpaCal corresponds to 28 radiation lengths X_0, and a depth for showers of two interaction lengths λ_{int}. Roughly 1150 channels are read out for the electromagnetic section of the SpaCal. The SpaCal covers the backward region $153° < \theta < 178°$ and is used in this analysis to complete the measurement of charged and neutral particles. A resolution of $\sigma(E)/E \approx 7\%/\sqrt{E/GeV} \oplus 1\%$ is achieved for electrons, as determined in test-beam measurements [100]. During the HERA machine upgrade 2001, modifications to the beam pipe made the redesign of inner part of the SpaCal necessary, to fit additional super-conducting beam focussing magnets into the detector, resulting in a small loss of acceptance.

Magnet, Tailcatcher and Muon System

The tracking system and the LAr calorimeter inside the cryostat are surrounded by the main solenoid magnet and its iron return yoke [95]. The solenoid magnet with a superconducting coil generates a uniform magnetic field of 1.16 T with field lines parallel to the beam axis. The iron yoke is instrumented with limited streamer tubes (LST) for two purposes. First, the instrumented iron is part of the muon system allowing the reconstruction of minimum ionising particles. Secondly, the LST act as a tailcatcher and allow the detection of hadronic shower leakage from the LAr.

The muon system of the H1 detector is formed by the LST and the forward muon system [95]. The LST system consists of the iron yoke interleaved with LST and dedicated muon chambers, so called muon boxes, between the cryostat and the iron. A total of 160000 channels is read out for the LST system. 16 wire, 5 strip and 11 pad layers are available for track reconstruction in the LST system with a resolution of $3 - 4$ mm and $10 - 15$ mm for wire and strip hits, respectively. The pads have a coarse resolution of about 10 cm. The instrumented iron covers nearly the full solid angle. The reconstruction efficiency was determined with cosmic runs to 89% in the plateau region above a threshold of 2 GeV, limited mainly due to the geometrical acceptance. The forward muon system consists of a set of drift chamber planes mounted on an iron toroidal magnet with an outer radius of 2.9 m which generates a magnetic field of $1.5 - 1.7$ T. The forward muon system allows the reconstruction of muons in the forward region $3° < \theta < 17°$.

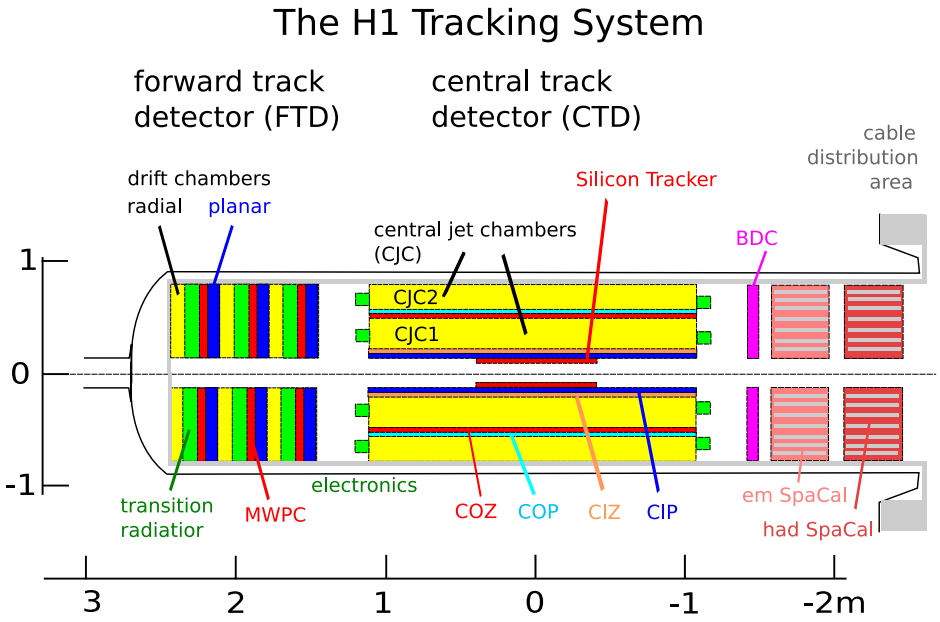

Figure 3.4: Schematic view of the longitudinal cross section of the tracking system of the H1 detector before the 2001 upgrade [95]. Several components were replaced during the upgrade: a new FTD consisting of three supermodules made from drift chambers replaced the shown setup; the CIZ was removed; the CIP was replaced by an improved CIP2k; and the BDC was replaced by the BPC. Additional detectors for the time-of-flight system were installed in the forward region. The silicon tracker was also modified during the upgrade.

The Tracking System

The tracking system of the H1 detector consists of several subdetectors. In particular, due to the asymmetric beam energies of HERA, the tracker consists of a central (CTD) and a forward track detector (FTD) [95]. In the central region, closest to the beam pipe, is situated a silicon vertex detector [101; 102], which comprises of a central and backward silicon detector in HERA-I. Two concentric drift chambers enclose the central silicon detector: the central jet chambers (CJC1 and CJC2), with wires strung along the z-axis, provide a spatial resolution of 170 μm in the $r\phi$ plane and about 1% of the wire length in z. The chambers are complemented by two thin drift chambers with sense wires perpendicular to the z-axis, the central inner (CIZ) and outer z-chambers (COZ), providing a spatial resolution of 300 μm in z and $1-2\%$ of 2π in ϕ. The forward track detector contains three layers, each consisting of a multiwire proportional chamber (MWPC) and a transition radiator, enclosed by radial and planar drift chambers. MWPCs, additional central inner (CIP), and outer proportional chambers (COP), and a backward drift chamber (BDC) provide information for triggering purposes in the central, forward and backward region over the full solid angle. A schematic view of the tracking system with its subcomponents is shown in Figure 3.4. During the HERA upgrade, changes to the central tracking system were performed, the CIP and the CIZ were removed for HERA-II operation. In place of the CIP an improved CIP2k was

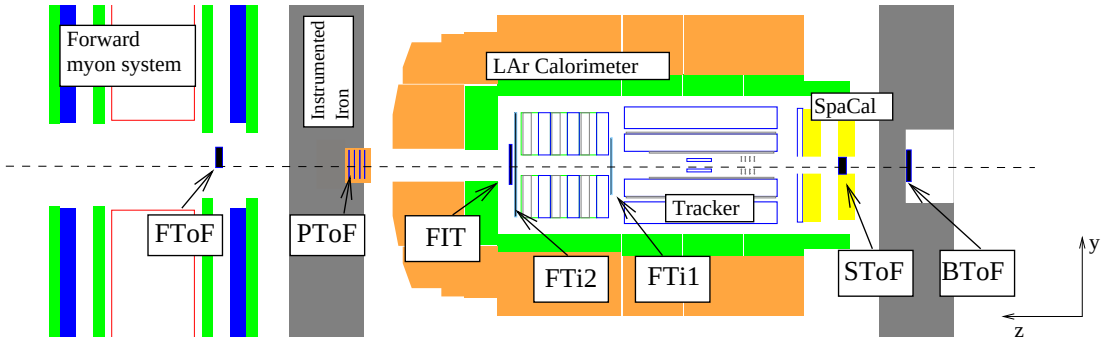

Figure 3.5: Schematic view of the time-of-flight system of the H1 detector after the HERA upgrade 2001 [106]. The FIT, FTi2 and FTi1 components were installed during the upgrade.

installed for HERA-II operation containing five layers of MWPCs, which were used for a fast z-vertex reconstruction. The CIP2k allowed the determination of the z-vertex with a spatial resolution of $\sigma_z \sim 16$ cm after 2.3 μs [103]. This upgrade made the COZ less important for the z-vertex reconstruction. Also the COP was not used during HERA-II operation. The forward tracking system was also changed during the 2001 upgrade. Instead of the described combination of MWPCs, drift chambers and radiators, three supermodules, each consisting of five drift chambers (four drift chambers for the most forward supermodule), were installed. Three planar drift chambers and two radial drift chambers (one for the most forward) with wires strung perpendicular to the beam direction provided improved track reconstruction in the forward direction. The BDC was replaced by a backward proportional chamber (BPC) during the 2001 upgrade. Due to the increased size of the beam pipe after the upgrade, the silicon tracker had to be reassembled, and a forward silicon tracker was added.

The CTD covers $20° < \theta < 160°$ and the FTD covers $7° < \theta < 25°$ providing information to reconstruct charged particle trajectories and the primary interaction vertex. The resolution achieved with the central tracking system for transverse momentum reconstruction of charged particles is $\sigma_{P_T}/P_T = 0.005 P_T/\text{GeV} \oplus 0.015$ [104].

The Time-of-Flight System

The time-of-flight (ToF) system is comprised of several subdetectors made from plastic scintillators, which were placed at various distances to the interaction point close to the beam pipe [105]. In combination with so called veto walls, the ToF system could be used to reject beam induced backgrounds where charged particles were produced at very low polar angles, and backgrounds induced by the proton beam before entering the detector. During the 2001 upgrade additional ToF subsystems were installed in the forward region [106]. See Figure 3.5 for an illustration of the ToF system after the upgrade.

The Luminosity System

The luminosity system of the H1 detector relies on a photon detector (PD) located in the vicinity of the beam pipe at $z = -102.9$ m, *i.e.* in the electron beam direction. In HERA-I the PD is a crystal calorimeter, covered by two radiation length of lead shielding and a water Cerenkov counter of one radiation length [95]. An electron tagger (ET) at $z = -33.4$ is used to detect scattered electrons at very low angles deflected by a bending magnet, in coincidence with the photon dectector. The PD is used to measure the rate of the Bethe-Heitler [107] process $ep \to ep\gamma$ which can be used to infer on the luminosity. The ET is used as a cross check. In HERA-II the PD was exchanged for a quartz-fibre scintillating calorimeter with tungsten absorber. In order to cope with the increased radiation, due to the increased instantaneous luminosity after the 2001 HERA upgrade, a two radiation length thick Berylium filter, and a water Cerenkov counter of one radiation length were installed in front of the PD.

The Trigger System

The trigger system of the H1 detector uses multiple trigger levels to select interesting events and reject background events. At a bunch crossing rate of 10.4 MHz, the trigger system has to decide which events should be kept by the data acquisition system, and reduce the initial rate by several orders of magnitude down to ~ 20 Hz [95]. Three basic types of background have to be dealt with by the trigger: synchrotron radiation from the electron beam, proton gas interactions in the beam pipe vacuum of $\approx 10^{-9}$ mbar, and stray protons producing particle showers. Furthermore, the rate of cosmic muons traversing the detector volume, and the rate of ep events are too high to keep all events. The first level trigger is required to be completely deadtime free. The demand for a low deadtime of the readout system, despite the background situation and the short bunch time interval, requires a central, fully pipelined system keeping all detector information stored, until a decision by the first trigger level is available. In parallel, all trigger calculation and decision logic has to be pipelined to determine a trigger decision for each bunch crossing. Decisions of increased complexity, *i.e.* particle identification and event classification, are taken by consecutive trigger levels. The second and third trigger levels run synchronously to the primary deadtime of the readout system, followed by an asynchronous event filter system (level four), realised by a fast processor farm, which makes full event reconstruction possible online.

The Central Trigger Level 1

The first trigger level [108] evaluates the information from several different trigger systems of certain subdetectors and is completely realised in hardware due to the limited time available for decision making. The trigger systems can be divided into vertex position oriented triggers, calorimetric triggers and muon triggers. Vertex oriented triggers use the information from the backward time-of-flight system and triggers from the central jet chambers. The z-vertex triggers were formed by CIP, COP and the first layer of the forward proportional chamber in HERA-I, and in HERA-II the z-vertex trigger was delivered by the CIP2k, and the COP was not used anymore. Most important for this analysis are the calorimetric triggers, which use the information from the LAr

and the SpaCal calorimeters, and allow triggering on electrons, hadronic transverse energy and missing transverse energy. Muons originating from ep interactions as well as cosmic muons are triggered by the LST and the forward muon system. A total of 256 bits, so called trigger elements, is generated by the subdetectors which are used to form up to 128 subtriggers satisfying certain threshold and coincidence requirements. At least one positive decision from the first level is needed to transfer an event to the subsequent trigger levels. The first level delivers a trigger decision every 96 ns. The final level 1 trigger decision is available 24 bunch crossings after the real ep event time. For a positive level 1 decision, the readout deadtime begins. The pipeline length varies between 27 and 35 bunch crossings depending on the subdetector.

The Intermediate Trigger Levels 2 and 3

Trigger levels 2 and 3 operate synchronously during the deadtime of the readout when the first level provided a positive decision. Level 2 decides after typically 20 μs whether an event is accepted for further treatment, or immediately rejected. Complex topological filter and a neural network evaluating correlations between various subsystems are used for the level 2 decision. The decision of level 3 is typically available after a few hundred μs. The calculations at the intermediate level 2 use the information provided by the level 1 system. Additionally, a fast track trigger [109], implemented in dedicated hardware, is used at level 2 and 3 (FTT L2 and FTT L3) evaluating track based quantities, and also muon and calorimeter information at FTT L3 [110]. As a consequence of the trigger latency and the total deadtime of the readout of about 1 ms for fully accepted events, the trigger accept rates are constrained to 1000 Hz for level 1 and 200 Hz for level 2, to reach an overall deadtime below 10% when running the experiment. The typical output rate of the third level is 50 Hz.

The Event Filter Trigger Level 4

The level 4 filter farm is based on very fast hardware and runs asynchronously to the rest of the trigger system. The complete raw data of detector information is available for the decision algoritms. More complex decisions needed for event topologies found in heavy quark and photoproduction events can be evaluated at this level. A general classification of events into physics classes is performed, resulting in a final output rate of $10 - 20$ Hz, which is suitable for permanent storage with typical event sizes of 100 kByte. Level 4 also provides calibration and monitoring capabilities.

Evaluating Trigger Decisions Offline

The method of prescaling triggers is applied if the rate for interesting physics processes exceeds the limited bandwidth of the data acquisition system. The application of a prescale factor of n for a certain subtrigger means that this subtrigger only gives positive decisions for each n-th event of a certain kind. This method reduces the rates of subtriggers, and allows to measure physics processes with enormous cross sections. The trigger system uses raw and actual bits in order to keep track of the trigger decisions for events which have been prescaled. A certain subtrigger with prescale n sets for the first $n - 1$ events only the raw bit, and only for the n-th event the raw

and the actual bit. Only if at least one actual bit is set by a subtrigger, the event is permanently stored. Deterministic prescaling is used for individual subtriggers in the H1 trigger system. Dynamical and automatic adjustment of prescale factors to the actual background conditions is used in H1. In an offline analysis, weights have to be determined for events that were recorded with prescaled triggers. When combining data recorded by several subtriggers, a sophisticated method must be used to infer on the original rate of events [111]. In this analysis, events with high transverse momentum objects are studied. The rate of these events is already very low, and the triggers used did not have to be prescaled at all.

4 Event Generators

A search for new phenomena in the HERA data needs to use the complete knowledge about SM processes. The simulation of SM processes, as well as the generation of SUSY signal events is discussed in the following chapter. The Monte Carlo generators used, and the simulated SUSY signal grid for the masses of supersymmetric particles will be reviewed.

4.1 Standard Model Event Generator

The squark decay processes studied in this work have the same final state as SM processes, resulting in an irreducible SM background to SUSY events. In addition, background from SM processes with mis-identified particles contributes. A detailed simulation of the SM background processes contributing to the final state topologies, discussed in section 2.5, is needed to allow a statistical separation of the processes. The main background is expected to come from neutral current and charged current deep-inelastic scattering events. The huge cross section for photoproduction events leads to non-negligible contributions to the signal topologies through frequent mis-identification and subsequent mis-classification of these type of events. Additional small contributions are expected from lepton pair production and single W boson production.

The RAPGAP [112] event generator which implements the Born-level, QCD Compton and boson-gluon fusion matrix elements, is used to model inclusive NC DIS events. Initial state and final state radiation of photons from electrons via QED radiative effects are simulated using the HERACLES [113] program. The PYTHIA [114] event generator is used to simulate photoproduction of jets in direct and resolved processes as well as prompt photon production. Born level scattering matrix elements and radiative corrections are calculated within PYTHIA. Both event generators, PYTHIA and RAPGAP, simulate jet production from higher order QCD radiation using leading logarithmic parton showers, referred to as matrix element plus parton showers (MEPS) [115], simulating the parton cascades in a DGLAP-like approach [116], *i.e.* a strong ordering in the transverse momenta k_T of partons is assumed, and only soft ordering for the fractional momenta x. The Lund string fragmentation [117] is used for the hadronisation of free partons as implemented in the JETSET [118] program. Inclusive CC DIS events are simulated using the DJANGO [119] event generator which implements first order leptonic QED radiative corrections based on HERACLES. Higher order CC DIS processes, in the sense of the production of two or more jets, is accounted for in DJANGO using the color dipole model (CDM) approach [120] as implemented within ARIADNE [121]. The CDM approach models the parton cascade in a BFKL-like [122] approach, *i.e.* assuming no ordering in the tranverse momenta k_T of partons.

For the generation of NC DIS events, the CTEQ5L [123; 124] leading order (LO) pdfs for the proton structure were used. For CC DIS events, the MRS [125; 126] pdf were

used, which include electroweak radiative corrections. The generated photoproduction events are also based on CTEQ5L and on the GRV-LO [127] leading order pdf for the photon structure. The LO MC prediction of two or more jets with high transverse momentum in NC DIS, CC DIS and photoproduction events is scaled up by a factor of 1.2 to account for the incomplete description of higher order processes in the MC generators [128; 129]. It has been shown in previous analyses, that the CDM model has problems describing the data in the particular phase space domain studied also in this analysis [34]. An additional reweighting [130] is applied for CC DIS events with two or more jets with high transverse momentum, discussed in the following section.

The production of single W bosons and the production of multilepton events are simulated using the EPVEC [131] and GRAPE [132] programs, respectively.

Systematic model uncertainties are attributed to the event generators due to the incomplete description of higher order processes. Conservatively, a 10% model error is attributed for NC DIS and CC DIS processes with only one high P_T jet in the kinematic region considered in this analysis [129]. Higer order processes, leading to two high P_T jets in the final state of NC DIS and γp events, are attributed a 15% uncertainty [129]. The normalisation uncertainty for the prediction from CC DIS processes with at least two high P_T jets is estimated to be 20% [130]. The production of single W bosons is attributed a 15% uncertainty. A smaller uncertainty is attributed to the prediction from multilepton events (5%). The uncertainties are designed to cover effects from the proton parton distribution functions and missing higher order QCD corrections. The uncertainty on the SM background prediction is determined by adding the effects of model uncertainties and experimental systematic uncertainties (see section 8.5) in quadrature.

The amount of generated MC for each process exceeds at least 10 times the data luminosity. Generated events are passed through a GEANT [133] based simulation of the H1 detector (see section 3.2), which takes into account the actual running conditions of the data taking. The same program chain is used for the reconstruction and analysis of MC events as is used for the data.

Reweighting of Charged Current Monte Carlo

The DJANGOH program, is used to simulate SM background events from the CC DIS process. The hadronisation cascades are simulated using the colour-dipole model [120] (CDM). It is known, that the CDM model (as well as the MEPS model) has problems describing the data in the particular phase space domain considered also in this analysis with multiple high P_T jets and large missing transverse momentum [34; 130]. A reweighting is applied to the CC Monte Carlo, in order to achieve a better description of the jet energy distributions in the selected phase space region for the charge current multijet process with two or more high P_T jets. The weights were derived in a search for excited neutrinos at H1 [130] using the same Monte Carlo set for the SM background prediction in a similar phase space, with two high P_T jets $P_T^{\mathrm{jet1,2}} > 20, 15$ GeV and high missing transverse momentum $P_T^{\mathrm{miss}} > 20$ GeV. The reweighting was derived from a comparison of *pseudo-CC* data events to the CC DIS MC on the reconstruction level in the two quantities [134]: $\Delta\phi = \cos^{-1}\cos(\phi^{\mathrm{jet1}} - \phi^{\mathrm{jet2}})$, and the energy flow ratio V_{ap}/V_p (see section 6.4 for the definition of V_{ap}/V_p, and section 5.3 for the reconstruction of jets). The *pseudo-CC* events are produced from NC DIS events selected in data, where

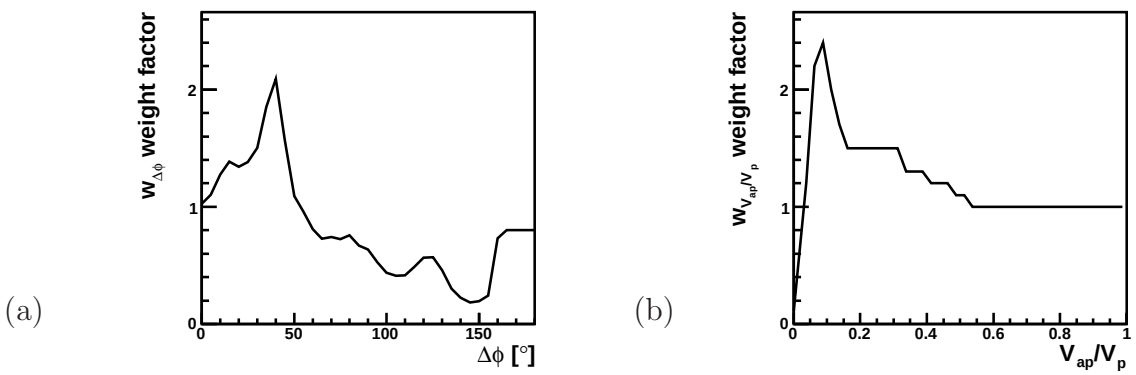

Figure 4.1: The reweighting functions (a) $\Delta\phi = \cos^{-1}\cos(\phi^{\text{jet1}} - \phi^{\text{jet2}})$ and (b) V_{ap}/V_p, which are applied to DJANGOH charge current MC events with two high P_T jets [134].

the scattered electron is artificially removed. Weights are applied on the reconstruction level. The two reweighting functions are shown in Figure 4.1. Events with two high P_T jets with $P_T^{\text{jet1,2}} > 10$ GeV are reweighted with a factor $w_{\Delta\phi}$. Events with two high P_T jets above $P_T^{\text{jet1,2}} > 15$ GeV are also applied a weight factor w_{V_{ap}/V_p}. The reweighting increases the event weights for CC DIS events with close-by high P_T jets, and for CC DIS events with a large imbalance in the energy flow $V_{ap}/V_p \ll 1$. Kinematic quantities and the reconstructed mass $M_{rec,\nu}$ are better described after the MC reweighting.

4.2 Supersymmetric Event Generator

The simulation and calculation of supersymmetric processes in this work uses the LEGO [135] and SUSYGEN3 [32] software. LEGO is a generator developed to study the production of leptoquarks [42], which has a very similar phenomenology as R-parity violating squark production. The direct $\not{R}_p$ decays of squarks into electron-quark and neutrino-quark pairs are simulated using the LEGO generator. The SUSYGEN3 generator is used for the generation of squark decays involving a gaugino, or a cascade of two gauginos. SUSYGEN3 is capable of calculating masses and mixings in the gaugino sector of MSSM models depending on the parameters μ, M_1, M_2, M_3 and $\tan\beta$. The sfermion masses and the mixing for the third generation are treated as free parameters in MSSM models. A constrained version of the MSSM, using the unification requirement of gauge couplings at the GUT scale, reduces the required parameters for the gauginos sector to μ, M_2 and $\tan\beta$. The squark production cross sections [42] are corrected for next-to-leading order (NLO) effects using multiplicative k-factors, which are extracted from a comparison of NLO and LO calculations [44].

Also models considering a specific breaking mechanism for the supersymmetry can be studied using SUSYGEN3. For instance, the popular SUGRA (gravity mediated SUSY breaking) and mSUGRA (minimal SUGRA) models, as well as GMSB (gauge mediated SUSY breaking) models can be simulated. This work makes use of the mSUGRA implementation which is interfaced to SUSPECT2.1 [136] for the determination of the particle spectrum for given parameters: $m_0, m_{1/2}, \tan\beta, A_0$ and the sign of μ. The

calculations are performed using one-loop or two-loop renormalisation group equations solved using a Runge-Kutta numerical algorithm [32].

The decay of SUSY particles in the MSSM and mSUGRA models proceeds via processes with conserved and violated R-parity, for the latter assuming one dominant non-zero $\not{R}_p$ coupling.

Systematics

The following systematic uncertainties are attributed to the signal cross section. A theoretical uncertainty is attributed to the squark production cross section, which varies between $7 - 50\%$, increasing with the squark mass, estimated from the missing higher order corrections [44]. An uncertainty of 7% is attributed to the scale at which the pdfs are evaluated [34], to account for the limited knowledge of the pdfs. Experimental systematics on the selection efficiencies (see section 8.5) are also considered. The limited statistics for simulated signal events is treated with a 10% systematic uncertainty, attributed to the determination of the signal efficiencies, in addition to the statistical uncertainty. The total systematic uncertainty on the signal prediction is calculated for each channel, adding the theoretical and experimental systematic uncertainties in quadrature.

Signal Grids for Sub–processes

Signal events have been simulated for a wide range of masses of supersymmetric particles involved in the decay of squarks [34]. For each decay channel, a dedicated simulation of processes leading to these final states is used. The squark mass is varied for each decay channel from 100 GeV to 290 GeV in steps of typically 25 GeV. For higher squark masses, effects from the kinematic limit invalidate the assumption for the resonant production mechanism and finite squark decay width. For cascade decays involving a direct $\not{R}_p$ gaugino decay, the process $\tilde{q} \rightarrow \chi_1^0 q$ is generated for gaugino masses ranging between 30 GeV and the squark mass M_{squark}. Cascade gauge decays involving two gauginos are studided via the processes $\tilde{q} \rightarrow q\chi_1^{\pm} \rightarrow q\chi_1^0 f f'$ and $\tilde{q} \rightarrow q\chi_2^0 \rightarrow q\chi_1^0 f \bar{f}$, and are generated for gaugino masses ranging between 40 GeV and M_{squark}, and LSP masses ranging between half the mass of the higher mass gaugino, and the mass of the higher mass gaugino. The masses of gauginos are varied typically in steps of 10 GeV. The mass limits are motivated by exclusion limits obtained at LEP [33].

The grid size is chosen such, that linear interpolation between the simulated mass configurations can be used to derive the efficiencies for any possible combination of masses involved in the decay chains. For mass combinations outside the mass grid, a vanishing efficiency is assumed. For processes in specific scenarios, the signal efficiencies in the decay channels can be combined with the specific squark branching ratio into the decay channel for a global efficiency. The branching ratios into the decay channels are calculated using the SUSYGEN3 software, as the sum over branching fractions leading to the selected final state topologies, rescaled to a given value of the $\not{R}_p$ coupling.

The generated signal event samples, used for the determination of selection efficiencies, are reconstructed for the HERA-I running period. It has been checked that event samples reconstructed for the HERA-II running period, taking account the changes to the detector, yield the same efficiencies within statistical uncertainties.

5 Object Reconstruction

The measurement of physics processes in high-energy physics relies on the identification of the involved particles in the detector. The particles are *seen* by the detector as energy deposits in the electromagnetic and hadronic part of the calorimeter, and in the case of charged particles also as tracks by the tracker, or signals of minimum ionizing particles in the muon system. Reconstructed particles from these measurements are the ingredients for further physics analyses. The energy of these objects has to be correctly calibrated before analysis is possible. In the following, the reconstruction of electrons, muons and the more complex treatment of the hadronic final state is presented.

5.1 Electron Identification

The identification of an electron in the H1 detector is based on the characteristic shower shape in the LAr and SpaCal calorimeters. Separate dedicated finder algorithms exist at H1 as the signatures of electromagnetic showers differ significantly in these detectors. The LAr [137] and SpaCal [138] calorimeter electron finders efficiently identify high energy electrons. For the identification of low energy electrons, produced mainly in heavy quark meson decays, other dedicated finder algorithms must be used [139; 140]. In the present analysis, electrons identified by the high energy LAr electron finder are used since the signal topologies consist predominantly of high P_T objects. The identification of high energetic LAr electron candidates will be discussed in more detail in the following.

Electrons initiate electromagnetic showers which are mostly contained in the electromagnetic section of the LAr calorimeter. In contrast to hadrons, a more compact energy deposition is expected from electrons, resulting in a smaller transverse and longitudinal extent of the shower. The fine granularity of the LAr calorimeter allows the discrimination between hadronic and electromagnetic showers. The algorithm uses a cone with an opening-angle of 7.5 degrees around the axis defined by the position of the shower centre and the primary reconstructed vertex. The cone opens $\sim$ 100 cm before the inner side of the calorimeter. A second cone, the electron shower envelope, with an opening-angle of 0.25 in $\eta - \phi$, starting at the primary reconstructed vertex around the same axis is used to veto showers leaking from the inner cone. The cones are used for the efficient separation of electron and pion induced showers in the calorimeter, and a reduction of the pion mis-identification probability to a level of $\sim 10^{-2}$ is achieved [141]. The electron shower envelope is designed to ideally contain the complete electromagnetic shower independent of its energy [141]. An electron four-vector is created from combined cluster and track information. For central electrons, a reconstructed track must be matched to a calorimetric cluster, with a distance of closest approach between the cluster and the track smaller than 12 cm. The energy E_e and polar angle θ_e information are derived from the cluster position relative to the primary vertex, while the azimuthal angle ϕ_e is extracted from a helix fitted to the drift cham-

ber track at the vertex. The energy of reconstructed electrons is calibrated with high Q^2 NC DIS events with overconstrained kinematics. The method [142; 143] exploits the momentum balance between the scattered electron and the hadronic final state in the azimuthal plane in high Q^2 NC DIS events, and the fact, that the kinematics can be determined by measuring only the angles of the electron and the hadronic final state. A reconstructed electron is flagged as isolated if in an isolation cone of 0.5 in $\eta - \phi$ around the electron shower envelope not more than an additional 5 % of the reconstructed electron energy is found.

Reconstructed electrons entering the calorimeter in transition regions of subdetectors, so called cracks, are excluded from the analysis. These crack regions are defined within $\pm 2^\circ$ of the ϕ-cracks between the ϕ-octants, and within ± 2 cm of the z-crack regions in the central and forward barrel wheels $CB1/CB2$, $CB2/CB3$, $FB1/CB3$ and $FB1/FB2$ (see Figure 3.3).

Charge Measurement and Charge Significance

The curvature of charged tracks κ, measured in the central tracking detector, allows a determination of the charge of traversing particles. For low momenta of charged particles, a clear identification of the charge is possible, because the tracks are significantly curved. For increasing transverse momenta, the tracks of charged particles become increasingly straight. The uncertainty on the curvature $\Delta\kappa$ is then of the same size as the curvature itself. For electrons in the final state, the charge measurement is useful for discriminating new physics events, where the charge does not agree with the charge of the beam lepton. The charge measurement is only reliable for central electrons, which have traversed enough volume of the CTD, to produce sufficient information for the track fitting. A measure of the significance of the charge measurement in the CTD is given by the charge significance multiplied by the measured electron charge Q_e^{measured} and the initial electron beam charge Q_e^{beam}:

$$\sigma_\kappa = |\frac{\kappa}{\Delta\kappa}| \cdot Q_e^{\text{measured}} \cdot Q_e^{\text{beam}}$$

Multiplication of the beam charge with the measured charge ensures positive values for electrons measured to have an identical charge with respect to the incident electron, which is expected for events with a single electron from SM processes in ep collisions.

5.2 Muon Identification

The identification of muons in the H1 detector is based on their minimum ionizing particle signature due to ionisation processes in the traversed material. Muons, contrary to electrons and hadrons, do not initiate showers in the calorimeters. The energy loss of a muon in iron is of the order of 10 MeV/cm. Therefore, muons of a few GeV already penetrate the calorimeter, and the surrounding muon systems, leaving the detector volume. Their energy-loss due to ionisation is almost constant and leads to energy deposits evenly distributed in the calorimeter contained inside a narrow cylinder along the muon track. The characteristic signatures in the LAr calorimeter, the instrumented iron yoke and the forward muon detector are used for the muon identification. Mo-

mentum information of the muon is provided by the forward muon system, as well as the forward and central tracking system. This analysis uses only high quality muons with reconstructed tracks in the inner tracker and the muon system, which could be linked by a fit in the reconstruction or could be matched in $\eta - \phi$. A muon four-vector is reconstructed from the reconstructed tracks. Preference is given to tracks in the forward muon detector, which provides the best resolution at the low angles that are of interest in this analysis. The energy E_μ, the polar angle θ_μ and the azimuthal angle ϕ_μ of the muon are derived from the track measurement. In order to determine the isolation of muons, a cylinder with radius 35 cm around tracks extrapolated to the electromagnetic section of the LAr calorimeter, and 75 cm around tracks extrapolated to the hadronic section is defined. Muon candidates are flagged as isolated if the energy in that cylinder does not exceed 5 GeV on the electromagnetic scale, and the muon track must be isolated against tracks by 0.5 in $\eta - \phi$ in the central and forward tracking system.

5.3 Hadronic Final State Reconstruction

The hadronic final state (hfs) is reconstructed after electrons and muons have been identified. Tracks and calorimeter clusters not identified as e's or μ's are used as input by the hfs finder algorithm Hadroo2 [144]. The reconstruction of the hfs uses an energy flow algorithm which combines the information from several subdetectors in order to maximise the experimental resolution. Either the track curvature measurement or the calorimeter energy measurement is used, depending on the uncertainty associated with the track measurement. For particles with a high energetic cluster, the calorimeter measurement is used. For charged particle trajectories with energies up to ~ 12 GeV in the forward tracker, and ~ 25 GeV in the central tracker, the track measurements are considered to be more accurate and a matching calorimeter energy is discarded. The algorithm uses extended noise rejection. Jets are reconstructed from the list of hfs objects via the kt-algorithm [145; 146]. The energy of jets E_{jet} is given by the sum over the calibrated hfs objects inside the jet. The polar angle θ_{jet}, and the azimuthal angle ϕ_{jet} are derived from the position of the centre-of-gravity of the jet. The absolute energy calibration of the hfs using reconstructed jets is suitable for the analysis of events with high transverse momentum jets [144]. A four-vector for the total hfs system is reconstructed by summing up the four-vectors of calibrated reconstructed jets, energy depositions which could not be attributed to leptons, and reconstructed non-isolated leptons in the event. The hadronic inclusive polar angle θ_h is derived from the hfs system using the relation [144]:

$$\tan(\theta_h/2) = \frac{\sum(E - P_z)_h}{P_T^h} \ ,$$

where the sum runs over all jets in the event, and P_T^h is the transverse momentum of the hfs system, given by the absolute value of the transverse component of the total hfs system four-vector.

Check of HFS Calibration

The calibration of the hfs system is checked using the double angle method [147] for the calculation of the total hadronic transverse momentum from the position of the scattered electron and the hadronic final state system in NC DIS events. The total hadronic transverse momentum P_T^{da} is reconstructed using the relation [144]:

$$P_T^{\mathrm{da}} = \frac{2E_0^e}{\tan\theta_e/2 + \tan\theta_h/2} \ .$$

The total transverse momentum reconstructed with the double angle method allows to cross check the total transverse momentum of the hfs using only quantities of the scattered electron. For this purpose, the inclusive hadronic polar angle can also be reconstructed using the energy and position measurement from the reconstructed scattered electron [144]:

$$\tan(\theta_h^e/2) = \frac{2E_0^e - (E_e - P_{z,e})}{P_T^e} \ .$$

Previous checks of the calibration show that an agreement with the absolute jet energy scale of the order of 2% is achieved by the calibration method [130; 144; 148]. In order to check the hfs calibration in this analysis, the ratio $P_T^{\mathrm{bal}} = P_T^h/P_T^{\mathrm{da}}$ is calculated in data and MC and compared to each other. It is expected that the ratio $P_T^{\mathrm{bal}}(Data)/P_T^{\mathrm{bal}}(MC)$ equals 1, showing agreement between the hadronic calibration in data and MC. Figure 5.1 shows results obtained in a cross check of the calibration in this analysis. A good overall agreement within 2% is observed for most of the bins. Only for the 2 jet sample, the highest P_T bin deviates by 3%. The formula for the reconstruction of θ_h^e assumes QPM events, *i.e.* quasi-free, non-interacting partons inside the proton, and thus the cross check with the one jet sample is more significant. For the final H1 dataset, a new calibration scheme was developed [149] which achieves an agreement on the level of 1% for the hfs system. This improved calibration has not been used in the current analysis because it became available only recently.

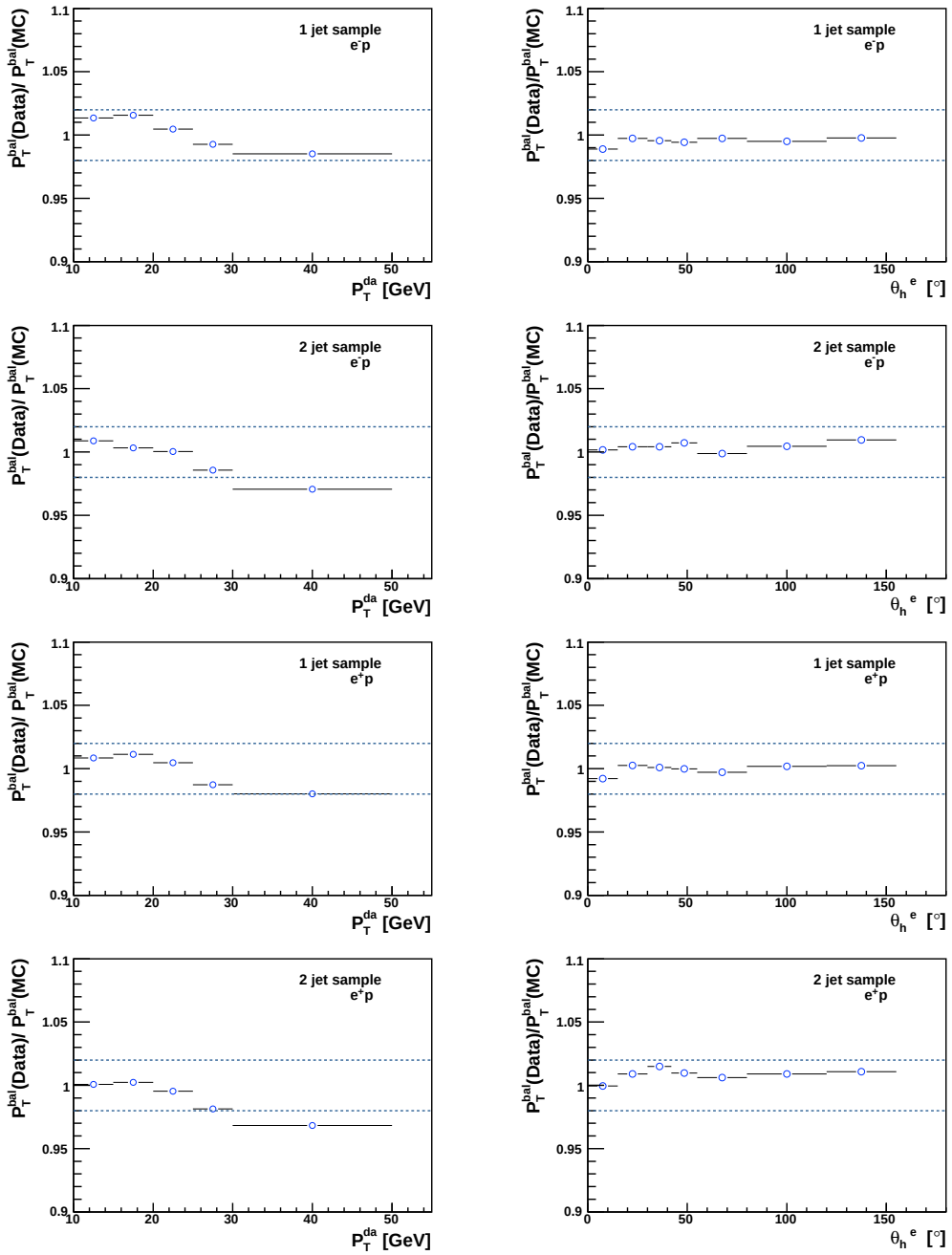

Figure 5.1: Shown is the ratio of the P_T^{bal} distributions in data and MC for e^-p and e^+p data for 1 jet and 2 jet test samples in bins of P_T^{da} and θ_h^e. An overall agreement within 2% is achieved, indicated by the dashed lines. The event sample selections for the 1 jet and the 2 jet samples is described elsewhere [144].

6 Global Event Quantities

6.1 Reconstruction of Kinematic Event Variables

The global event kinematics, defined by the Lorentz-invariant quantities inelasticity y, negative four-momentum squared Q^2 and Bjorken's scaling variable x (see section 2.2), can be reconstructed either by the measurement of the scattered electron energy and position or by the reconstruction of the hadronic final state [95].

Via the electron method, y_e, Q_e^2 and x_e are reconstructed as follows

$$y_e = 1 - \frac{E_e(1-\cos\theta_e)}{2E_e^0}, \quad Q_e^2 = \frac{P_{T,e}^2}{1-y_e}, \quad x_e = \frac{Q_e^2}{y_e s},$$

with the polar angle θ_e, the energy E_e and the transverse momentum P_T^e of the electron with the highest P_T in the event. If no electron is reconstructed in the event, the quantities can be calculated using the Jacquet–Blondel method [150] from the hadronic final state variables:

$$y_h = \frac{\sum (E-P_z)_h}{2E_e^0}, \quad Q_h^2 = \frac{P_{T,h}^2}{1-y_h}, \quad x_h = \frac{Q_h^2}{y_h s},$$

where $P_{T,h}$ is the transverse momentum of the hadronic final state system, see section 5.3. The sum $\sum (E-P_z)_h$ runs over all jets in the event, and does not include any electrons or muons in the event. The quantity which includes electrons is denoted by $\sum (E-P_z)$, and provides a measure of the longitudinal energy balance of an event. Neutral current events, for instance, are expected to produce $\sum (E-P_z)$ of twice the incident electron energy E_e^0: $\sum (E-P_z) \approx 2 \cdot E_e^0 \approx 55$ GeV, when all final state particles are identified and reconstructed in the detector. In charged current events, the neutrino removes a significant fraction of the incident electron energy from the event reconstruction, and therefore values smaller than 55 GeV are expected for $\sum (E-P_z)$.

6.2 Missing Transverse Momentum Reconstruction

In the initial state the incident electron and proton have no transverse momenta, and the total four-vector of an event must be conserved. A significant imbalance in the sum of transverse momenta of detected particles must be therefore due to undetected particles from the interaction, leaving the detector volume. An imperfect detector description or mis-measurement may also lead to an imbalance. The transverse component $\vec{P}_T^{\,\mathrm{miss}} = (p_x^{\mathrm{miss}}, p_y^{\mathrm{miss}})$ of the missing momentum four-vector $(p_x, p_y, p_z, E)^{\mathrm{miss}}$ can be calculated as the negative transverse component of the sum over four-vectors of the hadronic final state system, and all isolated electron and muon candidates in the event. The absolute value $P_T^{\mathrm{miss}} = |\vec{P}_T^{\,\mathrm{miss}}|$ is a measure for the energy-momentum conservation in the transverse plane in an event. Noise in the calorimeter electronics may have an effect, leading to the mis-identification/ mis-reconstruction of particle candidates and

the reconstruction of *fake* P_T^{miss}. The energy resolution of jets with large P_T can also have an effect on the P_T^{miss} reconstruction. In the following it is assumed, that significant P_T^{miss} in an event is due to the presence of a single or more neutrinos in the final state.

Reconstruction of the Neutrino Energy

Under the assumption that exactly one neutrino ν with significant energy is present in the final state, from which the P_T^{miss} of an event originates, the transverse momentum of the neutrino can be identified with the missing transverse momentum $P_T^\nu \equiv P_T^{\text{miss}}$. Exploiting energy and momentum balance

$$(E^\nu - P_z^\nu) = 2E_e^0 - \sum (E - P_z) = 55.2\,\text{GeV} - \sum (E - P_z) \ ,$$

and assuming massless neutrinos, the energy of the neutrino can be reconstructed as

$$E^\nu = \frac{(P_T^\nu)^2 + (E^\nu - P_z^\nu)^2}{2(E^\nu - P_z^\nu)} \ ,$$

using the measurement of the longitudinal energy balance $\sum (E - P_z)$.

6.3 Mass Reconstruction

For testing the hypothesis that events originate from the decay of a massive squark, a significant quantity is the reconstructed squark mass. An excess of events due to the decay of heavy particles of mass M would be visible as a peak in the reconstructed mass spectrum, if the particles are produced resonantly. For events selected in one of the final state topologies, the mass of an intermediate particle is reconstructed with one of the following methods:

- In two-body squark decays into an electron and a jet, the electron position and energy are well measured, allowing a good reconstruction of x_e. For the resonant production of a squark with mass M_{squark}, a resonance peak is expected in the x distribution at $x = M_{squark}^2/s$, which is exploited for the mass reconstruction in the eq channel:
$$M_e = \sqrt{x_e \cdot s}$$
- In squark decays into a neutrino and a jet, only the jet and missing transverse momentum can be reconstructed in the final state. The hadronic final state measurement is used for the reconstruction of x_h. The resonant production can be exploited for the squark mass reconstruction also in the νq channel:
$$M_h = \sqrt{x_h \cdot s}$$
- For the multijet topologies, as expected from $R\!\!\!/_p$ neutralino and chargino decays or cascade decays, the squark mass is reconstructed by summing up the energy of all reconstructed final state particles. Using the initial electron energy E_e^0, the quantities M_{rec} and $M_{rec,\nu}$ can be reconstructed as:

$$M_{rec} = \sqrt{4E_e^0 \cdot \left(\sum_{i=e,\mu,\text{jets}} (E_i) - E_e^0 \right)}$$

$$M_{rec,\nu} = \sqrt{4E_e^0 \cdot \left(\sum_{i=e,\mu,\text{jets},\nu} (E_i) - E_e^0 \right)}$$

The M_{rec} method is used for squark mass reconstruction in the $eMJ(RC)$ and $eMJ(WC)$ channels, and in the $eeMJ$ and $e\mu MJ$ channels. In the νMJ, $\nu\mu MJ$ and $e\nu MJ$ channel, the mass is reconstructed using $M_{rec,\nu}$ including the reconstructed energy of the neutrino in the sum.

6.4 Energy Flow Quantities

Important quantities, characterising the topology of an event, are the energy flow parallel V_p and anti-parallel V_{ap} to the vectorial sum of all energy deposits $\vec{V}$. The detector is divided into two hemispheres for their reconstruction, parallel and anti-parallel to the vectorial sum of all energy deposits above noise level in the LAr and SpaCal calorimeter. V_{ap} is defined as the absolute value of the vectorial sum of energy deposits pointing anti-parallel, and V_p parallel to the vectorial sum over all energy deposits:

$$V_{ap} = \left| \sum_{i\,:\,\vec{v}_i \cdot \vec{V} < 0} \vec{v}_i \right| \qquad V_p = \left| \sum_{i\,:\,\vec{v}_i \cdot \vec{V} > 0} \vec{v}_i \right|$$

$$\vec{v}_i = \begin{pmatrix} E_i \sin\theta_i \cos\phi_i \\ E_i \sin\theta_i \sin\phi_i \end{pmatrix} \qquad \vec{V} = \sum_i \vec{v}_i$$

The index i runs over all calorimeter cells above noise level in the LAr and SpaCal calorimeters. The energy E_i, the polar angle θ_i and the azimuthal angle ϕ_i of the i^{th} cell are corrected for energy losses in dead material and nuclear interactions with an energy weighting algorithm [151].

The ratio V_{ap}/V_p has discrimating power between events intrinsically balanced in P_T, where fluctuations lead to large *fake* P_T^{miss}, and events with undetected particles in the final state. In NC DIS events, which are intrinsically balanced, the ratio V_{ap}/V_p is close to 1, whereas undetected particles in CC DIS events lead to large V_p and small V_{ap} and thus V_{ap}/V_p close to 0 [130].

7 Data Quality Selection

7.1 Trigger Selection

The LAr calorimeter provides the main trigger for events in this analysis [152]. The efficiency for recording events depends on the trigger selection applied. At least one of the following subtriggers is required: Subtrigger $ST67$ is designed to trigger on the scattered electron in NC DIS events, and the subtriggers $ST66$ and $ST77$ are designed to trigger CC DIS events with large missing transverse energy:

- $ST66$ triggers events which pass a high E_T^{miss} threshold ($\gtrsim 6$ GeV) in coincidence with an energy deposit in the forward LAr region [153];
- $ST67$ triggers events above a θ dependent energy threshold ($\gtrsim 5$ GeV) in the electromagnetic section of the LAr [153];
- $ST77$ is the main trigger for CC DIS events with the lowest E_T^{miss} threshold ($\gtrsim 4.75$ GeV) and a loose central vertex requirement [153].

All these triggers require timing and veto conditions identifying ep interactions and rejecting non-ep background [153]. A very high efficiency is reached by these triggers for recording events with isolated electrons as well as events with isolated muons and high energetic jets. The efficiency for recording events with an electromagnetic deposit in the LAr calorimeter with an energy greater than 10 GeV is close to 100% [154]. Triggering events by hadronic jets is 95% efficient for jets with transverse momenta $P_T^{\text{jet}} > 20$ GeV and increases to almost 100% for $P_T^{\text{jet}} > 25$ GeV [155]. Events with missing (undetected) energy $E_T^{\text{miss}} > 20$ GeV have a trigger efficiency above 90%, and for $E_T^{\text{miss}} > 30$ GeV the efficiency reaches above 95% [130].

7.2 Run Selection

The data-taking periods of the H1 detector are divided into luminosity fills corresponding to one fill of the electron and proton beams in the HERA ring. These luminosity fills are further subdivided into shorter periods with stable experimental conditions, so called luminosity runs. The selection of good luminosity runs ensures that the experimental conditions in the analysed samples are stable and can be well understood. The quality of data-taking periods is determined by the operating conditions of the H1 detector subcomponents, and the actual background conditions during data-taking. The essential subdetectors for this analysis are the central jet chambers CJC1 and CJC2, the LAr and Spacal calorimeters, the time-of-flight system and the luminosity system (see section 3.2). These subdetectors must be powered with high voltage and in readout mode during data-taking. The integrated luminosities for the H1 data after the good run selection are shown in Table 7.1 for the individual periods and the sum of data sets.

year	collision type	integrated luminosity $\mathcal{L}_{\text{int}}$
1998/99	e^-p	14 pb^{-1}
1999/00	e^+p	66 pb^{-1}
2003/04	e^+p	53 pb^{-1}
2004/05	e^-p	112 pb^{-1}
2006	e^-p	58 pb^{-1}
2006/07	e^+p	136 pb^{-1}
$\sum e^-p$		183 pb^{-1}
$\sum e^+p$		255 pb^{-1}

Table 7.1: Integrated luminosities of data-taking periods after the run selection for the HERA-I and HERA-II periods at a centre-of-mass energy $\sqrt{s} = 319$ GeV.

7.3 Vertex Position

The position of the interaction of colliding electrons and protons is distributed around the nominal vertex position as a result of the spatial extension of electron and proton beam bunches. An approximately Gaussian distribution is found near the nominal interaction point in the beam direction with a spread of $\sigma_z \sim 10$ cm corresponding to the spatial extension of the proton bunches in the z-direction. Additional peaks in the distribution of interaction points, displaced by $\Delta z = \pm 150$ cm with respect to the nominal interaction point [156], are due to interactions from collisions with satellite bunches. As the detector geometry is optimised for ep-interactions at the nominal interaction point, only events within ± 35 cm of the interaction point are accepted in order to ensure good acceptance and resolution for reconstructed events and to reject sources of non-ep background in the data.

7.4 Rejection of non-ep Background

Three sources of non-ep background events are distinguished [157]. At every moment, cosmic muons can traverse the detector volume under different angles with respect to the vertical. Their signature is characterised by signals in the instrumented iron, the LAr calorimeter and the central jet chambers. If they pass close enough to the interaction point they may be mis-identified as dimuon events. Additionally, muons can be created in interactions of the proton beam with the beam pipe wall, or with residual gas atoms in the vacuum. These so called beam halo muons travel parallel to the beam axis through the detector volume at the same time as their accompanying proton bunches. Their signals are characterised by calorimetric deposits of energy, distributed parallel to the beam axis. The third source of non-ep background are the so called overlay events. An ep or γp event at small or medium energy is recorded in coincidence with a cosmic or halo muon. As a consequence, the events may not be correctly

reconstructed and could be attributed to some rare or exotic processes. Overlay events are the most important source of non-*ep* background for this analysis, since a *fake* high P_T hfs could be reconstructed in combination with high energetic muons. Several techniques exist for the suppression of cosmic and beam related background events. Timing vetoes and topological filters have been developed previously at H1 [151; 157; 158; 159; 160], which are used to reject non-*ep* background events.

8 Data Analysis

The complete HERA dataset for a centre-of-mass energy of $\sqrt{s} = 319$ GeV is used in a search for supersymmetric particles in R-parity violating SUSY. Selections of neutral and charged current events are presented to show the performance of the modelling of the most important background processes. The event topologies for the possible squark decay channels are introduced and the criteria for the event selections are discussed. The event selection is optimised using SUSY signal events.

8.1 Standard Model Control Sample

Neutral Current Selection

In neutral current deep inelastic scattering, an isolated electron and one or more hadronic jets are expected in the final state. The cross section for NC DIS is decreasing with an increasing number of jets in the event. The γ, Z^0 exchange does not affect flavour and charge of the electron. The selection of NC DIS events is therefore straightforward requiring a well-measured electron in the detector. An energy of $E^e > 11$ GeV is required for the electron to ensure a trigger efficiency above 99%. The electron is further required to be flagged as isolated lepton and not in the vicinity of the ϕ or z-crack regions. The highest P_T electron in the event is considered to be the scattered electron from the hard interaction. The position and energy of this electron are used to reconstruct the event kinematics x_e, y_e and Q_e^2 using the electron method (see section 6.1). The additional cuts 35 GeV $< \sum(\mathrm{E} - \mathrm{P_z}) <$ 70 GeV and $0.1 < y_e < 0.9$ ensure a clean NC DIS sample and remove remaining background from photoproduction and non-ep physics. By removing the low y_e region it is ensured, that the hfs is fully contained in the LAr, and not lost in the beam pipe. The high y_e region is excluded due to the degrading resolution of Q_e^2 with increasing y_e.

Figure 8.1 and 8.2 show distributions of kinematic observables and event quantities in a NC DIS selection for $Q_e^2 > 1000$ GeV^2 in the e^+p and e^-p data sets, respectively. After applying these criteria, a total of 39317 events is found in the e^+p data for 39590 ± 4096 events expected from the simulation. In e^-p data, 30348 events are found compared to 31056 ± 3216 events from the SM simulation. The uncertainty on the SM prediction contains model and experimental systematic uncertainties in quadrature (see section 8.5). The SM expectation for the sample consists of $\gtrsim$ 99% NC DIS events and $\lesssim$ 1% mis-identified background, mainly photoproduction and multielectron events, as determined from the MC simulation. The kinematic distributions are in excellent agreement with the SM expectation. Measured yields of electrons and jets in the forward and backward region are very well described by the simulation. No requirement on the jet momenta is made in the selection, thus a small amount of events with no identified jet are selected. The transverse momenta of jets and electrons as well as the reconstructed missing transverse momentum are well predicted over the complete range of measured momenta up to energies of 140 GeV, where small

fluctuations due to statistical limitations of the data are observed. For illustration, the SM prediction and data can be compared to an arbitrarily normalised signal of a squark with mass $M_{squark} = 150$ GeV, which decays into an electron and a jet simulated with SUSYGEN3. The distributions of transverse momenta of electrons and jets in the signal peak at the expected value of $P_T^{\mathrm{ele1,jet1}} \approx 75$ GeV, due to the two-body decay of the squark, and the squark being produced with no intrinsic transverse momentum. Differences in the polar angle distribution of electrons from the NC DIS process and electrons from squark decays are observed. The squark being heavy and produced with momentum along the proton beam direction, emits the electron and the jet typically boosted into the forward direction. The high energetic electron emitted in the forward direction leads to high values for the quantity Q_e^2, which does not correspond to the negative four-momentum transfer squared for signal events. The most prominent feature of the squark signal is found in the inelasticity distribution. The signal shows a flat y distribution for events from the isotropic squark decay, in contrast to a distribution falling as $1/y^2$ for the number of NC DIS events. The distributions can be used for a statistical discrimination of the processes.

For a high Q^2 NC DIS selection, with $Q_e^2 > 2500$ GeV^2, the same excellent agreement with the simulation is observed. In the e^+p data 8652 events are found for an expectation of 8615 ± 890 events from the SM simulation. In the e^-p data 7758 events for an expectation of 7894 ± 818 events are found. The distributions for the NC DIS selection with $Q_e^2 > 2500$ are shown in the appendix, figures A.3 and A.4.

Charged Current Selection

In charged current deep inelastic scattering, a neutrino and one or more jets are expected in the final state. The W^+, W^- exchange transports the charge of the electron and changes the quark flavour, as well as the electron into a neutrino. The cross section for CC DIS decreases with an increasing number of jets in the event. The neutrino escapes the detector volume without interaction. Exploiting conservation of energy and momentum, the missing energy can be reconstructed. The selection of CC DIS events is based on the measurement of the event kinematics and the reconstructed missing transverse momentum P_T^{miss}. The reconstruction of the kinematics x_h, y_h and Q_h^2 uses the measurement of the hadronic final state, referred to as hadron method (see section 6.1). Events are selected by requiring $P_T^{\mathrm{miss}} > 12$ GeV, and longitudinal energy momentum imbalance $\sum(E - P_z) < 50$ GeV. The choice of the P_T^{miss} cut ensures a high trigger efficiency for CC DIS events. The inelasticity is restricted to the region $0.1 < y_h < 0.9$ to remove photoproduction background, and ensure that there is no loss of hfs particles in the beam pipe. The high y_h region is excluded due to the poor Q_h^2 resolution. Further, the ratio V_{ap}/V_p is used to remove remaining photoproduction background faking high P_T^{miss} signatures, and small amounts of mis-measured NC DIS events. It is required that $V_{ap}/V_p < 0.35$ for events with $P_T^{\mathrm{miss}} > 25$ GeV, and $V_{ap}/V_p < 0.15$ otherwise [130].

Figure 8.3 and 8.4 show distributions of kinematic observables and event quantities in a CC DIS selection for $Q_h^2 > 500$ GeV^2 in the e^+p and e^-p data sets, respectively. Applying the CC DIS selection results in a total of 4373 events in the e^+p data for $4349 \pm$ 445 events expected from the simulation. In e^-p data, 6518 events are found compared to 6861 ± 710 events from the SM simulation. The uncertainty on the background

prediction contains model uncertainties and experimental systematic uncertainties in quadrature (see section 8.5). The SM prediction consists of $\gtrsim 99\%$ CC DIS events and $\lesssim 1\%$ mis-identified background, mainly photoproduction and a few single W boson production events, as determined from the MC simulation. The kinematic distributions for the CC DIS events are well described by the SM expectation. Similar to the NC DIS measurement, the transverse momenta of jets, and the reconstructed missing transverse momenta are well modelled by the simulation. Small statistical fluctuations are observed in the high P_T tails of these distributions. For events with a high number of jets $N_{\text{jets}} \geq 4$, more events are expected by the SM simulation than seen in the data. Only a small fraction $< 1\%$ of the overall statistics is affected. In the very forward region $\theta \lesssim 15°$, the description of the jet yield is overestimated by the MC, the effect being more obvious in the e^-p data. The higher number of events selected in the e^-p data set, with respect to the e^+p data set with a higher integrated luminosity, is due to the increased CC DIS cross section for e^-p scattering, which follows from the parton content of the proton. For illustration, the SM prediction and data are compared to an arbitrarily normalised signal of a squark with mass $M_{squark} = 150$ GeV, which decays into a neutrino and a jet. The distributions of the reconstructed missing transverse momentum, and the transverse momentum of the highest P_T jet peak at the expected value of $P_T^{\text{miss,jet1}} \approx 75$ GeV, due to the two-body decay of the squark. The high energetic jet and the neutrino emitted in the forward direction result in high values for the quantity Q_h^2 for signal events. The quantity Q_h^2 is not the negative four-momentum squared for signal events. The most prominent feature of the squark signal in the νq channel is found in the inelasticity distribution. For the number of CC DIS events also a distribution falling as $1/y^2$ is expected, whereas for events from the squark signal a flat y distribution is expected. The distributions allow a statistical discrimination of the processes.

A CC DIS selection for high $Q_h^2 > 2500$ GeV^2 events, yields also a very good agreement with the SM simulation. In the e^+p data 1742 events are found for an expectation of 1744 ± 180 events from the simulation. In the e^-p data 3673 events for an expectation of 3925 ± 408 events are found. The distributions for the CC DIS selection with $Q_h^2 > 2500$ are found in the appendix, figure A.5 and A.6.

8.2 Event Selection

The decays of supersymmetric particles in R-parity violating SUSY are expected to result in events with SM particles in the final state. Several exclusive signal event topologies are distinguished, which contribute according to their branching ratio to the squark decay width (see section 2.5). The main background to these topologies originates from NC DIS and CC DIS events. The presented NC and CC DIS event selections show the precise description of these processes by MC simulations in the HERA data. The selection criteria for selecting new physics candidate events are introduced in the following. The selection presented here is following the approaches taken before at H1 in searches for squarks of R-parity violating SUSY [34; 40; 52; 53]. The kinematic cuts for the selection of the different final states are presented in the following. The number of selected events in each topology after all selection cuts and the efficiencies for selecting the squark signal are summarised in Table 8.1, for the e^+p

Selection Channel	e^-p (183 pb^{-1}) Data	SM Expectation	e^+p (255 pb^{-1}) Data	SM Expectation	Range of Signal Efficiencies
eq	3121	3215 ± 336	2946	2899 ± 302	30% – 40%
νq	2858	2983 ± 358	–	–	50% – 60%
eMJ (RC)	147	158.3 ± 23.9	140	146.0 ± 21.4	10% – 40%
eMJ (WC)	0	1.3 ± 0.3	1	0.6 ± 0.4	5% – 20%
$eeMJ$	0	1.5 ± 0.5	2	1.7 ± 0.5	5% – 35%
$e\mu MJ$	0	0.03 ± 0.02	0	0.03 ± 0.03	5% – 15%
$e\nu MJ$	3	5.6 ± 1.2	5	8.2 ± 2.0	5% – 40%
νMJ	204	235.5 ± 63.3	113	134.0 ± 33.8	5% – 50%
$\nu\mu MJ$	0	0.04 ± 0.02	0	0.06 ± 0.03	5% – 20%

Table 8.1: Number of events selected in data and from SM simulation, and the range of signal efficiencies for the decay channels in e^-p and in e^+p collisions [1]. The range of efficiencies illustrates the extreme values for signal events with squark masses ranging from 100 GeV to 290 GeV and gaugino masses from 30 GeV up to the squark mass. The νq channel is not relevant for e^+p data since the $\tilde{u}_L$-type squarks produced in e^+p do not undergo this decay. Only $\tilde{d}_R$-type squarks, which are produced dominantly in e^-p collisions, can undergo direct decay leading to a νq final state. The total error on the SM prediction is determined by adding the effects of all model and experimental systematic uncertainties in quadrature.

and e^-p data sets separately.

Electron Based Selection Channels

The event selection in the electron based channels is presented in the following. All topologies have in common that high P_T objects, mainly emitted in the forward direction, are expected from heavy squark decays. The decay channels considered in the data analysis are discussed in section 2.5. Squark signals are expected to be visible in several decay channels simultaneously.

Electron-jet final state eq

A squark decaying into an electron and a quark fragmenting into a single jet yields the exact same signature as NC DIS events at high x and high Q^2. Squarks produced in the s-channel decay isotropically which leads to a flat $d\sigma/dy$ distribution. For NC DIS events, a distribution $\sim 1/y^2$ is expected allowing the statistical discrimination of the processes.

The event selection for the eq channel requires $P_T^{miss} < 15$ GeV and 40 GeV $< \sum(\mathrm{E} - \mathrm{P_z}) < 70$ GeV, which ensures that all particles produced in the ep collision are detected. An isolated electron with $P_T^e > 16$ GeV in the region $5° < \theta_e < 145°$ is required. A high trigger efficiency is ensured by the electron P_T threshold. The electron

must not to be in the vicinity of a ϕ or z-crack. Events have to fulfill $0.1 < y_e < 0.9$ and $Q_e^2 > 2500$ GeV^2 in order to reduce photoproduction background and enhance the ratio of signal to background events. A veto is applied for events with a second isolated electron $P_T^{e2} > 5$ GeV, an isolated muon $P_T^{\mu} > 5$ GeV or two jets with $P_T^{\mathrm{jet1,jet2}} > 15$ GeV in order to be exclusive with respect to the multilepton and multijet channels.

After these selection steps, 7061 events are observed in the e^+p data for 7187 ± 751 events from SM simulation. In the e^-p data a total of 6288 events are observed for 6580 ± 688 events from SM simulation (for the uncertainties, see section 8.5). A good agreement with the SM simulation is found (see Figure A.7 for kinematic distributions in the eq channel for e^+p and e^-p data). The signal is further enhanced using an M_e dependent cut on the inelasticity y_e. The cut has been determined by minimizing the expected limit. The cut ranges from $y_e \gtrsim 0.5$ for masses around 100 GeV, to $y_e \gtrsim 0.2$ for squark masses around 290 GeV. The cuts are shown in Figure 8.11a for the e^+p, and in Figure 8.12a for the e^-p sample (for details see section 8.3).

After this final selection step, a total of 2946 events in the e^+p data is found, compared to 2899 ± 302 events expected from simulation. In the e^-p data a total of 3121 events is selected, for 3215 ± 336 events predicted by the SM. Figure 8.5 shows kinematic distributions for the final selection in the eq channel. The reconstructed mass M_e for events passing all selection steps is shown for the e^+p data set in Figure 8.18a, and for e^-p in Figure 8.19a, together with the corresponding distributions for the other selection channels. A resolution of $\delta M_e = 4 - 10$ GeV is achieved for the reconstructed squark mass in signal events, determined from the signal MC. No significant excess is observed in the distributions of the reconstructed mass. Figures 8.10a and 8.10d show the event yield distributions of selected events in the integrated luminosity of the e^+p and e^-p data sets, respectively. A flat distribution is found for the event yield in both data sets.

In order to further reduce the background for setting limits, a sliding mass window is used, optimising the expected limit (for details see section 8.3). The mass window cuts are determined separately for the e^+p and e^-p selections, in a similar way to the optimised $y_e - M_e$ cut. The mass window is shown in Figure 8.13a for the e^+p selection, and in Figure 8.14a for the e^-p selection. The efficiency for signal events varies with the considered squark mass M_{squark}. After all selection steps it is in the range of $30\% - 40\%$. The signal efficiency is shown in Figure 8.15a for the e^+p and e^-p selection.

Multilepton-multijet final states eMJ(RC), eMJ(WC), eeMJ, eμMJ and eνMJ

Squark decays via neutralino or chargino radiation are expected to result in a higher multiplicity of objects in the final states. The signatures are similar to final states observed in higher order NC DIS processes at high x and high Q^2. A distinguishing feature of heavy squark decays is, that the decay products are mainly emitted into the forward direction. This feature will be used in the statistical discrimination of signal and background processes.

A basic common preselection is applied for the eMJ(RC), eMJ(WC), $eeMJ$, $e\mu MJ$ and $e\nu MJ$ channels. An isolated electron with $P_T^e > 6$ GeV and $E^e > 11$ GeV in $5^\circ < \theta_e < 145^\circ$ is required. Central electrons $\theta_e > 30^\circ$ are required to have a well measured track associated to the cluster with a distance of less than 12 cm between the

extrapolated track impact point and the centre-of-gravity of the cluster. Furthermore, two jets with $P_T^{\mathrm{jet1,jet2}} > 15$ GeV in the polar angle range $7° < \theta_{\mathrm{jet}} < 145°$ are required.

After the basic common preselection steps 8345 events are selected in the e^+p data for 8185 ± 843 from MC simulation. In the e^-p data 6433 events are selected for 6190 ± 639 events expected from simulation. The e^+p data contains 693 events with a second electron for 722 ± 75 events predicted by the simulation. In the e^-p data 574 events with a second electron are found, compared to 556 ± 59 events from SM expectation. Indeed, very good agreement is observed for data and MC for these more complex final states.

Further cuts are applied for the common preselection: The steep decrease of the NC DIS cross section with Q^2 is exploited, and the SM background is reduced by requiring $Q^2 > 1000$ GeV^2. This corresponds to an implicit upper cut on the polar angle of the electron θ_e, since Q^2 and the polar angle of the scattered electron are strongly correlated. A further explicit cut on the electron polar angle of $\theta_e < 110°$ exploits the forward topology of signal events. More cuts exploiting the fact that at least one of the squark decay products is expected to be emitted in the very forward region are applied. At least one of the two highest P_T jets, or the electron must be found in the region $\theta < 40°$. Moreover, of the two highest P_T jets, the one with the larger polar angle must satisfy the condition $\max(\theta_{\mathrm{jet1}}, \theta_{\mathrm{jet2}})[°] < (y_e - 0.3) \cdot 180°$. These cuts separate efficiently signal events from NC DIS background [34]. The distributions for $\max(\theta_{\mathrm{jet1}}, \theta_{\mathrm{jet2}})/180° - y_e$ and the polar angle of the most forward electron or jet $\theta_{e,\mathrm{jet1,jet2}}$ are shown in Figure 8.6 for the basic common preselection, for the e^+p and e^-p sample. For illustration of the discrimination power, the signal of a squark with mass $M_{squark} = 150$ GeV, which decays into an electron and multijets is also indicated.

Electron-multijet final states eMJ(RC) and eMJ(WC)

For squark decays via a single χ^0, $\chi^\pm$ with subsequent R-parity violating decay, only a single electron and multiple jets are expected in the final state. Both charge types, electron and positron, are expected from squark decays, as discussed in section 2.5. In SM processes only final states with a single electron are expected, where the charge of the electron corresponds to the initial charge of the incident electron. Thus, an essentially background free signal is expected for events with a single electron and multiple jets where the measured electron charge is opposite to the incident electron charge. For this purpose, selection channels labelled "right charge" (same sign) $eMJ(RC)$ channel and "wrong charge" (opposite sign) $eMJ(WC)$ channel are used for events fulfilling the selection and charge criteria. The distinction between the $eMJ(WC)$ channel and the $eMJ(RC)$ channel is based on the significance of the track curvature measurement in the central tracking detector. Events are allocated to the $eMJ(WC)$ channel if the track is well-measured in the CTD, which requires the electron to be in the polar angle range $30° < \theta_e < 110°$, and its charge to be determined opposite to the incident electron's charge with a charge significance greater than two standard deviations $\sigma_\kappa < -2$ [34]. Otherwise, events are allocated to the $eMJ(RC)$ channel. The determination of the charge significance is described in section 5.1.

To ensure that all particles from the ep collision are detected in an event, the selection requires $P_T^{\mathrm{miss}} < 15$ GeV and $40\ \mathrm{GeV} < \sum(\mathrm{E} - \mathrm{P_z}) < 70$ GeV. In order to be exclusive with respect to the multilepton topologies, events are vetoed if additional isolated

electrons or muons with $P_T^{e,\mu} > 5$ GeV are present.

After these selection steps, there is one candidate event observed for the $eMJ(WC)$ channel in the e^+p data for a SM expectation of 0.6 ± 0.4 from the SM simulation. In the e^-p data no candidate is present for an expectation of 1.3 ± 0.3 from SM simulation. The selection efficiencies after all these steps are shown in Figure 8.16a for squark decays via a single gaugino, and in Figure 8.16b for cascade decays of a squark with mass $M_{squark} = 250$ GeV. The signal efficiencies are typically in the range $5 - 20\%$.

In the $eMJ(RC)$ channel 226 events are found in the e^+p data for an expectation of 219 ± 33 events from SM MC. In the e^-p data 197 events are observed for 212 ± 32 events from simulation. A good agreement between data and simulation is observed (see Figure A.8 for kinematic distributions of jets and electrons in this sample). The background expectation is further reduced in the $eMJ(RC)$ channel by optimising the expected limit using an M_{rec} dependent cut on the inelasticity y_e, in a similar procedure as in the eq channel. The cut ranges from $y_e \gtrsim 0.7$ for masses around 100 GeV, to $y_e \gtrsim 0.5$ for squark masses around 290 GeV. The cuts are shown in Figure 8.11c for the e^+p, and in Figure 8.12c for the e^-p sample (for details see section 8.3). After the optimisation, there are 140 events left in the e^+p data for a SM expectation of 146.0 ± 21.4 events. For the e^-p data, a total of 147 events is found, for 158.3 ± 23.9 events from SM simulation. Figure 8.7 shows kinematic distributions for the final selection in the $eMJ(RC)$ channel. The reconstructed mass M_{rec} is shown for events passing all selection steps in Figures 8.18c and 8.19c for the e^+p and e^-p data sets, respectively. A resolution of $\delta M_{rec} = 6 - 10$ GeV is achieved with the mass reconstruction method in this channel, determined from the signal simulation. A good agreement between the data and the SM expectation is observed. Figures 8.10b and 8.10f show the event yield distributions of selected events in the integrated luminosity of the e^+p and e^-p data sets, respectively. Within the statistical uncertainties, a flat distribution is found for the event yield in both data sets.

A further reduction of the SM background is achieved using a sliding mass window similar to the eq channel (for details see section 8.3). The mass window is shown in Figure 8.13c for the e^+p selection, and in Figure 8.14c for the e^-p selection. The selection efficiency after all selection steps is in the range $10 - 40\%$, and shown for the e^+p and e^-p selections in Figures 8.15c and 8.15d, respectively, for squark decays via a single neutralino or chargino. Furthermore, selection efficiencies are determined for cascade decays of neutralinos and charginos leading to an electron multijet final state. The cascade decay efficiencies are slightly higher, since more high P_T jets are expected in the final state. The efficiencies are shown for the involved neutralino and chargino masses and a squark mass of $M_{squark} = 250$ GeV in Figures 8.15e and 8.15f for the e^+p and e^-p selections, respectively.

Electron-lepton-multijet final states eeMJ, eμMJ and eνMJ

The final states of squark decays are expected to consist of more than one isolated lepton and multiple jets in cascade decays of neutralinos and charginos. The expectation for these final states from SM processes is very low. The channels $eeMJ$ and $e\mu MJ$ require in addition to the common preselection the presence of an additional isolated lepton: An electron with the same criteria used in the common preselection in the $eeMJ$ channel or a muon with $P_T^\mu > 5$ GeV in the polar angle range $10^\circ < \theta_\mu < 110^\circ$

in the $e\mu MJ$ channel.

For the $eeMJ$ channel, two candidate events are observed in the e^+p data for 1.7 ± 0.5 from simulation. No event is found in the e^-p data for a SM expectation of 1.5 ± 0.5 events. The observations are well in agreement with the SM simulation. Signal efficiencies for cascade decays selected in the $eeMJ$ channel are in the range $5-35\%$, depending on the masses of the involved gauginos. The efficiency is shown for a squark mass $M_{squark} = 250$ GeV in Figure 8.17a. The reconstructed mass for the two candidate events in the e^+p data is shown in Figure 8.18d.

No candidate event is observed for the $e\mu MJ$ channel in the e^+p and e^-p data with 0.03 ± 0.03 and 0.03 ± 0.02 events from simulation, respectively. The signal efficiency for cascade decays producing final state are in the range $5-15\%$, depending on the masses of squarks and gauginos involved. For a squark mass $M_{squark} = 250$ GeV, the efficiency is shown in Figure 8.17b.

A neutrino is expected in the final state for events in the $e\nu MJ$ channel. A large reconstructed missing transverse momentum $P_T^{\text{miss}} > 15$ GeV is required in addition to the common preselection. Furthermore, it is exploited that a neutrino emitted in the forward direction reduces the quantity $\sum(E - P_z)$ significantly, which causes y_h to be substantially smaller than y_e, while for the main expected background, NC DIS events, $y_h \approx y_e$ is expected. A cut $y_e(y_e - y_h) > 0.04$ is used to increase the signal to background ratio [34]. Rejecting events with additional isolated electrons or muons with $P_T^{e,\mu} > 5$ GeV, ensures exclusivity with respect to the $eeMJ$ and $e\mu MJ$ channels. A total of three events is observed in the e^+p data for an expectation of 5.6 ± 1.2 events and five events are observed for the e^-p data for 8.2 ± 2.0 events from the simulation. The signal efficiency is in the range $5-40\%$, shown in Figure 8.17c for a squark mass $M_{squark} = 250$ GeV. Reconstructed masses for the candidate events in e^+p data and e^-p data are shown in Figures 8.18e and 8.19d, respectively.

Neutrino Based Selection Channels

The event selection for neutrino based channels is discussed in the following. High P_T objects, mainly emitted in the forward direction, are also expected from heavy squark decays in these topologies.

Neutrino-jet final state νq

Squarks decaying into a neutrino and a high P_T jet mimic the final states of CC DIS events with high missing transverse momentum. Just as in the eq channel, the isotropic decay of squarks produced in the s-channel allows a statistical separation of signal and background. The νq channel is only relevant for the decay of $\tilde{d}_R^k$ squarks produced in e^-p collisions. The $\tilde{u}_L^j$ squarks cannot decay into a neutrino and a single jet. The channel is analysed and shown for the e^+p data set only as a cross-check.

Events with neutrinos present in the final state, produced in the forward direction, are selected by requiring high reconstructed missing transverse momentum $P_T^{\text{miss}} > 30$ GeV and longitudinal energy momentum imbalance $\sum(E - P_z) < 50$ GeV. The phase space is restricted to $Q_h^2 > 2500$ GeV^2 and $0.1 < y_h < 0.9$ to increase the signal to background ratio, and remove remaining γp background. The low y_h region is excluded to ensure that the hfs is fully contained in the LAr, and the high y_h region

is excluded due to the poor Q_h^2 resolution. Exclusivity to the other selection channels is ensured by vetoing events with any electrons or muons with $P_T^{e,\mu} > 5$ GeV, or events with two jets with $P_T^{\text{jet1,jet2}} > 15$ GeV.

In the e^+p data 1497 events are observed for an expectation of 1476 ± 177 events from simulation. For the e^-p data, the selection yields 3197 events for 3372 ± 405 events from the simulation (kinematic distributions for the sample are shown in Figure A.9). In order to further reduce the SM background, an optimisation in the $y_h - M_h$ plane is also applied in this channel. The cut ranges from $y_h \gtrsim 0.2$ for masses around 100 GeV to $y_h \gtrsim 0.1$ for squark masses around 290 GeV (for details see section 8.3). The cut is illustrated in Figure 8.12b for the e^-p sample. After these selection steps, a total of 2858 events is observed in the e^-p data for a SM expectation of 2983 ± 358 events. A good agreement is observed between data and SM simulation. Kinematic distributions for this selection are shown in Figure 8.8 for the e^-p data set. The reconstructed mass M_h for events passing all selection steps is shown for the e^-p in Figure 8.19b. No significant excess is observed in the distributions of the reconstructed mass. The resolution for reconstructed squark masses, determined in the signal MC, is in the range $\delta M_h = 12 - 22$ GeV in this channel, worse than in the electron based channels, due to the indirect reconstruction of the neutrino. Figure 8.10e shows the event yield distribution of selected events in the integrated luminosity of the e^-p data set, respectively. A flat event yield is observed for the data set.

A mass window is determined, similar to the eq and $eMJ(RC)$ channel, which optimises the expected limit. The mass window cuts are shown in Figure 8.14b for the e^-p selection (for details see section 8.3). The signal efficiency after all these selection steps depends on the considered squark mass, and is typically in the range $50 - 60\%$, shown in Figure 8.15b.

Neutrino-multijet final state νMJ

Squark decays via neutralinos and charginos with single or multiple neutrinos and multiple jets in the final state mimic the final state of higher order CC DIS events with large missing transverse momentum.

The selection of candidate events requires a substantial reconstructed missing transverse momentum $P_T^{\text{miss}} > 26$ GeV. This value ensures a high trigger efficiency and increases the signal to background ratio. A cut $\sum(E - P_z) < 50$ GeV ensures the reconstructed neutrino energy is positive. Two jets with $P_T^{\text{jet1,jet2}} > 15$ GeV in the polar angle range $7^\circ < \theta_{\text{jet1,jet2}} < 145^\circ$ are required.

After these steps 275 events are selected in the e^+p data for an expectation of 301 ± 79 events from simulation. For the e^-p data, the selection yields 437 events for 503 ± 137 events from the simulation (for the uncertainties, see section 8.5). Though in agreement within the uncertainties, the data is slighty overestimated by the MC simulation (see Figure A.10 for kinematic distributions of candidate events in the sample). A further reduction of the SM background is applied, which exploits differences in the $y_h - M_{rec,\nu}$ distributions, and optimises the expected limit in a similar way to the previously discussed channels. The cut ranges from $y_h \gtrsim 0.5$ for masses around 100 GeV to $y_h \gtrsim 0.4$ for squark masses around 290 GeV (for details see section 8.3). The cut is illustrated in Figure 8.11d for the e^+p and in Figure 8.12d e^-p sample. The final event selection yields 113 events in the e^+p data for 134 ± 33.8 events predicted by the SM simulation

and 204 events in the e^-p data for a SM expectation of 235.5 ± 63.3 events. The data is in good agreement with the SM expectation. Figure 8.9 shows kinematic distributions for the final selection in the νMJ channel. The distributions of the reconstructed mass $M_{rec,\nu}$ for events after these selection steps are shown in Figures 8.18f and 8.19e for the e^+p and e^-p data, respectively. The resolution for the reconstructed squark mass is $\delta M_{rec,\nu} = 15 - 20$ GeV in this channel, determined in the signal MC. No significant deviation from the SM expectation is observed. Figures 8.10c and 8.10g show the event yield distributions of selected events in the integrated luminosity of the e^+p and e^-p data sets, respectively. A flat distribution is observed for the event yields in the three subperiods of both data sets. However, it is observed that the event yield in the last e^-p data set is slightly lower than in the first two subperiods. The effect may result from the large statistical uncertainties, which arise from the small statistics.

A mass window is also determined for this channel. The mass window is shown in Figure 8.13d for the e^+p, and in Figure 8.14d for the e^-p selection (for details see section 8.3). After all selection steps, the signal efficiency is typically $5-50\%$ for squark decays via a single neutralino or chargino. Figures 8.16c and 8.16d show the efficiency for the e^+p and e^-p selections, respectively. The signal efficiencies for cascade decays leading to a neutrino multijet final state are slightly higher, and shown in Figure 8.16e and 8.16f for a squark mass of $M_{squark} = 250$ GeV.

Neutrino-muon-multijet final state $\nu\mu$MJ

If an additional muon with $P_T^\mu > 5$ GeV in the polar angle range $10° < \theta_\mu < 110°$ is found in events fulfilling the common νMJ selection, before the $y_h - M_{rec,\nu}$ cut is applied, the event is attributed to the $\nu\mu MJ$ channel. No candidate events are found in this channel in e^+p and e^-p data, for very small expectations from SM processes of 0.06 ± 0.03 and 0.04 ± 0.02, respectively. The signal efficiency in the $\nu\mu MJ$ channel is in the range $5 - 20\%$, and shown for $M_{squark} = 250$ GeV in Figure 8.17d.

Selection Summary

The event rates and the SM expectation in the selection channels are summarised in Table 8.1. The selection channels are dominated mainly by irreducible, and small *fake* contributions from SM processes.

Event yields of selected data events in channels with a high SM expectation are shown in Figure 8.10 for the e^+p and e^-p data, in the different periods of data-taking. The selected number of events per pb^{-1} is mostly consistent with an expected flat distribution. Only for e^-p data, a slightly lower event yield is observed in the last period. The effect is attributed to large statistical fluctuations.

The distributions of the reconstructed mass for selected events are shown in Figures 8.13 and 8.14, for channels which contain data events in e^+p and e^-p data, respectively. No significant excess with respect to the SM background expectation has been observed in any of the selection channels. A good description of the differential distributions for the event kinematics and global quantities is observed. Some interesting SM events with high object multiplicity and high transverse momenta are selected in the data, mostly in the e^+p data. Channels with low data statistics show fluctuations,

but a good agreement with the SM expectation within the statistical uncertainties is observed throughout.

8.3 Optimisation of the Expected Limit

The method for the optimisation of the expected limit has been used in previous searches for squarks at H1 [34]. Since data samples with higher integrated luminosities are studied in this analysis in the same kinematic region, a higher contribution from SM background processes is expected. The optimisation is applied to all channels with a high amount of SM background, $N_{\text{events}} \gtrsim 100$ events. The expected limit is calculated as the exclusion limit s_{up}, averaged over the possible outcomes of the experiment assuming there is no signal contribution. The limit is corrected for detection inefficiencies. The expected limit is determined with a simple frequentist approach using the SM expectation N_{bg} and the signal selection efficiency ϵ. The optimal cut is found when $s_{\text{up}} = (\langle \mu^{95}_{BG} \rangle - N_{\text{bg}})/\epsilon$ is minimal for this cut value. This is the only place where the signal efficiency enters the calculation. For any possible observation n_{obs} the 95% confidence level (CL) limit is determined by adjusting the Poisson parameter $\mu^{95}(n_{\text{obs}})$, such that the probability to observe n_{obs} or less events equals $1 - 0.95$. The quantity $\langle \mu^{95}_{BG} \rangle$ is defined as the 95% CL limit averaged over all possible outcomes n_{obs} of the experiment, weighted by the Poisson probability to observe n_{obs} events in absence of a signal. The Poisson probability $P_{\text{poisson}}(n_{\text{obs}}; \mu)$ to observe n_{obs} events from a Poisson process with mean $\mu = N_{\text{bg}}$ is used:

$$\langle \mu^{95}_{BG} \rangle = \sum_{n_{\text{obs}}=1}^{\infty} P_{\text{poisson}}(n_{\text{obs}}; N_{\text{bg}}) \cdot \mu^{95}(n_{\text{obs}})$$

$$\text{with} \quad \mu^{95}(n_{\text{obs}}) \;:\; \sum_{i=0}^{i \leq n_{\text{obs}}} P_{\text{poisson}}(i; \mu^{95}(n_{\text{obs}})) \equiv 1 - 0.95$$

The probability (p) value of $1 - 0.95 = 0.05$ is introduced to yield one-sided 95% CL upper limits s_{up}. The quantity $\mu^{95}(n_{\text{obs}})$ is related to the quantiles $F^{-1}_{\chi^2}(p, 2(n_{\text{obs}} + 1))$ of a χ^2 distribution with n degrees of freedom via $\mu^{95}(n_{\text{obs}}) = F^{-1}_{\chi^2}(p, 2(n_{\text{obs}} + 1))/2$ at a p-value corresponding to $p = 1 - CL$ [6]. The interval $[0, s_{\text{up}}]$ is designed to cover the true value of the signal with a probability of $1 - p$ corresponding to the required confidence level.

Optimised $y - M$ Cuts

In selection channels with a high contribution from SM background processes cuts on the reconstructed inelasticity depending on the reconstructed mass are applied, which minimize the expected limit for the signal. The cuts are determined using the signal prediction for different generated squark masses: 100 GeV $< M_{squark} <$ 290 GeV in steps of typically 25 GeV. In channels with a signal contribution from decays involving gauginos, the cut is determined including all possible gaugino masses at a given squark mass. The optimal cut values, which yield the smallest expected limit s_{up}, are determined seperately for the e^+p and e^-p SM background and signal

expectations. A second order polynomial is fitted to the determined cut values in each channel, interpolating the cut for all reconstructed masses.

Figures 8.11 and 8.12 show the SM background distributions, the expected signal distributions for the reconstructed masses depending on the reconstructed inelasticities, and the functional form of the optimised cut. The SM expectations of NC DIS and CC DIS events in the eq and νq channels cluster at low reconstructed mass and low reconstructed inelasticity, whereas the signal is uniformly distributed in $y_{e,h}$. A degradation of the mass resolution is visible for signal events at low values of y_e in the eq channel, and for signal events in the νq channel for low and high y_h. The optimal cut removes events below a certain $y_{e,h}$, and is stronger in the low mass region. In the $eMJ(RC)$ channel, the SM expectation clusters at high values of y_e and low values of the reconstructed mass. The signal events peak towards high values of y_e, and the optimal cut removes more background at low reconstructed masses, and is less strong for higher masses. For the νMJ channel, the SM expectation clusters again at low reconstructed masses and low inelasticities y_h, whereas the signal events peak towards high inelasticities. The low y_h region is removed by the optimal cut, with only a small dependence on the reconstructed mass. Only small differences are observed in the optimal cut values for the e^+p and e^-p samples, which originate from the different background expectations, due to the different dominant processes, and the different integrated luminosities of the data sets.

Sliding Mass Window Method

In order to further reduce the number of events to set limits in channels with a high contribution from SM background processes, a sliding mass window optimisation is applied to the final selections. Figures 8.13 and 8.14 show signal and background distributions, and the cuts for the mass window in the eq channel, the νq channel, the $eMJ(RC)$ channel, and the νMJ channel, separately for the e^+p and e^-p background. The mass windows are determined in the same way as the optimised $y - M$ cuts. The mass window is typically broader for the e^+p selection with respect to the e^-p selection. The mass window width increases for higher squark masses, due to the decreasing resolution of the mass reconstruction methods and the lower background expectation. It is generally smaller for the electron based selection channels, and broader in the neutrino based selection channels, due to the worse resolution of the reconstructed mass. The upper bound of the mass window is typically divergent for higher squark masses, when the expected limit does not change with the increasing upper mass cut. The maximum value of M_{upper} is set to 500 GeV, which does not remove any data events. The highest events in data and MC have reconstructed masses smaller than < 400 GeV. The reconstructed mass value can be higher than the centre-of-mass energy, when misreconstruction, or jet resolution effects lead to an overestimation of the energy, or when $x_{e,h}$-values > 1 are reconstructed. For high squark masses, only the lower mass window cut significantly reduces the background contribution.

8.4 Signal Efficiencies

Signal efficiencies have been derived for the squark decays leading to the final states in the selection channels. The efficiencies are used for the optimisation of the $y - M$ cuts and the sliding mass windows. The efficiencies are different for the e^+p and e^-p selections, due to differences in the optimised selection cuts. The differences originate from two aspects: Data sets with different integrated luminosities are used for e^+p and e^-p scattering; and the involvement of different partons in the scattering processes in e^+p and e^-p SM interactions leads to differences in the shape of the background distributions. Figure 8.15 shows the efficiencies for the eq, νq and the $eMJ(RC)$ channels after all selection criteria are applied. The different optimisation cuts, which are determined separately for the e^+p and e^-p selections, lead to lower efficiencies in these channels for the signal from e^+p interactions. Figure 8.16 shows signal efficiencies for the $eMJ(WC)$ and the νMJ channels. For the νMJ channel, the signal efficiency is slightly higher in the e^+p selection with respect to the e^-p selection, due to the stronger $y-M$ cut in the e^-p selection. Identical selections for the $eMJ(WC)$ channel in e^+p and e^-p, have the same selection efficiency for signal events in e^+p and e^-p scattering. The efficiency for the $eMJ(WC)$ channel is significantly lower compared to the efficiencies determined in the $eMJ(RC)$ channel, due to the asymmetric charge significance cut, which attributes events only to the $eMJ(WC)$ channel if the charge measurement is significant. In figure 8.17, the selection efficiencies for cascade decays leading to the multilepton and multijet final states is shown for the selections.

The efficiencies are typically increasing for higher squark masses. In the eq channel, the efficiency has a minimum for squark masses of 175 GeV. The low efficiency at this mass results from the functional form of the $y_e - M_e$ cut in this channel, which is strongest at $\sim$ 175 GeV. For the νq channel, the efficiency has a rather flat plateau for squark masses between 125 GeV and 200 GeV, and decreases for lower and higher masses. The decrease of the efficiency is attributed to the degrading mass resolution, and the width of the mass window. For squark decays involving one gaugino, leading to the final states selected in the $eMJ(RC)$ and νMJ channels, the selection efficiency is highest in the regions, where the mass difference between the squark and the gaugino is large enough, to allow for high transverse momenta of the decay products, electron or neutrino and jets. For mass configurations where the gaugino mass is very small, or where the gaugino mass approaches the squark mass, one of the decay products typically gets only low P_T, and the event may be rejected by the requirements of the selection.

For decays which proceed via a cascade involving two gauginos, the efficiencies increase with the squark mass and the gaugino mass. The highest efficiency for these events is achieved typically for mass configurations, where the mass difference between the heavier gaugino and the squark is large enough for the decay products to pass the transverse momentum cuts in the selection. The efficiencies are typically higher for events with a light LSP in the cascade, so that particles produced in the gaugino decay also have large enough momenta to pass the selection criteria. For the shown squark mass of 250 GeV, the highest efficiency in cascade decays is achieved for a mass of the heavier gaugino of 220 GeV, and a LSP mass of 120 GeV.

8.5 Systematic Uncertainties

The influence of the following experimental systematic uncertainties on the selected toplogies has been considered:

- The uncertainty on the electromagnetic energy scale varies depending on the polar angle from 0.7% in the central region to 2% in the forward region [130]. The uncertainty of the polar angle measurement of electromagnetic clusters is 3 mrad.
- An uncertainty of 2% is attributed to the knowledge of the hadronic energy scale [130]. The polar angle measurement of jets is attributed an uncertainty of 10 mrad.
- The integrated luminosity measurement has an averaged uncertainty of 3%.

The effects of the above mentioned scale uncertainties on the electromagnetic and hadronic energy scale, and the polar angle measurement uncertainty of electromagnetic clusters and jets, are evaluated for the SM background prediciton and the signal efficiencies by varying the corresponding quantities within one standard deviation in the MC samples. The experimental systematic uncertainties for the selected topologies are estimated by propagating the variations to the final distributions. The resulting uncertainties are determined for the contribution of each process separately for the topologies, and added in quadrature. The effect on the overall event yields has been determined to 3% in the eq channel, 7% in the νq channel, and 4% in the $eMJ(RC)$ and $eMJ(WC)$ channel. In the $e\mu MJ$ and $e\nu MJ$ channel, an uncertainty of 7% is determined, 10% in the $eeMJ$ channel, and 20% in the νMJ and $\nu\mu MJ$ channels.

The total uncertainty on the SM background prediction in each channel is determined by adding all the experimental systematic uncertainties and model uncertainties (see section 4.1) in quadrature. A summary of the systematic uncertainties is compiled in Table 8.2.

	Background Prediction							
Uncertainty	Selection Channel							
Source	eq	$eMJ\,^{(RC)}_{(WC)}$	$eeMJ$	$e\mu MJ$	$e\nu MJ$	νq	νMJ	$\nu\mu MJ$
Em Scale ($0.7-2\%$) Em θ (3 mrad) Had Scale (2%) Had θ (10 mrad)	3%	4%	10%	7%	7%	7%	20%	20%
Luminosity	3%							
Dominant Model Uncertainty	10%	15%	15%	15%	15%	10%	20%	15%
Dominant SM Background	NC	RC : NC WC : $W/\gamma p$	NC	NC	NC	CC	CC	LL $W/\gamma p$

	Signal Prediction		
Source	Prod. Cross Section	PDF Scale	Limited MC Statistics
Uncertainty	$7-50\%$	7%	10%

Table 8.2: Summary of experimental and theoretical model systematic uncertainties for the background prediction in the selection channels, and for the signal prediction (see section 4.1 and section 4.2). The electromagnetic (Em) and hadronic (Had) scale and polar angle uncertainties are determined by variation within one standard deviation and propagation to the final distributions. The background model uncertainties on the NC DIS (NC), CC DIS (CC), γp, W boson (W) and multilepton (LL) production processes are considered to be conservative [129; 130]. The model uncertainty in the MJ channels is higher due to the two high P_T jets. The uncertainties attributed to the signal prediction are estimated from the imprecise knowledge of the pdfs contributing to the production cross section, the scale at which the pdfs are evaluated, and the limited statistics available for the signal at the different mass combinations [34].

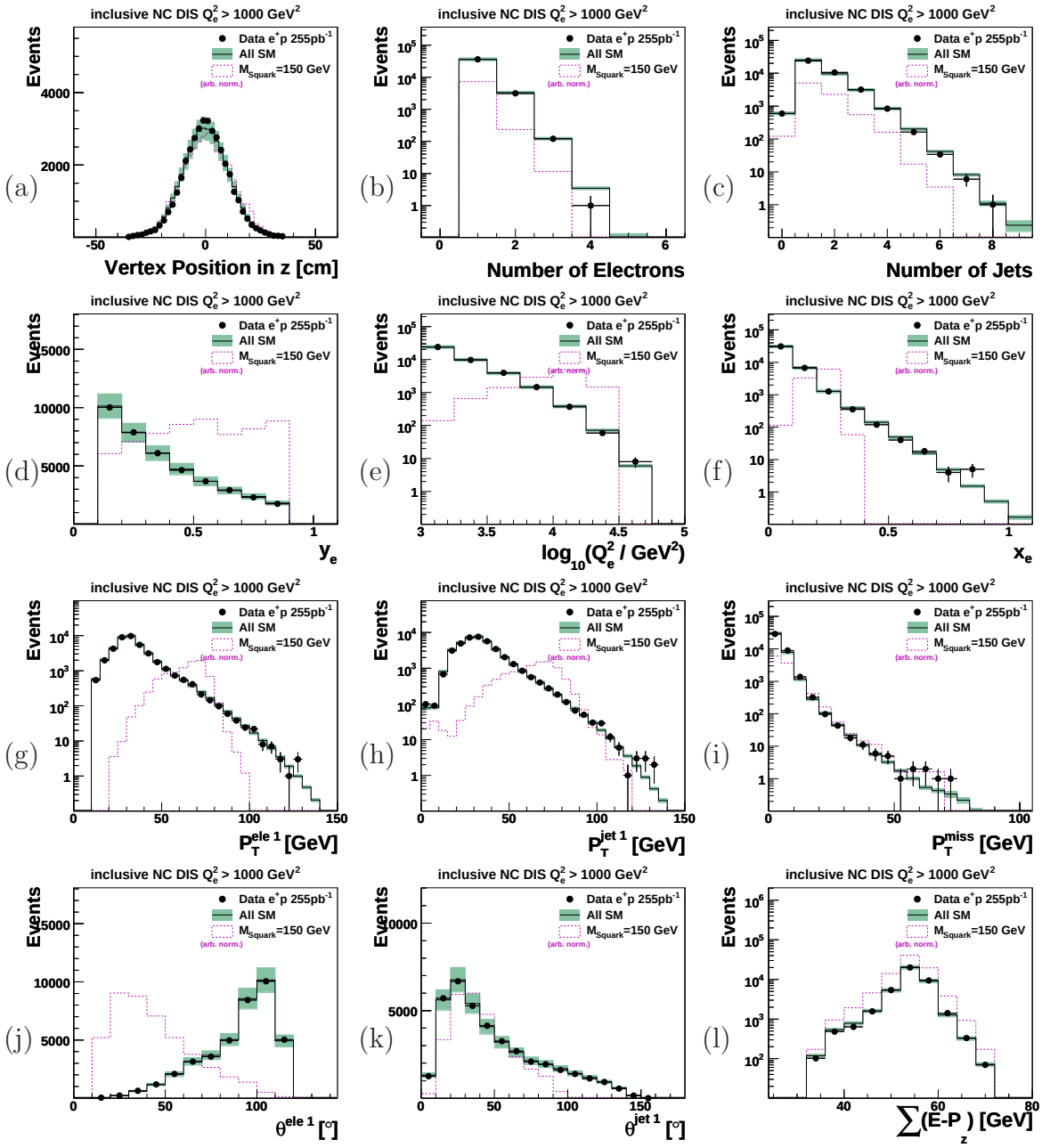

Figure 8.1: Distributions of (a) z-vertex position, (b) number of electrons per event, (c) number of jets per event, (d) inelasticity y_e and (e) virtuality $\log_{10}(Q_e^2)$ and (f) momentum fraction x_e reconstructed via the electron method, transverse momenta of (g) leading electrons P_T^{ele1} and (h) leading jets P_T^{jet1}, (i) reconstructed missing transverse momentum P_T^{miss}, polar angle of (j) leading electrons θ^{ele1} and (k) leading jets θ^{jet1}, and (l) longitudinal energy balance $\sum(E - P_z)$ in the **NC DIS** selection channel for $\mathbf{Q_e^2 > 1000\ GeV^2}$ with data (points) events from 255 pb^{-1} $\mathbf{e^+p}$ collisions compared to SM MC predictions. The error band gives all model and experimental systematic uncertainties on the SM prediction (solid histogram) added in quadrature. Error bars of data events show statistical uncertainties. The dashed histogram indicates the signal from a squark with $M_{squark} = 150\,\mathrm{GeV}$, which decays into an electron and a jet with arbitrary normalisation.

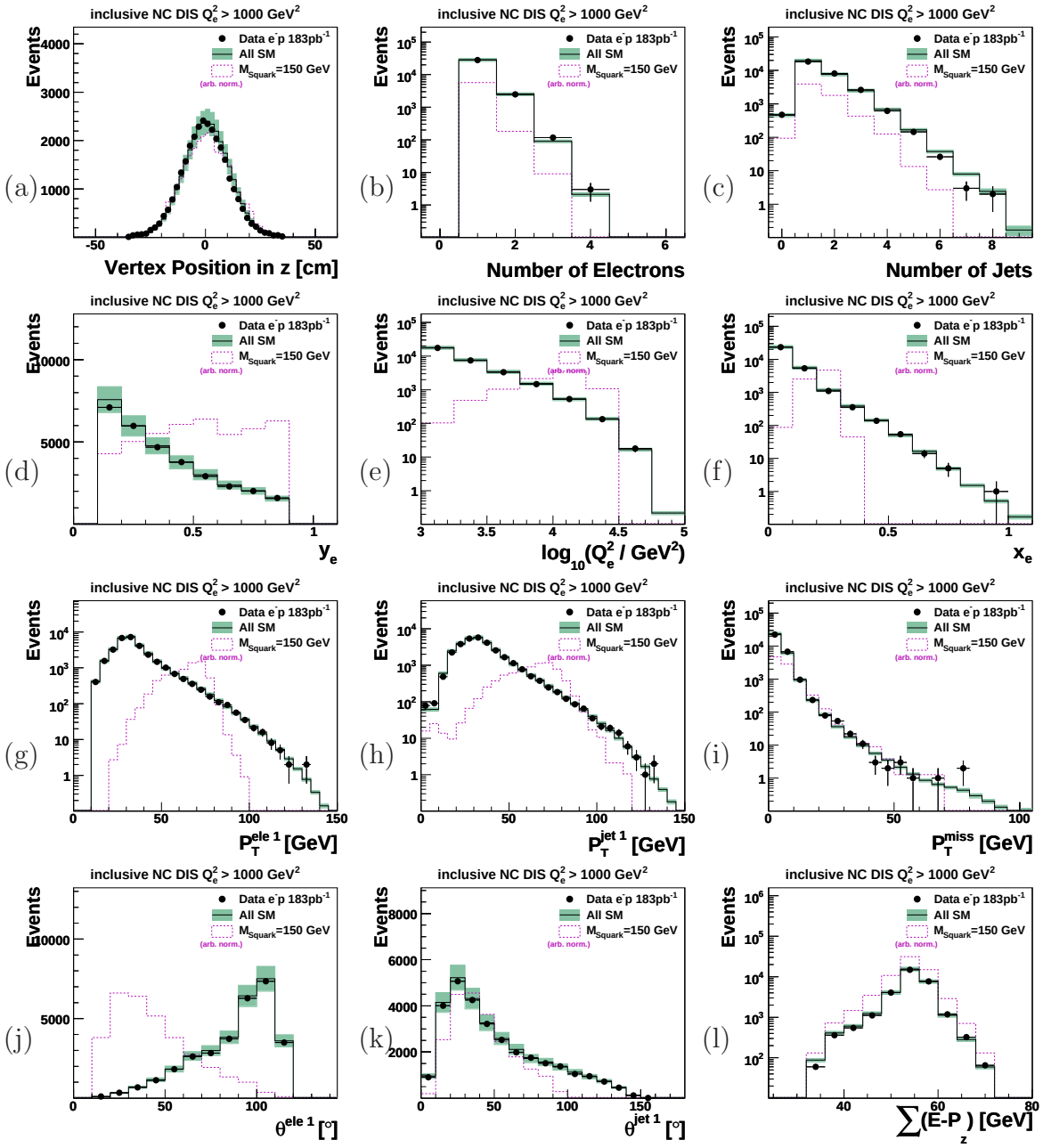

Figure 8.2: Distributions of (a) z-vertex position, (b) number of electrons per event, (c) number of jets per event, (d) inelasticity y_e and (e) virtuality $\log_{10}(Q_e^2)$ and (f) momentum fraction x_e reconstructed via the electron method, transverse momenta of (g) leading electrons P_T^{ele1} and (h) leading jets P_T^{jet1}, (i) reconstructed missing transverse momentum P_T^{miss}, polar angle of (j) leading electrons θ^{ele1} and (k) leading jets θ^{jet1}, and (l) longitudinal energy balance $\sum(E - P_z)$ in the **NC DIS** selection channel for $\mathbf{Q_e^2 > 1000\ GeV^2}$ with data (points) events from $183\,\mathrm{pb}^{-1}$ $\mathbf{e^-p}$ collisions compared to SM MC predictions. The error band gives all model and experimental systematic uncertainties on the SM prediction (solid histogram) added in quadrature. Error bars of data events show statistical uncertainties. The dashed histogram indicates the signal from a squark with $M_{squark} = 150\,\mathrm{GeV}$, which decays into an electron and a jet with arbitrary normalisation.

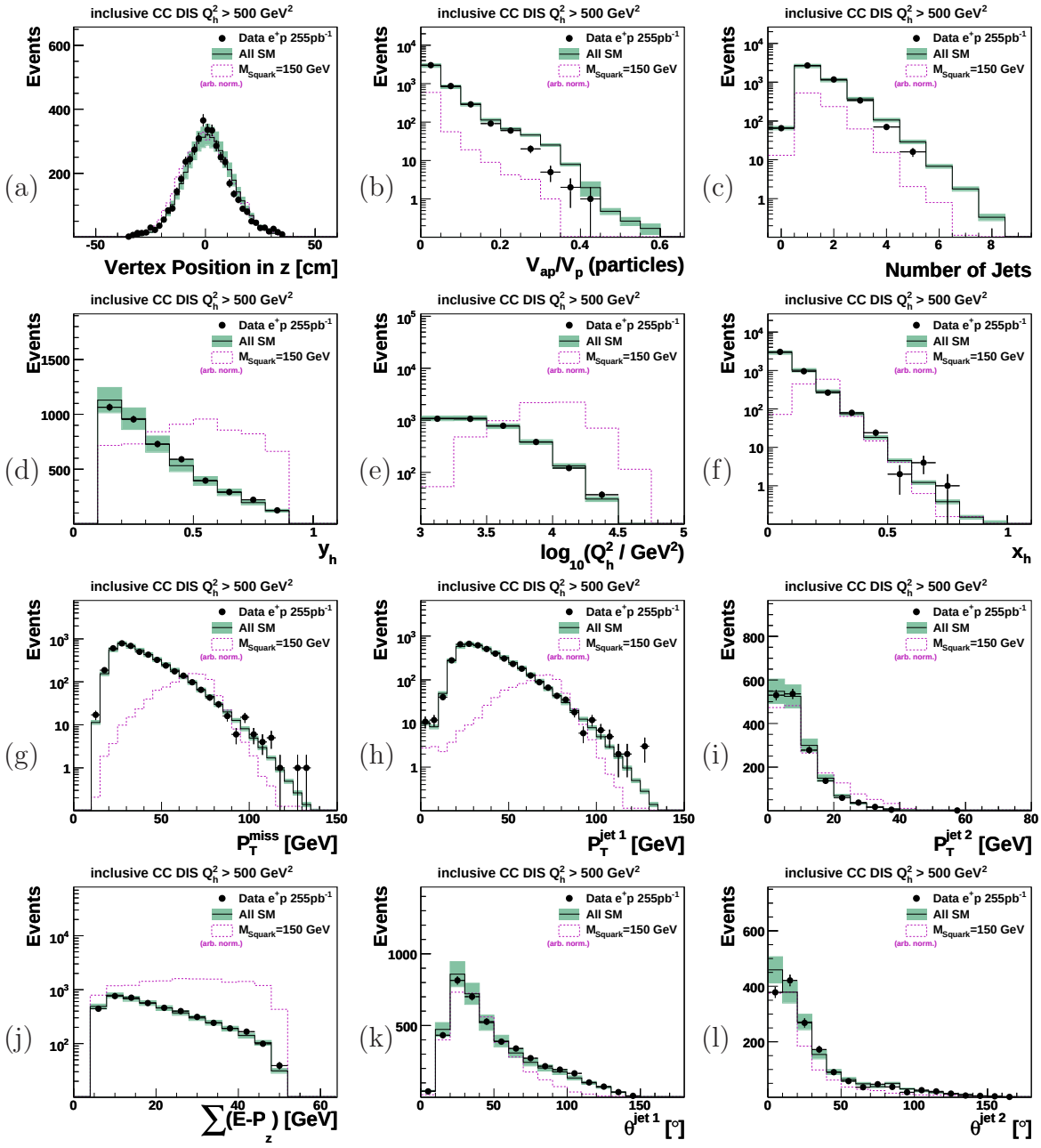

Figure 8.3: Distributions of (a) z-vertex position, (b) ratio of energy flow V_{ap}/V_p, (c) number of jets per event, (d) inelasticity y_h and (e) virtuality $\log_{10}(Q_h^2)$ and (f) momentum fraction x_h reconstructed via the hadron method, (g) reconstructed missing transverse momentum P_T^{miss}, transverse momenta of (h) leading jets P_T^{jet1} and (i) subleading jets P_T^{jet2}, (j) longitudinal energy balance $\sum(E - P_z)$, polar angle of (k) leading jets θ^{jet1} and (l) subleading jets θ^{jet2} in the **CC DIS** selection channel for $\mathbf{Q_h^2 > 500\ GeV^2}$ with data (points) events from $255\,\text{pb}^{-1}$ $\mathbf{e^+p}$ collisions compared to SM MC predictions. The error band gives all model and experimental systematic uncertainties on the SM prediction (solid histogram) added in quadrature. Error bars of data events show statistical uncertainties. The dashed histogram indicates the signal from a squark with $M_{squark} = 150\,\text{GeV}$, which decays into a neutrino and a jet with arbitrary normalisation.

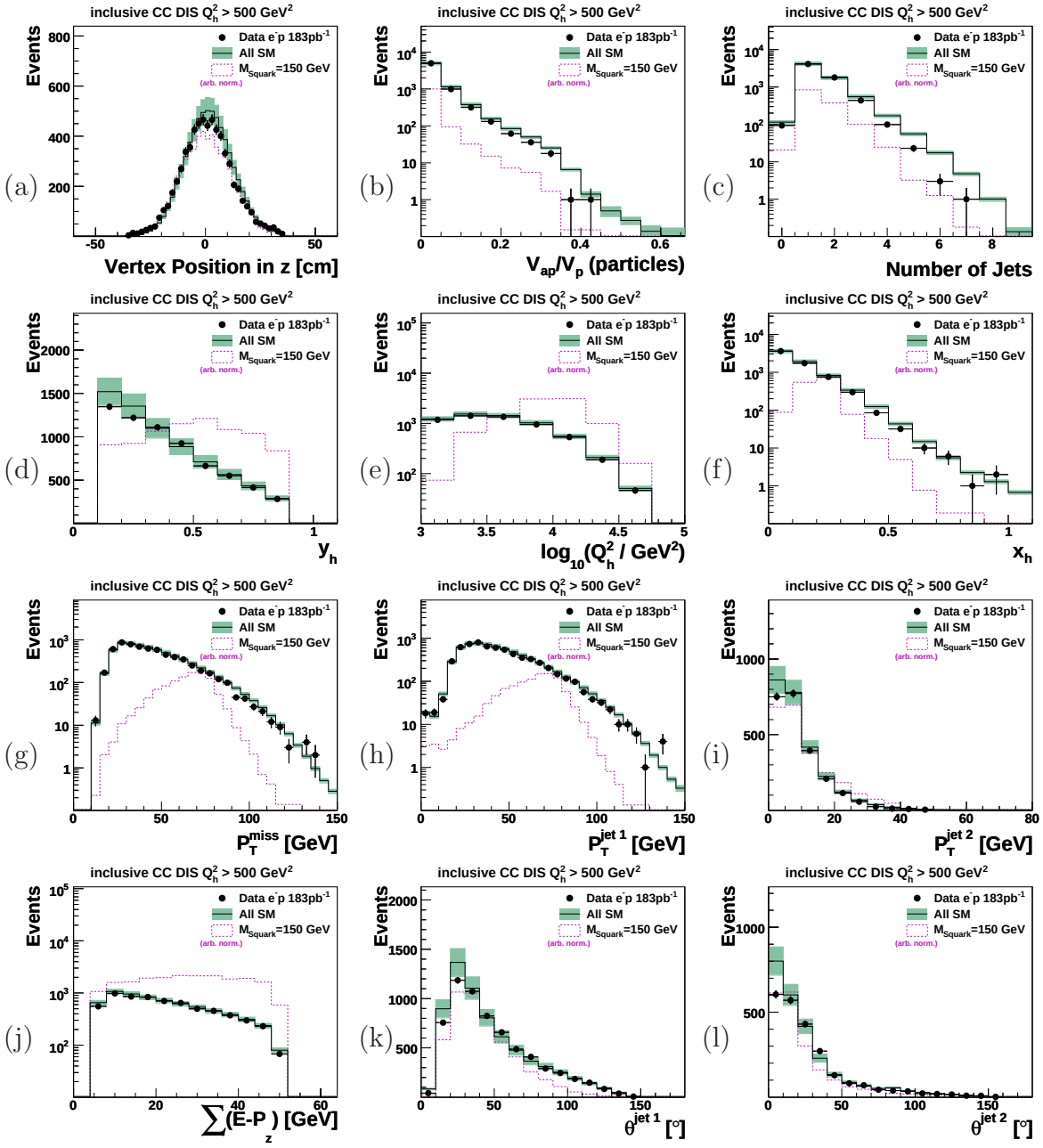

Figure 8.4: Distributions of (a) z-vertex position, (b) ratio of energy flow V_{ap}/V_p, (c) number of jets per event, (d) inelasticity y_h and (e) virtuality $\log_{10}(Q_h^2)$ and (f) momentum fraction x_h reconstructed via the hadron method, (g) reconstructed missing transverse momentum P_T^{miss}, transverse momenta of (h) leading jets P_T^{jet1} and (i) subleading jets P_T^{jet2}, (j) longitudinal energy balance $\sum(E - P_z)$, polar angle of (k) leading jets θ^{jet1} and (l) subleading jets θ^{jet2} in the **CC DIS** selection channel for $\mathbf{Q_h^2 > 500\ GeV^2}$ with data (points) events from $183\,\text{pb}^{-1}$ $\mathbf{e^-p}$ collisions compared to SM MC predictions. The error band gives all model and experimental systematic uncertainties on the SM prediction (solid histogram) added in quadrature. Error bars of data events show statistical uncertainties. The dashed histogram indicates the signal from a squark with $M_{squark} = 150\,\text{GeV}$, which decays into a neutrino and a jet with arbitrary normalisation.

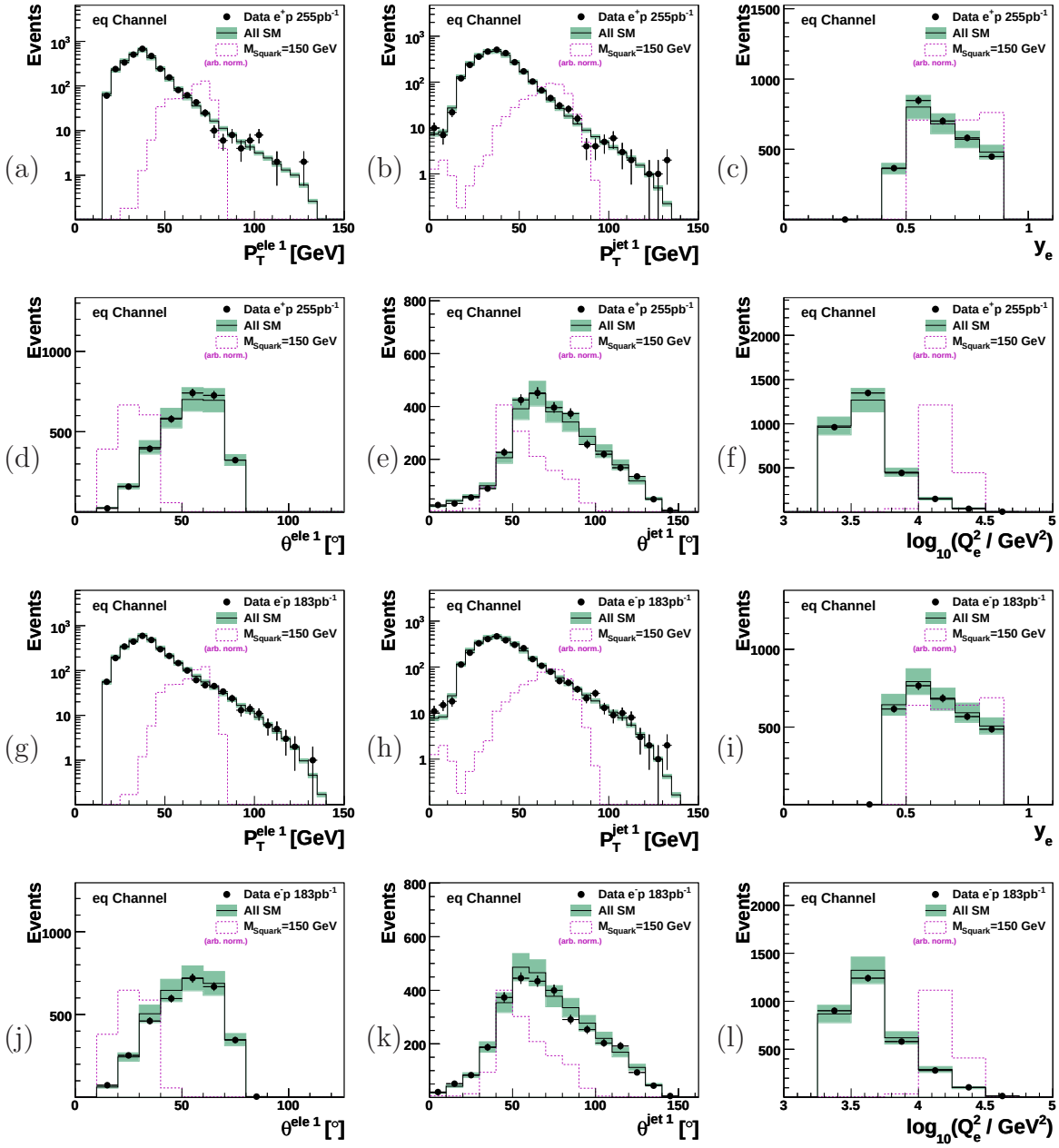

Figure 8.5: Kinematic distributions of selected events in the **eq channel** for (a-f) the $\mathbf{e^+p}$ and (g-l) the $\mathbf{e^-p}$ data (points) compared to SM MC predictions (solid histogram). Shown are the transverse momenta of (a,g) electrons P_T^{ele1} and (b,h) jets P_T^{jet1}, (c,i) the inelasticity y_e, the polar angle of (d,j) electrons θ^{ele1} and (e,k) jets θ^{jet1}, and (f,l) the virtuality $\log_{10}(Q_h^2)$. The error band gives all model and experimental systematic uncertainties on the SM prediction added in quadrature. Error bars of data events show statistical uncertainties. The dashed histogram indicates the signal from a squark with $M_{squark} = 150\,\mathrm{GeV}$, which decays into an electron and a jet with arbitrary normalisation.

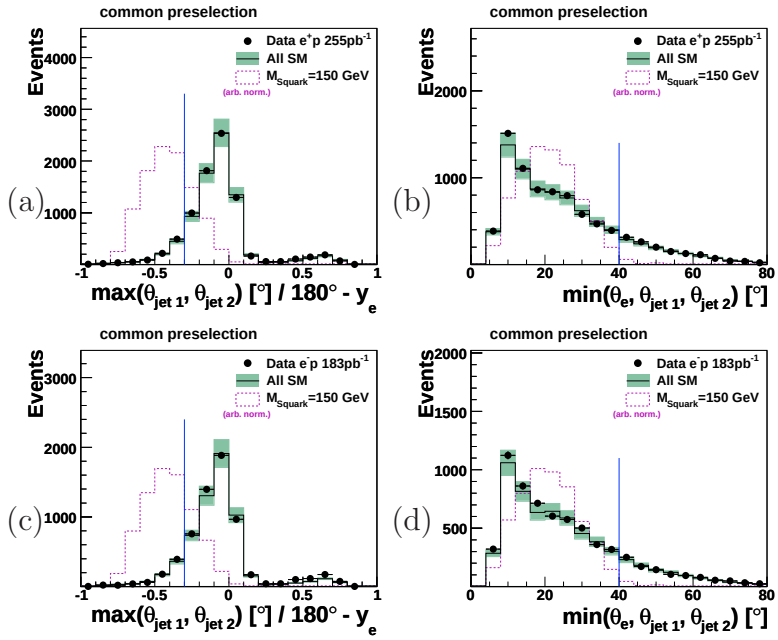

Figure 8.6: Distributions of (a,c) $\max(\theta_{\text{jet1}}, \theta_{\text{jet2}})/180° - y_e$ and (b,d) the polar angle of the most forward electron or jet $\theta_{e,\text{jet1,jet2}}$ for selected events after the basic **common preselection** in (a,b) the $\mathbf{e^+p}$ and (c,d) the $\mathbf{e^-p}$ data (points) compared to SM MC predictions (solid histogram). The error band gives all model and experimental systematic uncertainties on the SM prediction added in quadrature. Error bars of data events show statistical uncertainties. The dashed histogram indicates the signal from a squark with $M_{squark} = 150\,\text{GeV}$, which decays into an electron and multiple jets with arbitrary normalisation. The vertical lines indicate cut values which are used for the statistical separation of signal and background processes.

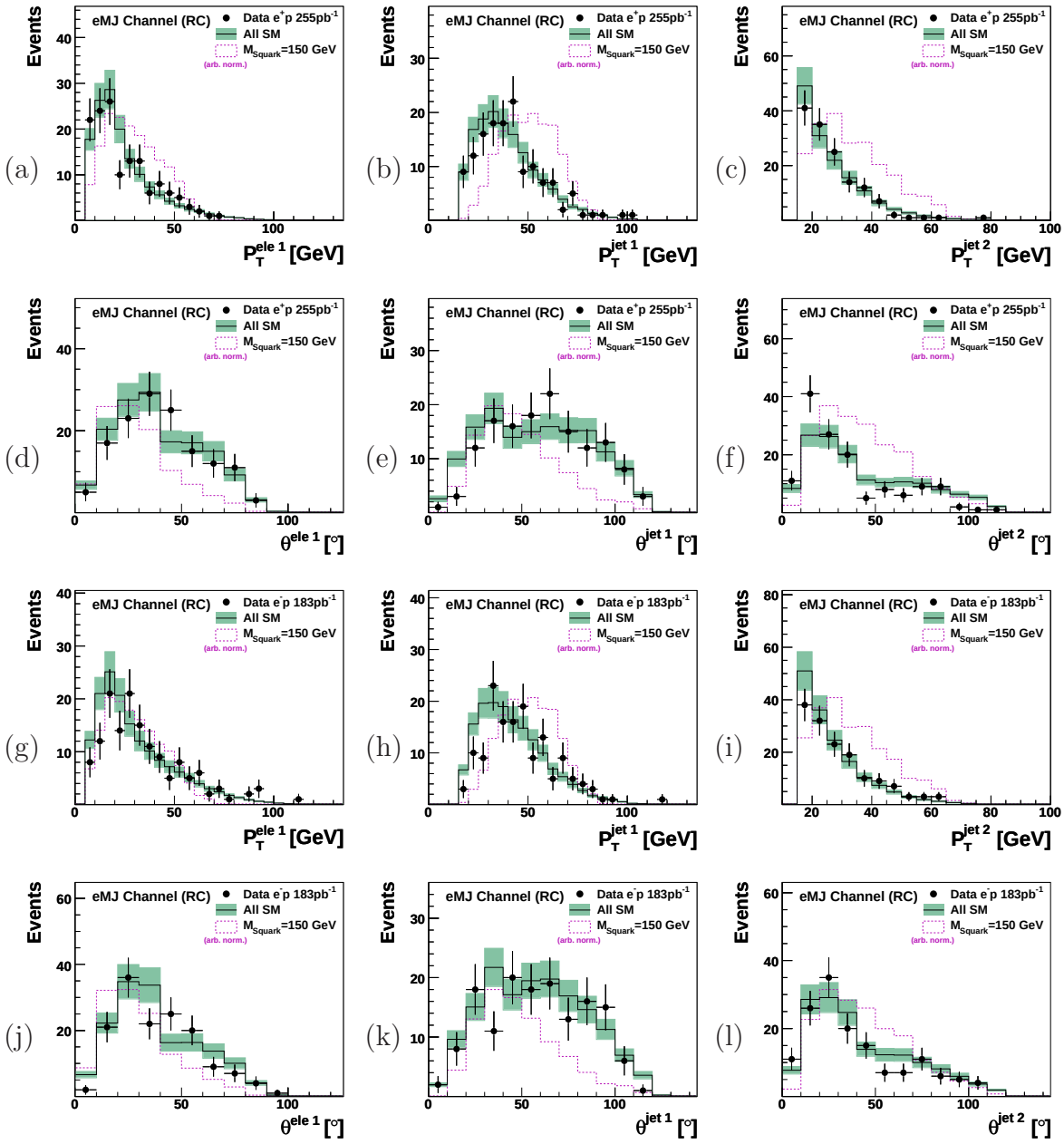

Figure 8.7: Distributions of the transverse momenta of (a,g) electrons P_T^e, (b,h) leading jets P_T^{jet1} and subleading (c,i) jets P_T^{jet2}, as well as the corresponding polar angle distributions of (d,j) electrons θ_e, leading jets θ_{jet1}, and subleading jets θ_{jet2} in the **eMJ(RC) channel** for (a-f) the $\mathbf{e^+p}$ and (g-l) the $\mathbf{e^-p}$ data (points) compared to SM MC predictions (solid histogram). The error band gives all model and experimental systematic uncertainties on the SM prediction added in quadrature. Error bars of data events show statistical uncertainties. The dashed histogram indicates the signal from a squark with $M_{squark} = 150\,\text{GeV}$, which decays into an electron and multiple jets with arbitrary normalisation.

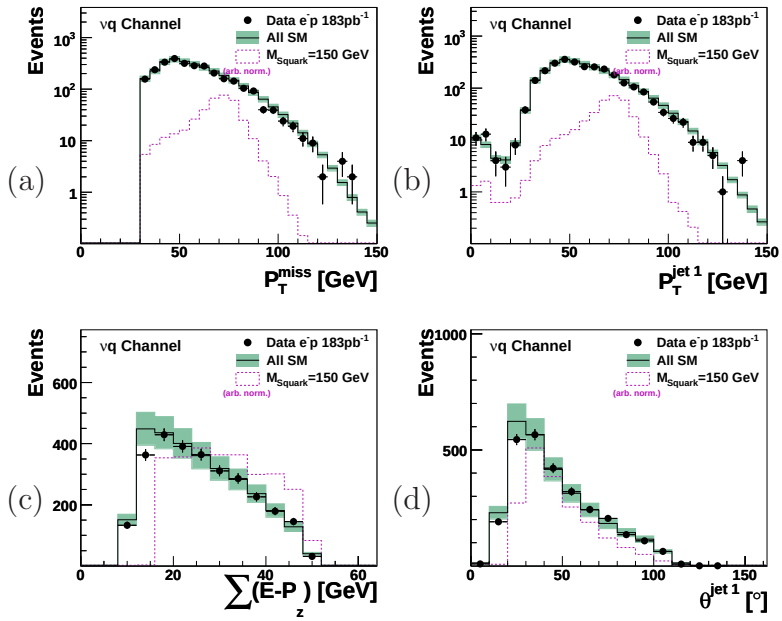

Figure 8.8: Distributions of (a) the reconstructed missing transverse momentum P_T^{miss}, momenta of (b) the leading jet P_T^{jet1}, as well as (c) the longitudinal energy momentum balance $\sum(E-P_z)$, and (d) the polar angle of the leading jets θ_{jet1} in the $\nu\mathbf{q}$ **channel** for the $\mathbf{e^-p}$ data (points) compared to SM MC predictions (solid histogram). The error band gives all model and experimental systematic uncertainties on the SM prediction added in quadrature. Error bars of data events show statistical uncertainties. The dashed histogram indicates the signal from a squark with $M_{squark} = 150\,\text{GeV}$, which decays into a neutrino and a jet with arbitrary normalisation.

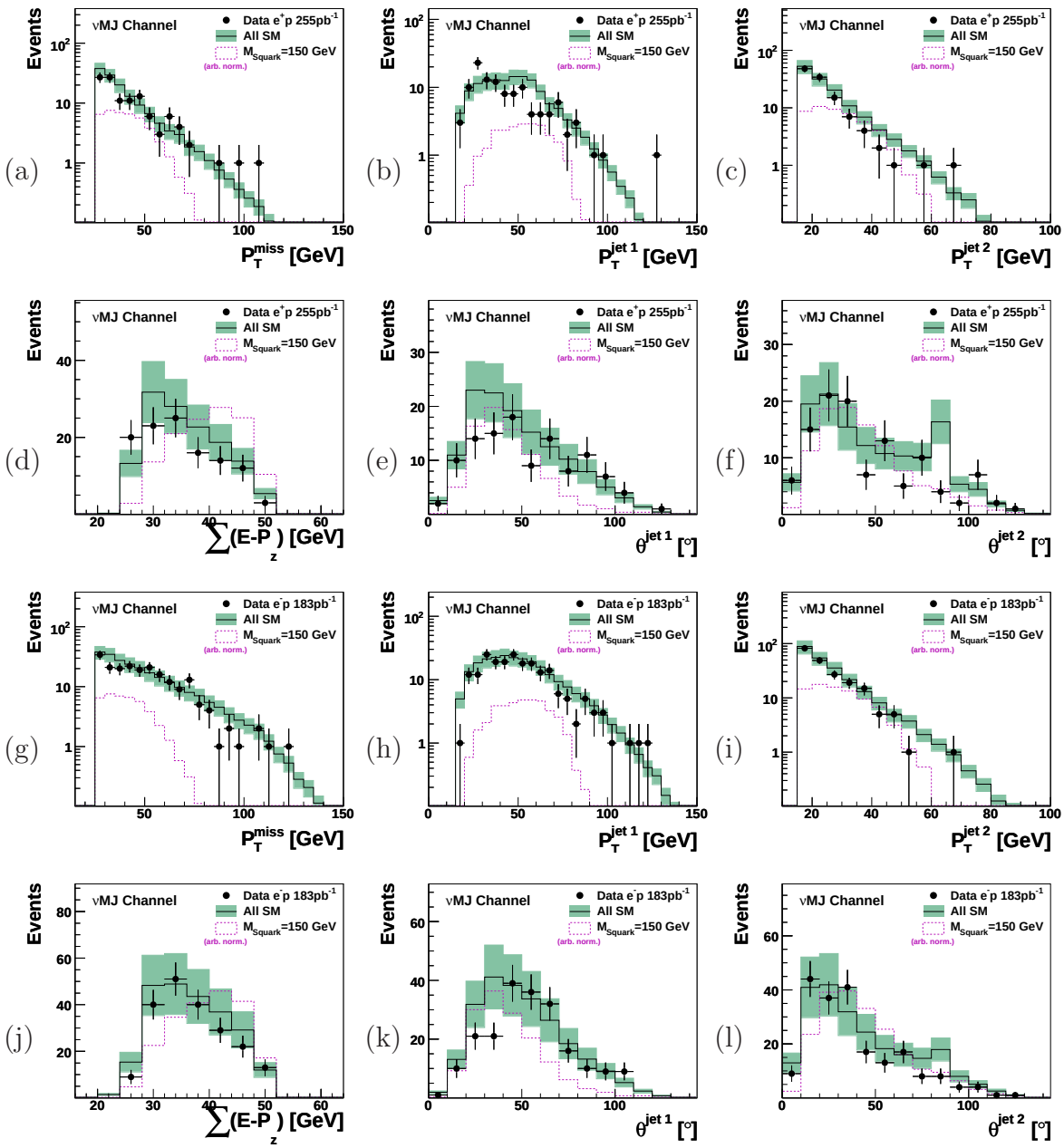

Figure 8.9: Distributions of the (a,g) reconstructed missing transverse momentum P_T^{miss}, momenta of (b,h) leading jets P_T^{jet1} and subleading (c,i) jets P_T^{jet2}, as well as the (d,j) longitudinal energy momentum balance $\sum(E-P_z)$, leading jets θ_{jet1}, and subleading jets θ_{jet2} in the ν**MJ channel** for (a-f) the $\mathbf{e^+p}$ and (g-l) the $\mathbf{e^-p}$ data (points) compared to SM MC predictions (solid histogram). The error band gives all model and experimental systematic uncertainties on the SM prediction added in quadrature. Error bars of data events show statistical uncertainties. The dashed histogram indicates the signal from a squark with $M_{squark} = 150\,\text{GeV}$, which decays into a neutrino and multiple jets with arbitrary normalisation.

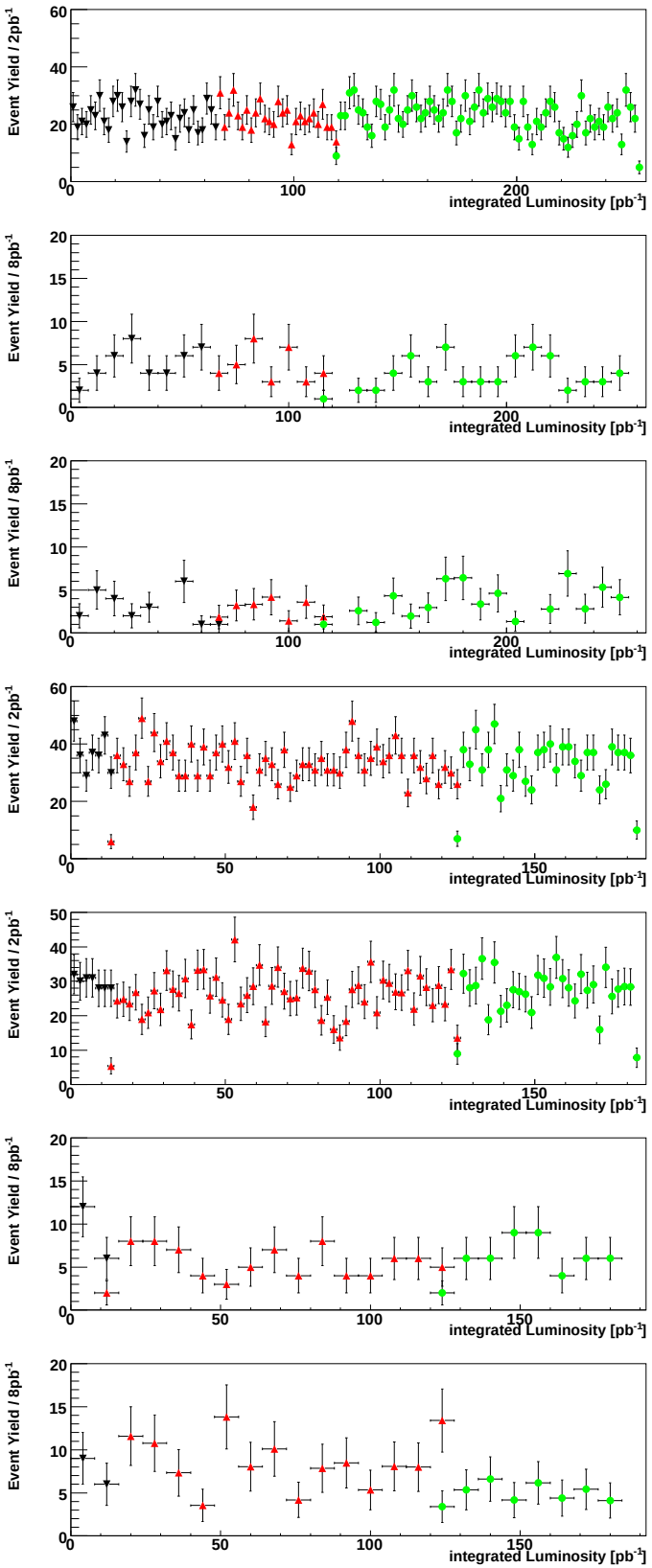

Figure 8.10: Event yields per 2 pb^{-1} for selected events in the final selections in the eq and νq channel, and per 8 pb^{-1} for selected events in the $eMJ(RC)$ and νMJ channels for (a-c) $\mathbf{e^+p}$ and (d-g) $\mathbf{e^-p}$ data. The sets of the different data-taking periods (see Table 7.1) are concatenated, and marked with different colors and symbols. At the beginning and end of the second and third period, binning effects can lead to extreme outliers in the overlapping bins.

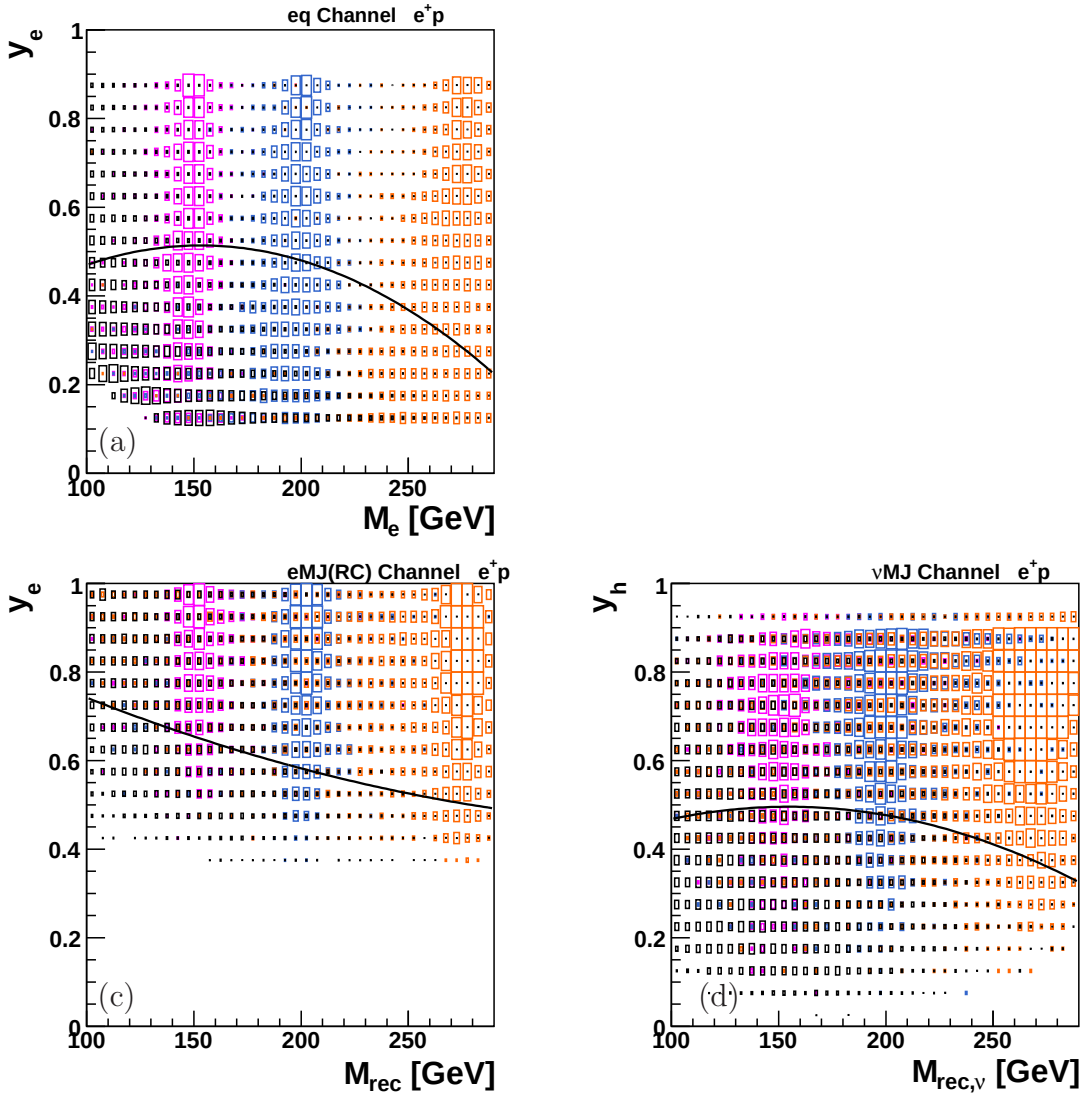

Figure 8.11: Distribution of $\mathbf{e^+p}$ SM background (black) and signal events for squark masses $M_{squark} = 150$ GeV (magenta), $M_{squark} = 200$ GeV (blue) and $M_{squark} = 275$ GeV (orange) in the $y - M$ plane, with $M = \{M_e,\ M_{rec}, M_{rec,\nu}\}$ depending on the topology. The size of the rectangles is proportional to the event count in the corresponding bin. The cut optimising the expected limit for each squark mass is indicated by a black curve, events below the curve are rejected. In the (a) eq and (c) $eMJ(RC)$ channel, the background prediction is dominated by NC DIS events, and in the (d) νMJ channel by CC DIS events. The decay into the νq channel is not possible for $\tilde{u}_L^j$ squarks expected in e^+p collisions.

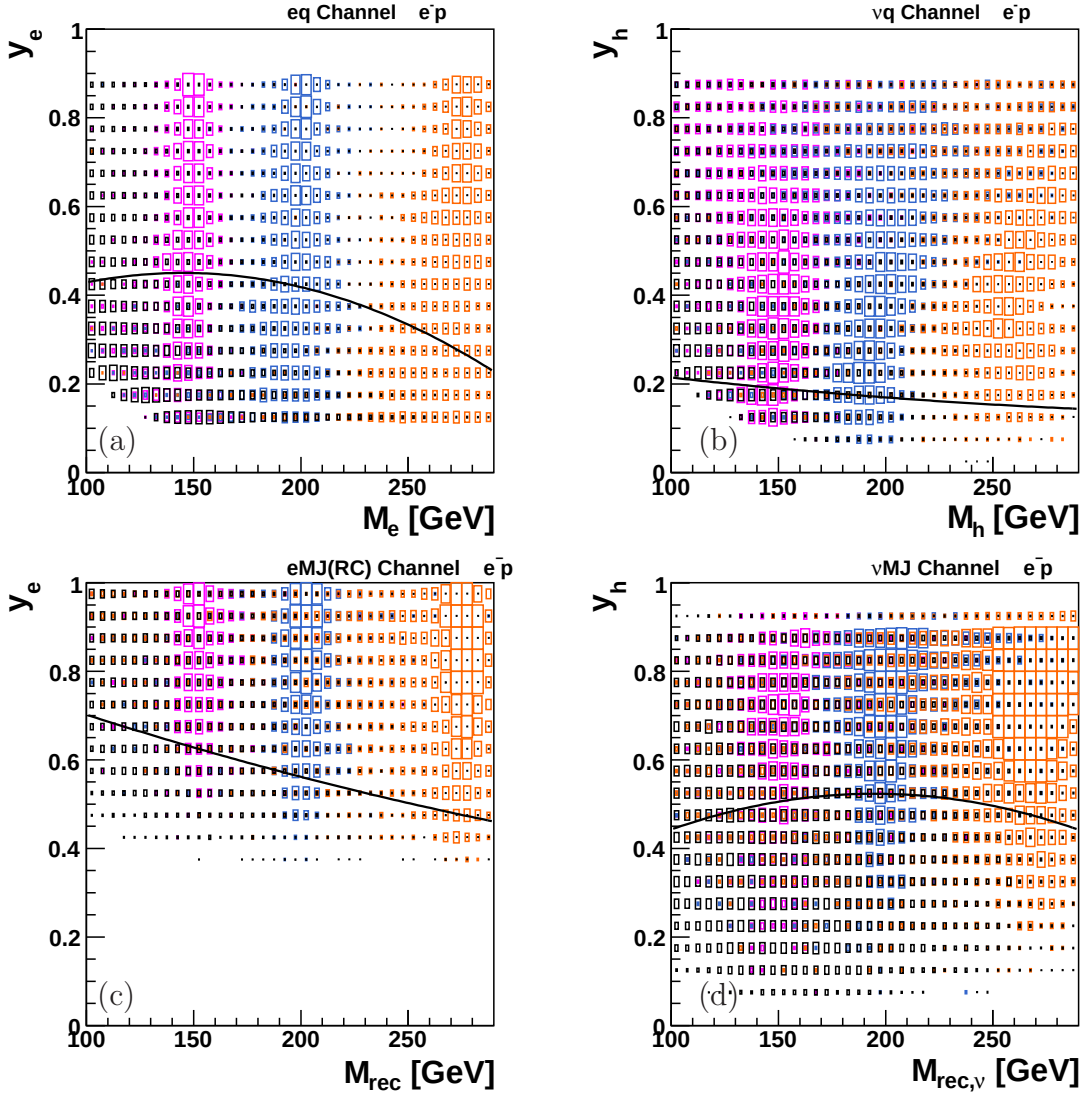

Figure 8.12: Distribution of $\mathbf{e^-p}$ SM background (black) and signal events for squark masses M_{squark} = 150 GeV (magenta), M_{squark} = 200 GeV (blue) and M_{squark} = 275 GeV (orange) in the $y - M$ plane, with $M = \{M_e,\ M_h\ ,\ M_{rec}, M_{rec,\nu}\}$ depending on the topology. The size of the rectangles is proportional to the event count in the corresponding bin. The cut optimising the expected limit for each squark mass is indicated by a black curve, events below the curve are rejected. In the (a) eq and (c) $eMJ(RC)$ channel, the background prediction is dominated by NC DIS events, and in the (b) νq and (d) νMJ channel by CC DIS events.

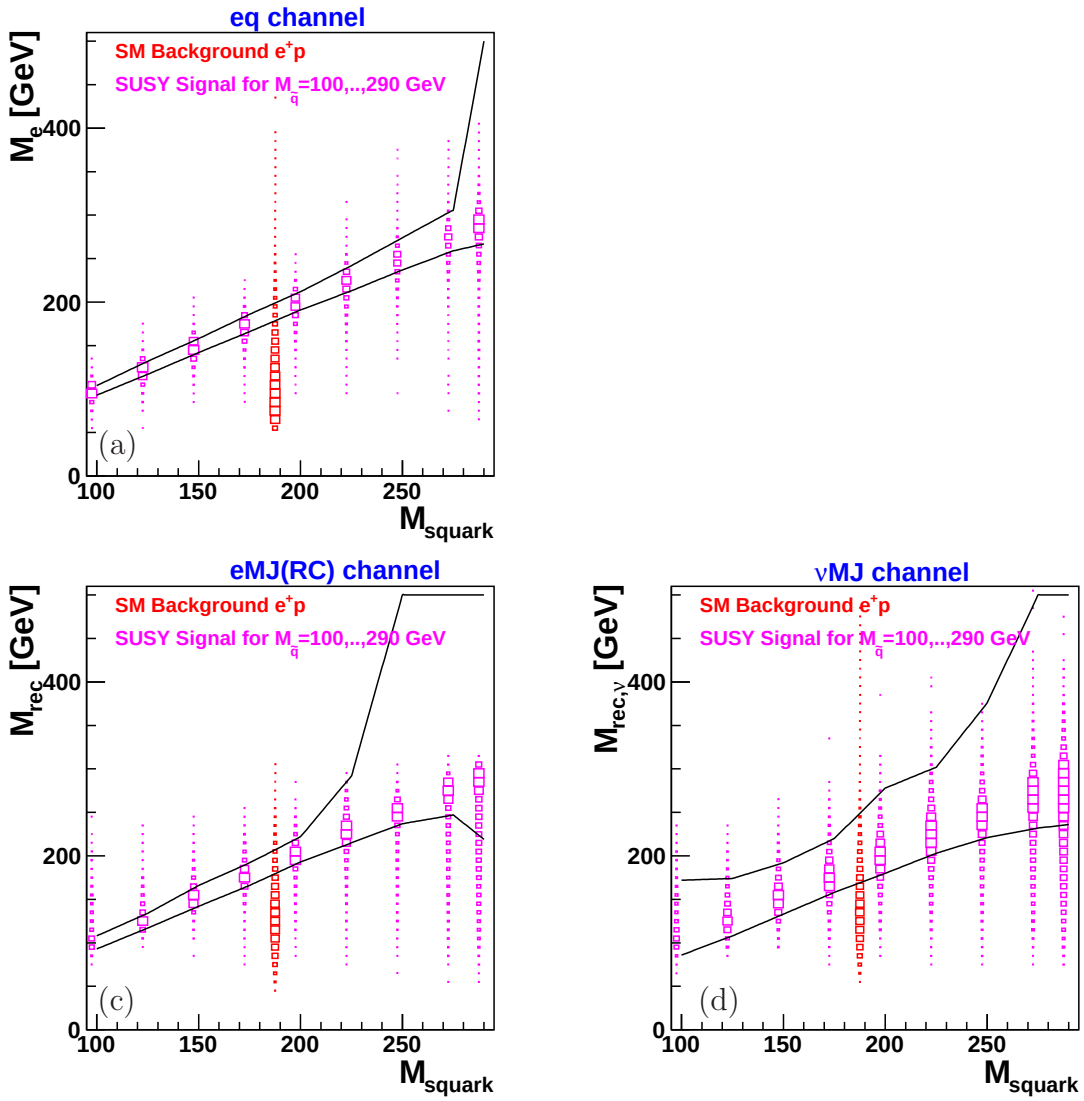

Figure 8.13: Lower and upper mass window cuts (black lines) derived from SUSY signal events (magenta) and the $\mathbf{e^+p}$ SM background prediction (red), in channels with a high amount of SM background. The mass window cuts are applied in (a) the eq channel, (c) the $eMJ(RC)$ channel and (d) the νMJ channel. In the eq and $eMJ(RC)$ channel, the background prediction is dominated by NC DIS events, and in the νMJ channel by CC DIS events. The decay into the νq channel is not possible for $\tilde{u}_L^j$ squarks expected in e^+p collisions. The size of the rectangles is proportional to the event count in the bin. For each squark mass, a dedicated simulation was used with the processes leading to the expected final state.

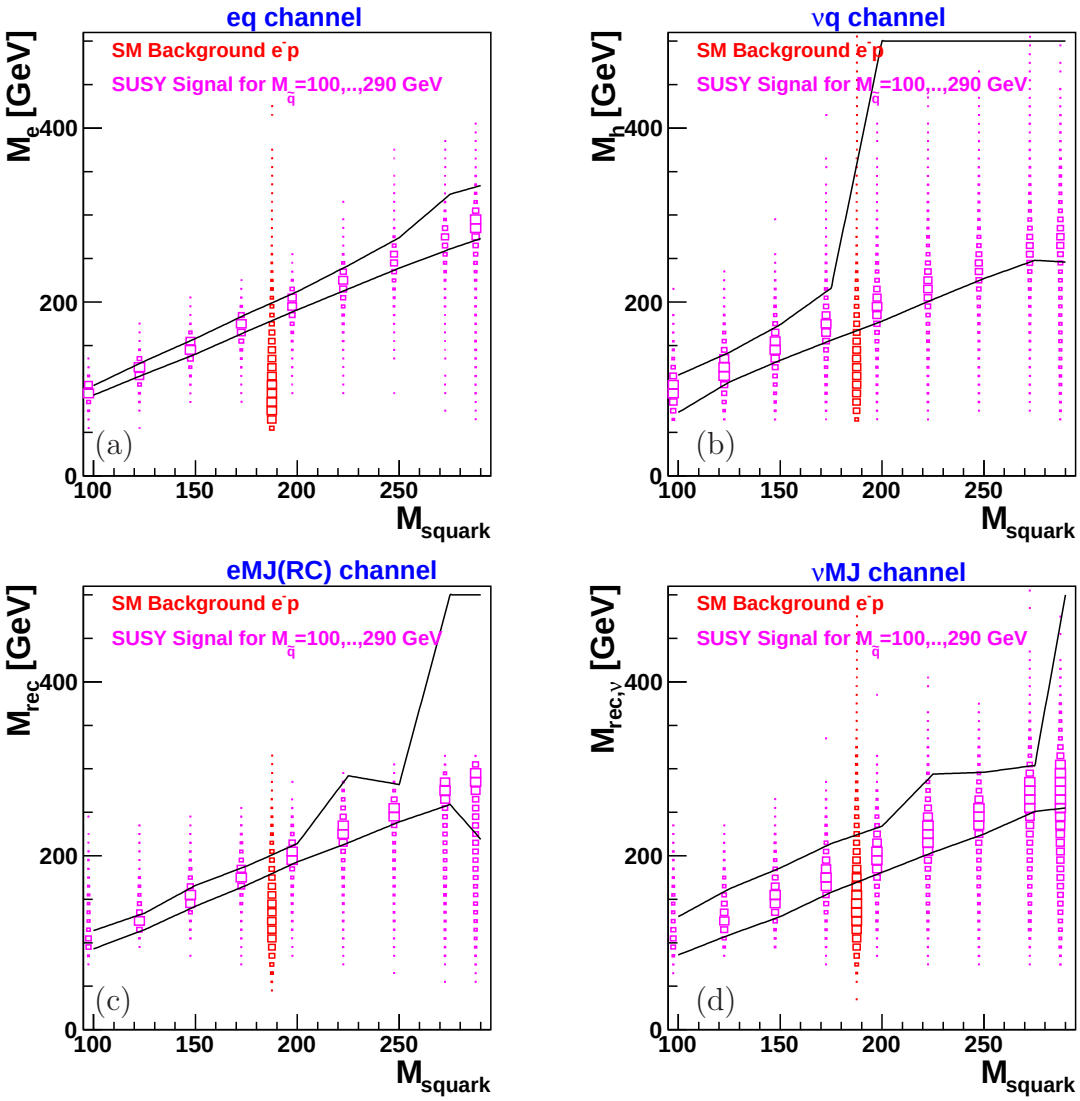

Figure 8.14: Lower and upper mass window cuts (black lines) derived from SUSY signal events (magenta) and the $\mathbf{e^-p}$ SM background prediction (red), in channels with a high amount of SM background. The mass window cuts are applied in (a) the eq channel, (b) the νq channel, (c) the $eMJ(RC)$ channel and (d) the νMJ channel. In the eq and $eMJ(RC)$ channel, the background prediction is dominated by NC DIS events, and in the νq and νMJ channel by CC DIS events. The size of the rectangles is proportional to the event count in the bin. For each squark mass, a dedicated simulation was used with the processes leading to the expected final state.

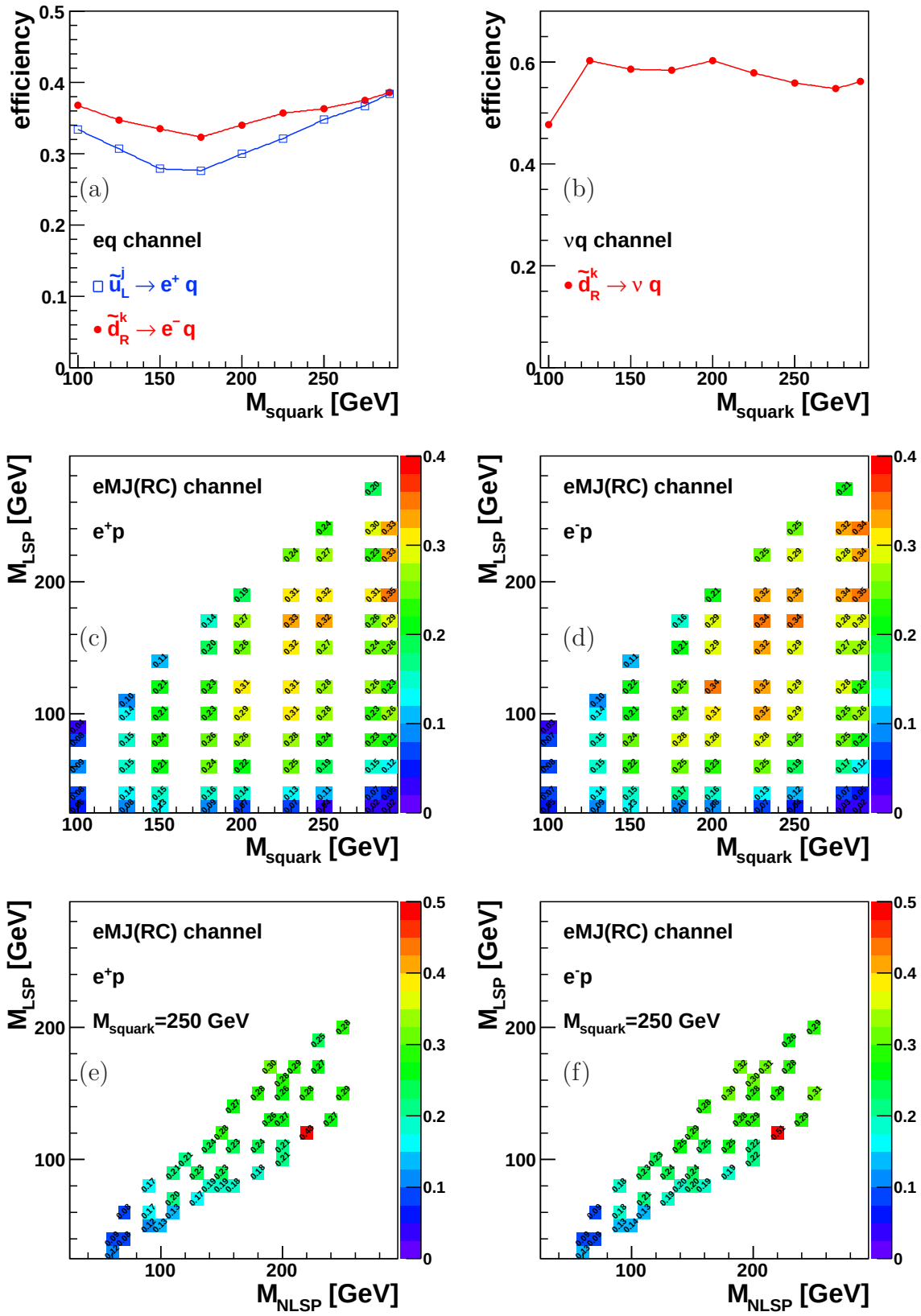

Figure 8.15: Efficiencies for SUSYGEN3 signal events simulating the squark decay into (a) the eq channel, (b) the νq channel, (c,d) the decay involving one gaugino into the eMJ(RC) channel, and (e,f) the cascade decay of gauginos for a squark mass $M_{squark} =$ 250 GeV. M_{LSP} and M_{NLSP} denote the mass of the LSP and the mass of the gaugino, which decays into the LSP, respectively.

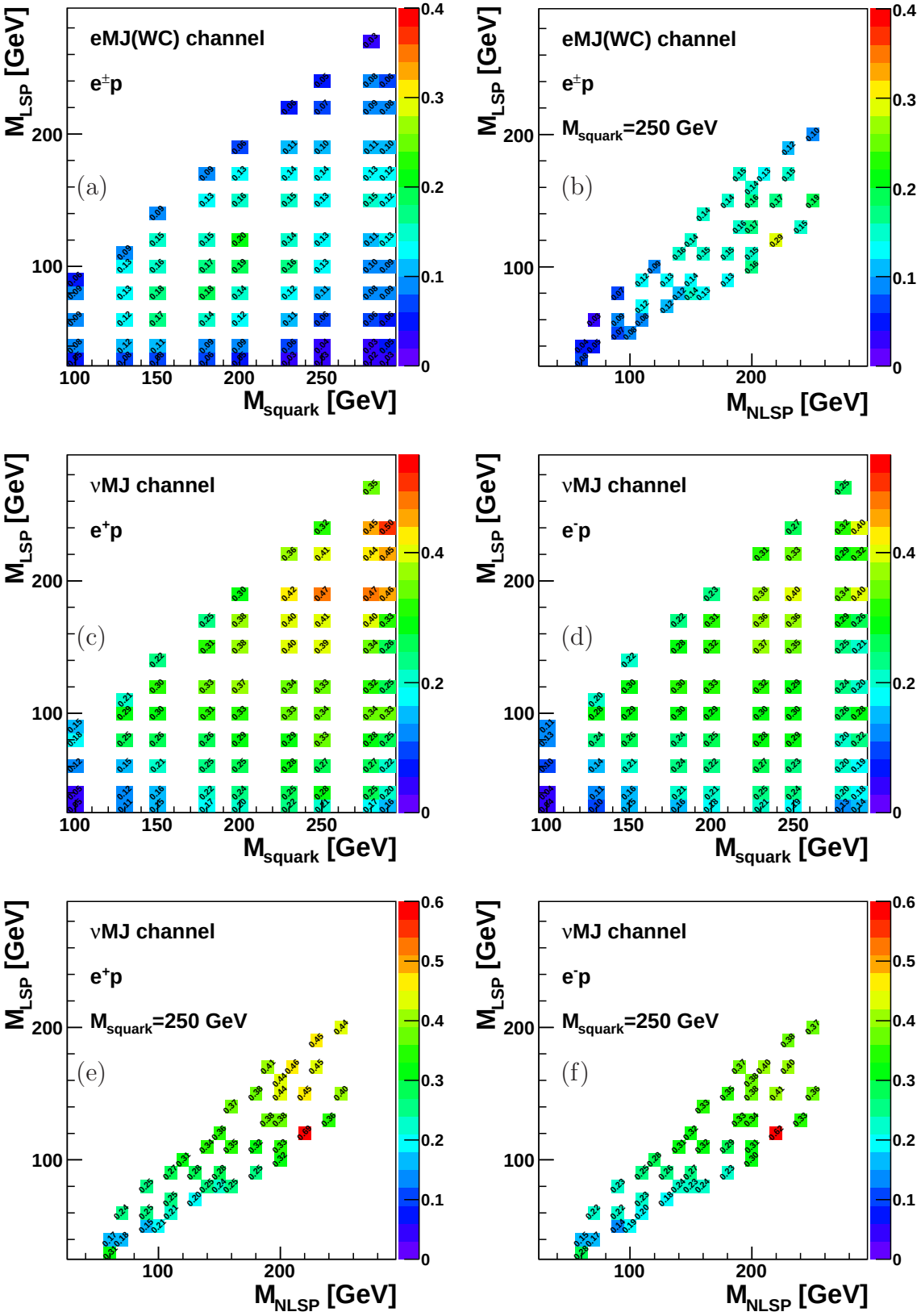

Figure 8.16: Efficiencies for SUSYGEN3 signal events simulating the squark decay into (a) the $eMJ(WC)$ channel involving one gaugino, (b) the cascade decay of gauginos into the $eMJ(WC)$ channel, (c,d) the decay into the νMJ channel involving one gaugino, and (e,f) the cascade decay of gauginos into the νMJ channel for a squark mass $M_{squark} = 250$ GeV. M_{LSP} and M_{NLSP} denote the mass of the LSP and the mass of the gaugino, which decays into the LSP, respectively.

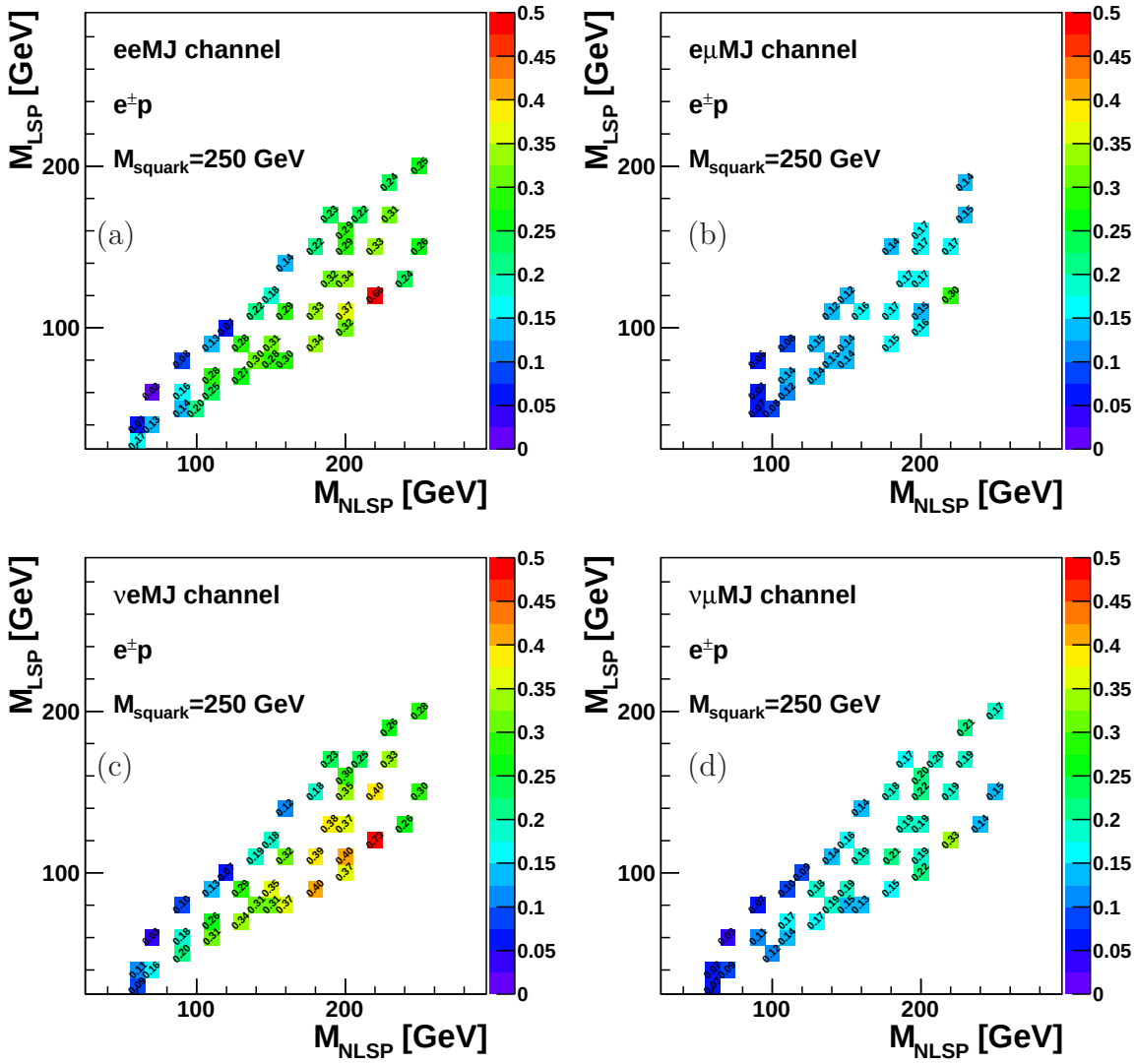

Figure 8.17: Efficiencies for SUSYGEN3 signal events simulating the gaugino cascade decay into (a) the $eeMJ$ channel, (b) the $e\mu MJ$ channel, (c) the νeMJ channel, and (d) the $\nu\mu MJ$ channel for a squark mass $M_{squark} = 250$ GeV. M_{LSP} and M_{NLSP} denote the mass of the LSP and the mass of the gaugino, which decays into the LSP, respectively.

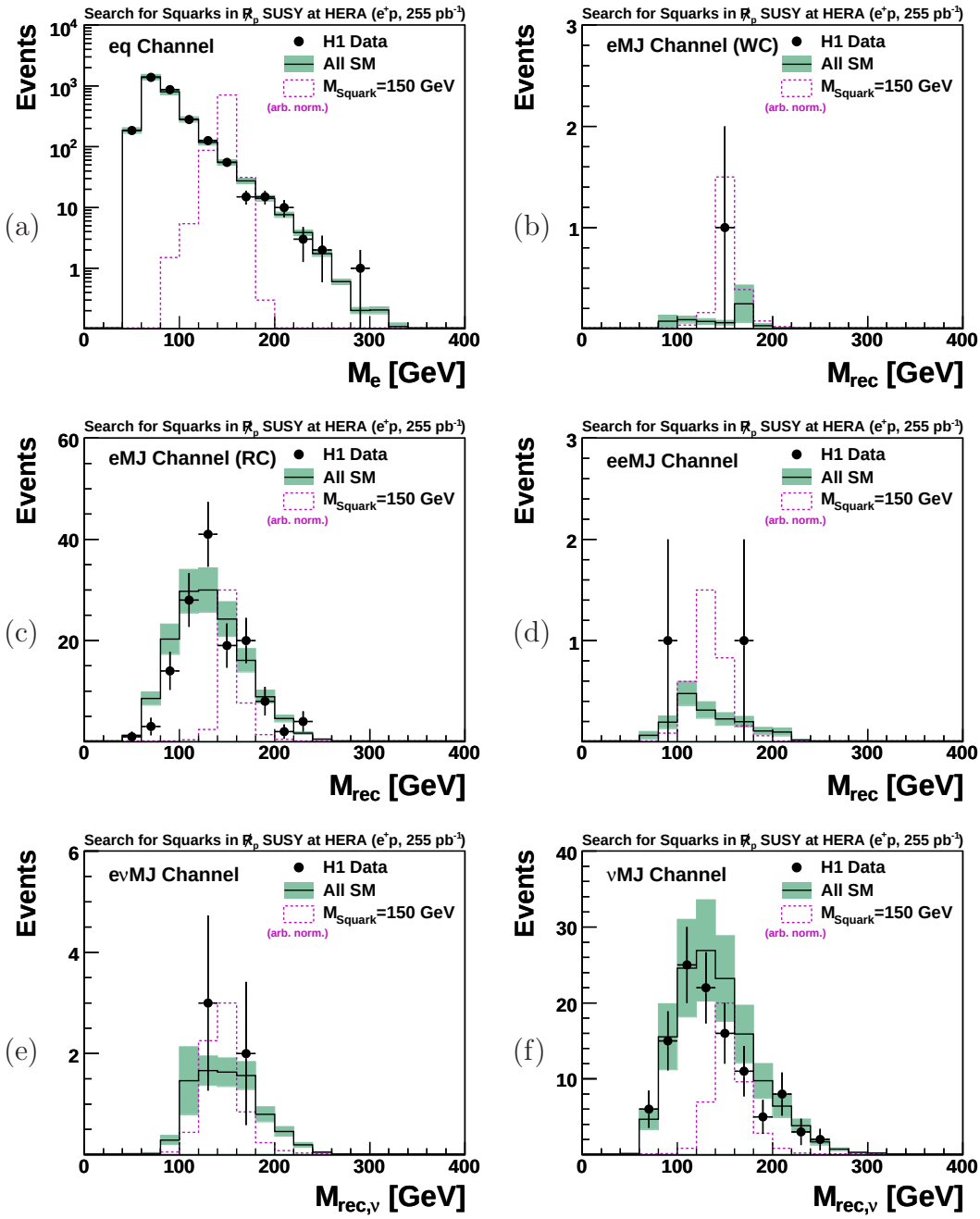

Figure 8.18: Reconstructed mass distributions in all selection channels with data (points) events from 255 pb^{-1} $\mathbf{e^+p}$ collisions compared to SM MC predictions [1]. The method used for the reconstruction of M_e, $M_{\rm rec}$ and $M_{{\rm rec},\nu}$ depends on the analysis channel. The error band gives all model and experimental systematic uncertainties on the SM prediction (solid histogram) added in quadrature. Error bars of data events show statistical uncertainties. The dashed histogram indicates the signal from a squark with $M_{squark} = 150\,\text{GeV}$ decaying into the indicated channel with arbitrary normalisation.

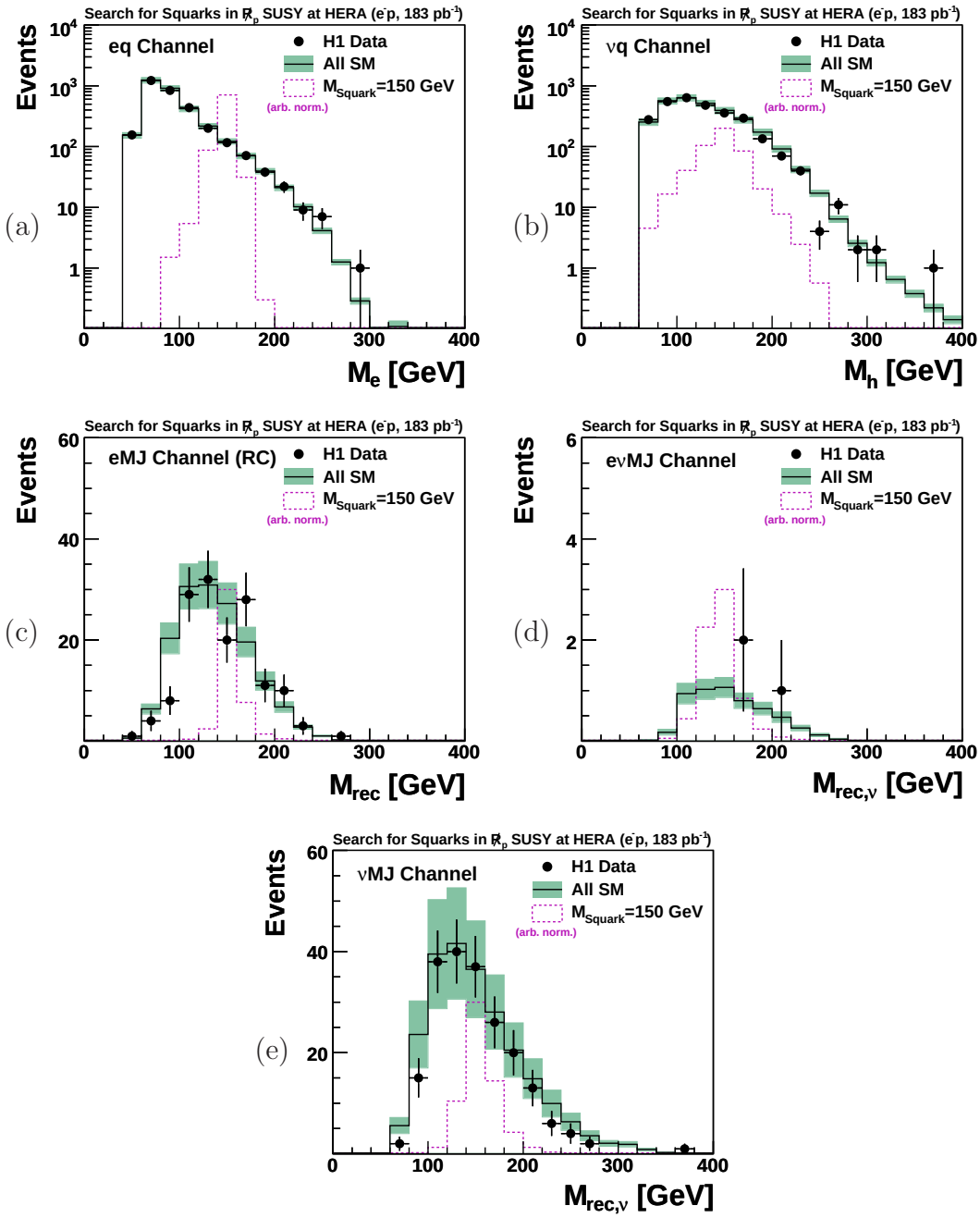

Figure 8.19: Reconstructed mass distributions in all selection channels with data (points) events from 183 pb^{-1} $\mathbf{e^-p}$ collisions compared to SM MC predictions [1]. The method used for the reconstruction of $M_e, M_h, M_{\mathrm{rec}}$ and $M_{\mathrm{rec},\nu}$ depends on the analysis channel. The error band gives all model and experimental systematic uncertainties on the SM prediction (solid histogram) added in quadrature. Error bars of data events show statistical uncertainties. The dashed histogram indicates the signal from a squark with $M_{squark} = 150\,\mathrm{GeV}$ decaying into the indicated channel with arbitrary normalisation.

9 Interpretation

No significant deviation from the SM predictions has been observed in data analysis of data sets corresponding to integrated luminosities of 183 pb^{-1} in electron-proton, and 255 pb^{-1} in positron-proton scattering. In order to constrain theoretical predictions of supersymmetric theories, a statistical method is adopted to calculate 95% confidence level (CL) limits. The CL_s procedure is explained in the next section. Using the CL_s method, limits are derived for the phenomenological MSSM model, and for the more constrained mSUGRA model with R-parity violation. The strength of R-parity violating couplings is constrained, and compared to existing exclusion limits from different experiments.

9.1 The $\mathrm{CL_s}$ Method

The method to calculate limits from the observed and expected event yields and signal efficiencies in the different event topologies uses the modified frequentist approach [161] based on a likelihood ratio test-statistic, also called the CL_s method. This method deviates from the unified approach [162] and the constructed confidence intervals do not have the same interpretation as traditional frequentist confidence intervals or Bayesian credible intervals [163]. The algorithm [164] used for the determination of the combined exclusion limit from all selection channels, includes the treatment of uncorrelated systematic uncertainties. A brief description of the CL_s method, and the combination of search channels is given in the following.

Confidence Interval Construction

An observable indicating the presence of new physics is the number of candidate events satisfying a certain set of criteria [163]. The interpretation of the data, *i.e.* the presence of a signal s in the observable, can be treated as hypothesis test [165; 166].

The null hypothesis is that the signal is absent in the data ($s = 0$), and the alternate hypothesis is the presence of the signal ($s = 1$). For testing the hypotheses, a test-statistic Q is constructed, which is a function of the observable and the signal model parameters [161]. The test-statistic is used to rank the outcomes of experiments, such that small Q is expected if the signal is absent, and large Q is expected in the presence of the signal.

In a counting experiment with n independent search channels, and the presence of background in the search channels, an optimal choice for the test-statistic Q, discriminating signal-like from background-like outcomes of experiments, is the likelihood ratio. Assuming the presence of the signal contribution s_i in the i-th channel with predicted background b_i, and observed candidates d_i, the test-statistic is given by $Q = \sum_i Q_i$

with [164]:

$$Q_i = \frac{e^{-(s_i+b_i)}(s_i+b_i)^{d_i}}{d_i!} / \frac{e^{-b_i} b_i^{d_i}}{d_i!}.$$

The probabilities for the $s+b$ hypothesis and the background-only hypothesis b are calculated as the Poisson probabilities P_{s+b}, P_b to observe values for the test-statistic less or equal to the observed Q_{obs} in data:

$$P_{s+b}(Q \leq Q_{obs}) = \sum_{Q(\{d_i'\}) \leq Q(\{d_i\})} \prod_{i=1}^{n} \frac{e^{-(s_i+b_i)}(s_i+b_i)^{d_i'}}{d_i'!}$$

and

$$P_b(Q \leq Q_{obs}) = \sum_{Q(\{d_i'\}) \leq Q(\{d_i\})} \prod_{i=1}^{n} \frac{e^{-(b_i)}(b_i)^{d_i'}}{d_i'!} \ ,$$

where $Q(\{d_i\})$ is the test-statistic computed in each channel for the observed set of candidates $\{d_i\}$, and $Q(\{d_i'\})$ is the test-statistic for the set of all possible outcomes $\{d_i'\}$ that yield values of the test-statistic less than or equal to the observed, summed over the number of independent search channels n [164].

Testing the signal hypothesis, a probability CL_{s+b} is defined as the probability to observe values of the test-statistic Q equal or smaller than the observed value Q_{obs}, assuming the presence of the signal:

$$CL_{s+b} = P_{s+b}(Q \leq Q_{obs}) \ .$$

The probability CL_{s+b} has a uniform distribution between 0 and 1 for the test-statistic Q if the signal is present. For absent signal, CL_{s+b} is expected to peak towards 0.

A similar probability is defined for the background-only hypothesis, assuming the signal is absent. The probability CL_b is defined as

$$CL_b = P_b(Q \leq Q_{obs}) \ ,$$

and expected to have a uniform distribution between 0 and 1 for the test-statistic Q if the signal is absent. If the signal is present, CL_b is expected to peak near 1, and shows poor compatibility with the background-only hypothesis [163].

Considering the presence of background in the data can result in unphysical results, *i.e.* negative signal cross sections may be derived if the observation suffers from a downward fluctuation of the background in the data. The approach taken to deal with this situation is to re-normalise the probability for the $s+b$ hypothesis to the probability of the background-only hypothesis, generalising the classical approach to confidence limits in single channel counting experiments [163; 167].

The modified frequentist confidence level for the signal hypothesis is given simply by

$$CL_s = \frac{CL_{s+b}}{CL_b} \ ,$$

and is a ratio of probabilities. The alternate hypothesis is rejected if the ratio CL_s is smaller than the specified confidence level $CL_s < 1 - CL$, where a confidence level

$CL = 0.95$ is used in this analysis. The test is considered to give more conservative results than the standard frequentist test $CL_{s+b} < 1 - CL$, because $CL_s \geq CL_{s+b}$. Especially in cases, where the experiment is not sensitive to a given signal, the difference between the signal + background and the background-only distribution is very small. The ratio CL_s is close to 1 in this case, and the signal hypothesis is not rejected. By contrast, the standard frequentist approach CL_{s+b} may reject theories also in insensitive regions, simply due to downward fluctuations of the background in the data.

For the construction of confidence intervals, many sets of the signal hypothesis are tested. A continuous parameter of the signal theory often has a region, where the signal is small and can not be distinguished from the null hypothesis. The CL_s method never rejects such insensitive regions. As the signal becomes more prominent for different values of the parameter, it is eventually rejected at some point by the observation in data. This point is also called the 95% exclusion limit. In other cases, exclusion limits may exist for changes of the parameter in both directions, leading to upper and lower limits. The non-excluded region for the parameter between such limits is also called confidence interval. The median expected limit is defined as the exclusion limit at a given confidence level, averaged over all possible outcomes of the experiment assuming there is no signal. Further implications and restrictions of the method exist [163], which exceed the aim of this brief introduction. The systematic uncertainties on signal and background predictions are taken into account assuming Gaussian distributions of the signal and background predictions. Details of the implementation of the method to compute confidence limits and the incorporation of systematic uncertainties are beyond the scope of this work and described elsewhere [164].

Exclusion Limit Derivation

The search results are used to derive 95% CL limits on the number of squark candidates for squark mass hypotheses M_{squark} in order to constrain the signal production cross section σ_{prod} [1]. The e^-p and e^+p data sets are used in separate analyses because of the different sensitivity to the couplings λ'_{11k} and λ'_{1j1}, respectively. SUSY model scenarios with signal cross sections leading to more events than the 95% CL limit on the number of events derived from data are excluded. At any squark mass, values of the couplings λ'_{11k} and λ'_{1j1} which lead to higher cross sections are excluded. In the following it is assumed, that only one non-zero R-parity violating coupling dominates, and that production and decay proceed via this single dominant coupling. The production cross section depends linearly on the squark mass M_{squark}, and the quadratically on the strength of the λ'_{11k} or λ'_{1j1} coupling involved. The branching ratio $\mathcal{BR}$ of squark decays into the selection channels depends on the model scenarios, and is determined using the SUSYGEN3 [32] software. The efficiencies for selecting squark decays in the selection channels are determined via simulated and reconstructed SUSYGEN3 MC events. A dense grid of SUSY particle masses involved in the decay modes of squarks is used to interpolate the selection efficiencies (see section 4.2). The product of signal efficiency times branching ratio is determined for each model scenario for the masses of SUSY particles involved in the squark decay leading to the final states selected in each selection channel. The nine selection channels of the e^-p data analysis are combined using the CL_s method to determine a limit on the coupling λ'_{11k}. The eight selection channels of the e^+p data analysis are combined using the CL_s method

to constrain the coupling λ'_{1j1}. The treatment of the systematic uncertainties on the background and signal prediction assumes Gaussian distributions for the uncertainties, discussed elsewhere [164]. The following quantities are used to determine 95% CL exclusion limits on the signal production cross section: the observed number of candidate events $N_{\mathrm{obs},i}$; the background expectation $N_{\mathrm{exp},i}$; the uncertainty on the background expectation $\Delta N_{\mathrm{exp},i}$; the product of signal efficiency times branching ratio $\mathcal{BR}_i \cdot \epsilon_i$; and the uncertainty attributed to the signal efficiency $\Delta\epsilon_i$ in the i-th channel. The uncertainty on the signal efficiency includes the experimental systematic uncertainties of the signal efficiencies, and the systematic uncertainties attributed to the signal cross section (see section 4.2). A sliding mass window technique is used in selection channels with high SM background, in order to further reduce the background expectation, and optimise the expected limit for a given squark mass hypothesis in the range $M_{squark} = 100 - 290$ GeV (see section 8.3).

Crosstalk Efficiency

Besides the direct sensitivity for decay chains leading to a specific final state, also indirect sensitivity, originating from cross talk between selection channels, is given by the selection topologies. Events from decay chains leading to a different final state may be mis-reconstructed, and therefore selected in one of the other topologies. The following cross talk is considered in the selection channels: Squark decay modes with an electron or neutrino and multijets may be selected in the eq and νq channels, respectively, if jets are not reconstructed correctly. The cross talk efficiency for squark decays leading to electron or neutrino and multijet final states, which are selected in the eq and νq channel, give additional sensitivity for the signal, and the cross talk efficiencies are included in the calculation of the efficiency times branching ratio for each channel. The cross talk efficiencies are also determined for events leading to the $eeMJ$ and $e\mu MJ$ final states, selected in the $eMJ(RC)$ channel, and for $e\nu MJ$ and $\nu\mu MJ$ final state decay modes selected in the νMJ channel, *e.g.* when leptons are not identified. The cross talk contribution from the $eeMJ$ and $e\mu MJ$ decay modes to the $e\nu MJ$ channel is also taken into account. The cross talk efficiencies are mostly $\lesssim 1\%$, only for nearly degenerate gaugino masses in cascade decays, or degenerate squark and gaugino masses, where the emitted particles get low transverse momenta, the cross talk efficiencies contribute with additional $10 - 20\%$. The overall effect on the exclusion limits is very small $\lesssim 1\%$.

Squark Width Correction

The resonant production of squarks leads to peaks in the invariant mass distributions for signal events in the decay channels. For the highest squark masses $M_{squark} \gtrsim 270 - 290$ GeV, close to the kinematic limit, the width of the squark increases. The increasing squark width at the kinematic limit results from the relatively large $\not{R}_p$ couplings involved, which can be tested with the available statistics. The resonance peak in the x distribution is reduced when the squark width increases, leading to a more prominent tail at lower invariant squark masses. This means, that the cross section decreases at the resonance peak region, leading to a smaller cross section contribution inside the region of the mass window in the eq, νq, $eMJ(RC)$ and $eMJ(WC)$ channels. The

signal efficiencies in this analysis have been determined for negligible squark widths, and the effect has to be compensated in the calculation of the selection efficiencies in channels where a mass window is applied. The fraction of the cross section leading to invariant masses outside the mass windows can not be recovered in the squark mass reconstruction for these events, and the selection efficiency has to be reduced accordingly [34]. Also the production cross section must be corrected in the same way. For squark masses above 290 GeV the assumption for the resonant production mechanism and the finite squark width are no longer reliable.

The analysis is therefore restricted to the resonance peak region, and squarks with invariant masses lower than the generated mass are neglected, although they could be included in the selections. The approach is therefore considered to yield conservative results [34].

9.2 MSSM Interpretation

A phenomenological version of the MSSM is considered in the following interpretation of the search results [1]. The masses of squarks and sleptons are set to fixed values and the gaugino masses are determined via the set of parameters μ, M_2, and $\tan\beta$. Thus, the complete spectrum for the neutralino and chargino masses, and their mixture of photino $\tilde{\gamma}$, zino $\tilde{Z}$, and higgsino $\tilde{H}_1, \tilde{H}_2$, or wino $\tilde{W}^{\pm}$, and charged higgsino $\tilde{H}_1^+, \tilde{H}_2^-$ components is derived. The gluino mass is expected to be large in these scenarios $M_{gluino} \sim M_3 \gg M_2$. Mixing effects in the sfermion sector are neglected for the first two squark generations. Sleptons are considered to be degenerate in mass, and their masses are set to 90 GeV. The effect of higher slepton masses affects the results only in certain model scenarios, as will be shown. The branching ratios into the selection channels are calculated using the SUSYGEN3 software, adding the contributions from processes leading to the selected final states, considering direct $\not{R}_p$ squark decays, decays involving a single gaugino, and decays involving a cascade of two gauginos. Decay chains involving more than two gauginos, or decay chains leading to tau leptons in the final state are not considered in the calculation of branching ratios.

Two of these scenarios are shown for illustration in the following. These scenarios are example cases, where the neutralino is either dominated by a photino or a zino component (see section 2.4 for the dependence of the composition of the neutralino on the supersymmetric parameters). These extreme cases are useful to study the coverage of the analysis in terms of excluded scenarios by the studied topologies.

Photino $\tilde{\gamma}$ dominated lightest neutralino

For the choice of parameters $\tan\beta = 2, \mu = -200$ GeV and $M_2 = 80$ GeV, a supersymmetric scenario is expected, in which the lightest SUSY particle is the neutralino, and the dominant component is the photino. The coupling of the photino leads to the dominant production of charged leptons in the decays of the neutralino. Thus, squark decays into topologies with charged leptons have the highest branching ratio in this scenario. Figure 9.1 shows 95% CL limits on the couplings λ'_{11k} and λ'_{1j1} for $j, k = 1, 2$ in this model scenario. Also shown are the branching ratios for squark decays into the considered topologies at the observed limit. For the low squark mass region,

the $\tilde{d}_R^k$ squark decays leading to final states selected in the $eMJ(RC)$ and $eMJ(WC)$ channels have the highest branching ratio, each contributing with $\mathcal{BR} \approx 40\%$. In the case of $\tilde{u}_L^j$ squark decays the $e\ell MJ$ channels with $\ell = e, \mu$ dominate the branching ratio $\mathcal{BR} \approx 40\%$. The decays of $\tilde{u}_L^j$ squarks proceed via chargino states, and thus additional charged leptons are expected in the final states. For squark masses near the kinematic border, the limit on the couplings decreases and directly R-parity violating squark decays begin to dominate the branching ratio. The channels eq and νq in case of $\tilde{d}_R^k$ squarks, and the channel eq for $\tilde{u}_L^j$ squarks start to dominate the branching for $M_{squark} \gtrsim 280$ GeV. Channels with the highest branching ratio set typically the strongest limit in the combination of all decay channels. The sum of branching ratios of all considered decay topologies is close to 100% for the $\tilde{d}_R^k$ decays. For $\tilde{u}_L^j$ squarks the sum of branching ratios of all considered decay channels only covers $\sum \mathcal{BR} \approx 70-80\%$, due to the high probability of cascade decays of charginos. The missing fraction of the branching ratio is due to decays involving more than two gauginos in the cascade decays, or the production of tau leptons in the final state, for which the efficiency has not been determined in this analysis, and for which the corresponding processes have been neglected in the calculation of branching ratios. The constraints are compared to previous limits obtained by H1 in an analysis of a smaller dataset [53]. Due to the increased luminosity of the analysed data sets by a factor of 183 pb^{-1}/13.5 pb^{-1} ≈ 13 for the e^-p and a factor of 255 pb^{-1}/64.3 pb^{-1} ≈ 4 for the e^+p data sample, constraints could be set in a previously unexplored region. The limit reaches as low as $\lambda'_{11k,1j1} < 5 \cdot 10^{-3}$ for low squark masses $M_{squark} = 100$ GeV, decreasing to $\lambda'_{1j1} < 5 \cdot 10^{-1}$, and $\lambda'_{11k} < 10^{-1}$ for high squark masses $M_{squark} = 290$ GeV approaching the kinematic limit. The e^-p data sample allows a similar exclusion as the e^+p data sample at low squark masses, and even stronger exclusion at high squark masses, due the increased cross section by the quark content of the proton, though the data set corresponds to a considerably smaller integrated luminosity.

The observed limits for the λ'_{11k} and λ'_{1j1} couplings are compared to the median expected limit in Figures 9.3a and 9.3b in the photino scenario. The observed limit for λ'_{11k} is typically stronger than the median expected limit over the complete mass range, because a slight deficit in data compared to the SM background prediction is observed. For the highest squark masses, the observed limit is very close to the median expected limit. The observed limit for λ'_{1j1} is very close to the median expected limit over the complete mass range. Observed and median expected exclusion limits in the same scenarios for degenerate squark and slepton masses have also been derived. The effect of the increased slepton mass reduces the branching ratios for cascade decays involving sleptons. Therefore slightly weaker exclusion limits are obtained for $\tilde{u}_L^j$ squark production, while the effect for $\tilde{d}_L^j$ squarks is negligible. The observed limits show the same behaviour regarding the median expected limit.

Zino $\tilde{\mathrm{Z}}$ dominated lightest neutralino

For a different choice of parameters, $\tan\beta = 2, \mu = 200$ GeV and $M_2 = 150$ GeV, a supersymmetric scenario with the neutralino being the lightest SUSY particle, dominated by a zino component, is expected. The weak coupling of the zino leads to increased neutrino production in the decays, thus final states with neutrinos are expected to dominate squark decays involving the LSP in this scenario. In figure 9.2, limits derived

for this model scenario are shown, together with the branching ratios into the decay channels at the observed limit. Complementary topologies dominate the branching of squarks in this model scenario with respect to the photino dominated neutralino case. The decays of $\tilde{d}_R^k$ squarks into the νMJ channel have the highest branching ratio, covering 90% for a wide range of squark masses. Only at the highest squark masses an additional contribution from the eq and νq channels is expected. For $\tilde{u}_L^j$ squarks, the $\nu\ell MJ$ channel with $\ell = e, \mu$ has the highest branching ratio $\mathcal{BR} \approx 50\%$, followed by the νMJ channel with $\mathcal{BR} \approx 10 - 20\%$. Again, for the highest squark masses, the eq channel is starting to dominate the branching. The sum of branching ratios covers nearly 100% for $\tilde{d}_R^k$ squarks. For $\tilde{u}_L^j$ squarks, the decays involving more than two gauginos in the cascade have not been considered in the calculation of the branching ratios, which results in a sum of branching ratios of the analysed decay channels of only $\sum \mathcal{BR} \approx 70 - 80\%$. The missing fraction of the total branching ratio is due to decays involving more than 2 gauginos. The limits in the zino dominated neutralino scenario are slightly weaker than in the photino case at low squark mass, due to the dominant decay into final states involving neutrinos, for which higher systematic uncertainties than in the electron based decay channels have been determined. For high squark mass, a similar sensitivity is achieved in both cases due to the dominant direct $\not{R}_p$ squark decays.

The observed limits for λ'_{11k} and λ'_{1j1} are compared to the median expected limit in Figures 9.3c and 9.3d for the zino case. The observed limit is for both couplings stronger than the median expected limit, due to slightly more predicted events than observed in data. The strong contribution of the νMJ decay channel leads for some masses to larger deviations from the expected limit, due to a slight overestimation of the data by the background MC in these mass ranges. For degenerate squark and slepton masses, the observed and median expected exclusion limits in the same scenarios have also been derived. The effect of the increased slepton mass is most visible in the limits for the λ'_{1j1} coupling, where the decay to charginos leads to a high branching into the $\nu\ell MJ$ channels, which have the strongest contribution from sleptons in the decay chains, resulting in less stringent limits.

Scan of supersymmetric scenarios in the MSSM

In order to constrain the parameters of the MSSM, a full scan of model scenarios is performed [1]. Only models with a mass for the LSP bigger than 30 GeV are considered. The sleptons are again considered to be degenerate and their mass is set to 90 GeV in all scenarios. As seen from the example cases discussed before, similar results can be expected for degenerate sleptons and squarks. The example cases of photino-like and zino-like neutralinos show, that a similar sensitivity is reached with the considered decay channels for complementary model scenarios. In the following, limits are set on the strength of the R-parity violating couplings λ'_{11k} and λ'_{1j1} for $j, k = 1, 2, 3$ in MSSM models in the range of parameters -300 GeV $< \mu <$ 300 GeV, and 70 GeV $< M_2 <$ 350 GeV for values of $\tan\beta = 2$ and $\tan\beta = 6$. The different 95% exclusion regions are shown in Figure 9.4 for the coupling λ'_{11k} using the e^-p data sample, and in Figure 9.5 for the λ'_{1j1} coupling using the e^+p data sample. Values of the couplings excluded in all investigated scenarios, and values excluded only for parts of the parameter space are marked, accordingly. Constraints are set for all three generations of squarks. For

third generation squark production, limits are calculated taking the mixing between the stop states (sbottom states) into account. The mixing influences the masses of the stop eigenstates, and also their production cross sections. The method conservatively considers only the eigenstate which yields the bigger sensitivity, which is not necessarily the lighter stop [34]. Therefore the limits on λ'_{113} and λ'_{131} are shown separately from the results of λ'_{11k} and λ'_{1j1} for $j, k = 1, 2$.

Compared to previous results obtained by H1 [53], couplings λ'_{11k} smaller by a factor $1.5 - 2$ could be excluded over the complete mass range, for all generations using the much increased luminosity of the e^-p data sample. For the limit on λ'_{1j1}, using the higher luminosity e^+p sample, a factor of $1.2 - 1.5$ is reached with respect to previous H1 limits. The direct limit surpasses the indirect limits on λ'_{112} and λ'_{113} from charge current universality [35; 48] in the considered model scenarios up to squark masses of 250 GeV. The constraints on λ'_{121} and λ'_{131} from atomic parity violation [35; 49] are surpassed by the direct limits up to squark masses of 240 GeV. The indirect limit from the non-observation of neutrinoless double β decay [35; 47] through $\not{R}_p$ processes, sets more severe indirect limits on the coupling λ'_{111}.

$\not{R}_p$ couplings of comparable strength to the electromagnetic coupling strength λ'_{1j1} or $\lambda'_{11k} = \sqrt{4\pi\alpha_{em}} = 0.3$, can be excluded in all investigated model scenarios up to squark masses of 275 GeV for $\tilde{u}^j_L$ squarks, and up to 290 GeV for $\tilde{d}^k_R$ squarks.

9.3 mSUGRA Interpretation

In the following, limits are set on the parameters of the mSUGRA model [1]. The mSUGRA model is completely defined by the following set of parameters: the common mass at the GUT scale for scalar particles m_0; the common mass for gauginos $m_{1/2}$; the ratio of Higgs vacuum expectation values $\tan\beta$; as well as the common trilinear coupling A_0; and the sign of the Higgs mixing parameter μ. By the choice of these five parameters, the low energy solution of masses and composition of all supersymmetric particles is determined, thus fixing the branching ratios into the signal topologies as discussed. By contrast to the MSSM, also masses of squarks and sleptons are derived by the set of parameters. Model configurations which lead to a LSP mass smaller than 30 GeV are considered in this scan, but a vanishing efficiency is assumed for channels with gauge decays ending in a neutralino or chargino with mass < 30 GeV. Model configurations which lead to a scalar LSP are not considered.

A scan of the parameters m_0 and $m_{1/2}$ at fixed values of $\tan\beta$, and a choice for the sign of μ is performed. The parameter A_0 is set to zero, since its influence has been determined to be negligible [34]. For a fixed strength of the couplings λ'_{1j1} and λ'_{11k}, branching ratios into the decay topologies are calculated. The limit is set in these scenarios mostly by the eq channel, or the eq and νq channels, since channels involving gauginos in the decay cascade only contribute, as long as the LSP mass stays above 30 GeV.

Figures 9.6 and 9.7 show results of this scan in the $m_0 - m_{1/2}$ plane for $\lambda'_{1j1} = 0.3$ and $\lambda'_{11k} = 0.3$, respectively, when values of $A_0 = 0$, $\mu < 0$ and $\tan\beta = 2,\ 6$ and 10 are assumed. The limits from third generation squark production are indicated separately, since mixing effects lead to light stop and sbottom states with respect to the other squark flavours, which allows to set more severe constraints on the parameters m_0

and $m_{1/2}$. The effect is more severe in the limit for $\lambda'_{1j1} = 0.3$, since the strongest mixing effects are expected for the stop squark at these $\tan\beta$ values. The limits follow approximately curves of constant squark mass, only at high m_0 and low $m_{1/2}$ a degradation in the limit, due to the loss of efficiency in the multijet channels when the LSP mass drops below 30 GeV, is observed. The limit excludes values for $m_0 - m_{1/2}$ leading to squark masses of $M_{squark} = 280$ GeV for a coupling $\lambda'_{11k} = 0.3$ from first and second generation squark production. For a coupling $\lambda'_{1j1} = 0.3$, the limit for $m_0 - m_{1/2}$ excludes almost throughout first and second generation squarks with masses of $M_{squark} = 275$ GeV. The third generation limit excludes higher values of $m_0 - m_{1/2}$ than the first and second generation limit, though the squark mass limit is considerably weaker. The domain $m_{1/2} < 10$ GeV is not considered for third generation squarks, since the decay into $\nu b\bar{d}$ is kinematically not accessible due to the light mass of the LSP. The gap, that occurs for $m_0 \approx 75$ GeV in Figure 9.7, originates from an enhancement of decay modes involving more than two gauginos, for which the branching ratio has not been considered, since the efficiencies are only determined for cascade decays involving at most two gauginos.

The limits obtained in this analysis are extending the previous limits obtained by the H1 experiment by a few GeV in the excluded squark mass range. The limits can also be compared to results obtained in complementary physics processes at LEP [75] and the TeVatron [78], where also constraints were derived on the parameters m_0 and $m_{1/2}$ in $\not{R}_p$ SUSY models. For high values of m_0, the D0 limit is independent of m_0 and exceeds the constraints on $m_{1/2}$ derived here. The limit derived by the L3 experiment constrains more severely the parameter $m_{1/2}$ for low values of m_0 at $\tan\beta = 2$. The HERA limits extend the existing bounds especially in the domain of medium $m_0 \approx m_{1/2}$ compared to the LEP and TeVatron limits.

Dependence of mSUGRA Results on $\tan\beta$

The dependence of the exclusion limits in the mSUGRA model on the parameter $\tan\beta$ has been studied in a scan of models for $\lambda'_{1j1} = 0.3$ and $\lambda'_{11k} = 0.3$, respectively, assuming values of $A_0 = 0$, $\mu < 0$. Exclusion limits on the parameter $M = m_0 = m_{1/2}$ are derived, assuming a common mass parameter for sfermions and gauginos. Figure 9.8 shows the resulting exclusion domains. The limits for the first two squark generations are independent of $\tan\beta$, the limit on down-type squarks ($M > 110$ GeV) is slightly higher than for up-type squarks ($M > 105$ GeV). For the third generation squarks, the constraints depend on the mixing in the sfermion sector. For sbottom production, the mixing effects increase the exclusion for increasing $\tan\beta$, leading to excluded values of up to $M = 150$ GeV at the highest accessible $\tan\beta$. In case of stop production, a step at $\tan\beta \approx 38$ is visible in the limits, which originates from an increased branching into decay modes involving tau leptons in the final state, for which the branching has not been considered and the efficiencies have not been determined, and which have therefore not been included in the calculation of branching ratios. The stop limit excludes values of of up to $M = 148$ GeV at moderate $\tan\beta$.

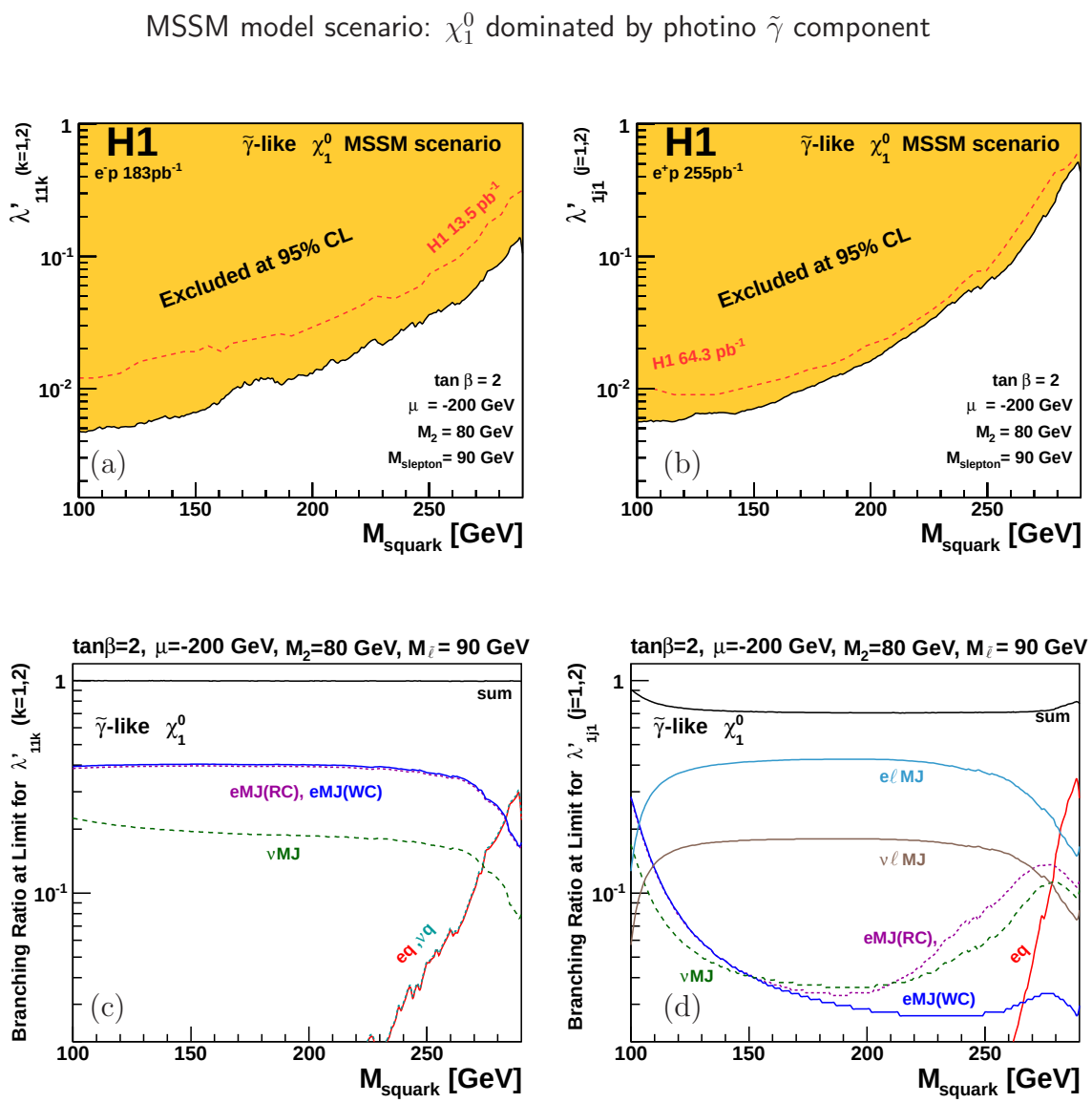

Figure 9.1: In a phenomenological MSSM with a photino ($\tilde{\gamma}$) like neutralino (χ_1^0) exclusion limits at 95% CL on (a) $\lambda'_{11k}\,(k = 1, 2)$ and on (b) $\lambda'_{1j1}\,(j = 1, 2)$ [1]. For comparison, the corresponding limit from the previous analysis [53] is also indicated. Also shown are branching ratios to the decay channels considered in this analysis for (c) λ'_{11k} and (d) λ'_{1j1} values at the observed limit.

MSSM model scenario: χ_1^0 dominated by zino $\tilde{Z}$ component

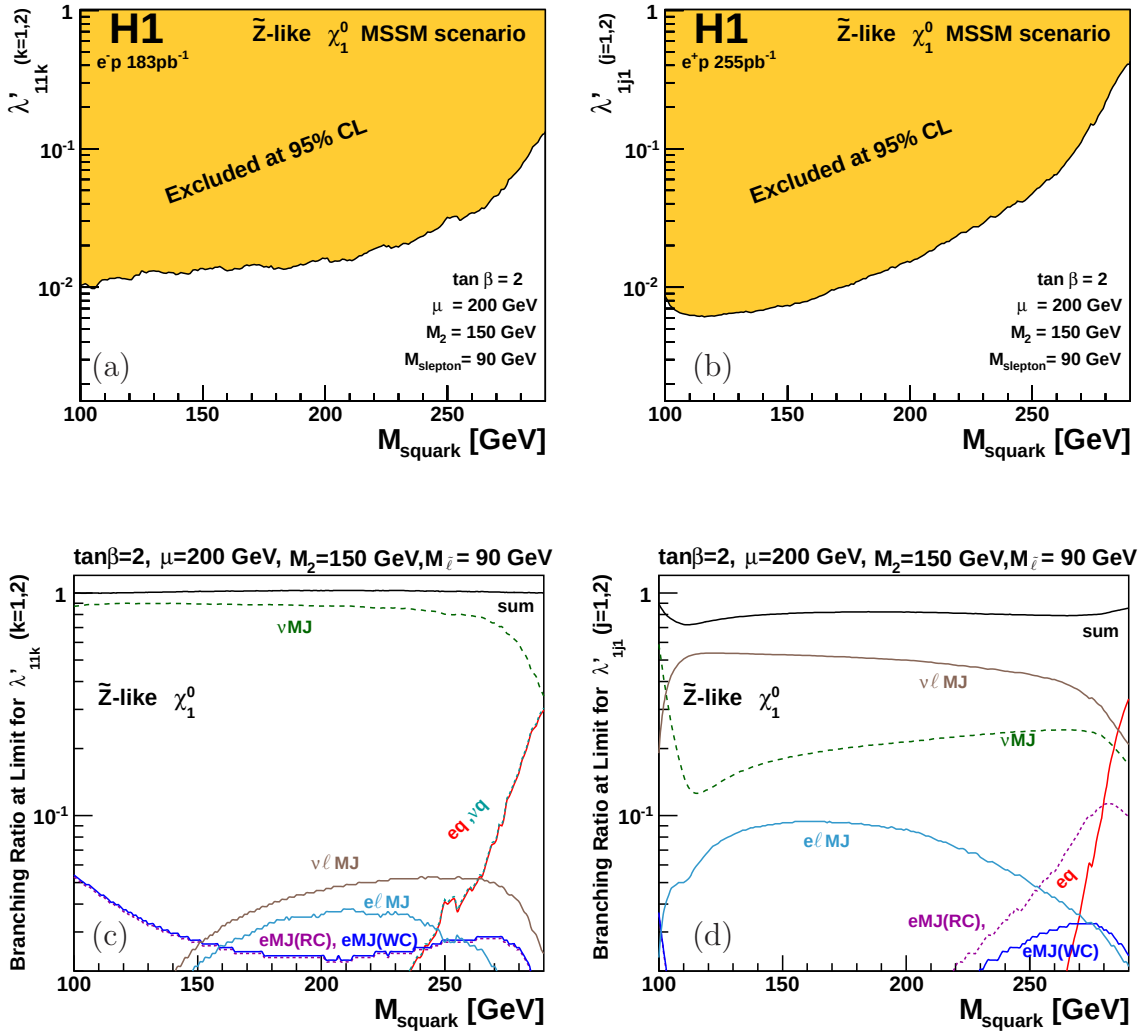

Figure 9.2: In a phenomenological MSSM with a zino ($\tilde{Z}$) like neutralino (χ_1^0) exclusion limits at 95% CL on (a) λ'_{11k} ($k = 1, 2$) and on (b) λ'_{1j1} ($j = 1, 2$) [1]. Also shown are branching ratios to the decay channels considered in this analysis for (c) λ'_{11k} and (d) λ'_{1j1} values at the observed limit.

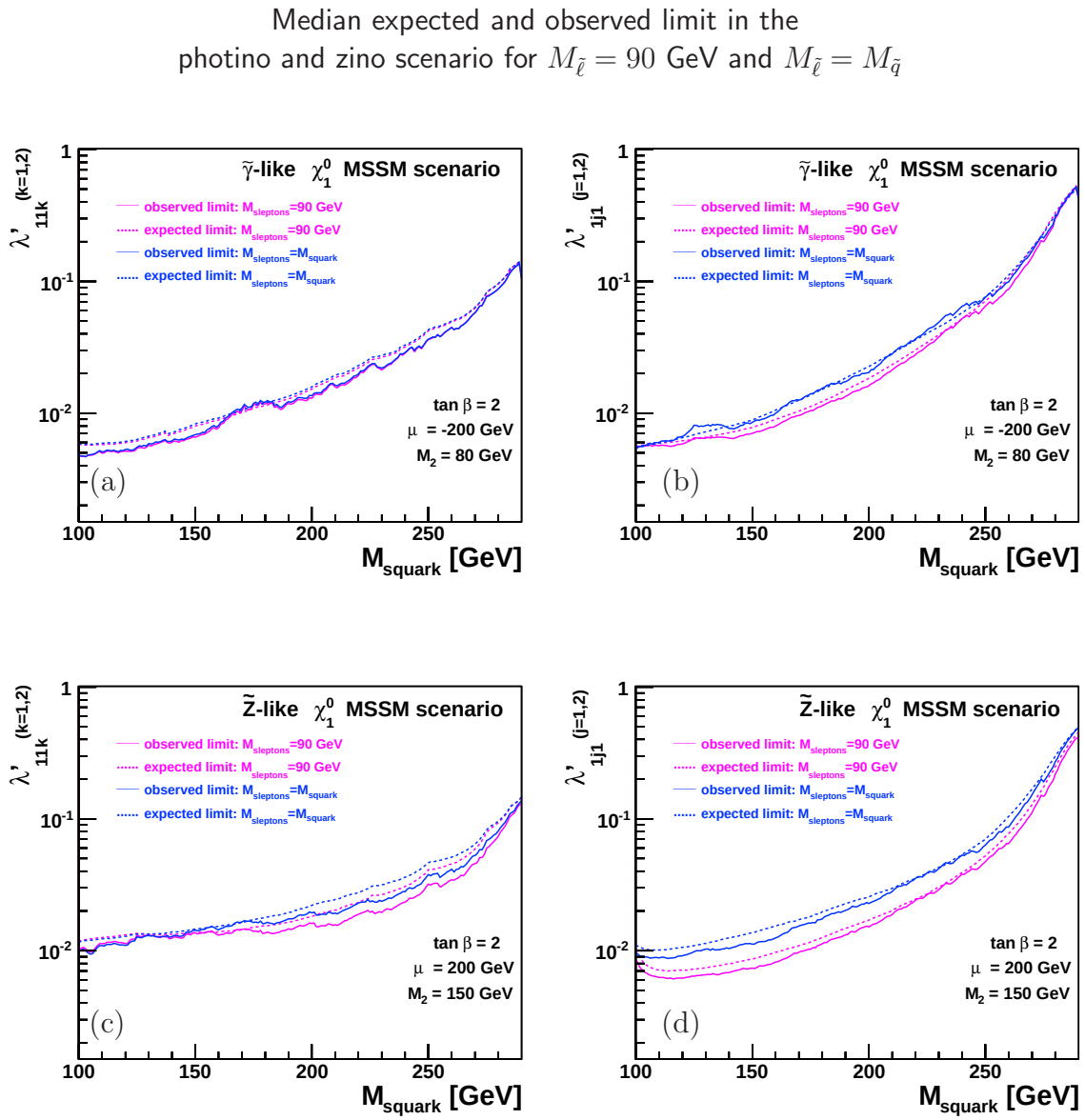

Figure 9.3: Comparison of observed and median expected exclusion limits on (a,c) $\lambda'_{11k}\,(k = 1, 2)$ and (b,d) $\lambda'_{1j1}\,(j = 1, 2)$ in the (a,b) photino and (c,d) zino dominated neutralino scenario at 95% CL for slepton masses set to 90 GeV, and for slepton masses identical to the squark mass.

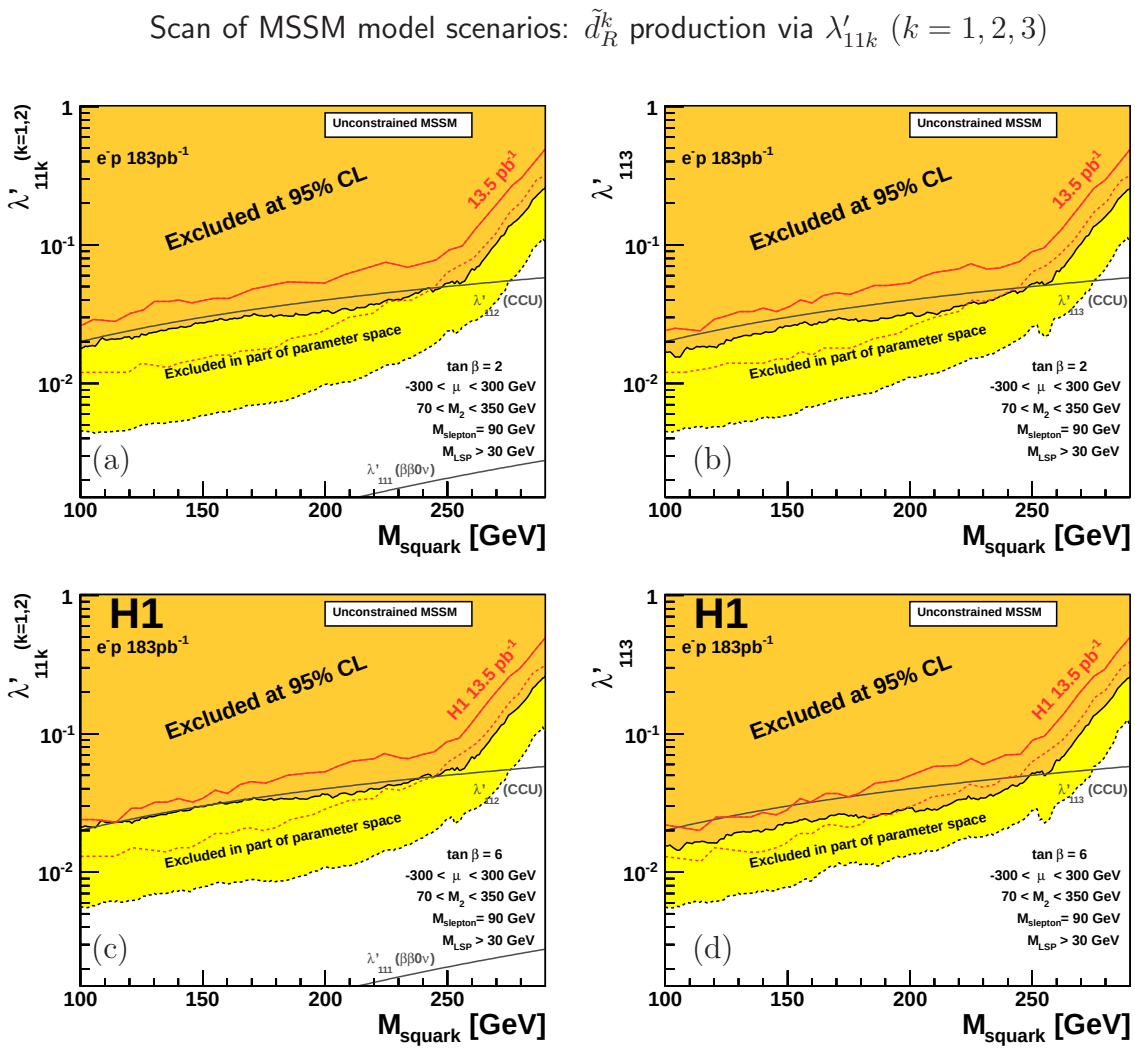

Figure 9.4: Exclusion limits (95 % CL) on λ'_{11k} for (a) $k = 1, 2$ and (b) $k = 3$ as a function of the squark mass derived from a scan of the MSSM parameter space, as indicated in the Figures using 183 pb^{-1} of e^-p collision data [1]. The dark shaded region indicates values of the coupling λ'_{11k} excluded in all investigated scenarios, whereas the light shaded region is excluded only in part of the scenarios. Indirect limits from neutrinoless double beta decay experiments ($\beta\beta0\nu$) [35; 47] and tests of charged current universality (CCU) [35; 48] are also shown. For comparison, the corresponding H1limits from the previous analysis [53] (c,d), as well as unpublished results [34] (a,b), based on the same luminosity of 13.5 pb^{-1} are also indicated.

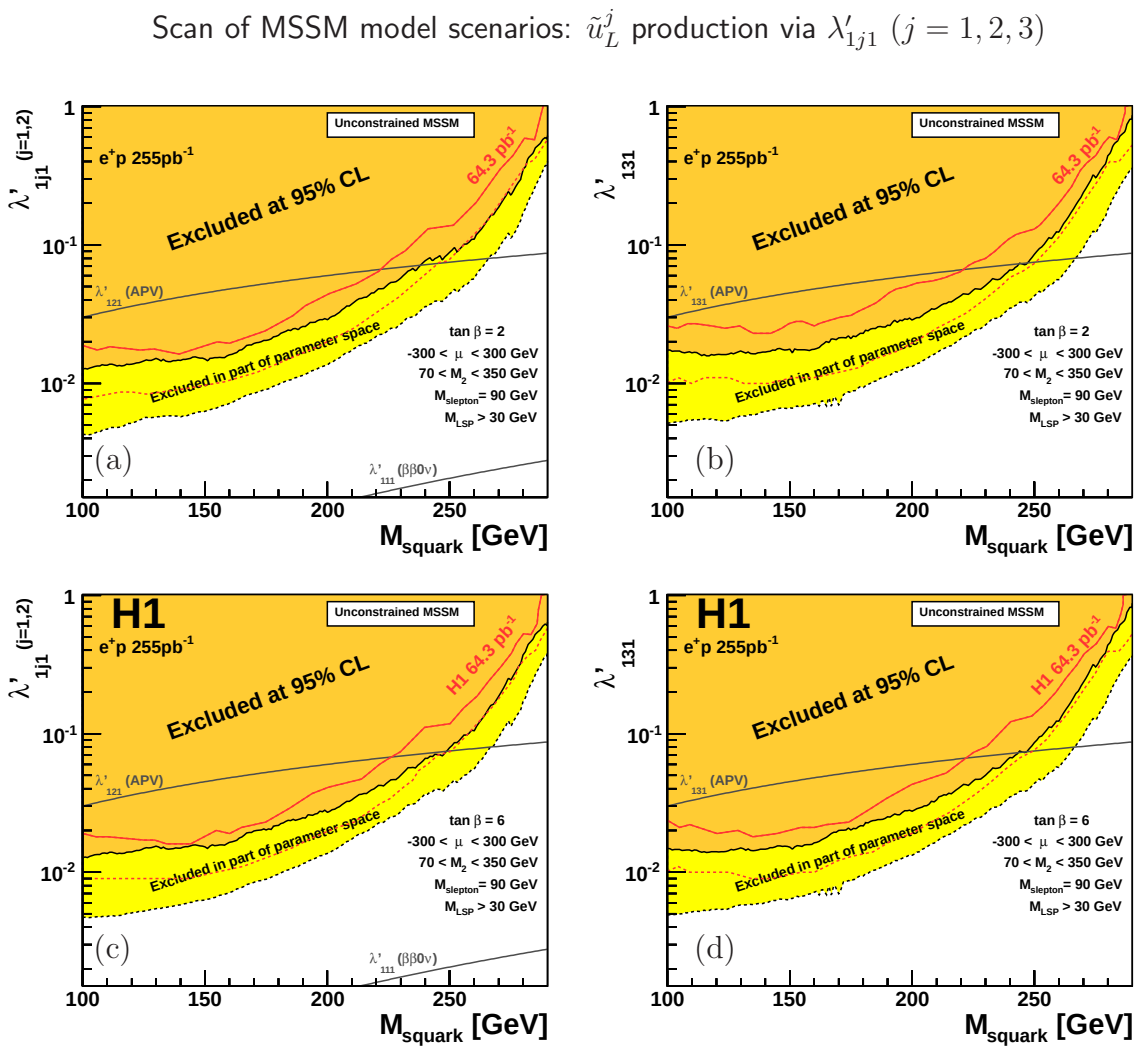

Figure 9.5: Exclusion limits (95 % CL) on λ'_{1j1} for (a) $j = 1, 2$ and (b) $j = 3$ as a function of the squark mass derived from a scan of the MSSM parameter space, as indicated in the Figures using 255 pb^{-1} of e^-p collision data [1]. The dark shaded region indicates values of the coupling λ'_{1j1} excluded in all investigated scenarios, whereas the light shaded region is excluded only in part of the scenarios. Indirect limits from neutrinoless double beta decay experiments ($\beta\beta0\nu$) [35; 47] and atomic parity violation (APV) [35; 49] are also shown. For comparison, the corresponding H1 limits from the previous analysis [53] (c,d), as well as unpublished results from [34] (a,b) based on the same luminosity of 64.3 pb^{-1} are also indicated.

(a)

(b)

(c)

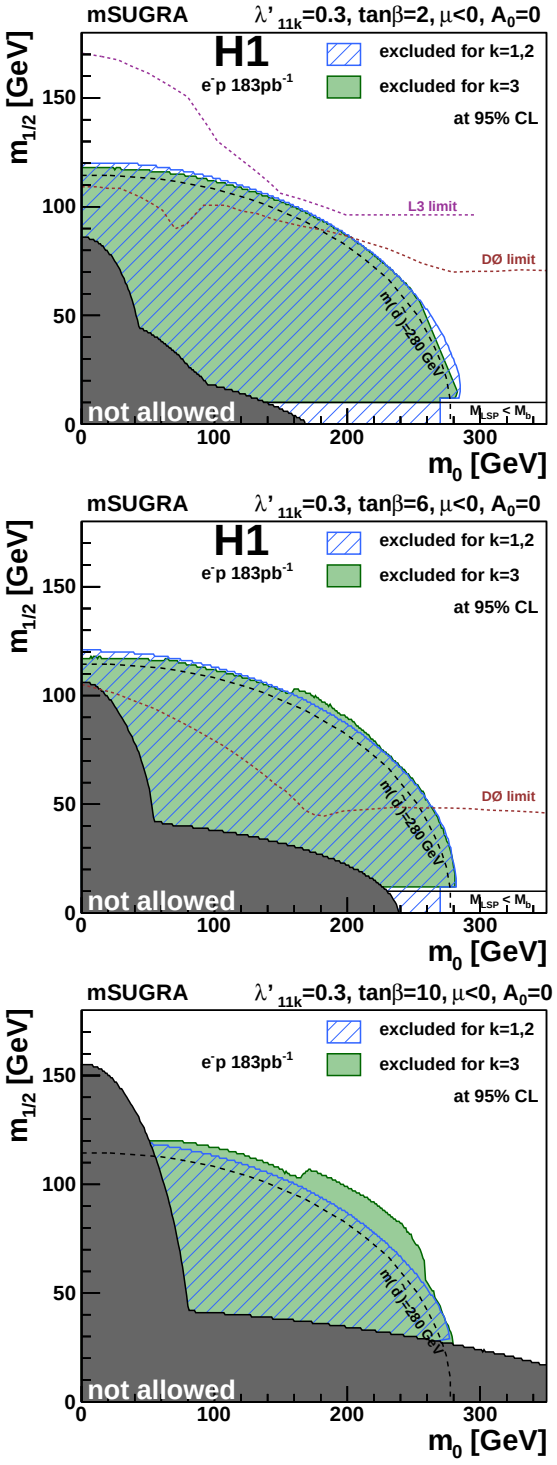

Figure 9.6: Exclusion limits (95 % CL) in $m_0, m_{1/2}$ plane assuming $\lambda'_{11k} = 0.3$ for (a) $\tan\beta = 2$, (b) $\tan\beta = 6$ and (c) $\tan\beta = 10$ for $k = 1, 2$ hatched dark, and $k = 3$ filled light region [1]. A curve of constant squark mass is indicated for $m(\tilde{d}) = 280$ GeV. Also indicated are constraints obtained by the L3 experiment at LEP [75] and the D0 experiment at the Tevatron [78]. The dark region labelled as "not allowed" indicates where no REWSB solution is possible or where the LSP is a sfermion.

(a)

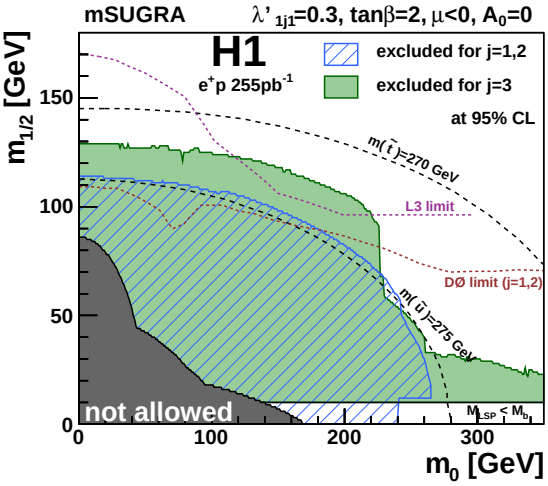

(b)

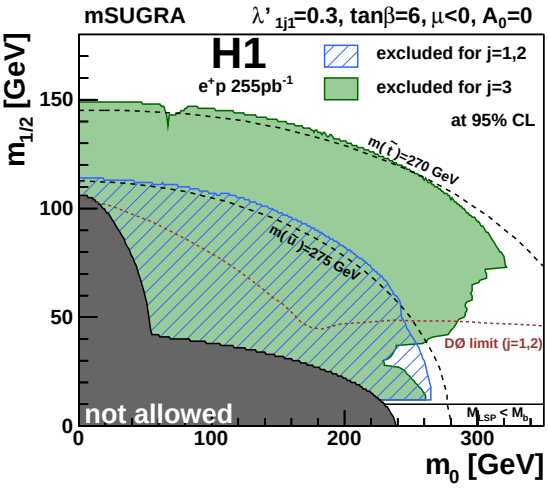

(c)

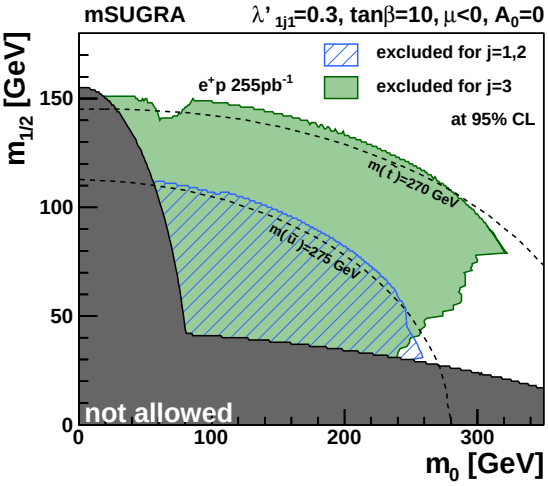

Figure 9.7: Exclusion limits (95 % CL) in $m_0, m_{1/2}$ plane assuming $\lambda'_{1j1} = 0.3$ for (a) $\tan\beta = 2$, (b) $\tan\beta = 6$ and (c) $\tan\beta = 10$ for $j = 1, 2$ hatched dark, and $j = 3$ filled light region [1]. Curves of constant squark mass are indicated for $m(\tilde{u}) = 275$ GeV and $m(\tilde{t}) = 270$ GeV. Also indicated are constraints obtained by the L3 experiment at LEP [75] and the D0 experiment at the Tevatron [78]. The dark region labelled as "not allowed" indicates where no REWSB solution is possible or where the LSP is a sfermion.

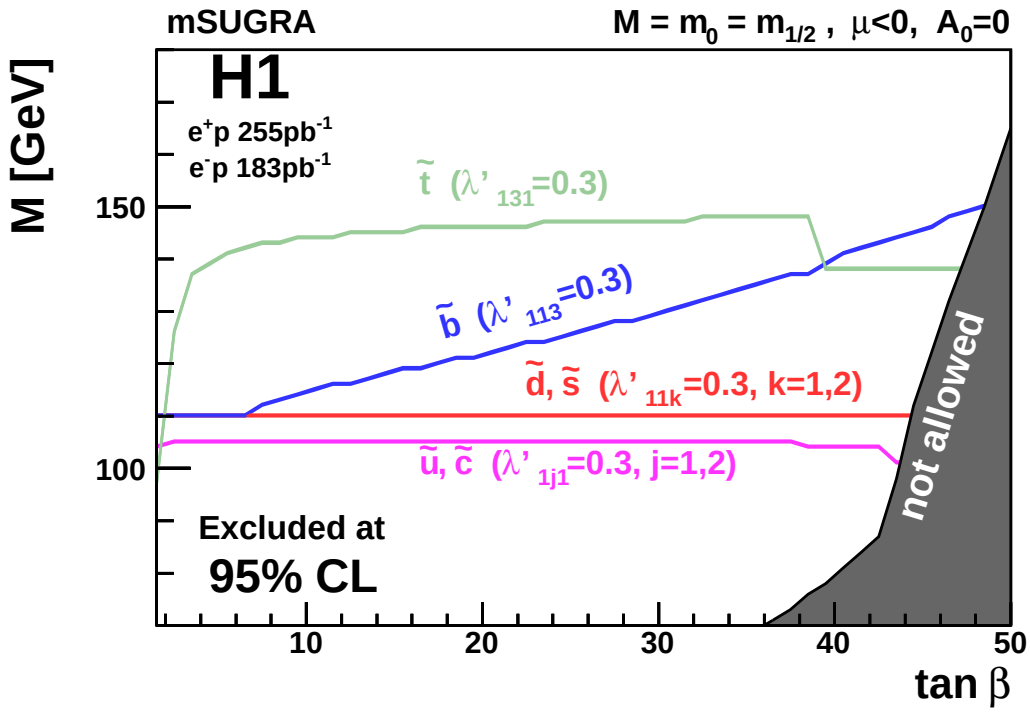

Figure 9.8: Exclusion limits for $M = m_0 = m_{1/2}$ in mSUGRA as function of $\tan\beta$ [1]. Shown are the 95 % CL exclusion domains for the model parameters from the production of first and second generation squarks ($\tilde{u}, \tilde{c}$ and $\tilde{d}, \tilde{s}$), and of third generation squarks ($\tilde{t}, \tilde{b}$), assuming a value of $\lambda' = 0.3$ for the respective couplings. The area below the curves is excluded. The dark region labelled as "not allowed" indicates where no REWSB solution is possible or where the LSP is a sfermion.

10 Conclusion

A search for squarks in R-parity violating supersymmetry is presented in this thesis, using the final data set of the H1 detector at HERA. The single resonant production of squarks via a lepton-quark-squark coupling λ' in electron-quark fusion is expected. Direct squark decays, and squark decays involving gauginos are considered, leading to final states with electrons, neutrinos, muons and jets in different multiplicities. Several exclusive selection channels, based on the final states expected from squark decays are examined with respect to the standard model expectation. No significant deviation from the SM predictions could be observed in the analysis of data sets corresponding to integrated luminosities of 183 pb^{-1} of electron-proton, and 255 pb^{-1} of positron-proton collision data, collected at a centre-of-mass energy of $\sqrt{s} = 319$ GeV. The differential kinematic distributions are well described in all selection channels, and even for more complex final states a reasonable description of the data by the SM expectation is observed. The non-observation of a signal is interpreted in the framework of the MSSM and the mSUGRA models, assuming the single coupling dominance hypothesis. Exclusion limits on the strength of the $\not{R}_p$ couplings λ'_{1j1} and λ'_{11k}, depending on the squark mass hypothesis, are derived in the MSSM by a scan of the supersymmetric parameters 70 GeV $< M_2 <$ 350 GeV and -300 GeV $< \mu <$ 300 GeV at $\tan\beta = 2$ and 6. The exclusion limits improve the existing boundaries, and exclude couplings λ'_{1j1} and λ'_{11k} at the level $\lambda' \lesssim 0.5 \cdot 10^{-2}$ at $M_{squark} = 100$ GeV, and $\lambda' \lesssim 0.5$ at $M_{squark} = 290$ GeV for all three squark generations $j, k = 1, 2, 3$. For an $\not{R}_p$ coupling strength comparable to the electromagnetic coupling strength, λ'_{1j1} or $\lambda'_{11k} = \sqrt{4\pi\alpha_{em}} = 0.3$, squark masses up to 275 GeV are excluded for $\tilde{u}^j_L$ squarks, with $\tilde{d}^k_R$ squarks further excluded up to 290 GeV for all three squark generations $j, k = 1, 2, 3$. An interpretation in the mSUGRA model, assuming an $\not{R}_p$ coupling strength comparable to the electromagnetic coupling strength, yields exclusion limits on the supersymmetric parameters m_0 and $m_{1/2}$, which superseed previous constraints obtained at HERA. The excluded region of supersymmetric scenarios is similar to the excluded region obtained at the LEP and TeVatron colliders, and competes with indirect limits derived from precision electroweak data. In the light of the LHC, which now quickly accumulates more data at unprecedented centre-of-mass energies, more severe constraints may become available in the near future. Although searches at the LHC experiments concentrate mostly on R-parity conserved SUSY models, first searches for combinations of non-zero $\not{R}_p$ couplings have been performed. The LHC may quickly discover $\not{R}_p$ SUSY, since the pair-production of squarks with high masses is possible, and the $\not{R}_p$ couplings may lead to final states easily visible at a hadron collider. However, no better testing ground than HERA exists so far for direct searches for new particles which couple to leptons and quarks. Furthermore, a high-energetic lepton beam interacting with the proton beam of the LHC, as proposed in form of the LHeC, would allow extended studies of $\not{R}_p$ couplings with an immensely increased sensitivity [168]. It is now up to the LHC and TeVatron experiments to decide the fate of supersymmetry and other new physics scenarios in the beginning millenium.

Appendix

A Supplementary Material

Some supplementary material is compiled at this place. Views of the H1 detector layout are shown for illustrative purposes. Additional Figures show preselections of the data and SM expectation in channels, where further optimisation cuts are applied.

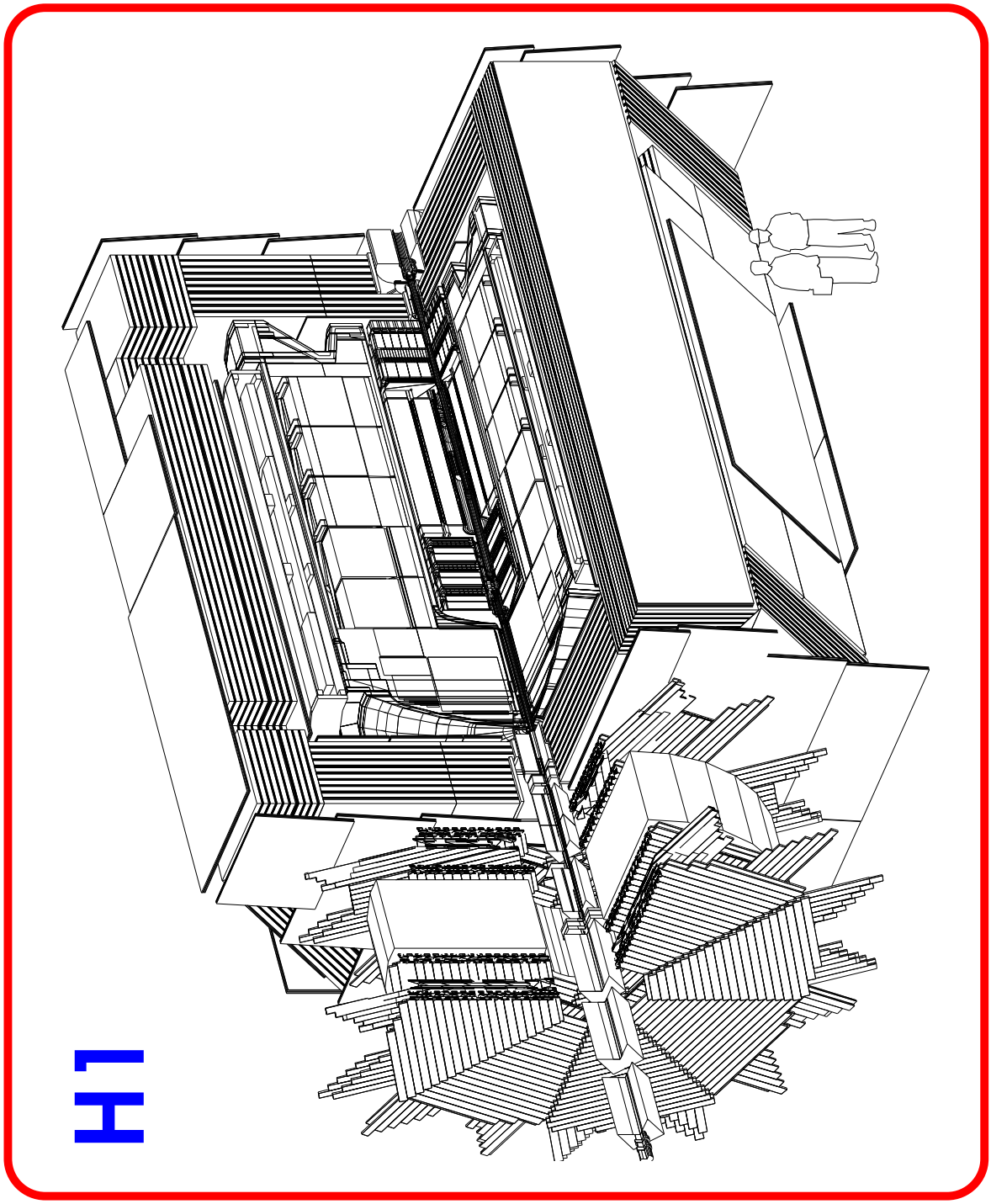

Figure A.1: A 3-dimensional view of the H1 Detector, as implemented in GEANT in the H1 software [169].

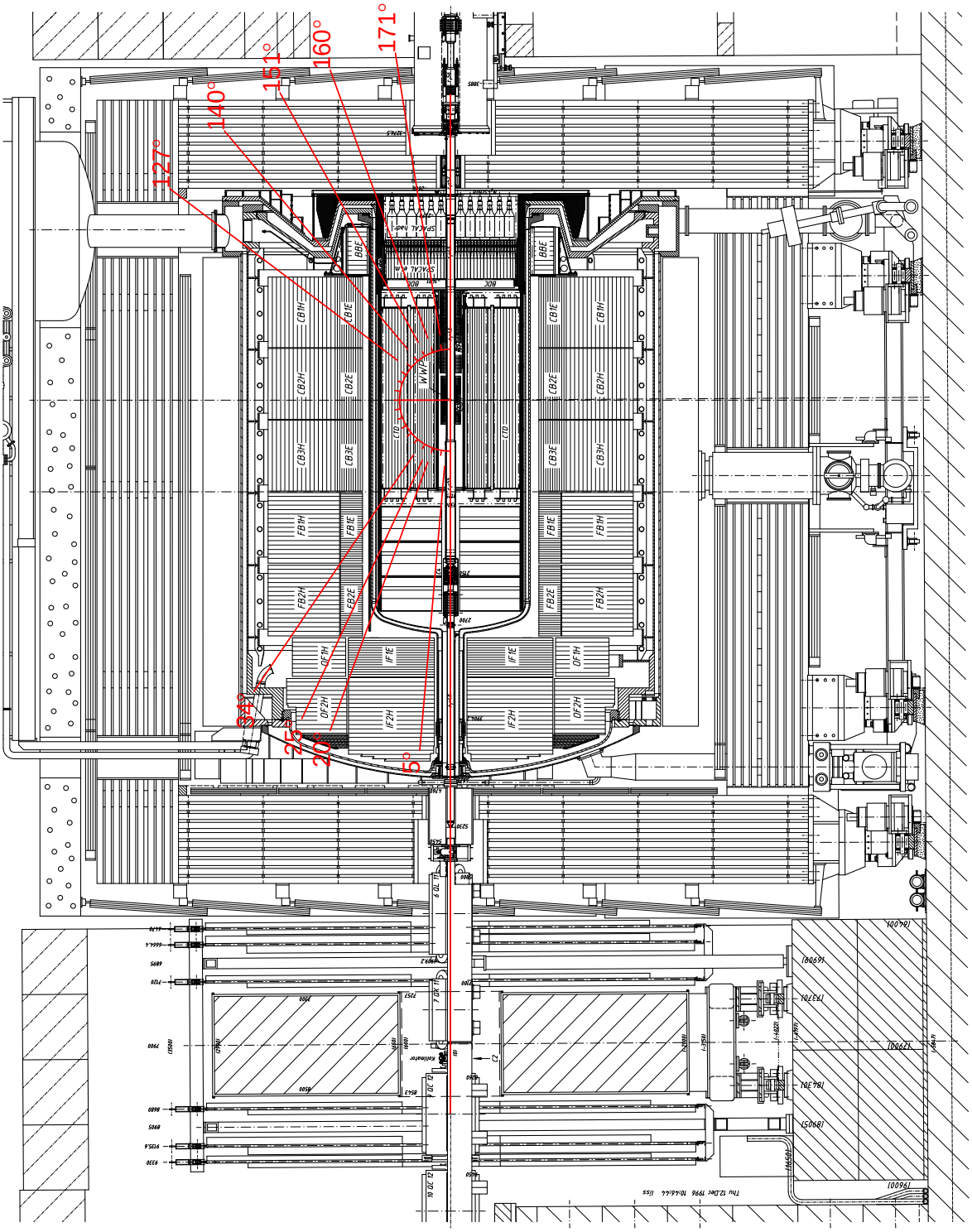

Figure A.2: Technical drawing of the H1 Detector. The sketched trajectories show where particles under different θ angles traverse the detector volume [169].

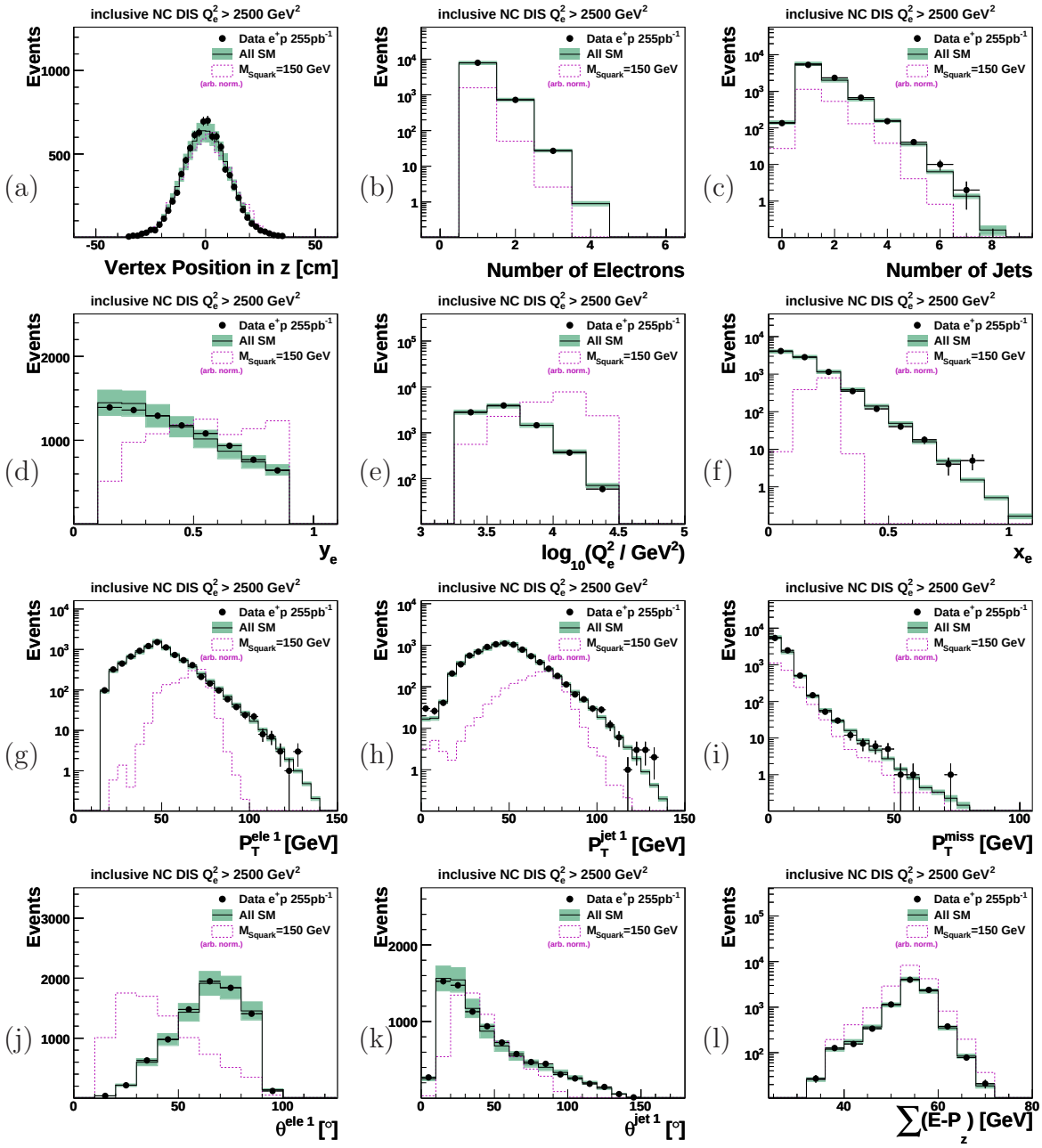

Figure A.3: Distributions of (a) z-vertex position, (b) number of electrons per event, (c) number of jets per event, (d) inelasticity y_e and (e) virtuality $\log_{10}(Q_e^2)$ and (f) momentum fraction x_e reconstructed via the electron method, transverse momenta of (g) leading electrons P_T^{ele1} and (h) leading jets P_T^{jet1}, (i) reconstructed missing transverse momentum P_T^{miss}, polar angle of (j) leading electrons θ^{ele1} and (k) leading jets θ^{jet1}, and (l) longitudinal energy balance $\sum(E - P_z)$ in the NC DIS selection channel for $\mathbf{Q_e^2 > 2500}$ GeV^2 with data (points) events from 255 pb^{-1} $\mathbf{e^+p}$ collisions compared to SM MC predictions. The error band gives all model and experimental systematic uncertainties on the SM prediction (solid histogram) added in quadrature. Error bars of data events show statistical uncertainties. The dashed histogram indicates the signal from a squark with $M_{squark} = 150$ GeV decaying into an electron and a jet with arbitrary normalisation.

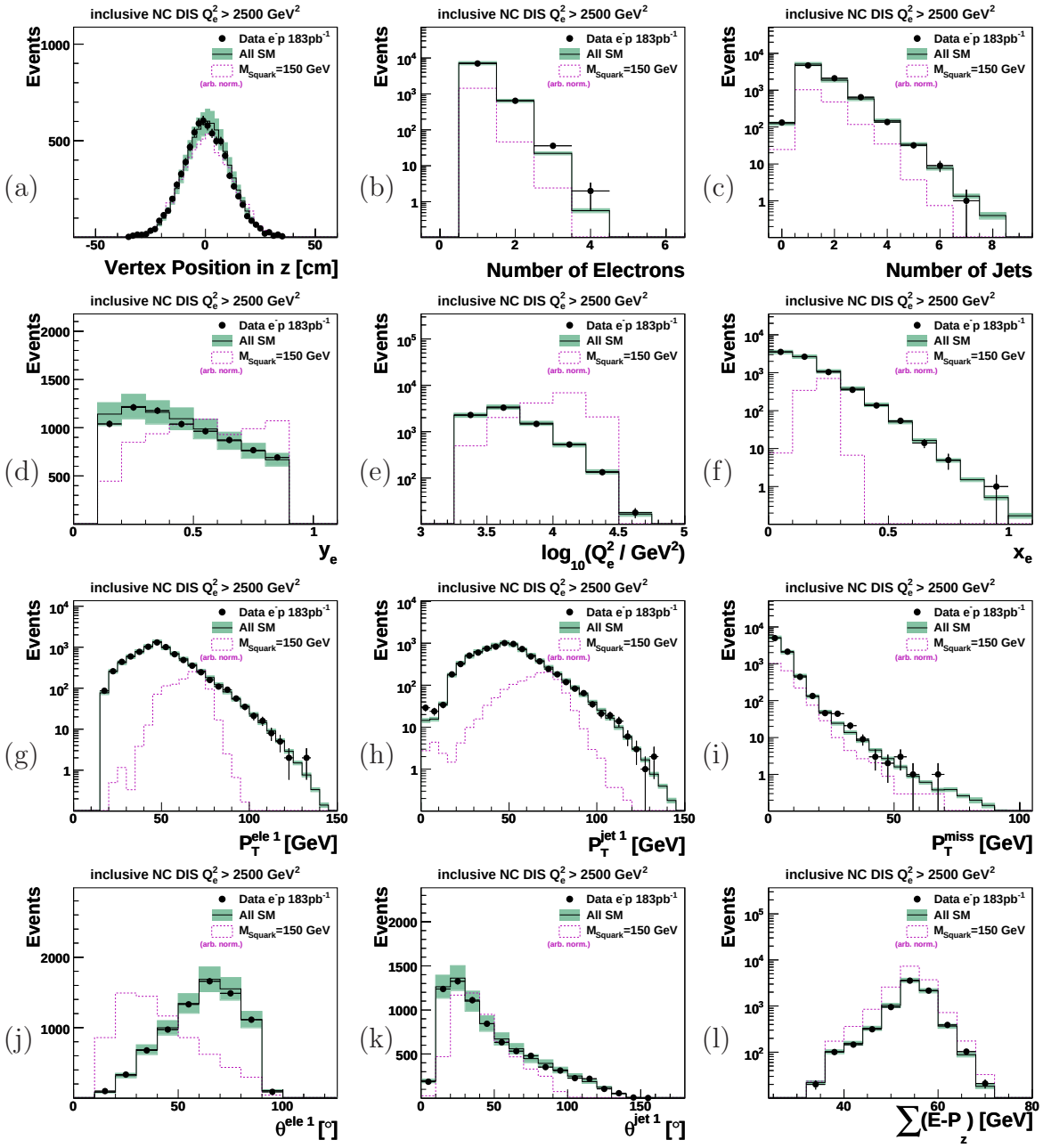

Figure A.4: Distributions of (a) z-vertex position, (b) number of electrons per event, (c) number of jets per event, (d) inelasticity y_e and (e) virtuality $\log_{10}(Q_e^2)$ and (f) momentum fraction x_e reconstructed via the electron method, transverse momenta of (g) leading electrons P_T^{ele1} and (h) leading jets P_T^{jet1}, (i) reconstructed missing transverse momentum P_T^{miss}, polar angle of (j) leading electrons θ^{ele1} and (k) leading jets θ^{jet1}, and (l) longitudinal energy balance $\sum(E - P_z)$ in the NC DIS selection channel for $\mathbf{Q_e^2 > 2500}$ GeV^2 with data (points) events from 183 pb^{-1} $\mathbf{e^-p}$ collisions compared to SM MC predictions. The error band gives all model and experimental systematic uncertainties on the SM prediction (solid histogram) added in quadrature. Error bars of data events show statistical uncertainties. The dashed histogram indicates the signal from a squark with $M_{squark} = 150$ GeV decaying into an electron and a jet with arbitrary normalisation.

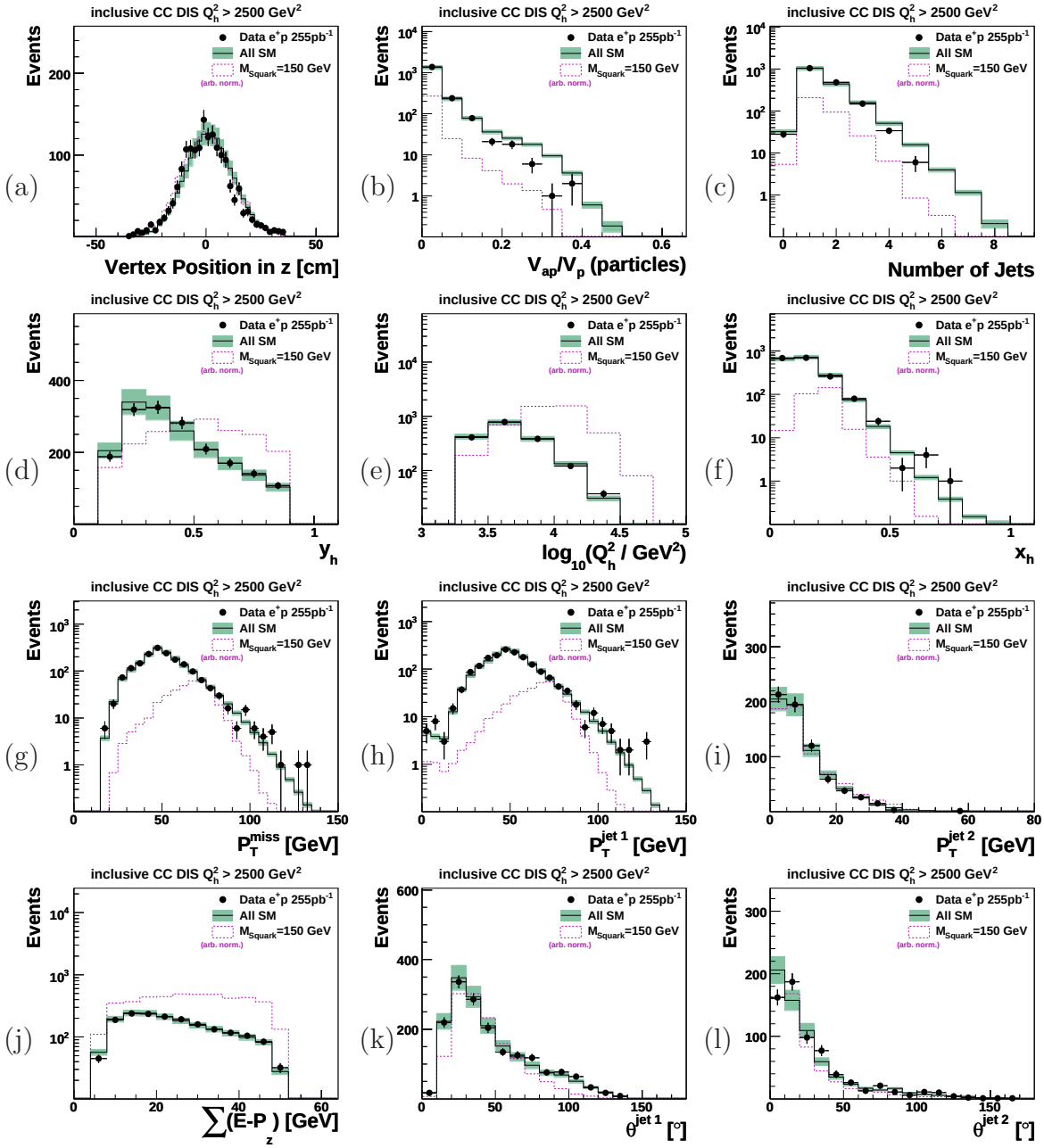

Figure A.5: Distributions of (a) z-vertex position, (b) ratio of energy flow V_{ap}/V_p, (c) number of jets per event, (d) inelasticity y_h and (e) virtuality $\log_{10}(Q_h^2)$ and (f) momentum fraction x_h reconstructed via the hadron method, (g) reconstructed missing transverse momentum P_T^{miss}, transverse momenta of (h) leading jets P_T^{jet1} and (i) subleading jets P_T^{jet2}, (j) longitudinal energy balance $\sum(E - P_z)$, polar angle of (k) leading jets θ^{jet1} and (l) subleading jets θ^{jet2} in the CC DIS selection channel for $\mathbf{Q_h^2 > 2500}$ GeV^2 with data (points) events from 255 pb^{-1} $\mathbf{e^+p}$ collisions compared to SM MC predictions. The error band gives all model and experimental systematic uncertainties on the SM prediction (solid histogram) added in quadrature. Error bars of data events show statistical uncertainties. The dashed histogram indicates the signal from a squark with $M_{squark} = 150$ GeV decaying into a neutrino and a jet with arbitrary normalisation.

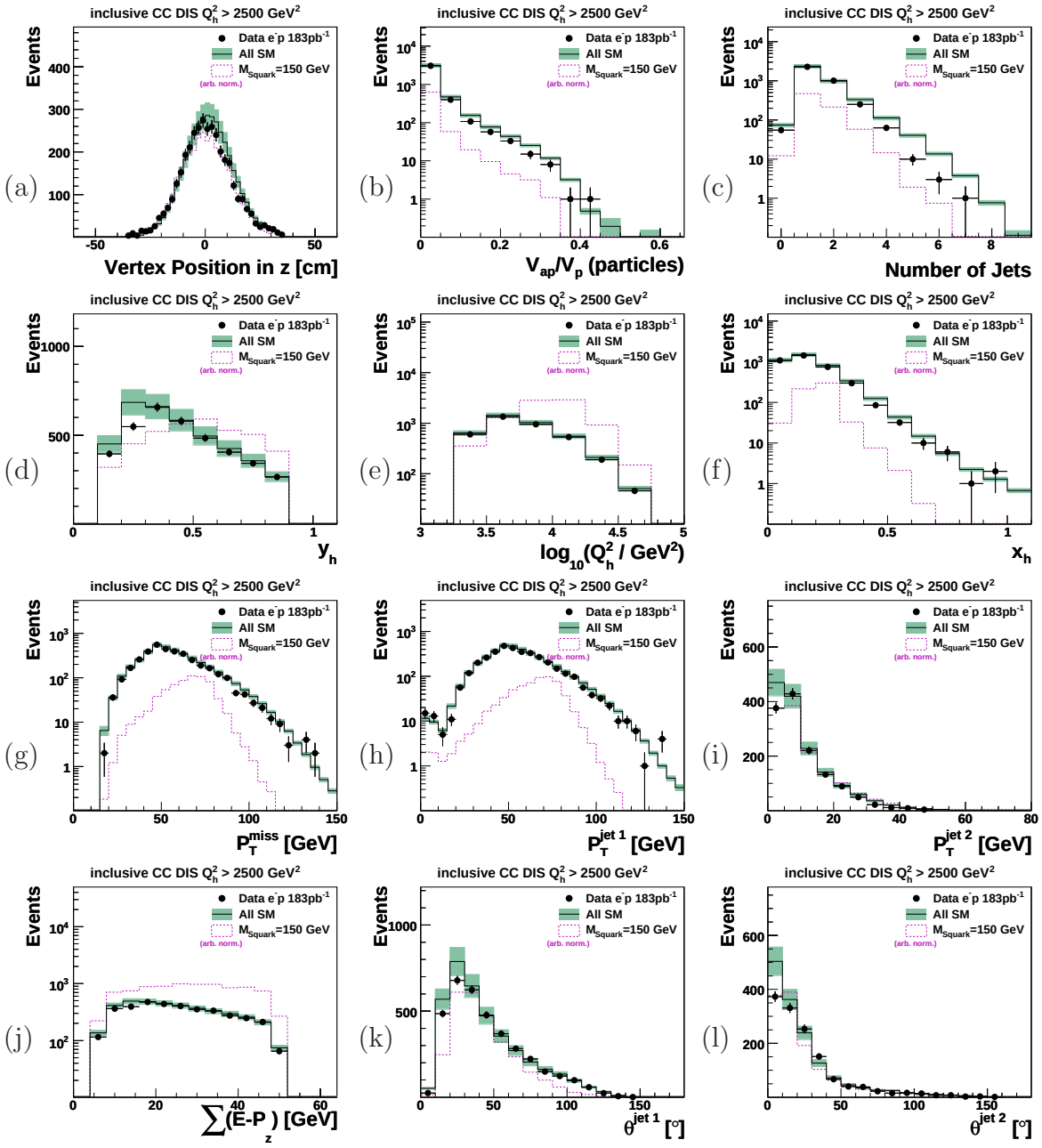

Figure A.6: Distributions of (a) z-vertex position, (b) ratio of energy flow V_{ap}/V_p, (c) number of jets per event, (d) inelasticity y_h and (e) virtuality $\log_{10}(Q_h^2)$ and (f) momentum fraction x_h reconstructed via the hadron method, (g) reconstructed missing transverse momentum P_T^{miss}, transverse momenta of (h) leading jets P_T^{jet1} and (i) subleading jets P_T^{jet2}, (j) longitudinal energy balance $\sum(E - P_z)$, polar angle of (k) leading jets θ^{jet1} and (l) subleading jets θ^{jet2} in the CC DIS selection channel for $\mathbf{Q_h^2 > 2500}$ GeV^2 with data (points) events from 183 pb^{-1} $\mathbf{e^-p}$ collisions compared to SM MC predictions. The error band gives all model and experimental systematic uncertainties on the SM prediction (solid histogram) added in quadrature. Error bars of data events show statistical uncertainties. The dashed histogram indicates the signal from a squark with $M_{squark} = 150$ GeV decaying into a neutrino and a jet with arbitrary normalisation.

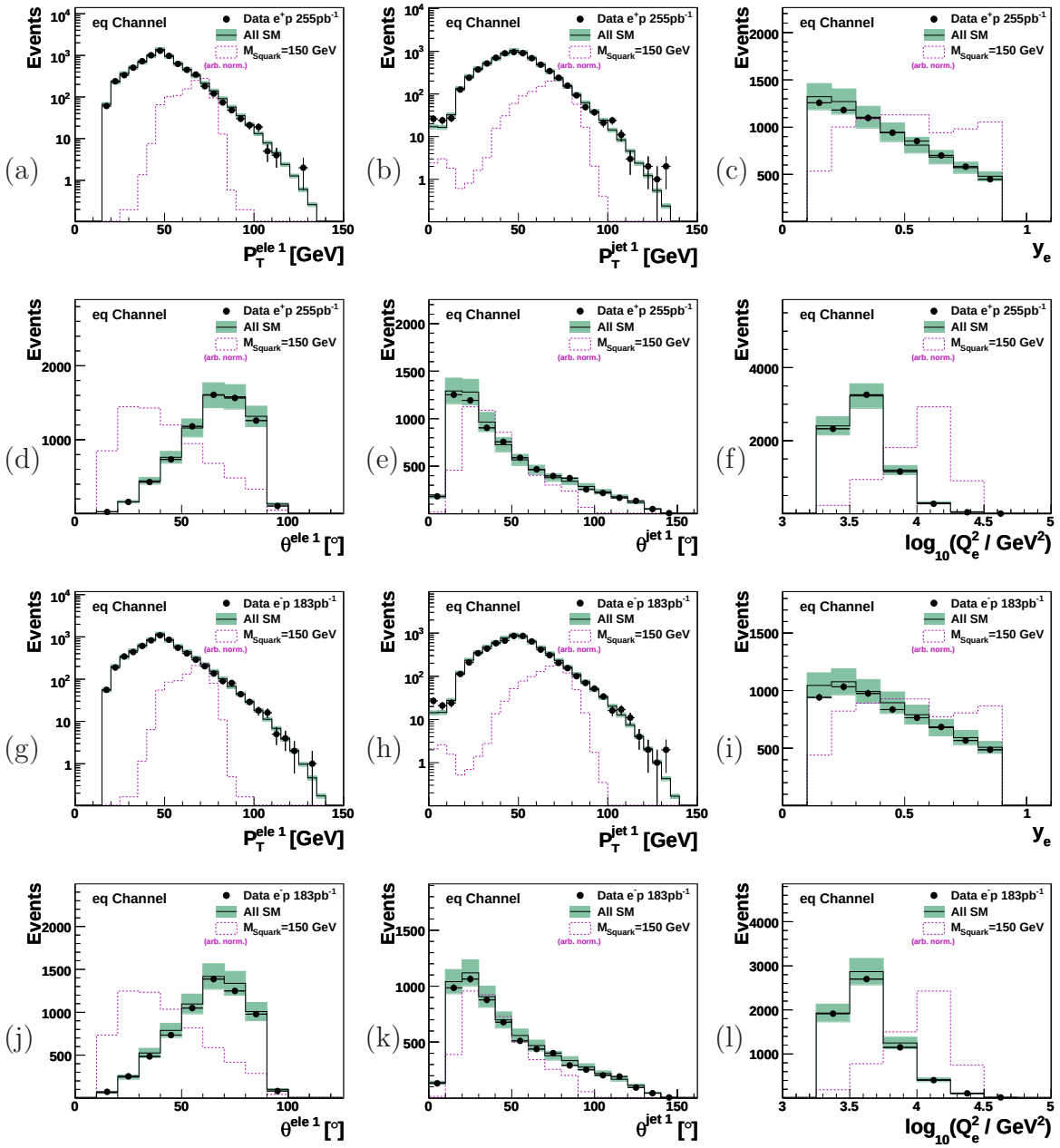

Figure A.7: Kinematic distributions of selected events in the **eq channel** for (a-f) the $\mathbf{e^+p}$ and (g-l) the $\mathbf{e^-p}$ data (points) compared to SM MC predictions (solid histogram) **before the** $y-M$ **optimisation**. Shown are the transverse momenta of (a, g) electrons P_T^{ele1} and (b, h) jets P_T^{jet1}, (c, i) the inelasticity y_e, the polar angle of (d, j) electrons θ^{ele1} and (e, k) jets θ^{jet1}, and (f, l) the virtuality $\log_{10}(Q_h^2)$. The error band gives all model and experimental systematic uncertainties on the SM prediction added in quadrature. Error bars of data events show statistical uncertainties. The dashed histogram indicates the signal from a squark with $M_{squark} = 150\,\mathrm{GeV}$ decaying into an electron and a jet with arbitrary normalisation.

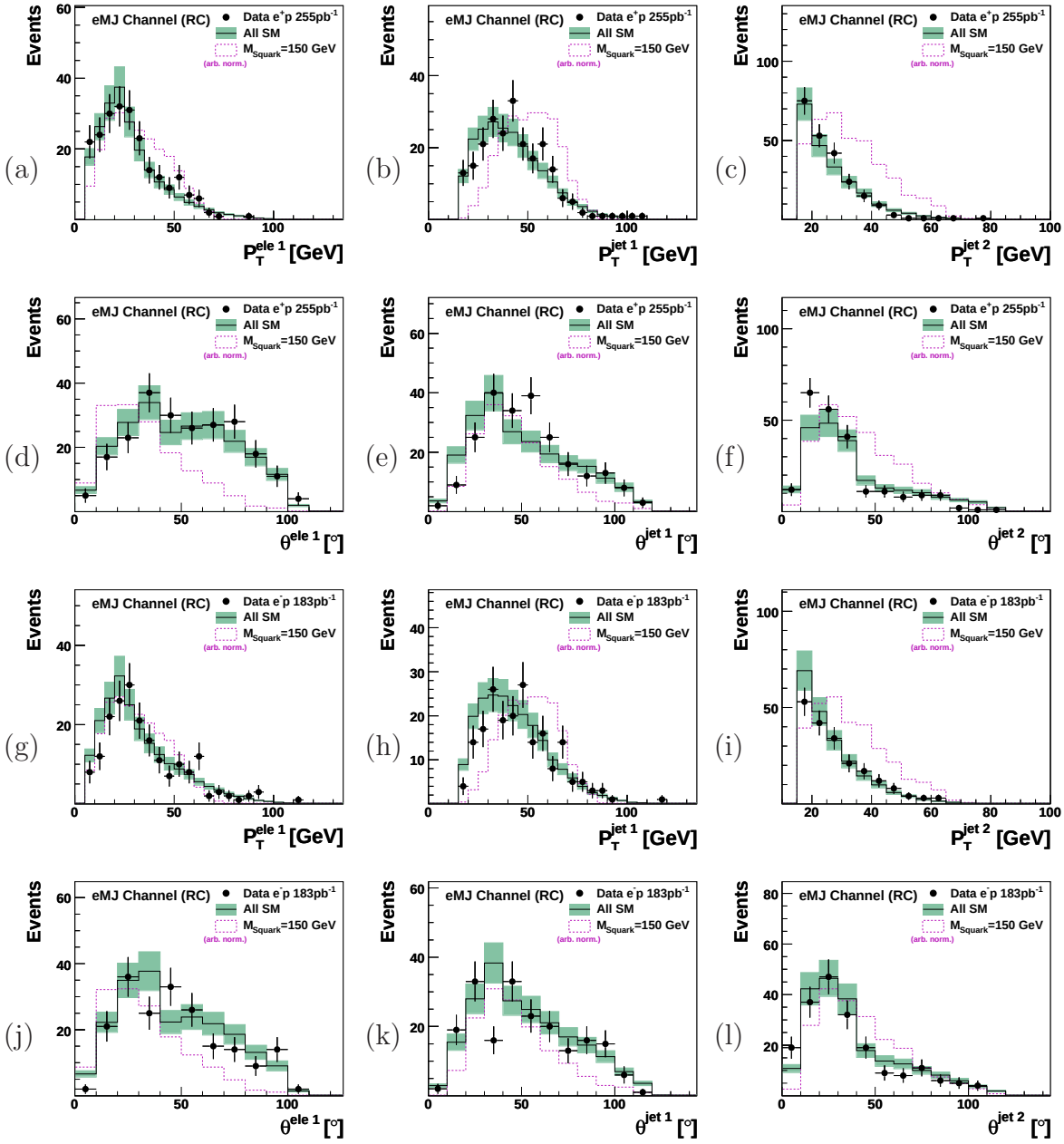

Figure A.8: Distributions of the transverse momenta of (a, g) electrons P_T^e, (b, h) leading jets P_T^{jet1} and subleading (c, i) jets P_T^{jet2}, as well as the corresponding polar angle distributions of (d, j) electrons θ_e, leading jets θ_{jet1}, and subleading jets θ_{jet2} in the **eMJ(RC) channel** for (a-f) the $\mathbf{e^+p}$ and (g-l) the $\mathbf{e^-p}$ data (points) compared to SM MC predictions (solid histogram) **before the** $y - M$ **optimisation**. The e^+p data are not expected to contain signal events from squark decays in this channel. The error band gives all model and experimental systematic uncertainties on the SM prediction added in quadrature. Error bars of data events show statistical uncertainties. The dashed histogram indicates the signal from a squark with $M_{squark} = 150\,\mathrm{GeV}$ decaying into an electron and multiple jets with arbitrary normalisation.

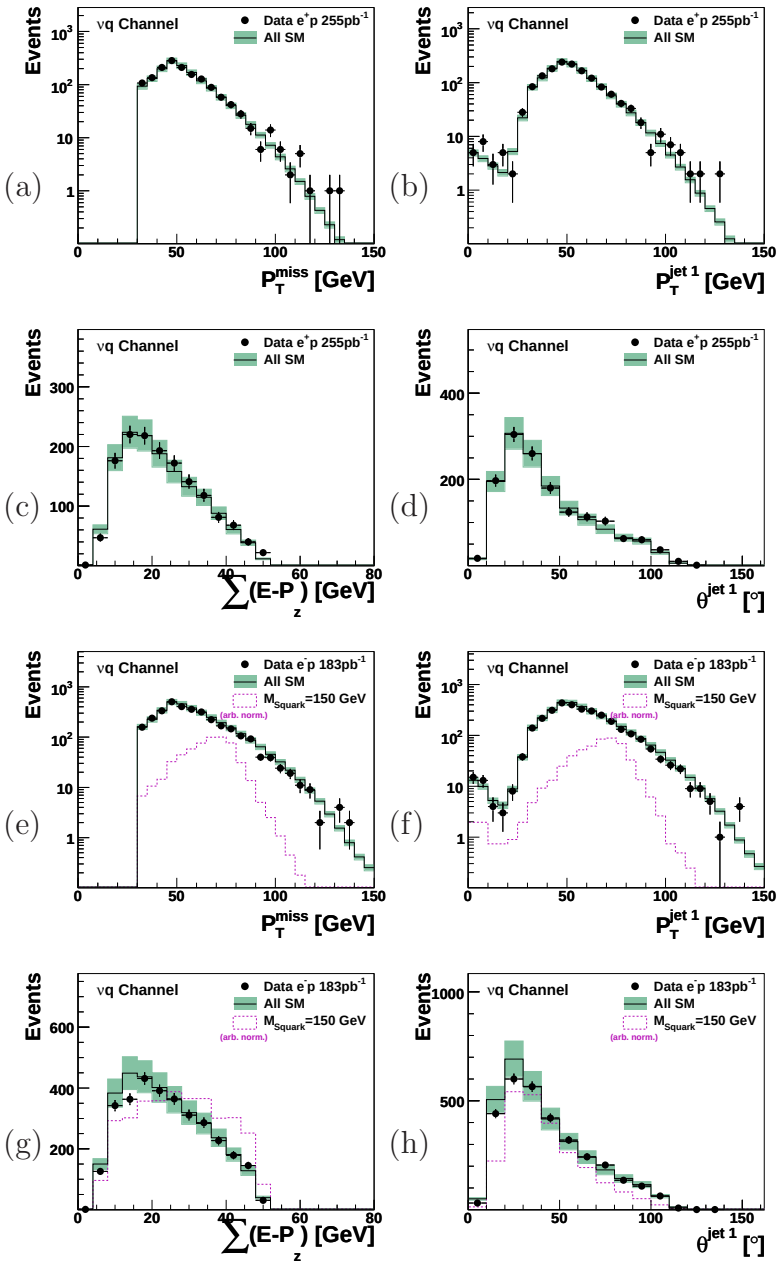

Figure A.9: Distributions of (a,e) the reconstructed missing transverse momentum P_T^{miss}, momenta of (b,f) the leading jet P_T^{jet1}, as well as (c,g) the longitudinal energy momentum balance $\sum(E - P_z)$, and (d,h) the polar angle of the leading jets θ_{jet1} in the $\nu\mathbf{q}$ **channel** for (a-d) the $\mathbf{e^+p}$ and (e-h) the $\mathbf{e^-p}$ data (points) compared to SM MC predictions (solid histogram) **before the** $y - M$ **optimisation**. The error band gives all model and experimental systematic uncertainties on the SM prediction added in quadrature. Error bars of data events show statistical uncertainties. The dashed histogram indicates the signal from a squark with $M_{squark} = 150\,\text{GeV}$ decaying into a neutrino and a jet in e^-p interactions with arbitrary normalisation.

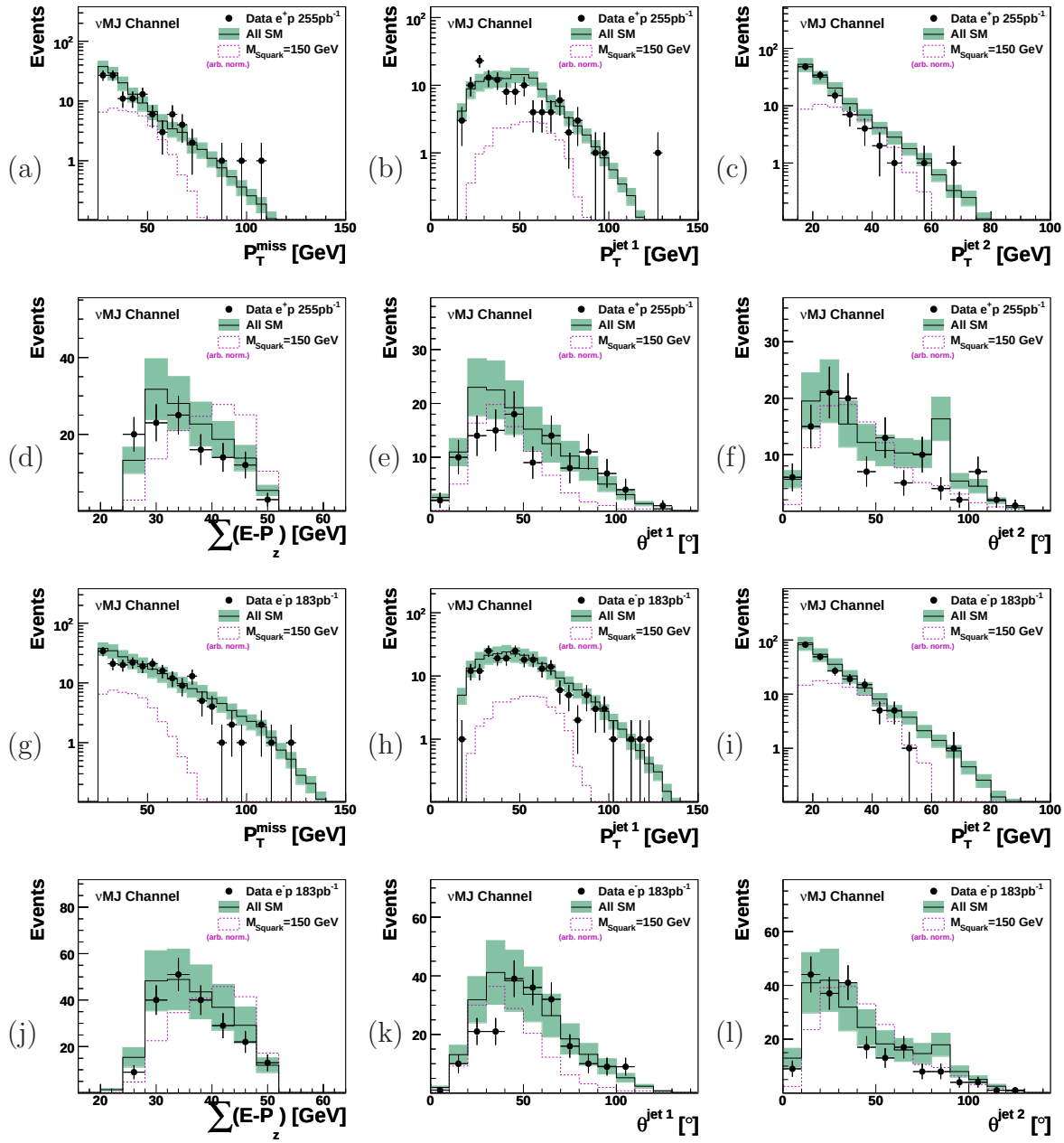

Figure A.10: Distributions of the (a,g) reconstructed missing transverse momentum P_T^{miss}, momenta of (b,h) leading jets P_T^{jet1} and subleading (c,i) jets P_T^{jet2}, as well as the (d,j) longitudinal energy momentum balance $\sum(E-P_z)$, leading jets θ_{jet1}, and subleading jets θ_{jet2} in the ν**MJ channel** for (a-f) the $\mathbf{e^+p}$ and (g-l) the $\mathbf{e^-p}$ data (points) compared to SM MC predictions (solid histogram) **before the** $y-M$ **optimisation**. The error band gives all model and experimental systematic uncertainties on the SM prediction added in quadrature. Error bars of data events show statistical uncertainties. The dashed histogram indicates the signal from a squark with $M_{squark} = 150\,\text{GeV}$ decaying into a neutrino and multiple jets with arbitrary normalisation.

B Zero Lepton Search for SUSY at the ATLAS Experiment

In the course of my PhD, I have been given the opportunity to participate in the work of the ATLAS experiment at CERN. A cross check of the expected signal contributions to the signal regions in a search for SUSY in channels with high P_T jets, high missing energy, and zero leptons has been performed. A cross check of the exclusion limits for R_p conserving SUSY in the $M_{squark} - M_{gluino}$ plane has been done for the individual signal regions considering, only a subset of the systematic uncertainties for the signal. A small overview of the analysis and the results is presented in the following.

Overview

First searches for the production of supersymmetric particles in proton-proton collisions at ATLAS have been performed in a data set corresponding to an integrated luminosity of $\mathcal{L}_{int} = 35$ pb^{-1} [81] taken at a centre-of-mass energy $\sqrt{s} = 7$ TeV. Final states with multiple high P_T jets and large missing energy E_T^{miss} are expected for supersymmetric models, in which squarks and gluinos can be produced pair-wise ($\tilde{q}\tilde{q}, \tilde{q}\bar{\tilde{q}}, \tilde{g}\tilde{g}, \tilde{q}\tilde{g}$) in proton-proton collisions. The considered SUSY models assume that R-parity is conserved, thus a stable lightest supersymmetric particles is expected, which leads to the missing energy signature. No significant excess has been observed in any of the considered signal regions. Exclusion limits for parameters of the MSSM and the mSUGRA model (with conserved R_p) have been derived, excluding equal masses of squarks and gluinos up to 870 GeV at 95% CL.

A short description of the analysis procedure, the method for the calculation of exclusion limits, and the results obtained in a simplified ansatz are summarized. A description of the ATLAS experiment, and more details of the analysis are found elsewhere [81].

Squark and Gluino Creation and Decay in Proton-Proton Collisions

The production of squark-pairs proceeds at lowest order via the t-channel exchange of gluinos between quarks in the initial state. Gluino-squark pair production proceeds at lowest order via the s-channel, or the t-channel exchange of squarks or gluinos between quarks and gluons in the initial state. For the production of gluino pairs and squark-antisquark pairs, the lowest order processes are given by s- and t-channel exchange of squarks and gluinos between quark-antiquark, or gluon-gluon initial states [170]. NLO corrections for squark and gluino production in hadron collisions are also considered [170]. Figure B.1 shows the NLO production cross section σ^{NLO} for squarks and gluinos. Figure B.2 shows the production NLO cross section for the different subprocesses $\sigma^{\text{NLO}}_{\text{subprocess}}$ in the $M_{squark} - M_{gluino}$ plane. The relative contribution of each subprocess to the total cross section is shown in Figure B.3. At small values for the

squark mass, the squark-squark and squark-antisquark processes contribute most significantly. At low gluino masses, the gluino-squark process dominates. The production of gluino pairs contributes most for approximately equal squark and gluino masses.

Squarks and gluinos decay in R-parity conserving models via cascades of gauginos into the lightest supersymmetric particle, which is assumed to be a weakly interacting neutralino χ_1^0. The neutralino is expected to be stable, and escapes detection after its creation, thus leading to high missing energy in the reconstruction of events. Supersymmetric events from the processes $\tilde{q} \rightarrow q\chi_1^0$, and $\tilde{g} \rightarrow qq\chi_1^0$ have been generated using the HERWIG++ [171] event generator v2.4.2, and passed through a full ATLAS detector simulation.

Search Strategy and Event Selection

Four overlapping signal regions $A-D$ are defined for candidate events which originate from squark and gluino decays. The criteria for the selection are summarised in Table B.1. The signal regions are chosen for maximal exclusion in the $M_{squark} - M_{gluino}$ plane, for a set of simplified models, where the mass of the lightest neutralino is assumed to be massless, and the masses of other supersymmetric particles are set to values beyond the reach of the LHC.

For maximal reach in the $M_{squark} - M_{gluino}$ plane, signal regions with two or more jets (for the $\tilde{q}\tilde{q}$ region), and signal regions with three or more jets (for the $\tilde{q}\tilde{g}$ and $\tilde{g}\tilde{g}$ regions) are defined. After the object reconstruction (for details see [81]), events are discarded if they contain electrons or muons, or if jets fail any of the quality criteria, or if the requirements for the primary vertex reconstruction are not fulfilled (for details see [81]). The selection criteria for the signal region are based on high P_T jets, and high reconstructed missing energy E_T^{miss} (see Table B.1). Additional cuts on the azimuthal separation between the missing transverse momentum vector $\vec{P}_T^{miss}$ and jets, on the ratio of E_T^{miss} and the reconstructed effective mass m_{eff}, the effective mass, and the mass hypothesis m_{T2} are applied to enhance the signal to background ratio in the signal regions (for definitions of the observables and more details see [81]).

After these selection steps, good agreement is observed for candidate events selected in the signal regions and the SM expectations. Table B.2 summarises the findings in the signal regions in data and the SM expectation, as well as the uncertainties attributed to the SM expectation from uncorrelated error sources, the jet energy scale, and the luminosity. The signal regions are dominated by irreducible and *fake* SM background events from $W + jets$ production, $Z + jets$ production, single top, top pair production and QCD background processes (for details on the uncertainties and the background contributions see [81]). No significant deviation from the SM predictions is observed. Thus, exclusion limits are derived on the SUSY parameters. The acceptance for the signal $\mathcal{A}^{\text{SR}_i}$ in each signal region $i = A - D$ is shown in Figure B.4. The formula

$$N_{\text{signal}}^{\text{SR}_i} = \sum_{\text{subprocess: } \tilde{q}\tilde{q},\tilde{q}\bar{\tilde{q}},\tilde{g}\tilde{g},\tilde{q}\tilde{g}} \mathcal{A}_{\text{subprocess}}^{\text{SR}_i} \times \sigma_{\text{subprocess}}^{\text{NLO}} \times \mathcal{L}_{int}$$

is used to estimate the number of signal events $N_{\text{signal}}^{\text{SR}_i}$ expected in each signal region in the $M_{squark} - M_{gluino}$ plane.

Exclusion Limits

Exclusion limits on the number of signal events in the signal regions are calculated with the CL_s method, using the profile likelihood ratio as test-statistic in pseudo-experiments. The limit setting is implemented using the RooStats [172] software, which is part of the RooFit package. Using the observed number of events, the SM background expectation, and the attributed uncertainties, as well as the predictions for the signal cross section, and experimental uncertainties on the expected number of events from signal processes, a one-sided upper limit on the signal contribution is determined. The limit is derived interpolating the equivalent gaussian Z significance [173], which is given by the distance from 0 in a normalised Gaussian distribution for a given p-value. Model configurations which lead to $Z > 1.645$, which corresponds to a p-value of 0.05, are excluded. This procedure yields 95% confidence exclusion limits. The method is explained in detail elsewhere [174].

A simplified ansatz, which does not take into account the full systematic uncertainties, has been used to cross check the official ATLAS results. The exclusion limits are based on the official numbers published for the signal regions. The systematic uncertainties on the background prediction in the signal regions (see Table B.2) are taken into account, and the jet energy scale uncertainty has been determined for the signal for each of the mass combinations in the signal grid. The jet energy resolution is not taken into account for the signal processes. For the uncertainty on the signal cross section prediction a global relative uncertainty of 15% is assumed, by contrast to the official ATLAS results, which are based on the uncertainty obtained from PROSPINO. The luminosity uncertainty is treated with a relative uncertainty of 11%, attributed to the signal and background predicitions. The observed limits, obtained with this simplified method in three of the four signal regions, are shown in Figure B.6, and can be compared to the published limits in each signal region [175]. The results show a good agreement with the published observed exclusion limits in the signal regions A and C. Significant deviations are observed in signal region B, where the effect of the simplified uncertainty treatment changes the contour of the limit in some regions. In signal region D no limit could be derived with the simplified ansatz. The simplified treatment of the systematics does not permit the calculation of a limit in this region, due to the small numbers involved from the background and signal expectation. A strong influence of the systematic treatment on the exclusion limits is expected in the signal regions B and D. The simplified ansatz does also not reproduce the full features of the official ATLAS limits, *i.e.* in the regions where LEP and the TeVatron already put strong constraints.

Conclusion

A search for SUSY in the first data available at the LHC in channels with high P_T jets, large missing transverse energy and zero leptons has shown no deviation from the expectations of the SM model in the considered signal regions. Equal masses of squarks and gluinos up to 870 GeV are excluded by the observation at 95% CL. A cross check of the ATLAS results, taking not the full systematic uncertainties into account, shows a good agreement in the signal regions A and C with large statistics. In the

signal regions B and D with a low SM expectation and low signal expectation a more thorough treatment of the systematics is needed, as applied by the ATLAS experiment for the published results. The results of this analysis show that the limit contour depends especially in these signal regions on the correct treatment of all systematic uncertainties. For signal region B the largest deviations from the ATLAS limits are visible for low squark masses. The extremely low statistic in signal region D allows the calculation of exclusion limits, only if the systematic uncertainties are fully considered.

The LHC is now quickly accumulating more integrated luminosity, and there will be soon updates for all the SUSY searches. The much increased integrated luminosity will allow tests of SUSY models at higher masses, where SUSY may reside, waiting for its discovery.

	Signal Regions			
	A	B	C	D
N_{jets}	≥ 2	≥ 2	≥ 3	≥ 3
$P_T^{\text{leading jet}}$ [GeV]	> 120			
$P_T^{\text{leading jet}}$ [GeV]	> 40			
E_T^{miss} [GeV]	> 100			
$\Delta\phi(\text{jet}, \vec{P}_T^{\text{miss}})_{\text{min}}$	> 0.4			
$E_T^{\text{miss}}/m_{\text{eff}}$	> 0.3	–	> 0.25	> 0.25
m_{eff} [GeV]	> 500	–	> 500	> 1000
m_{T2} [GeV]	–	> 300	–	–

Table B.1: Selection criteria for the non-exclusive signal regions $A - D$ [81].

Signal Region	Data ($\mathcal{L}_{int} = 35$ pb^{-1})	Total SM Expectation
A	87	$118 \pm 25[\text{u}]\ ^{+32}_{-23}[\text{j}] \pm 12[\mathcal{L}]$
B	11	$10.0 \pm 4.3[\text{u}]\ ^{+4.0}_{-1.9}[\text{j}] \pm 1.0[\mathcal{L}]$
C	66	$88 \pm 18[\text{u}]\ ^{+26}_{-18}[\text{j}] \pm 9[\mathcal{L}]$
D	2	$2.5 \pm 1.0[\text{u}]\ ^{+1.0}_{-0.4}[\text{j}] \pm 0.2[\mathcal{L}]$

Table B.2: Event yields from SM predictions and from $\mathcal{L}_{int} = 35$ pb^{-1} of first data (collected in 2010) in the signal regions $A - D$. The SM prediction is dominated in all signal regions by $W+jets$ and $Z+jets$ production, with additional smaller contributions from single top and top pair production, and QCD processes. The uncertainty on the SM prediction contains uncertainties due to Monte Carlo statistics, data statistics in control regions, and other sources of uncorrelated systematic uncertainties, as well as the jet energy resolution and lepton efficiencies [u], the uncertainty on the jet energy scale [j], and the uncertainty on the integrated luminosity [$\mathcal{L}$] [81].

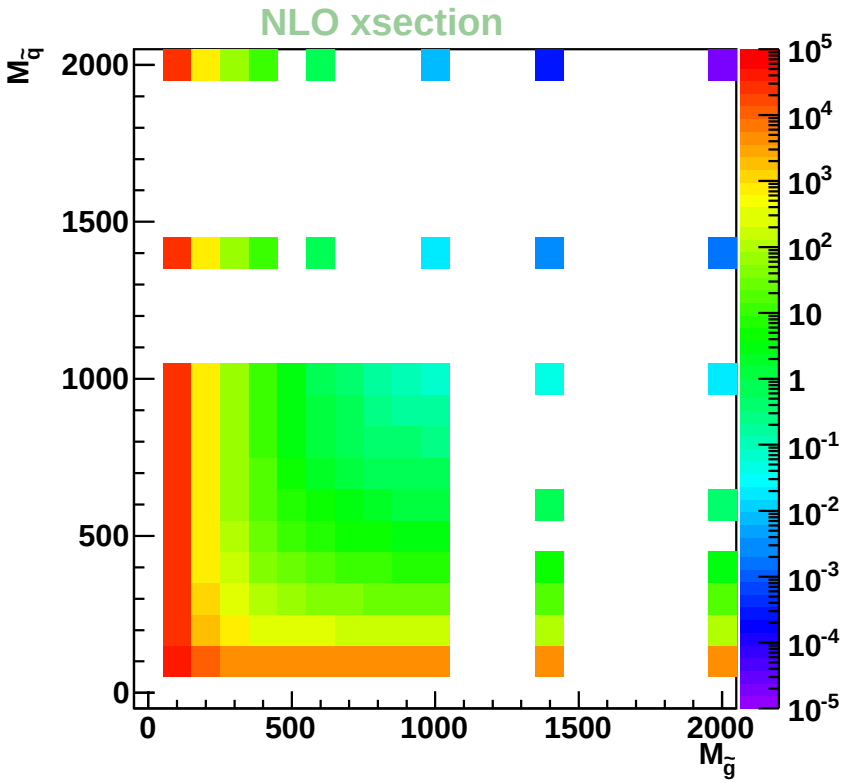

Figure B.1: Total NLO cross section in pb^{-1} in the $M_{squark} - M_{gluino}$ plane, for squark and gluino production at the LHC at a centre-of-mass energy of $\sqrt{s} = 7$ TeV, calculated with PROSPINO v2.1 [170]

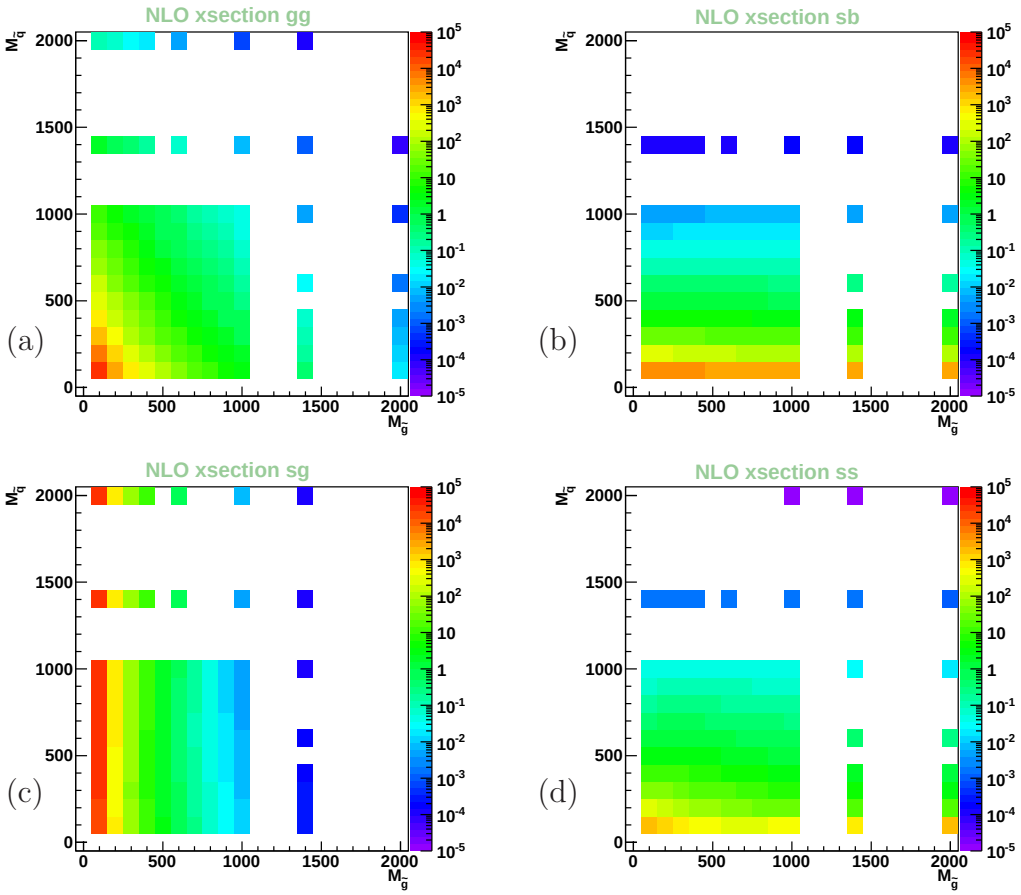

Figure B.2: NLO cross sections in pb^{-1} for the subprocesses (a) gluino-gluino, (b) squark-antisquark, (c) squark-gluino, and (d) squark-squark production in the $M_{squark} - M_{gluino}$ plane, which contribute to the total cross section, for squark and gluino production at the LHC at a centre-of-mass energy of $\sqrt{s} = 7$ TeV, calculated with PROSPINO v2.1 [170].

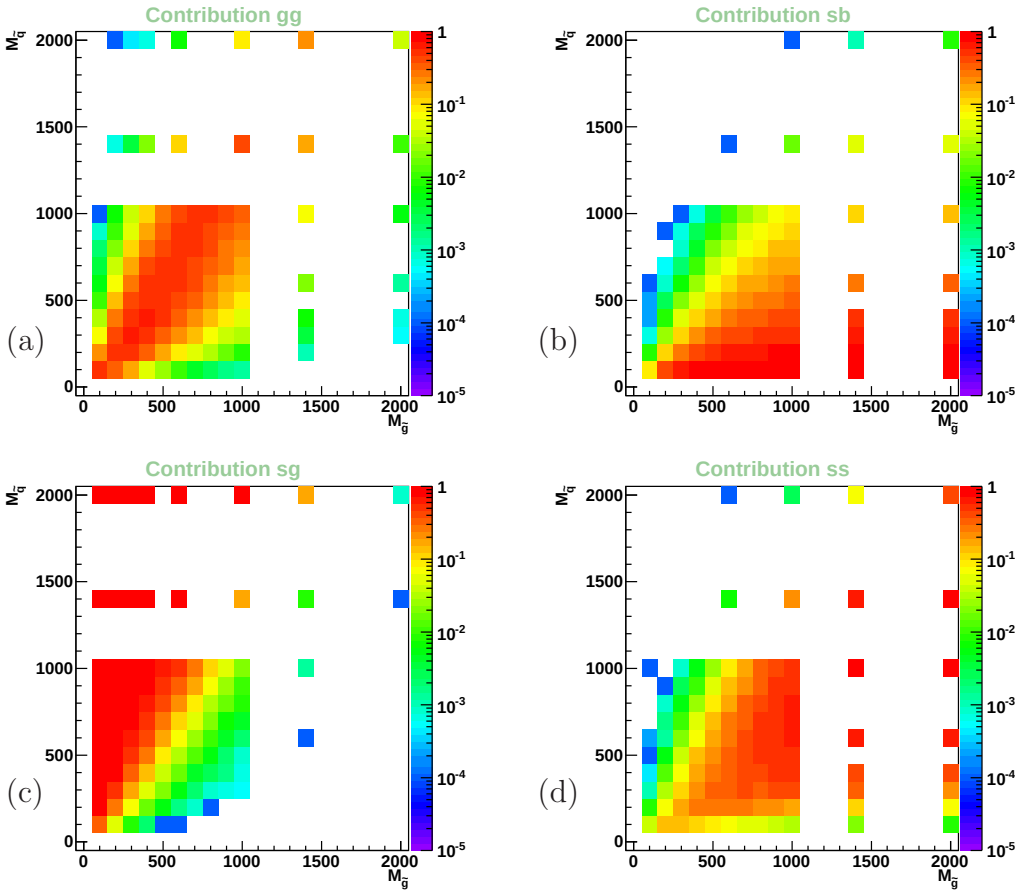

Figure B.3: Relative contribution of subprocesses (a) gluino-gluino, (b) squark-antisquark, (c) squark-gluino, and (d) squark-squark production to the total NLO cross section in the $M_{squark} - M_{gluino}$ plane.

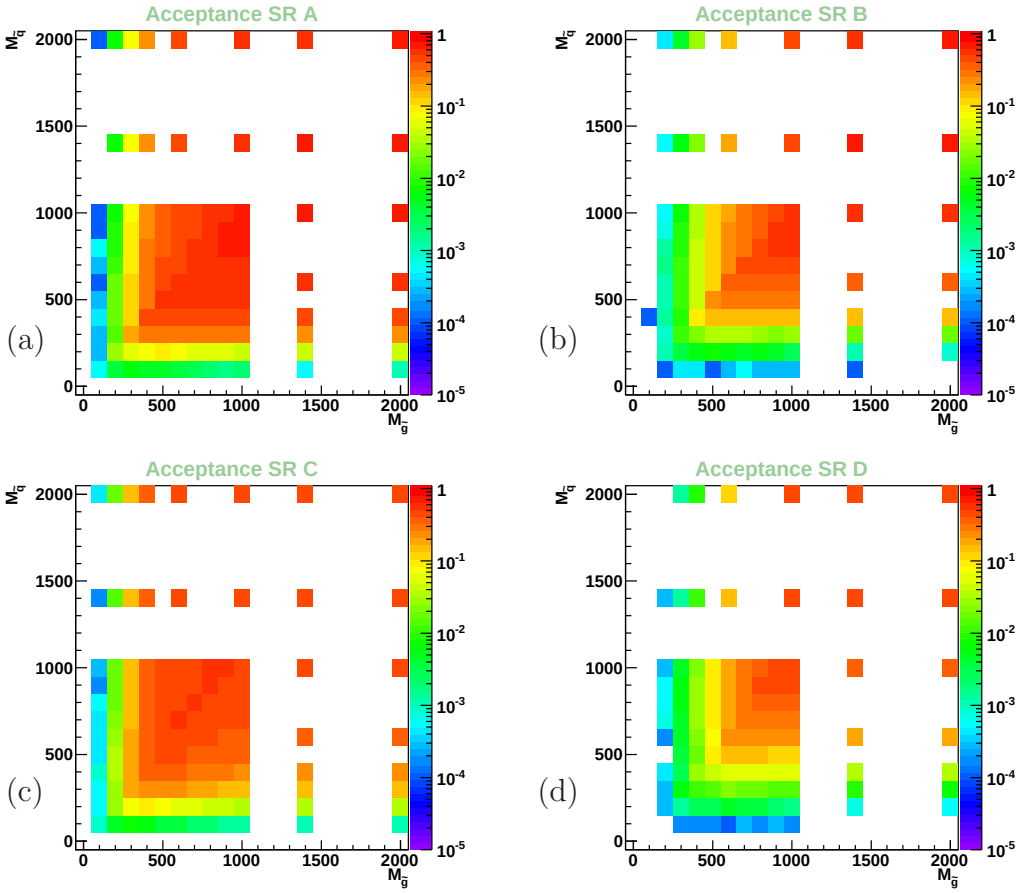

Figure B.4: Acceptance for SUSY signal events in the four signal regions (a) A, (b) B, (c) C, and (d) D in the $M_{squark} - M_{gluino}$ plane, determined from 10000 generated events at each mass combination using HERWIG++, passed through a full ATLAS detector simulation. The contributions of the subprocesses are weighted by their relative contribution to the total cross section.

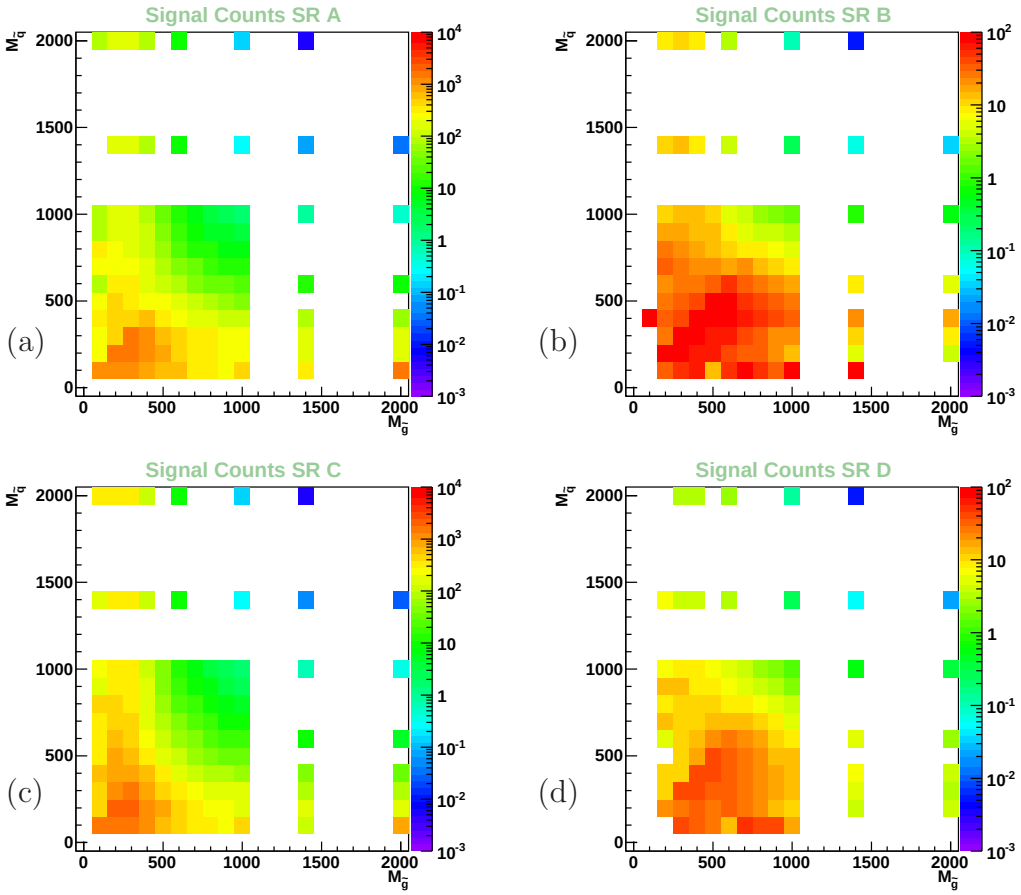

Figure B.5: Expected Signal Count for SUSY signal events in the four signal regions (a) A, (b) B, (c) C, and (d) D in the $M_{squark} - M_{gluino}$ plane in $\mathcal{L}_{int} = 35$ pb^{-1}.

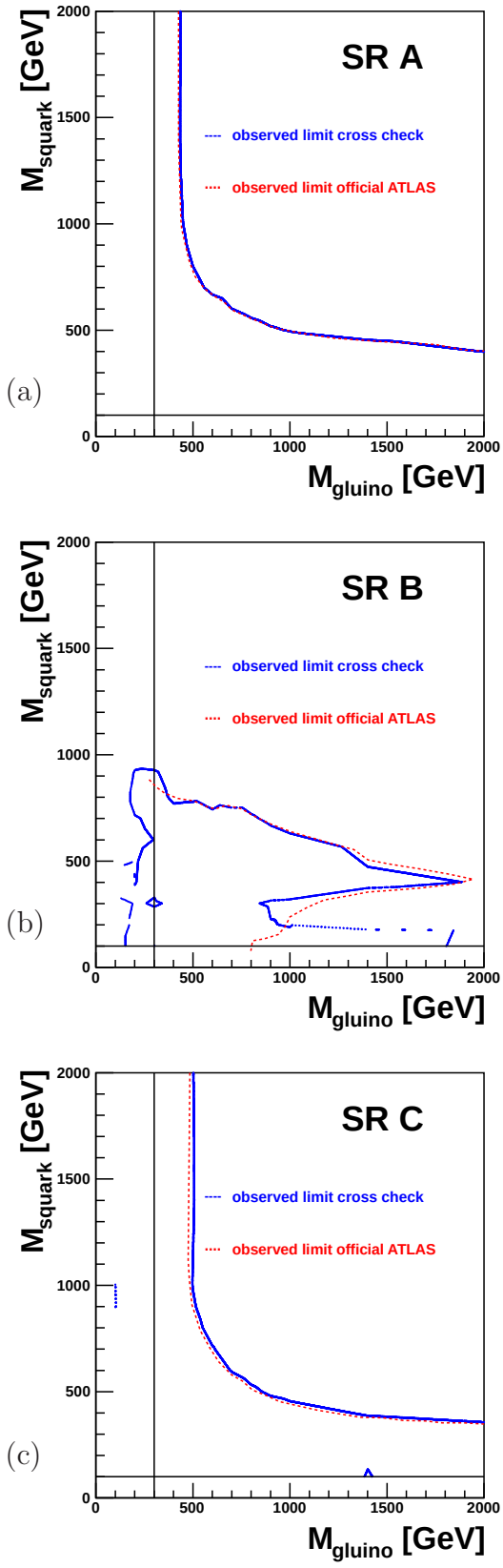

Figure B.6: Observed limits in three of the four signal regions (a) A, (b) B, and (c) C in the $M_{squark} - M_{gluino}$ plane. The limits can be compared, as a cross check, to the official ATLAS results in the different signal regions [175]. Only a part of the ATLAS limits is shown in the plot. The vertical line sketches the exclusion limit from TeVatron experiments, and the horizontal line sketches the limit from the LEP experiments.

Bibliography

[1] F. D. Aaron *et al.* [H1 Collab.], "Search for Squarks in R-Parity violating Supersymmetry in ep Collisions at HERA", Eur. Phys. J. **C71** (2010) 1572, arXiv:1011.6359.

[2] O. Nachtmann, "Phänomene und Konzepte der Elementarteilchenphysik", Vieweg Verlag, Braunschweig, 1986.

[3] D. W. Perkins, "Hochenergiephysik", Addison Wesley, 1991.

[4] M. Gell-Mann and Y. Ne'eman, "The Eightfold Way", New York, W.A. Benjamin (1964).

[5] S. L. Glashow, "Partial Symmetries of Weak Interactions", Nucl. Phys. **22** (1961) 579; A. Salam and J. C. Ward, "On a Gauge Theory of Elementary Interactions", Nuovo Cimento **19** (1961) 166; A. Salam and J. C. Ward, "Electromagnetic and weak interactions", Phys. Lett. **13** (1964) 168; A. Salam and J. C. Ward, "Gauge Theory of Elementary Interactions", Phys. Rev. **B136** (1964) 763; S. Weinberg, "A Model of Leptons", Phys. Rev. Lett. **19** (1967) 1264; S. Weinberg, "Effects of a Neutral Intermediate Boson in Semileptonic Processes", Phys. Rev. **D5** (1972) 1412. A. Salam, "Weak and Electromagnetic Interactions" Proceedings of the 8^{th} Symposium, Lerum, Sweden, (1968) 367.

[6] K. Nakamura *et al.* (Particle Data Group), "The Review of Particle Physics", J. Phys. **G37** 075021 (2010) and 2011 partial update for the 2012 edition.

[7] C. S. Wu, E. Amber, R. W. Hayward, D. D. Hoppes and R. P. Hudson, "Experimental Test of Parity Conservation in Beta Decay", Phys. Rev. **105** (1957) 1413.

[8] N. Cabibbo, "Unitary Symmetry and Leptonic Decays", Phys. Rev. Lett. **10** (1963) 531; M. Kobayashi, T. Maskawa, "CP-Violation in the Renormalizable Theory of Weak Interaction", Prog. Theor. Phys. **49** (1973) 652.

[9] Z. Maki, M. Nakagawa and S. Sakata, "Remarks on the Unified Model of Elementary Particles", Prog. Theor. Phys. **28** (1962) 870; B. Pontecorvo, "Neutrino Experiments and the Problem of Conservation of Leptonic Charge", Sov. Phys. JETP **26** (1968) 984 [Zh. Eksp. Teor. Fiz. **53** (1967) 1717].

[10] D. I. Kazakov, "Beyond the Standard Model (In Search of Supersymmetry)", (2000), [hep-ph/0012288v2].

[11] P. W. Higgs, "Broken Symmetries and the Masses of Gauge Bosons" Phys. Rev. Lett. **13** (1964) 508.

[12] G. Abbiendi *et al.* [ALEPH, DELPHI, L3 and OPAL Collaboration], "Search for the Standard Model Higgs Boson at LEP", Phys. Lett. **B565** (2003) 61, [hep-ex/0306033v1].

[13] `http://lepewwg.web.cern.ch/LEPEWWG/` .

[14] `http://tevnphwg.fnal.gov/` .

[15] The CDF, D0 Collaborations, and the TeVatron New Phenomena, Higgs Working Group, "Combined CDF and D0 Upper Limits on Standard Model Higgs Boson Production with up to 8.6 fb^{-1} of Data", FERMILAB-CONF-11-354-E (2011) arXiv:1107.5518v1.

[16] The ATLAS Collaboration, "Update of the Combination of Higgs Boson Searches in 1.0 to 2.3 fb^{-1} of pp Collisions Data Taken at $\sqrt{s} = 7$ TeV with the ATLAS Experiment at the LHC", ATLAS-CONF-2011-135 (2011), available at `http://cdsweb.cern.ch` .

[17] The CMS Collaboration, "Combination of Higgs Searches", CMS-PAS-HIG-11-022 (2011), available at `http://cdsweb.cern.ch` .

[18] `http://lepewwg.web.cern.ch/LEPEWWG/plots/summer2011/` .

[19] R. Devenish, A. Cooper-Sarkar, "Deep Inelastic Scattering", Oxford University Press, 2004.

[20] R. Feynman, "Photon-Hadron Interactions", Benjamin, New York, (1972).

[21] A. Arbuzov, D. Bardin, J. Blümlein, L. Kalinovskaya, T. Riemann, "HECTOR 1.00, A Program for the Calculation of QED, QCD and Electroweak Corrections to ep and $\ell^{\pm}N$ Deep Inelastic Neutral Scattering and Charged Current Scattering", Comput. Phys. Commun. **94** (1996) 128 [hep-ph/9511434].

[22] C. Adloff *et al.* [H1 Collaboration], "Measurement and QCD Analysis of Neutral and Charged Current Cross Sections at HERA," Eur. Phys. J. **C30** (2003) 1 [hep-ex/0304003].

[23] A. Aktas *et al.* [H1 Collab.], "First Measurement of Charged Current Cross Sections at HERA with Longitudinally Polarised Positrons", Phys. Lett. **B634** (2006) 173, [hep-ex/0512060].

[24] F. D. Aaron *et al.* [H1 and ZEUS Collab.], "Combined Measurement and QCD Analysis of the Inclusive ep Scattering Cross Sections at HERA", JHEP01 (2010) 109, arXiv:0911.0884.

[25] U. Amaldi, W. de Boer and H. Fürstenau, "Comparison of Grand Unified Theories with Electroweak and Strong Coupling Constants Measured at LEP", Phys. Lett. **B260** (1991) 447.

[26] J. Wess and B. Zumino, "Supergauge Transformations in Four-Dimensions", Nucl. Phys. **B70** (1974) 39.

[27] H. P. Nilles, "Supersymmetry, Supergravity and Particle Physics", Phys. Rept. **110** (1984) 1;
H. E. Haber and G. L. Kane, "The Search for Supersymmetry: Probing Physics Beyond the Standard Model", Phys. Rept. **117** (1985) 75.

[28] S. P. Martin, "A Supersymmetry Primer", (1997), [hep-ph/9709356v5].

[29] M. Drees and M. M. Nojiri, "Radiative Symmetry Breaking in minimal N= 1 Supergravity with Large Yukawa Couplings", Nucl. Phys. **B369** (1992) 54; H. Baer and X. Tata, "Aspects of Radiative Electroweak Breaking in Supergravity Models", Phys. Rev. **D47** (1993) 2739; G. L. Kane, C. Kolda, L. Roszkowski and J. D. Wells, "Study of Constrained Supersymmetry", Phys. Rev. **D49** (1994) 6173.

[30] J. F. Gunion, H. E. Haber, "Higgs Boson in Supersymmetric Models (I)", Nucl. Phys. **B272** (1986) 1.

[31] A. Heister *et al.* [ALEPH Collaboration], "Search for Supersymmetric Particles with R-Parity Violating Decays in e+e- Collisions at $\sqrt{s}$ up to 209GeV", Eur. Phys. J. **C31** (2003) 1 [hep-ex/0210014]; A. Heister *et al.* [ALEPH Collaboration], "Search for R-Parity Violating Production of Single Sneutrinos in e+e- Collisions at $\sqrt{s} = 189 - 209$ GeV", Eur. Phys. J. **C25** (2002) 1 [hep-ex/0201013]; P. Abreu *et al.* [DELPHI Collaboration], "Search for Spontaneous R-Parity Violation at $\sqrt{s} = 183$ GeV and 189 GeV", Phys. Lett. **B502** (2001) 24 [hep-ex/0102045]; P. Abreu *et al.* [DELPHI Collaboration], "Search for R-Parity Violation with a Ubar Dbar Dbar Coupling at $\sqrt{s} = 189$ GeV", Phys. Lett. **B500** (2001) 22 [hep-ex/0103015]; P. Abreu *et al.* [DELPHI Collaboration], "Search for SUSY with R-Parity Violating $LL\bar{E}$ Couplings at $\sqrt{s} = 189$ GeV", Phys. Lett. **B487** (2000) 36 [hep-ex/0103006]; P. Achard *et al.* [L3 Collaboration], "Search for R-Parity Violating Decays of Supersymmetric Particles in e+e- Collisions at LEP", Phys. Lett. **B524** (2002) 65 [hep-ex/0110057]; G. Abbiendi *et al.* [OPAL Collaboration], "Search for R-Parity Violating Decays of Scalar Fermions at LEP", Eur. Phys. J. **C33** (2004) 194 [hep-ex/0310054]; G. Abbiendi *et al.* [OPAL Collaboration], "Searches for R-Parity Violating Decays of Gauginos at 183 GeV at LEP", Eur. Phys. J. **C11** (1999) 619 [hep-ex/9901037].

[32] S. Katsanevas and P. Morawitz, "SUSYGEN 2.2 - A Monte Carlo Event Generator for MSSM Sparticle Production at e^+e^- Colliders", Comput. Phys. Commun. **112** (1998) 227 [hep-ph/9711417];
N. Ghodbane, S. Katsanevas, P. Morawitz and E. Perez, "SUSYGEN 3 an Event Generator for Linear Colliders", [hep-ph/9909499].

[33] A. Heister *et al.* [ALEPH Collaboration], "Absolute Mass Lower Limit for the Lightest Neutralino of the MSSM from e^+e^- data at $\sqrt{s}$ up to 209 GeV", Phys. Lett. **B583** (2004) 247.

[34] J. Haller, "Search for Squark Production in R-Parity Violating Supersymmetry at HERA", Ph.D. thesis, University of Heidelberg, (2003), DESY-THESIS-2003-035,
available at `http://www-h1.desy.de/publications/theses_list.html`.

[35] R. Barbier *et al.*, "R-Parity-Violating Supersymmetry", Phys. Rept. **420** (2005) 1.

[36] J. Butterworth and H. Dreiner, "R-Parity Violation at HERA", Nucl. Phys. **B397** (1993) 3, [hep-ph/9211204].

[37] S. Raychaudhuri, "Trilinear R-Parity Violation: Theory to Experiment", IITK-PHY-99-51 (1999), arXiv:hep-ph/9905576v1.

[38] H. K. Dreiner, C. Luhn, H. Murayama, M. Thormeier, "Baryon Triality and Neutrino Masses from an Anomalous Flavor $U(1)$", Nucl. Phys. **B774** (2007) 127, arXiv:hep-ph/0610026.

[39] J. C. Romão, "Supersymmetric Theories with R-Parity Violation", (1998) [hep-ph/9811454].

[40] E. Perez, "Recherche Particules Supersymetriques dans l'Experience H1" Ph.D. thesis, Université de Paris VI, (1996),
available at `http://www-h1.desy.de/publications/theses_list.html`.

[41] A. Djouadi, Y. Mambrini, "Three-body Decays of SUSY Particles", Phys. Lett. **B493** (2000) 120.

[42] W. Buchmüller, R. Rückl and D. Wyler, "Leptoquarks in Lepton-Quark Collisions," Phys. Lett. **B191** (1987) 442 and Phys. Lett. **B448** (1999) 320.

[43] G. Abbiendi *et al.* [OPAL Collaboration], "Search for Single Leptoquark and Squark Production in Electron-Photon Scattering at $\sqrt{s_{ee}} = 189$ GeV at LEP", Eur. Phys. J. **C23** (2001) 1 [hep-ex/0106031].

[44] T. Plehn, H. Spiesberger, M. Spira and P. M. Zerwas, "Formation and Decay of Scalar Leptoquarks/Squarks in ep Collisions," Z. Phys. **C74** (1997) 611 [hep-ph/9703433].

[45] H. Dreiner, P. Morawitz, "Signals for Supersymmetry at HERA", Nucl. Phys. **B428** (1994) 31.

[46] H. Dreiner, S. Lola, P. Morawitz, "Chargino Pair Production at LEP2 with Broken R-Parity: 4-jet Final States", Phys. Lett. **B389** (1996) 62.

[47] R. N. Mohapatra, Phys. Rev. **D34** (1986) 3457; J. D. Vergados, Phys. Lett. **B184** (1987) 55; M. Hirsch, H. V. Klapdor-Kleingrothaus and S. G. Kovalenko, Phys. Lett. **B352** (1995) 1 [hep-ph/9502315]; M. Hirsch, H. V. Klapdor-Kleingrothaus and S. G. Kovalenko, Phys. Rev. Lett. **75** (1995) 17; M. Hirsch, H. V. Klapdor-Kleingrothaus and S. G. Kovalenko, "Supersymmetry and Neutrinoless Double Beta Decay", Phys. Rev. **D53** (1996) 1329 [hep-ph/9502385].

[48] V. Barger, G. F. Giudice and T. Han, "Some New Aspects of Supersymmetry R-Parity Violating Interactions", Phys. Rev. **D40** (1989) 2987.

[49] P. Langacker, "Parity Violation in Muonic Atoms and Cesium", Phys. Lett. **B256** (1991) 277.

[50] T. Ahmed *et al.* [H1 Collaboration], "A Search for Leptoquarks and Squarks at HERA", Z. Phys. **C64** (1994) 545.

[51] S. Aid *et al.* [H1 Collaboration], "A Search of Squarks of R_p-Violating SUSY at HERA", Z. Phys. **C71** (1996) 211, [hep-ex/9604006v2].

[52] C. Adloff *et al.* [H1 Collaboration], "Searches at HERA for Squarks in R-parity Violating Supersymmetry", Eur. Phys. J. **C20** (2001) 639, [hep-ex/0102050].

[53] A. Aktas *et al.* [H1 Collaboration], "Search for Squark Production in R-Parity Violating Supersymmetry at HERA," Eur. Phys. J. **C36** (2004) 425 [hep-ex/0403027].

[54] H. Abramowicz, A. Caldwell, "HERA Collider Physics", Rev. Mod. Phys. **71** (1999) 1275 [hep-ex/9903037v1].

[55] F. D. Aaron *et al.* [H1 Collab.], "Measurement of the Inclusive $e^{\pm}p$ Scattering Cross Section at High Inelasticity y and of the Structure Function F_L", Eur. Phys. J. **C71** (2011) 1579, arXiv:1012.4355.

[56] F. D. Aaron *et al.* [H1 Collab.], "Jet Production in ep Collisions at Low Q^2 and Determination of α_s", Eur. Phys. J. **C67** (2010) 1, arXiv:0911.5678.

[57] F. D. Aaron *et al.* [H1 Collab.], "Inelastic Production of J/ψ Mesons in Photoproduction and Deep Inelastic Scattering at HERA", Eur. Phys. J. **C68** (2010) 401, arXiv:1002.0234.

[58] F. D. Aaron *et al.* [H1 Collab.], "Measurement of the Charm and Beauty Structure Functions using the H1 Vertex Detector at HERA", Eur. Phys. J. **C65** (2010) 89, arXiv:0907.2643.

[59] F. D. Aaron *et al.* [H1 Collab.], "Measurement $D*^{\pm}$ Meson Production and Determination of $F_2^c c$ at low Q^2 in Deep-Inealstic Scattering at HERA", submitted to Eur. Phys. J. **C** (2011), arXiv:1106-1028.

[60] F. D. Aaron *et al.* [H1 Collab.], "General Search for New Phenomena at HERA", Phys. Lett. **B 674** (2009), arXiv:0901.0507.

[61] F. D. Aaron *et al.* [H1 Collab.], "Search for First Generation Leptoquarks in *ep* Collisions at HERA", submitted to Phys. Lett. **B** (2011), arXiv:1107.3716.

[62] F. D. Aaron *et al.* [H1 Collab.], "Search for Lepton Flavour Violation at HERA", accepted by Phys. Lett. **B** (2011), arXiv:1103.4938.

[63] F. D. Aaron *et al.* [H1 Collab.], "Search for Excited Quarks in ep Collisions at HERA", Phys. Lett. **B 678** (2009) 335, arXiv:0904.3392.

[64] F. D. Aaron *et al.* [H1 Collab.], "Search for Contact Interactions in $e^{\pm}p$ Collisions at HERA", submitted to Phys. Lett. **B** (2011), arXiv:1107.2478.

[65] F. D. Aaron *et al.* [H1 Collab.], "Search for Single Top Quark Production at HERA", Phys. Lett. **B 678** (2009) 450, arXiv:0904.3876.

[66] F. D. Aaron *et al.* [H1 and ZEUS Collab.], "Events with an Isolated Lepton and Missing Transverse Momentum and Measurement of W Production at HERA", JHEP03 (2010) 035, arXiv:0911.0858.

[67] C. Adloff *et al.* [H1 Collaboration], "Observation of Events at Very High Q^2 in *ep* Collisions at HERA", Z. Phys. **C74** (1997) 191, [arXiv:9702012].

[68] H. K. Dreiner, P. Morawitz, "High Q^2 Anomaly at HERA and Supersymmetry", Nucl. Phys. **B503** (1997) 55, [hep-ph/9703279].

[69] D. E. Acosta, S. K. Blessing, "Leptoquark Searches at HERA and the TeVatron", An. Rev. Nucl. Part. Sci. **49** (1999) 389.

[70] S. Y. Choi, J. Kalinowski, H.-U. Martyn, R. Rückl, H. Spiesberger, P. M. Zerwas, "Isolated Lepton Events at HERA: SUSY R-Parity Violation?", Eur. Phys. J. **C51** (2007) 543, arXiv:0612302v2.

[71] J. Breitweg *et al.* [ZEUS Collaboration], "Search for Selectron and Squark Production in $e^{+}p$ Collisions at HERA", Phys. Lett. **B434** (1998) 214.

[72] S. Chekanov *et al.* [ZEUS Collaboration], "Search for Stop Production in R-Parity-Violating Supersymmetry at HERA", Eur. Phys. J. **C50** (2007) 269.

[73] ALEPH, DELPHI, L3, OPAL Collaborations, "Combined LEP Stop and Sbottom Results 183 – 208 GeV", `http://lepsusy.web.cern.ch/lepsusy/www/squarks_summer04/stop_combi_208_final.html`.

[74] ALEPH, DELPHI, L3, OPAL Collaborations, "Combined LEP Selectron/ Smuon/ Stau Results, 183 – 208 GeV", `http://lepsusy.web.cern.ch/lepsusy/www/sleptons_summer04/slep_final.html` .

[75] M. Acciarri *et al.* [L3 Collaboration], "Search for R-Parity Violating Decays of Supersymmetric Particles in e+e- Collisions at $\sqrt{s} = 189$ GeV," Eur. Phys. J. **C19** (2001) 397 [hep-ex/0011087].

[76] V. Abazov, *et al.* [D0 Collaboration], "Search for Squarks and Gluinos in Events with Jets and Missing Transverse Energy using 2.1 fb^{-1} of $p\bar{p}$ Collision Data at $\sqrt{s} = 1.96$ TeV", Phys. Lett. **B660** (2007) 449, arXiv:0712.3805v2.

[77] D. Acosta *et al.* [CDF Collaboration], "Search for Pair Production of Scalar Top Quarks in R-Parity Violating Decay Modes in $p\bar{p}$ Collisions at $\sqrt{s} = 1.8$ TeV," Phys. Rev. Lett. **92** (2004) 051803 [hep-ex/0305010]; F. Abe *et al.* [CDF Collaboration], "Search for R-Parity Violating Supersymmetry using Like-Sign Dielectrons in $p\bar{p}$ Collisions at $\sqrt{s} = 1.8$ TeV," Phys. Rev. Lett. **83** (1999) 2133 [hep-ex/9908063]; V. M. Abazov *et al.* [D0 Collaboration], "Search for the Production of Single Sleptons through R-Parity Violation in $p\bar{p}$ Collisions at $\sqrt{s} = 1.8$ TeV," Phys. Rev. Lett. **89** (2002) 261801 [hep-ex/0207100]; V. M. Abazov *et al.* [D0 Collaboration], "Search for R-Parity Violating Supersymmetry in Dimuon and Four-Jets Channel," Phys. Rev. Lett. **89** (2002) 171801 [hep-ex/0111053]; B. Abbott *et al.* [D0 Collaboration], "Search for R-Parity Violation in Multilepton Final States in $p\bar{p}$ Collisions at sqrts=1.8 TeV," Phys. Rev. **D62** (2000) 071701 [hep-ex/0005034].

[78] B. Abbott *et al.* [D0 Collaboration], "Search for R-Parity Violating Supersymmetry in the Dielectron Channel," Phys. Rev. Lett. **83** (1999) 4476 [hep-ex/9907019].

[79] C. Autermann, "Resonant Second Generation Slepton Production at the TeVatron", Ph.D. thesis, RWTH Aachen, (2006), available at `http://www-d0.fnal.gov/results/publications_talks/thesis/`.

[80] D. Kaefer, "Search for R-Parity Violating Supersymmetry in Multilepton Final States with the D0 Detector", Ph.D. thesis, RWTH Aachen, (2006), available at `http://www-d0.fnal.gov/results/publications_talks/thesis/`.

[81] The ATLAS Collaboration, "Search for Squarks and Gluinos using Final States with Jets and Missing Transverse Momentum with the ATLAS Detector in $\sqrt{s} = 7$ TeV Proton-Proton Collisions", Phys. Lett. **B701** (2011) 186, arXiv:1102.5290v1.

[82] The ATLAS Collaboration, "Search for Supersymmetry using Final States with One Lepton, Jets, and Missing Transverse Momentum with the ATLAS Detector in $\sqrt{s} =$ 7 TeV pp", submitted to Phys. Rev. Lett. (2011) arXiv:1102.2357v2.

[83] The ATLAS Collaboration, "Search for Stable Hadronising Squarks and Gluinos with the ATLAS Experiment at the LHC", submitted to Phys. Lett. **B** (2011) arXiv:1103.1984v1.

[84] The ATLAS Collaboration, "Search for Supersymmetric Particles in Events with Lepton Pairs and Large Missing Transverse Momentum in $\sqrt{s} = 7$ TeV Proton-Proton Collisions with the ATLAS Experiment", submitted to Eur. Phys. J. **C** (2011) arXiv:1103.6214v1.

[85] The ATLAS Collaboration, "Search for an Excess of Events with an Identical Flavor Lepton Pair and Significant Missing Transverse Momentum in $\sqrt{s} = 7$ TeV Proton-Proton Collisions with the ATLAS Detector", submitted to Eur. Phys. J. **C** (2011) arXiv:1103.6208v1.

[86] The ATLAS Collaboration, "Search for a Heavy Particle Decaying into an Electron and a Muon with the ATLAS Detector in $\sqrt{s} = 7$ TeV pp Collisions at the LHC", submitted to Phys. Rev. Lett. (2011) arXiv:1103.5559v1.

[87] D. E. Morissey, T. Plehn, T. M. P. Tait, "Physics Searches at the LHC", (2009) arXiv:0912.3259v2.

[88] H. K. Dreiner, G. G. Ross, "R-Parity Violation at Hadron Colliders", Nucl. Phys. **B 365** (1991) 597; J. Blumlein, E. Boos, A. Kryukov, "Leptoquark Pair Production in Hadronic Interactions", Z. Phys. **C 76** (1997) 137 [hep-ph/9610408]; M. Krämer, T. Plehn, M. Spira, P. M. Zerwas, "Pair Production of Scalar Leptoquarks at the Tevatron", Phys. Rev. Lett. **79** (1997) 341 [hep-ph/9704322]; M. Krämer, T. Plehn, M. Spira, P. M. Zerwas, "Pair Production of Scalar Leptoquarks at the LHC", Phys. Rev. **D 71** (2005) 057503 [hep- ph/0411038].

[89] The ATLAS Collaboration, "Search for Pair Production of First or Second Generation Leptoquarks in Proton-Proton Collisions at $\sqrt{s} = 7$ TeV using the ATLAS Detector at the LHC", submitted to Phys. Rev. **D** (2011) arXiv:1104.4481v2.

[90] U. Schneekloth (editor), "The HERA Luminosity Upgrade", DESY-HERA 98-05 (1998).

[91] A. A. Sokolov, I. M. Ternov, "On Polarization and Spin Effects in Synchrotron Radiation Theory", Sov. Phys. Dokl. **8** (1964) 1203.

[92] D. P. Barber *et al.*, "The First Achievement of Longitudinal Spin Polaritzation in a High Energy Electron Storage Ring", Phys. Letts. **B343** (1995) 436.

[93] F. Willeke, "Experiences with the HERA Lepton-Proton Collider", Proceedings of "Asian Particle Accelerator Conference 2007 (APAC07)" (2007) 843.

[94] available at `http://www-h1.desy.de/h1det/lumi/lplots/HERA_12_2007.eps`.

[95] I. Abt *et al.* [H1 Collaboration], "The H1 Detector", Nucl. Instrum. Meth. **A386** (1997) 310 and 348.

[96] H1 Collaboration, "Proposal for Tagging High Energy Photon in the H1 Detector", H1-08/96-485.

[97] B. Andrieu *et al.* [H1 Calorimeter Group Collaboration], "The H1 Liquid Argon Calorimeter System," Nucl. Instrum. Meth. **A336** (1993) 460.

[98] B. Andrieu *et al.* [H1 Calorimeter Group], "Beam Tests and Calibration of the H1 Liquid Argon Calorimeter with Electrons", Nucl. Instrum. Meth. **A350** (1994) 57;
B. Andrieu *et al.* [H1 Calorimeter Group], "Results From Pion Calibration Runs for the H1 Liquid Argon Calorimeter and Comparisons with Simulations", Nucl. Instrum. Meth. **A336** (1993) 499.

[99] R. D. Appuhn *et al.* [H1 SPACAL Group Collaboration], "The H1 Lead/Scintillating-Fibre Calorimeter," Nucl. Instrum. Meth. **A386** (1997) 397.

[100] T. Nicholls *et al.* [H1 SpaCal Group], "Performance of an Electromagnetic Lead/ Scintillating Fiber Calorimeter for the H1 Detector", Nucl. Instr. and Meth. **A374** (1996) 149.

[101] D. Pitzl *et al.*, "The H1 Silicon Vertex Detector", Nucl. Phys. **A454** (2000) 334.

[102] B. List, "The H1 Silicon Tracker", Proceedings of VERTEX2003, Nucl. Instr. and Meth. **A549** (2005) 33.

[103] M. C. Urban, "The new CIP2k z-Vertex Trigger for the H1 Experiment at HERA", Ph.D. thesis, University Zürich, (2004),
available at `http://www-h1.desy.de/publications/theses_list.html`.

[104] C. Kleinwort [H1 Collaboration], "H1 Alignment Experience," Proceedings of the Workshop "First LHC Detector Alignment Workshop", eds. S. Blusk *et al.*, CERN (2006), CERN-2007-04.

[105] C. Wissing, "Bestimmung der Charakteristika des Flugzeitsystems des H1-Detektors zur Messung des Strahluntergrundes", Diploma thesis, University Dortmund, (1998),
available at `http://www-h1.desy.de/publications/theses_list.html`.

[106] A. Beglarian, J. Dainton, M. Fleischer, C. Wissing, "Short Description of the Modifications of the H1 Time-of-Flight System in the Framework of the H1/HERA Upgrade", unpublished H1 note (1999), available at `http://www-h1.desy.de/h1det/tracker/tof/`.

[107] H. A Bethe and W. Heitler, "On the Stopping of Fast Particles and on the Creation of Positive Electrons", Proc. R. Soc. London **A146** (1934) 83.

[108] F. Sefkow *et al.*, "Experience with the First Level Trigger of H1", Proceedings of "Nucl. Science Symposium 1994", IEEE Trans. Nucl. Sci. **Vol 42** No. 4 (1995) 900.

[109] A. Schöning and H1 Collaboration, "A Fast Track Trigger for the H1 Collaboration", Nucl. Instr. and Meth. **A518** (2004) 542.

[110] A. W. Jung *et al.*, "First Results from the Third Level of the H1 Fast Track Trigger", Proceedings of "15th IEEE-NPSS Real-Time Conference 2007", **ISBN** 1-4244-0867-9 (2007) 1.

[111] V. Lendermann, J. Haller, M. Herbst, K. Krueger, H. C. Schultz-Coulon, R. Stamen, "Combining Triggers in HEP Data Analysis", Nucl. Instr. Meth. **A604** 707 (2009).

[112] H. Jung, RAPGAP version 3.1, "Hard Diffractive Scattering in High-Energy *ep* Collisions and the Monte Carlo Generation RAPGAP," Comput. Phys. Commun. **86** (1995) 147,
available at `http://www.desy.de/~jung/rapgap/`.

[113] A. Kwiatkowski, H. Spiesberger and H. J. Möhring, "Heracles: An Event Generator for *ep* Interactions at HERA Energies Including Radiative Processes: Version 1.0," Comput. Phys. Commun. **69** (1992) 155.

[114] T. Sjöstrand *et al.*, PYTHIA version 6.1,
"High-Energy-Physics Event Generation with PYTHIA 6.1," Comput. Phys. Commun. **135** (2001) 238 [hep-ph/0010017],
available at `http://home.thep.lu.se/~torbjorn/Pythia.html`.

[115] G. Ingelmann, DJANGOH version 1.4, "Django: The Interface for The Event Generators Heracles and Lepto", Proceedings of the Workshop "Physics at HERA", eds. W. Buchmüller and G. Ingelman, DESY (1991), vol. 3, p. 1366.

[116] V. N. Gribov and L. N. Lipatov, "Deep Inelastic *ep* Scattering in Perturbation Theory", Sov. J. Nucl. Phys. **15** (1972) 438;
G. Altarelli and G. Parisi, "Asymptotic Freedom in Parton Language", Nucl. Phys. **B126** (1977) 298;
Y. L. Dokshitzer, "Calculation of the Structure Functions for Deep Inelastic Scattering and e^+e^- Annihilation by Perturbation Theory in Quantum Chromodynamics", Sov. Phys. JETP **46** (1977) 641.

[117] B. Andersson, G. Gustafson, G. Ingelman and T. Sjöstrand, "Parton Fragmentation and String Dynamics", Phys. Rept. **97** (1983) 31.

[118] T. Sjöstrand, "PYTHIA 5.7 and JETSET 7.4 Physics and Manual", Lund Univ. preprint LU-TP-95-20 (August 1995) 321pp;
idem, CERN TH-7112 (1993) [hep-ph/9508391].

[119] G. A. Schuler and H. Spiesberger, DJANGOH version 1.4, "Django: The Interface for The Event Generators Heracles and Lepto", Proceedings of the Workshop "Physics at HERA", eds. W. Buchmüller and G. Ingelman, DESY (1991), vol. 3, p. 1419.

[120] G. Gustafson and U. Pettersson, "Dipole Formulation of QCD Cascades", Nucl. Phys. **B306** (1988) 746;
idem, *addendum* Lund University preprint LU-TP-87-19, (October 1987) 4;
B. Andersson, G. Gustafson, L. Lönnblad and U. Pettersson, "Coherence Effects in Deep Inelastic Scattering", Z. Phys. **C43** (1989) 621;
B. Andersson, G. Gustafson, L. Lönnblad, "Gluon Splitting in the Colour Dipole Cascades", Nucl. Phys. **B339** (1990) 393.

[121] L. Lönnblad, "ARIADNE version 4 - A Program for Simulation of QCD Cascades Implementing the Colour Dipole Model", Comput. Phys. Commun. **71** (1992) 15.

[122] I. I. Balitsky, L. N. Lipatov, "The Pomeranchuk Singularity in Quantum Chromodynamics", Sov. J. Nucl. Phys. **28** (1978) 822.

[123] H. L. Lai, "Global QCD Analysis of Parton Structure of the Nucleon: CTEQ5 Parton distributions", Eur. Phys. J. **C12** (2000) 375.

[124] `http://www.phys.psu.edu/~cteq/`.

[125] A. D. Martin, W. J. Stirling and R. G. Roberts, "New Information on Parton Distributions", Phys. Rev. **D47** (1993) 867; A. D. Martin, W. J. Stirling and R. G. Roberts, "Parton Distributions Updated", Phys. Lett. **B306** (1993) 145.

[126] `http://durpdg.dur.ac.uk/hepdata/mrs.html`.

[127] M. Glück, E. Reya, A. Vogt, "Photonic Parton Distributions", Phys. Rev. **D46** (1992) 1973.

[128] C. Adloff *et al.* [H1 Collaboration], "Measurement of Dijet Cross Sections in Photoproduction at HERA," Eur. Phys. J. **C25** (2002) 13 [hep-ex/0201006].

[129] A. Aktas *et al.* [H1 Collaboration], "A General Search for New Phenomena in *ep* Scattering at HERA," Phys. Lett. **B602** (2004) 14 [hep-ex/0408044].

[130] T. N. Trinh, "Recherche de Leptons Excités sur le Collisionneur HERA avec le Détecteur H1", Ph.D. thesis, Université de la Méditerranée Aix-Marseille II, (2008), available at `http://www-h1.desy.de/publications/theses_list.html`.

[131] U. Baur, J. A. Vermaseren and D. Zeppenfeld, "Electroweak Vector Boson Production in High-Energy *ep* Collisions", Nucl. Phys. **B375** (1992) 3.

[132] T. Abe, GRAPE-Dilepton version 1.1, "GRAPE-Dilepton (Version 1.1): A Generator for Dilepton Production in *ep* Collisions," Comput. Phys. Commun. **136** (2001) 126 [hep-ph/0012029].

[133] R. Brun *et al.*, "GEANT3", CERN-DD/EE/84-1.

[134] *private communication with Emmanuel Sauvan* .

[135] K. Rosenbauer, LEGO 0.02, "Suche nach Leptoquarks und Leptogluonen im H1-Experiment bei HERA", Ph.D. thesis, RWTH Aachen, PITHA 95/16 (1995), available at `http://www-h1.desy.de/publications/theses_list.html`.

[136] A. Djouadi, J. L. Kneur and G. Moultaka, "SUSPECT 2.1" Comput. Phys. Commun. **176** (2007) 426, [hep-ph/0211331].

[137] P. Bruel, "Recherche d'Interactions au-delà du Modèle Standard à HERA", Ph.D. Thesis, Université Paris XI (1998), available at `http://www-h1.desy.de/publications/theses_list.html`.

[138] A. Glazov, "Measurement of the Proton Structure Functions $F_2(x, Q^2)$ and $F_L(x, Q^2)$ with the H1 Detector at HERA", Ph.D. thesis, Humboldt-University Berlin (1998), available at `http://www-h1.desy.de/publications/theses_list.html`.

[139] B. Naroska, S. Schiek, G. Schmidt, "Lepton Identification in the H1 Detector at Low Momenta", H1-internal note H1-05/97-518, (1997).

[140] M. D. Sauter, "Measurement of the Beauty Photoproduction at Threshold using Di-Electron Events with the H1 Detector at HERA", Ph.D. thesis, ETH Zürich (2009), available at `http://www-h1.desy.de/publications/theses_list.html`.

[141] B. Andrieu *et al.* [H1 Collaboration], "Electron/Pion Separation with the H1 LAr Calorimeters, Nucl. Instr. Meth. **A344** 492 (1994).

[142] B. Heinemann, "Measurement of Charged Current and Neutral Current Cross Sections in Positron-Proton Collisions at $\sqrt{s} = 300$ GeV", Ph.D. thesis, University of Hamburg (1999), available at `http://www-h1.desy.de/publications/theses_list.html`.

[143] O. Henshaw, "A First Measurement of the Neutral Current Cross Section at High Q^2 in Longitudinally Polarised e^+p Scattering with the H1 Detector", Ph.D. thesis, University of Birmingham (2005),
available at `http://www-h1.desy.de/publications/theses_list.html`.

[144] M. Peez, B. Portheault, E. Sauvan, "An Energy Flow Algorithm for Hadronic Reconstruction in OO: Hadroo2", H1-internal note H1-01/05-616, (2005).

[145] S.D. Ellis and D.E. Soper, "Successive Combination Jet Algorithm For Hadron Collisions", Phys. Rev. **D48** (1993) 3160 [hep-ph/9305266].

[146] S. Catani *et al.*, "Longitudinally-Invariant k_T-Clustering Algorithms for Hadron-Hadron Collisions", Nucl. Phys. **B406** (1993) 187.

[147] U. Bassler, G. Bernardi, "On the Kinematic Reconstruction of Deep Inelastic Scattering at HERA: the Σ Method", Nucl. Instr. Meth. **A361** (1995) 197, [hep-ex/9412004v1].

[148] M. Jacquet, Z. Zhang, V. Brisson, S. Kermiche and C. Vallée, "Absolute Hadronic Jet Calibration of the H1 Liquid Argon Calorimeter", H1-internal note H1-04/99-571, (1999).

[149] R. Kogler, "Measurement of Jet Production in Deep-Inelastic *ep* Scattering at HERA", Ph.D. thesis, University of Hamburg, (2010),
available at `http://www-h1.desy.de/publications/theses_list.html`.

[150] A. Blondel and F. Jacquet, Proceedings of "The Study of an *ep* Facility for Europe", ed. U. Amaldi, DESY 79/48 (1979) 391.

[151] C. Veelken, "Search for Events with Isolated Leptons and Large Missing Transverse Momentum in ep Collisions at HERA", Ph.D. thesis, University of Liverpool, (2005),
available at `http://www-h1.desy.de/publications/theses_list.html`.

[152] C. Adloff *et al.* [H1 Collaboration], "Measurement and QCD Analysis of Neutral and Charged Current Cross Sections at HERA", Eur. Phys. J. **C30** (2003) 1 [hep-ex/0304003].

[153] R. Placakyte, "First Measurement of Charged Current Cross Sections with Longitudinally Polarized Positrons at HERA", Ph.D. thesis, University Munich, (2006),
available at `http://www-h1.desy.de/publications/theses_list.html`.

[154] A. Nikiforov, "Measurements of the Neutral Current $e^{\pm}p$ Cross Sections Using Longitudinally Polarised Lepton Beams at HERA II", Ph.D. thesis, Ludwig-Maximilians University (2007),
available at `http://www-h1.desy.de/publications/theses_list.html`.

[155] M. Peez, "Recherche de d'Éviations au Modèle Standard dans les Processus de Grande Énergie Transverse sur le Collisionneur Électron - Proton HERA", Ph.D. thesis, Université de Lyon (2003), DESY-THESIS-2003-023,
available at `http://www-h1.desy.de/publications/theses_list.html`.

[156] D. Hoffmann, "Zwei-Elektronen-Ereignisse im H1-Detektor", Ph.D. thesis, University of Hamburg (2000),
available at `http://www-h1.desy.de/publications/theses_list.html`.

[157] I. Negri, "Recherche de Fermions Excités dans l'Expérience H1 auprès du Collisionneur Positron-Proton HERA", Ph.D. thesis, Université de la Méditerranée Aix-Marseille II, (1998), CPPM-T-1998-02, DESY-THESIS-1998-022,
available at `http://www-h1.desy.de/publications/theses_list.html`.

[158] E. Chabert, C. Diaconu, S. Kermiche, I. Négri, C. Vallée, "QBGFMAR - An Updated PHAN Package for Cosmic and Halo Muon Topological Rejection in High P_T Physics Analysis", H1-internal note H1-11/98-556, (1998).

[159] C. Veelken, "H1NonepBgFinder - Rejection of Cosmic Muon and Beam-Halo Events in the H1OO Framework", H1-internal note H1-09/02-603, (2002).

[160] B. Portheault, "Première Mesure des Sections Efficaces de Courant Chargé et Neutre avec le Faisceau de Positrons Polarisé à HERA II et Analyses QCD-Électrofaibles", Ph.D. thesis, Université Paris XI (2005), LAL-05-05,
available at `http://www-h1.desy.de/publications/theses_list.html`.

[161] A. L. Read, "Modified Frequentist Analysis of Search Results (the CL_s Method)", Proceedings of "1st Workshop on Confidence Limits" at CERN, (2000) 81, CERN-OPEN-2000-205.

[162] G. Feldman, R. Cousins, "A Unified Approach to the Classical Statistical Analysis of Small Signals", Phys. Rev. **D57** (1998) 3873.

[163] A. L. Read, "Presentation of Search Results: the CL_s Technique" J. Phys. G: Nucl. Part. Phys. **28** (2002) 2693.

[164] T. Junk, "Confidence Level Computation for Combining Searches with Small Statistics," Nucl. Instrum. Meth. **A434** (1999) 435 [hep-ex/9902006].

[165] W. Kohn, "Datenanalyse und Wahrscheinlichkeitsrechnung", Springer Verlag, Berlin, Heidelberg (2005).

[166] E. L. Lehmann, "Testing Statistical Hypotheses", Springer, New York (2005).

[167] G. Zech, "Upper Limits in Experiments with Background or Measurement Errors", Nucl. Instr. Meth. **A277** (1988) 608.

[168] W. Hong-Tang *et al.*, "Probe R-parity Violating Stop Resonances at the LHeC", JHEP 1107:003 (2011) arXiv:1107.4461v1.

[169] taken from `https://www-h1.desy.de/idet/idrawings/` .

[170] W. Beenakker, R. Höpker, M. Spira, P. M. Zerwas, "Squark and Gluino Production at Hadron Colliders", Nucl. Phys. **B492** (1997) 51, [hep-ph/9610490].

[171] M. Bähr *et al.*, "HERWIG++ Physics and Manual", Eur. Phys. J. **C58** (2008) 639, arXiv:0803.0883.

[172] L. Moneta *et al.*, "The RooStats Project", ACAT2010 Conference Proceedings (2010) arXiv:1009.1003v2.

[173] *private communication with Teng Jian Khoo* .

[174] G. Cowan, K. Cranmer, E. Gross, O. Vitels, "Asymptotic Formulae for Likelihood-Based Tests of New Physics", Eur. Phys. J. **C71** 1554 (2011) arXiv:1007.1727v2.

[175] more information at
`http://atlas.web.cern.ch/Atlas/GROUPS/PHYSICS/PAPERS/susy-0lepton_01/` .

Acknowledgement

I would like to use these last pages to thank all of my friends and colleagues from which this work has profited.

An erster Stelle möchte ich meinem Doktorvater Herrn Professor Hans-Christian Schultz-Coulon meinen großen Dank aussprechen. Er hat es mir ermöglicht durch Forschungsaufenthalte am DESY aktiv in einer internationalen Kollaboration mitzuarbeiten und mich in einem spannenden, wie aktuellen Forschungsgebiet zu betätigen. Durch ihn konnte ich an Doktorandenschulen, Workshops und internationalen Konferenzen teilnehmen und meine Ergebnisse einem Fachpublikum vorstellen. Ich danke ihm dafür, dass er stets ein offenes Ohr für meine Angelegenheiten hatte und mich in schwierigen Phasen stets unterstützt und motiviert hat. Herrn Professor Ulrich Uwer möchte ich auch herzlich dafür danken, dass er sofort zugesagt hat, das Zweitgutachten für diese Arbeit zu übernehmen.

Desweiteren möchte ich Katja Krüger und Gerhard Brandt für die umfassende Betreuung während meiner Zeit am DESY danken. Meine Forschungsarbeit hat erheblich durch ihr profundes Wissen und ihre Computerkenntnisse profitiert. Ihre professionelle und freundliche Art Kritik an meinen Ergebnissen zu äußern, half mir stets meine Motivation zu bewahren. Katja danke ich auch für ihre große Hilfe beim Korrekturlesen des Manuskripts.

In diesem Zusammenhang möchte ich auch Emmanuelle Perez und Prof. Johannes Haller danken, die mir durch ihr Wissen und ihre uneingeschränkte Bereitschaft zu helfen vieles erleichtert haben. Merci beaucoup! Emmanuelle Perez und Felix Sefkow möchte ich zudem danken, dass sie mich auf dem Weg zu meiner Veröffentlichung mit viel Hilfe bei den wesentlichen Details unterstützt haben.

Mein großer Dank gilt auch allen Mitgliedern der H1 Kollaboration, die stets meinen meist halb-stündigen Vorträgen mit Interesse gefolgt sind. Ganz besonders möchte ich dabei den Mitgliedern der REX Gruppe bei H1 danken, die in etlichen Vorträgen immer wieder den Status meiner Arbeit begutachtet haben. Vielen Dank David South, Emmanuel Sauvan, Stefan Schmitt, Cristinel Diaconu, Jenny List, Prof. Joachim Meyer und Prof. Dietrich Wegner. David South und Stefan Schmitt möchte ich auch danken, dass Sie Teile dieses Manuskripts gelesen haben. Für zahlreiche Erklärungen und Diskussionen beim Kaffeetrinken danke ich auch Benno List, Eberhard Wünsch und Prof. André Schöning. Mein Dank gilt auch jenen H1 Mitgliedern, die zu einer sehr angenehmen Arbeitsatmosphäre beigetragen haben. Danke Voica Radescu, Karin Daum, Hieu Tran Trong, Ringaile Placakyte, Roman Kogler, Shiraz Habib, Michael Steder und Monica Dobre. Besonderer Dank gilt auch meinen Heidelberger Bürokollegen am DESY Eva Hennekemper, Andreas Jung, Klaus Urban, Michel Sauter, Florian Huber und Hayk Pirumov, sowie Fatih Argin und Charlotte Debus. Danken möchte ich auch Antje Hüttmann für ihr kritisches Interesse an meinen Ergebnissen.

Auch den Kollegen Alexander Tadday und Alexander Kaplan vom ILC Experiment in Heidelberg möchte ich danken für die gelegentlichen Abendessen in Hamburg.

Ein ganz besonderer Dank gilt auch meinen ATLAS Büro Kollegen in Heidelberg,

die mir bei jeglichen Fragen mit Rat und Tat zur Seite standen. Danke Felix Müller, Michael Henke, Veit Scharf, Sahill Poddar, Thorsten Dietzsch, Julia Hoffmann, George Victor Andrei, Rainer Stamen und Victor Lendermann für die nette Atmosphäre am KIP und die tollen Barbecues. Nicht zu vergessen Jürgen Stiewe für umfassende Erklärungen zu allen allgemeinen physikalischen Fragen.

Natürlich wäre ich heute nicht soweit, hätte es nicht diese besonderen Leute im ersten Semester gegeben. Allen voran danke ich Holger Rapp für seine Freundschaft. Zudem danke ich Richard Schmidt, Philipp Ronzheimer, Alexander Urich, Diana Vogel, Simon Sindbert, Caroline Müllenbroich, Hagen Triendl und Alexander Rohlf, sowie allen die ich hier vergessen haben sollte.

Auch meinen Hamburger Mitbewohnerinnen Anne und Claudia möchte ich für die schöne Zeit in Eimsbüttel danken. Natürlich dürfen meine Heidelberger Mitbewohner an dieser Stelle nicht fehlen. Danke Heike, Katharina, Franzi, Felix, Krys und Manu für unser gutes Verhältnis.

Ganz besonderer Dank gilt auch Guido und Marcus für ihre grenzenlose Gastfreundschaft. Rüdiger und Simone danke ich für das fantastische Fahrrad. Nicht zuletzt danke ich auch meinen Freunden aus der alten Heimat: Daniel, Eike, Johannes, Lars und den Leuten von the Overdraft.

Meiner Freundin Christine danke ich für ihre Geduld und ihr Verständnis, speziell während den schwierigen Phasen meiner Doktorarbeit.

Meinen zahlreichen Brüdern Oliver, Sebastian und Simon möchte ich für ihre unverwechselbare Art danken. Meiner kleinen Schwester Julia danke ich einfach dafür, dass es sie gibt.

Ohne meine Neffen und meine Nichte wüßte ich nicht wie schön es ist Onkel zu sein. Danke Jonas Elijah, Gianna Elaine und Jan Oliver.

Hier an letzter Stelle, möchte ich meinen Eltern Gabriele und Winfried ganz besonders danken. Ohne ihre liebevolle Fürsorge und einfach wunderbare Art wäre ich heute nicht derjenige der ich bin. Sie haben mich immer meine eigenen Entscheidungen treffen und meine eigenen Wege gehen lassen, und mir all die Unterstützung zukommen lassen, die ich gebraucht habe. Dafür möchte ich mich bei Euch bedanken!